



Ultrafast acoustic phonon and strain dynamics in ferroic materials

Ruizhe Gu

► To cite this version:

Ruizhe Gu. Ultrafast acoustic phonon and strain dynamics in ferroic materials. Materials. Le Mans Université, 2022. English. NNT : 2022LEMA1010 . tel-03772494

HAL Id: tel-03772494

<https://theses.hal.science/tel-03772494>

Submitted on 8 Sep 2022

HAL is a multi-disciplinary open access archive for the deposit and dissemination of scientific research documents, whether they are published or not. The documents may come from teaching and research institutions in France or abroad, or from public or private research centers.

L'archive ouverte pluridisciplinaire **HAL**, est destinée au dépôt et à la diffusion de documents scientifiques de niveau recherche, publiés ou non, émanant des établissements d'enseignement et de recherche français ou étrangers, des laboratoires publics ou privés.

THÈSE DE DOCTORAT DE

LE MANS UNIVERSITÉ
ÉCOLE DOCTORALE N° 596
Matière, Molécules, Matériaux
Spécialité : *Ondes et Matériaux*

Par

Ruizhe GU

Ultrafast acoustic phonon and strain dynamics in ferroic materials

Thèse présentée et soutenue à Le Mans, le 27 juin 2022

Unité de recherche : Institut des Molécules et Matériaux du Mans, UMR CNRS 6283

Thèse N° : 2022LEMA1010

Rapporteurs avant soutenance :

Matias BARGHEER Professeur, Universität Potsdam, Germany
Daniel LANZILLOTTI KIMURA Chargé de Recherche CNRS, HDR, C2N (UMR 9001), Université Paris Saclay

Composition du Jury :

Président :	Vincent GARCIA	Chargé de Recherche CNRS, HDR, UMPy CNRS/Thales, Université Paris Saclay
Examineurs :	Agnès HUYNH	Maître de conférences, UPMC INSP, Sorbonne Université
	Vincent GARCIA	Chargé de Recherche CNRS, HDR, UMPy CNRS/Thales, Université Paris Saclay
Dir. de thèse :	Pascal RUELLO	Professeur, IMMM (UMR CNRS 6283), Le Mans Université
Co-dir. de thèse :	Vitaly GOUSSEV	Professeur, LAUM (UMR CNRS 6613), Le Mans Université

Invité(s) :

Vincent JUVÉ Chargé de Recherche CNRS, IMMM (UMR CNRS 6283), Le Mans Université

Acknowledgement

Foremost, I would like to acknowledge Le Mans university and IMMM laboratory for the PhD offer and the financial support during the sanitary crisis, which helped me finish this dissertation. Also I would like to acknowledge The National Research Agency (ANR) for the financial support of the research project (ANR-18-VE09-0026) which covers my PhD career.

In the first place, I would like to express my sincere gratitude to my PhD director, Professor Pascal RUELLO, for his support and guidance during my PhD career. His vital advice and support help me improve my work and encourage me to overcome the difficulties encountered experimentally.

Secondly, I would also like to convey my gratitude to my PhD co-director Professor Vitaly GUSSEV for his generous advice on the theoretical issues related to my research topic.

Last but not least, I would like to express my appreciation to all the colleagues in NOVA team, especially Vicent JUVE, Gwenaëlle Vaudel and Mads WEBER for their support in the laboratory, as well as their generous assistance during the experiments.

In the mean time, I would like to extend my thanks to all the collaborators in various research groups for the preparation of different samples, for their valuable scientific discussions and for their support on both scientific comprehension and experimental realization.

I would also like to thank my friends for their help and support and finally, I want to express my recognition to my parents for their immense support and encouragement, their support strongly motivates me to carry on.

Contents

Acknowledgement	i
1 Introduction and research motivations	1
2 Ultrafast photoinduced strain: Theory and literature survey	5
2.1 A short overview of photostrictive materials and photoinduced strain . .	7
2.2 Generation and detection of ultrafast strain pulses and acoustic phonons	8
2.2.1 General equation of motion: case of the longitudinal acoustic wave generation and propagation	8
2.2.2 Mechanisms involved in ultrafast photogeneration process in solids . .	11
2.2.2.1 Thermo-elasticity (TE)	11
2.2.2.2 Deformation potential (DP)	13
2.2.2.3 Inverse piezoelectric process (IPE)	15
2.2.2.4 Electrostriction (ES)	17
2.2.2.5 Magnetostriction (MS)	18
2.2.3 Detection of ultrafast acoustic phonons and strain	19
2.2.3.1 Detection with optical pump probe method	19
2.2.3.2 Detection by X-ray diffraction	25
3 Experimental Methods	29
3.1 Ultrafast optical spectroscopy	31
3.1.1 Principle of ultrafast optical spectroscopy	31
3.1.2 Experimental setup	31
3.1.3 Image of the focused pump and probe beams	34
3.2 Time-resolved X-ray diffraction (TRXRD)	34
3.2.1 Description of detectors	36
3.2.2 Experimental setup for time-resolved X-ray diffraction with BiFeO ₃ single crystal	37
3.2.3 Experimental setup for time-resolved X-ray diffraction with thin BiFeO ₃ film	40
3.2.4 Time-resolved X-ray diffraction with asymmetric Bragg planes: method- ology for the extraction of both the longitudinal and shear strains . . .	42
3.2.4.1 Time-resolved diffraction with asymmetric Bragg planes in rhombo- hedral (001) _c BiFeO ₃ single crystal	43
3.2.4.2 Time-resolved diffraction with asymmetric Bragg planes in mono- clinic (110) _c BFO thin film	47

4 Photoinduced coherent acoustic phonons in germanium telluride (GeTe)	51
4.1 Introduction	53
4.2 Presentation of germanium telluride (GeTe)	54
4.2.1 GeTe as phase change material	54
4.2.2 Phase diagram of GeTe	55
4.2.3 Several physical properties of GeTe	58
4.3 State-of-art of photoinduced strain in GeTe and motivations	62
4.4 Experimental results and analysis	66
4.4.1 GeTe sample description	66
4.4.2 Raman scattering experiments in GeTe	67
4.4.3 Typical signal recorded in optical pump probe experiments	68
4.4.4 Calibration of the experiment	69
4.4.5 Photogeneration and detection of coherent acoustic phonons in amorphous & crystalline GeTe	72
4.4.5.1 Ultrafast carrier dynamics	73
4.4.5.2 Evolution of the acoustic phonon spectrum	75
4.4.6 Analysis and discussion: ultrafast non-thermal transport of energy	77
4.4.6.1 Simulation of the bipolar acoustic strain in GeTe	78
4.4.6.2 Heat diffusion contribution	81
4.4.6.3 Acoustic phonon dispersion	82
4.4.6.4 Nonlinear acoustic effect	83
4.4.6.5 Hot carrier diffusion contribution	84
4.5 Conclusion	87
 5 Photoinduced strain in BiFeO₃ based compounds	 89
5.1 Introduction	91
5.2 General properties of BiFeO ₃ : bulk and thin films	92
5.2.1 Physical properties of BiFeO ₃ bulk material	93
5.2.2 Physical properties of BiFeO ₃ thin films	97
5.3 Literature survey on photoinduced strain in BiFeO ₃ based materials	98
5.4 Experimental results	103
5.4.1 Study of photoinduced strain in (001) _c BiFeO ₃ single crystal	103
5.4.1.1 Characterization of [001] _c BiFeO ₃ single crystal	103
5.4.1.2 Study of coherent acoustic phonon in BiFeO ₃ by means of ultrafast optical spectroscopy	104
5.4.1.3 Photoinduced strain in a BiFeO ₃ single crystal by means of ultrafast time-resolved X-ray diffraction	105
5.4.1.4 Lattice dynamics and photoinduced strain microscopic mechanisms: models and discussion	110
5.4.1.5 Conclusion on the ultrafast light-induced strain dynamics in the BiFeO ₃ single crystal	118
5.4.2 Study of photoinduced strain in monoclinic BiFeO ₃ thin films	119
5.4.2.1 Preparation of a single domain BiFeO ₃ thin film	119
5.4.2.2 Study of coherent acoustic phonons in BiFeO ₃ by means of ultrafast optical spectroscopy	123

5.4.2.3	Study of ultrafast photoinduced strain in single domain BiFeO ₃ thin film by means of time-resolved X-ray diffraction	128
5.4.2.3.1	Characterisation of selected Bragg planes	128
5.4.2.3.2	Time-resolved X-ray patterns	128
5.4.2.4	Determination of photoinduced longitudinal (η_L) and shear (η_T) strain in single domain BiFeO ₃ thin film	133
5.4.2.5	Summary of results obtained by optical pump-probe and time-resolved X-ray diffraction experiments	135
5.4.2.6	Conclusion on the ultrafast light-induced phonons and strain dynamics in a single domain BiFeO ₃ thin film	139
5.5	Conclusion	139
6	Conclusions and perspectives	141
	Bibliography	145
A	X-ray beam path in the grazing incidence geometry	161
B	Optical pump fluence dependency of transient optical reflectivity in single domain BiFeO₃ thin film	163
C	θ-2θ scans for 4 chosen planes	165
D	Additional analysis of θ-2θ scans of time-resolved X-ray diffraction on single domain BiFeO₃ thin film	175

Chapter **1**

Introduction and research motivations

The photostrictive effect can be described as a conversion of light energy directly into mechanical energy (strain). It holds great promise for converting existing electrically-driven mechanical devices into devices controlled and driven by light. For this purpose, a profound understanding of light-matter interaction is required to envision to control electrostriction, piezoelectric effect, or magnetostrictive effect with light. Since its discovery in the 1960s, the photostrictive effect has been studied in semiconductors, ferroelectrics, organic polymers, chalcogenide glasses, and other materials. This concept of photostrictive effect has been summarized in the different reviews of C. Chen, Z. Yi [1] and of Kundys [2] as well, where the different techniques, selected materials as well as the applications are presented. Most of pioneer studies were conducted in a static regime with continuous light source (cw sources).

With the advent of ultrashort pulse lasers such as femtosecond lasers, the situation has evolved towards the development of ultrafast photostriction also called ultrafast photoinduced strain or sometimes picosecond acoustics. The development of ultrafast science, which is the study of physical phenomena and processes that occur on extremely small time scales, such as attoseconds, femtoseconds and picoseconds, has of course concerned other fundamentals branches of solid state physics. For example, the use of pulsed lasers has opened new perspectives for time-domain measurements of ultrafast electronic and magnetic processes in diverse materials. The experimental investigations in the ultrafast science community, is usually based on a pump-probe scheme: a pump pulse stimulates the matter, triggering diverse dynamics (electron, phonon, spin), and a probe pulse detects, as a function of a controlled time, the progression of transient particle states. This provides a unique way to understand the different out-of-equilibrium processes involving the collision, recombination and transport of these particles. Among all these processes, knowing how the lattice is distorted after a short interaction with a laser is one of the basic and fundamental information we discuss in this PhD manuscript. The light-induced strain can be probed either with optical means such as the phonon-photon collision in a Brillouin scattering process or by diffraction with a pulsed X-ray sources (plasma source, synchrotron, X-free electron laser). Note that the electron microscopy can also be used to evaluate the effect of visible light on materials lattice parameters.

In this manuscript, we investigate the ultrafast light-induced strain, i.e. ultrafast photostriction, in two important families of materials. The first one is germanium telluride (GeTe), a member of chalcogenide glass which is also a central element of the phase-change material family (PCM). The second material is a multiferroic oxide perovskite, the bismuth ferrite (BiFeO_3). Both these materials are ferroic materials holding many promising applications [1]. In particular, driving some of their functional properties with light remains a challenge both from the fundamental and application points of view.

Phase-change-materials (PCMs) have become an important part of modern computing architectures [3], from arithmetic to neuromorphic computing and, more recently, matrix-vector multiplications for machine-learning and artificial-intelligence applications [4, 5]. The need for fast writing-erasing processes in emerging GHz-THz information technologies could benefit from ultrafast photoinduced transformation in the future. For that, it requires a better understanding of electron and phonon

dynamics at short time and space scales in nonequilibrium states for which only partial understanding has been reported in the literature. Then, in this thesis the results of the investigation of photocarriers and acoustic phonon dynamics will be carried out by using a time-resolved optical pump-probe method. In particular, we will discuss these dynamics in the amorphous and crystalline state of GeTe, which are the two switchable states used in the applications of PCM.

The BiFeO₃ is a multiferroic materials which holds many promising applications since lattice, polar and magnetic orders can be coupled [6]. Such material is then a multifunctional material. With a band gap $E_g < 3$ eV, the photoexcitation process appears quite “easy” compared to other commercial ferroelectric materials (PbTiO₃, BaTiO₃). For these reasons, many photonic applications could be expected. Among them, BiFeO₃ appears as an interesting source of acoustic nanowaves in GHz-THz frequency scale. The generation of GHz-THz acoustic phonons has already been reported in the literature but at the moment, the community has only a partial view on the distortion of the crystallographic unit cell under light excitation. This full description is though a necessary step. To address this challenge, in the thesis, different BiFeO₃ materials are studied such as a single crystal and a single domain thin film BiFeO₃ and both ultrafast optical spectroscopy and time-resolved X-ray diffraction are employed to reveal the process of ultrafast photoinduced strain in these latter systems.

This dissertation is organized with the following chapters.

In chapter 2, the principle of photoinduced strain phenomena will be described with two main parts dedicated to the generation and the detection of ultrafast strain and coherent acoustic phonons. The possible mechanisms that might be involved in the generation processes will be briefly introduced as well.

In chapter 3, a detailed description will be given concerning the experimental methods employed during my PhD research. To study the photoinduced ultrafast dynamics of electron and phonon, optical pump-probe method using a femtosecond laser source will be presented. Another setup, based on the time resolved X-ray diffraction will be also introduced. The latter one is located at the French synchrotron facility, Synchrotron SOLEIL (CRISTAL Beamline).

In chapter 4, experimental results on the photogeneration and photodetection of coherent acoustic phonon in both amorphous and crystalline GeTe will be presented. In particular, a discussion about the interplay between the hot carriers and the acoustic phonon generation will be developed.

In chapter 5, the investigations on the photogeneration and detection of longitudinal and shear strain in different BiFeO₃ based samples will be presented. Rhombohedral BiFeO₃ single crystal and monoclinic BiFeO₃ thin film will be considered. In this chapter we will present a comprehensive study where ultrafast optical spectroscopy and time-resolved X-ray diffraction are combined to reconstruct the temporal evolution of the unit cell of photoexcited BiFeO₃.

A conclusion and some perspectives will be presented at the end of this manuscript.

Ultrafast photoinduced strain: Theory and literature survey

Contents

2.1	A short overview of photostrictive materials and photoinduced strain	7
2.2	Generation and detection of ultrafast strain pulses and acoustic phonons	8
2.2.1	General equation of motion: case of the longitudinal acoustic wave generation and propagation	8
2.2.2	Mechanisms involved in ultrafast photogeneration process in solids	11
2.2.3	Detection of ultrafast acoustic phonons and strain	19

2.1 A short overview of photostrictive materials and photoinduced strain

Photostriction is the physical phenomenon involving the generation of strain, namely “striction”, in a material when it receives a light excitation, referring to the term “photo”. Said differently, this corresponds to a conversion of the light energy into a mechanical energy. The term “photostriction” comes from the 70s when pioneering experiments were conducted in ferroelectric and semiconductor materials using continuous light excitation [2]. The materials that have a photostrictive effect under light-matter interactions are called photostrictive materials. These materials constitute an important class of functional smart materials since light can drive and/or modulate different solid properties [2]. Besides the evident thermal effect (thermal expansion), the photostrictive subclass involves light-matter interactions that result in non-thermal sample deformation. Depending on the type of material under investigation, the photostriction can have different physical origins. In electrically polar materials, photostriction is defined as photoinduced lattice deformation coupled with a change in the internal electric field, resulting in an inverse piezoresponse in photovoltaic compounds [7–9]. Light can cause huge volumetric changes in organic polymers by causing a change in molecular structure [10]. Light can also modify the electric field in polar semiconductors via free charges production at the surface [11, 12] causing an elastic strain due to the piezoelectric effect. Light irradiation of non-polar semiconductors, such as Si [13] or Ge [14–16], causes an excess of electron-hole pairs in the conduction band and holes in the valence band, causing deformation of the sample directly or via a change in atomic bonds.

When the light action is not continuous, but has a defined duration, the photoinduced strain in the material leads to the generation of acoustic waves whose frequency range can be very broad from MHz up to THz [17, 18]. This is the field of photoacoustics, optoacoustics and picosecond acoustics, i.e. ultrafast acoustics. The latter domain of research is at the core of this PhD. In section 2.2, the basics of ultrafast generation and detection of acoustic phonon (ultrafast photoinduced strain) will be presented which concern mainly phenomena occurring at sub-nanosecond timescale.

In the correspondent chapter, two typical photostrictive materials will be discussed in detailed, which are germanium telluride (GeTe), one of the members of chalcogenide glasses in the category of polar semiconductor (refer to **Chapter 4**); and bismuth ferrite (BiFeO_3) single crystal and thin film, the typical multiferroic ferroelectric material (refer to **Chapter 5**).

2.2 Generation and detection of ultrafast strain pulses and acoustic phonons

2.2.1 General equation of motion: case of the longitudinal acoustic wave generation and propagation

To give the salient feature of the motion equation and the generation processes, we present first the situation of an isotropic medium. The more complex situation found in anisotropic medium (that will be the case of BiFeO₃ materials under investigation) will be discussed in a more focused way in the dedicated **Chapter 5**.

When an optical radiation impinges onto a material, a part of the optical energy is absorbed and a stress is set up; acoustic waves are then excited by sources distributed through the volume of the medium. This effect of the light is taken into account as a source term (σ_{pi} , pi stands for photoinduced) in the following wave equation (2.1). In general, this equation is tensorial, but in the following, for simplicity, we describe only the generation of a plane longitudinal acoustic wave [17]:

$$\frac{\partial^2 u}{\partial t^2} = \frac{1}{\rho} \frac{\partial \sigma(z, t)}{\partial z} = \frac{1}{\rho} \frac{(\partial \sigma_{elas}(z, t) + \sigma_{pi}(z, t))}{\partial z} \quad (2.1)$$

With $\sigma_{elas} = \rho C_a^2 \frac{\partial u}{\partial z}$ is the elastic stress (elastic response of the material) where $u(z, t)$ describes the displacement of the particles inside the material, C_a denotes the longitudinal acoustic velocity, ρ is the volumetric mass density. This former equation can be rewritten as:

$$\frac{\partial^2 u}{\partial t^2} - C_a^2 \frac{\partial^2 u}{\partial z^2} = \frac{1}{\rho} \frac{\partial \sigma_{pi}(z, t)}{\partial z} \quad (2.2)$$

The photoinduced stress σ_{pi} can be composed of different contributions including thermoelasticity (TE), deformation potential (DP), inverse piezoelectricity (IPE), electrostriction (ES) and magnetostriction (MS) that will be discussed latter on. The spectrum of the emitted acoustic phonon strain, noted as $\eta(z, \omega)$ can be theoretically found by applying integral transforms of this wave equation as documented in the literature [2, 7–9].

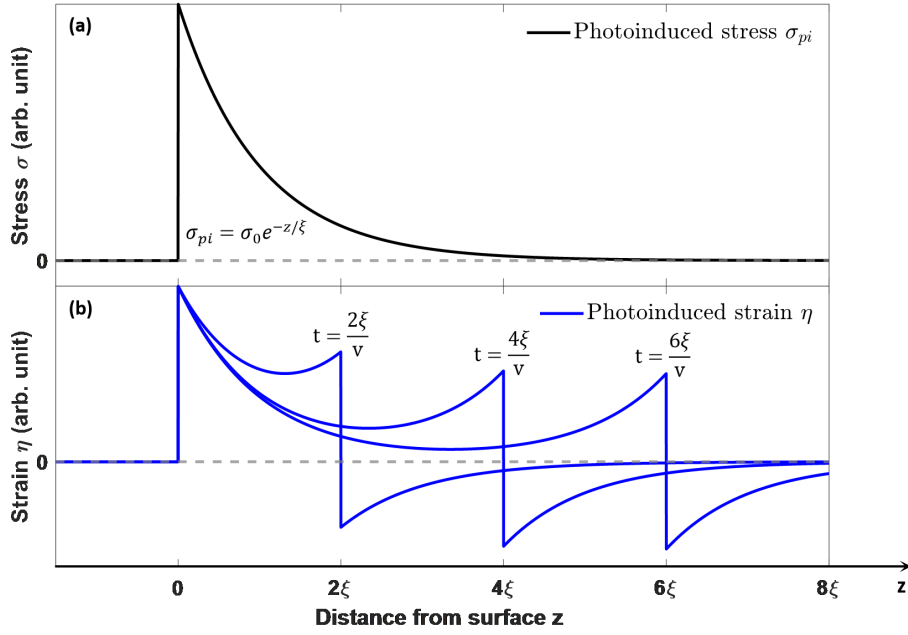


Fig 2.1: (a) Sketch of the photoinduced stress σ in the region of the pump penetration depth in a semi-infinite system. (b) Photoinduced strain η emitted from the surface and propagating perpendicularly to the irradiated surface while the elastic strain stays near the surface, which compensates the photoinduced stress.

Beside the aforementioned general case, the expression of the photoinduced strain can be obtained for a simple situation where, for a semi-infinite system, the stress is limited to the penetration depth of the pump beam (ξ) as shown in **Fig 2.1(a)** (in the following we will write $\alpha = 1/\xi$). In the case of photoexcitation in a thin film, if the condition $\xi \gg d$ is achieved, where d is the thickness of the sample, then the following description of photoinduced stress and strain is also correct. Moreover, we consider in this model that the photoinduced stress has a temporal component defined by the Heaviside function $H(t)$. So that $\sigma_{pi} = \sigma_0 e^{-\alpha z} H(t)$. This means that the photoinduced stress exists for $t > 0$. This is typically the case when a laser leads to a thermal heating of a material for which, at $t = 0$ the light is absorbed by the material and the subsequent heating effect is considered as a long-living effect compared to time window of observation of phonons. With all these hypotheses, we can rewrite the equation (2.2) after a Fourier transform and by applying a space derivative ($\partial/\partial z$) as:

$$\frac{\partial^2 \eta(z, \omega)}{\partial z^2} + \frac{\omega^2}{C_a^2} \eta(z, \omega) = \alpha^2 \eta_0 e^{-\alpha z} H(\omega) \quad (2.3)$$

where $\eta_0 = \sigma_0 / \rho C_a^2$.

Without the right hand side of this linear partial differential equation, the general solution becomes:

$$\eta(z, \omega) = A e^{iqz} + B e^{-iqz} \quad (2.4)$$

where $\omega = C_a q$. Since there is no source far from the surface, the term Be^{-iqz} is excluded. With the right hand side of the partial differential equation (2.3), we can find a particular solution that follows the shape of the initial photoinduced strain (i.e. $\eta \propto e^{-\alpha z}$). The final general solution is then:

$$\eta(z, \omega) = Ae^{iqz} + \eta_0 \frac{\alpha^2}{\alpha^2 + q^2} e^{-\alpha z} H(\omega) \quad (2.5)$$

Considering the free surface does not undergo any stress at any moment ($\rho C_a^2 \eta(z = 0, w) + \sigma_{pi}(z = 0, w) = \rho C_a^2 [\eta(z = 0, w) - \eta_0 H(\omega)] = 0$), we can deduce the coefficient A . The final solution becomes:

$$\eta(z, \omega) = \eta_0 \left(\frac{q^2}{\alpha^2 + q^2} e^{iqz} + \frac{\alpha^2}{\alpha^2 + q^2} e^{-\alpha z} \right) H(\omega) \quad (2.6)$$

By inverse Fourier transform, the strain has the form [19]:

$$\eta(z, t) = \eta_0 \left[e^{-z/\xi} \left(1 - \frac{1}{2} e^{-vt/\xi} \right) - \frac{1}{2} e^{-|z-vt|/\xi} \text{sgn}(z - vt) \right] \quad (2.7)$$

Noting that at infinite time ($t \rightarrow \infty$), the strain expression in the vicinity of the free surface becomes $\eta(z, t) = \eta_0 e^{-z/\xi}$. This corresponds to the static contribution of the photoinduced strain, i.e. the non-propagating one. A typical time dependence of the light-induced strain is shown in **Fig 2.1(b)**.

This model is a simplification of more complex situations where the stress σ_{pi} can exhibit a more complex spatial and temporal dependence if the deposition of the absorbed energy is associated for instance to the diffusion of carriers and phonon [17]. In that case the solution of equation (2.1) is non linear in the integral form if non-reducible to space functions [17].

2.2.2 Mechanisms involved in ultrafast photogeneration process in solids

In this subpart the different physical mechanisms that are at play in the photoinduced strain generation process are briefly summarized. Extensive discussion of this physics can be found in [17] and also, in a shorter way, in the recent review [20].

2.2.2.1 Thermo-elasticity (TE)

Thermoelasticity is a phenomenon that involves a variation of the temperature of a solid and its corresponding elastic response. This mechanism is well recognized in the world of laser ultrasonics and has already been completely explained elsewhere in prior review and experimentally proved (at least in the static domain) (kHz, MHz regimes are discussed in Ref. [18]).

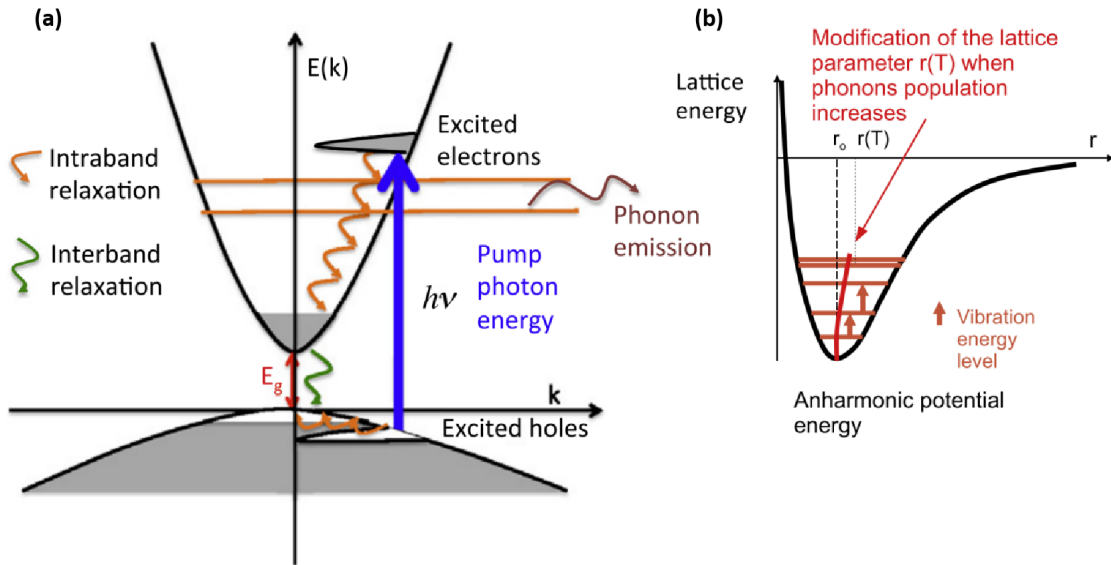


Fig 2.2: (a) Schematic view of the intraband relaxation process (indicated by orange arrows) which leads to incoherent phonon emission which contributes to the local increase of the phonon pressure. The interband process is sketched by the green arrow. (b) Modification of the mean interatomic distance $r(T)$ when the vibrational energy increases in an lattice anharmonic potential [20].

Lattice anharmonicity is required to generate a volume change with increasing temperature, i.e. thermal expansion [21]. The reciprocal effect is also feasible in the presence of an acoustic field, which causes an increase or decrease of lattice temperature in the matter. The mean lattice parameter $r(T)$ increases when vibrational energy rises (i.e. phonon population rises) only if the interatomic potential is anharmonic (r_0 is the lattice parameter at $T = 0$ K). This increase of phonon population comes from the energy release from the electronic subsystem (the first that absorbs the energy when the material is excited with a visible laser) to the lattice (phonon) subsystem. This transfer of energy is accomplished via intraband electron-phonon

coupling and non-radiative interband recombination as shown in **Fig 2.2(a)**. The increase of this vibrational energy in an anharmonic potential induces a shift of the mean lattice parameter from r_0 to $r(T)$ as sketched in **Fig 2.2(b)**.

The anharmonicity is defined by a non-zero thermal expansion coefficient β . The thermoelastic strain in an isotropic medium exhibiting a temperature variation of δT_L , is then:

$$\eta = \frac{\delta V}{V} = 3\beta\delta T_L \quad (2.8)$$

where β is the linear thermal expansion coefficient. The correspondent internal pressure, also known as thermoelastic pressure, is described as:

$$dP_{TE} = 3B\beta\delta T_L \quad (2.9)$$

where B is the bulk modulus. The isotropic thermoelastic (TE) stress is given by integrating equation (2.9) with respect to the variation of lattice temperature, as shown below:

$$\sigma_{TE} = -3B\beta\Delta T_L \quad (2.10)$$

For an anisotropic material, the tensorial expression becomes :

$$\sigma_{ij}^{TE} = -C_{ijkl}\beta_{kl}\Delta T_L \quad (2.11)$$

where C_{ijkl} is the stiffness tensor and the β_{ij} the tensorial thermal expansion coefficient. The contribution of TE can be easily observed in metals. For photogenerated acoustic waves with frequency up to hundreds of GHz (period much longer than the electron–phonon coupling time), it is indeed the dominating mechanism [22]. The fast intraband relaxation process leads to a transfer of electronic energy to the phonon subsystem which then leads to a rapid thermal heating of the metal. The out-of-equilibrium electrons (hot electrons) that contribute to the electronic pressure (Sommerfeld pressure) have a lifetime of roughly 1 ps. This makes possible the emission of THz acoustic phonons in metals through this “non-thermal process”. However, it is very difficult to detect these waves before they are attenuated [22].

Such electronic contribution is crucial in semiconductors. Contrary to metals indeed, the photogeneration of the coherent acoustic phonons (CAP) due to the contribution of TE can be hardly observed in semiconductor, because the excitation and contribution of CAP at GHz-THz range in semiconductors is mostly dominated by deformation potential (DP) (electronic contribution), which will be described in the following section.

2.2.2.2 Deformation potential (DP)

The deformation potential mechanism is the mechanism that relates the change in energy of the electronic distribution to the strain in a solid. In general, if the electronic distribution is altered (by the action of light or any other external disturbance), and regardless of the materials, the interactions between cations and electrons, cations and cations, and electrons and electrons are altered at the microscopic level. The interatomic forces are, in fact, fully reliant distribution of charges. If the interatomic forces are altered, the equilibrium positions of the atoms in the lattice start to change, leading to the emission of acoustic phonons. The fundamental relation between the strain and the change of the electronic energy is often written as [23, 24]:

$$\frac{\delta V}{V} = \frac{\delta U}{d_{eh}} \quad (2.12)$$

where d_{eh} (eV) denotes the deformation potential coefficient, U is the electronic energy and $\delta V/V$ is the strain, with V representing the volume. This equation emphasizes the direct relationship between changes in lattice strain and changes in electronic energy. If one of this parameter (δV or δU) is changed, the second will be changed as well. In reality, this relation has to be discussed taking into account the quantum nature of solids.

In the atomic point of view, a strain noted as $\eta(z.t)$, which can be either longitudinal or shear strain, arises when atoms in a crystal display relative displacements. Such strain modifies the distance between atoms or bond angle are changed, which change the orbitals overlap, inducing a shift in the electronic levels (δU). If the energy levels are shifted (up or down), the population of electrons adjusts their energy according to the quantum statistic law. As a result, the electronic density at different energy levels varies. Conversely, when an electron moves through a crystal or when electron-hole pairs are formed, the local density of carriers at specific energy levels k in the Brillouin zone is altered (**Fig 2.3(a)**). This means that the strength of the overlapping between orbitals is altered locally (enhanced or diminished according to the nature of the electronic bands involved). As a result, the strength of the atomic bonds in this region changes. This causes the atoms to be displaced, resulting in the creation or annihilation of some phonons.

The molecular picture can also be considered in order to describe the deformation potential mechanism. When carriers are excited by light, they are promoted towards empty electronic states, new bonds are formed or destroyed depending on the type of chemical bond (bonding or anti-bonding), leading to an increase or decrease of the interatomic distance.

For an isotropic medium, the photoinduced stress can be described as:

$$\sigma_{DP} = - \sum_k \delta n_e(k) E_k \gamma_k = \sum_k \delta n_e(k) \frac{\partial E_k}{\partial \eta} \quad (2.13)$$

where $\delta n_e(k)$ and E_k are the variation of the electronic concentration and the energy

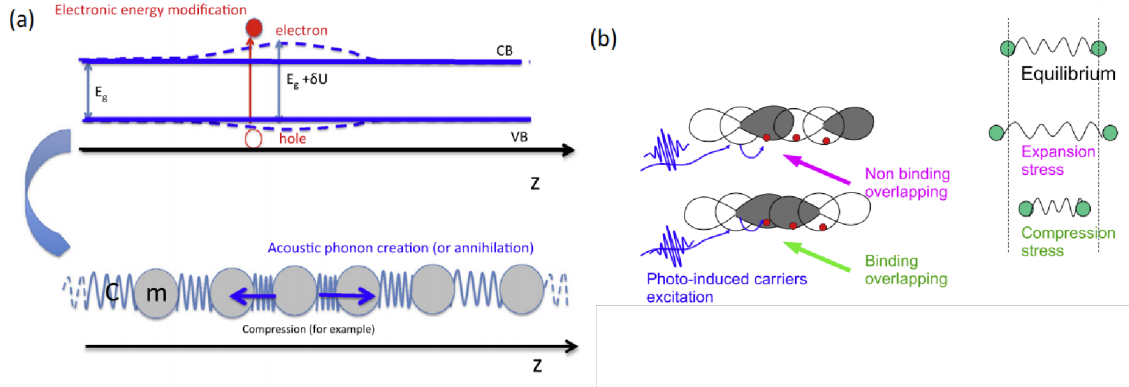


Fig 2.3: (a) Description of deformation potential with a semiconductor band structure. The highest occupied level of valence band (VB) and the lowest unoccupied level of conduction band (CB) is shown by blue solid line. When the electronic distribution is disorganised (for example the electron (red circle)-hole (white circle) pairs are excited), the interatomic interaction is changed (shown by dashed line), which causes the interatomic distances to change. This means that strain appears, hence phonons are created or annihilated, which can also be modeled with 1D atomic chain, with atomic mass m and interatomic elastic stiffness C . (b) Deformation potential in molecular point of view: the electrons are represented by red dots. Depending of the nature of the orbitals that are populated by photo-excited electrons, binding or non-binding orbitals overlapping occurs leading to either decrease or increase of interatomic distances. The model can also be considered as 2 binding particles, the non-binding and binding overlapping results in expansion and compression stress [20].

at level k , γ_k is the Grüneisen coefficient and $\frac{\partial E_k}{\partial \eta}$ is called the deformation potential parameter (d_{eh}).

In the case of solids with forbidden energy band separating occupied and non-occupied levels (semiconductors, oxides), the expression of the deformation potential stress can be written in a simple way. Indeed, if we assume that the out-of-equilibrium electrons (holes) are only situated in the bottom (top) of the conduction (valence) band, then equation (2.13) can be reduced to the following simplified equation:

$$\sigma_{DP} = N \frac{\partial E_g}{\partial \eta} = -d_{eh} N = -d_e n_e - d_h n_h \quad (2.14)$$

with N the photoexcited carriers (electrons and holes) concentration, E_g the band gap and d_{eh} the electron-hole deformation potential parameter. The deformation potential stress can be also separated into two contributions coming from electron (d_e) and hole (d_h), where n_e and n_h correspond the concentration of photoexcited electrons in the bottom of the conduction band and that of holes in the top of valence band, with the associated deformation potential parameters (d_e and d_h) respectively.

We can remind that if a solid is photo-excited with a photon energy that is equal

to the band gap (E_g), the light-induced stress will be purely of deformation potential nature (as long as the photoexcited carriers do not recombine). In that case, there is no intraband relaxation processes as depicted in **Fig 2.2(a)** and then no thermoelastic contribution. In semiconductors, if the exciting photon has an energy quanta $h\nu$ larger than the band gap, then the photoinduced stress is usually the summation of the thermoelastic contribution (proportional to $3B\beta[N(h\nu - E_g)/C_L]$, where C_L is the lattice heat capacity) and that of the deformation potential ($d_{eh}N$).

2.2.2.3 Inverse piezoelectric process (IPE)

There is a link between the strain (η) and the macroscopic electric field E that might exist inside non-centrosymmetric materials: this phenomenon is called piezoelectricity. When a non-centrosymmetric lattice is subjected to a strain, the barycenters of positive and negative charges may be separated, resulting in the appearance of a macroscopic polarization P . There is a variety of thermodynamic relationships that can be used to explain these phenomena [25]. When a material is subjected to an external stress, the direct piezoelectric effect (defined by the tensor d_{ij}) is represented in contracted tensorial form as:

$$P_i = d_{ij}\sigma_j, \text{ with } \begin{cases} i &= 1, 2, 3 \\ j &= 1, 2, 3, 4, 5, 6 \end{cases} \quad (2.15)$$

The inverse piezoelectric effect, which corresponds to the appearance of an internal strain if the material is submitted to an electric field E , is characterized by the tensor p_{ij} and can be described as:

$$\eta_j = p_{ij}E_i \quad (2.16)$$

While the induced stress can also be described by E and piezoelectric moduli e_{ij} :

$$\sigma_j = e_{ij}E_i \quad (2.17)$$

These piezoelectric properties are frequently used in research and industry, with piezoelectric transducers being used as generator and detector of acoustic waves for non-destructive testing. The perovskite family of materials, such as PZT and PMN, are among the most widely used ones [26]. When these materials are subjected to an external bias, they become sources of acoustic waves. Compared to the two other properties discussed previously, i.e. TE and DP, the light-controlled piezoelectric (PE) mechanism has distinctive features. The sign of photoinduced stress is directly related to the direction of applied electric field, which means that if the electric field changes its direction (from $E > 0$ to $E < 0$ and vice versa) then the photoinduced stress also changes its sign. If an electric field is applied for two opposite crystallographic orientations, the photoinduced stress will be oriented in opposite directions. This feature contrasts sharply with thermoelastic or deformation potential processes, in which a 180° shift in crystallographic orientation has no effect on the stress. This contrast can be explained by comparing the piezoelectric tensor p_{ij} , which is a third

rank tensor, with the deformation potential coefficient d_{eh} and the linear thermal expansion coefficient β_{ij} tensors, which are both second rank tensors.

The frequency range of the electrically driven piezo-transducers is usually limited to the kHz and MHz range. But it has been shown recently that it is possible to drive lattice motion with such effect at the GHz frequency [27–29]. A principle of this light-induced inverse piezoelectric effect is shown in **Fig 2.4(a)**.

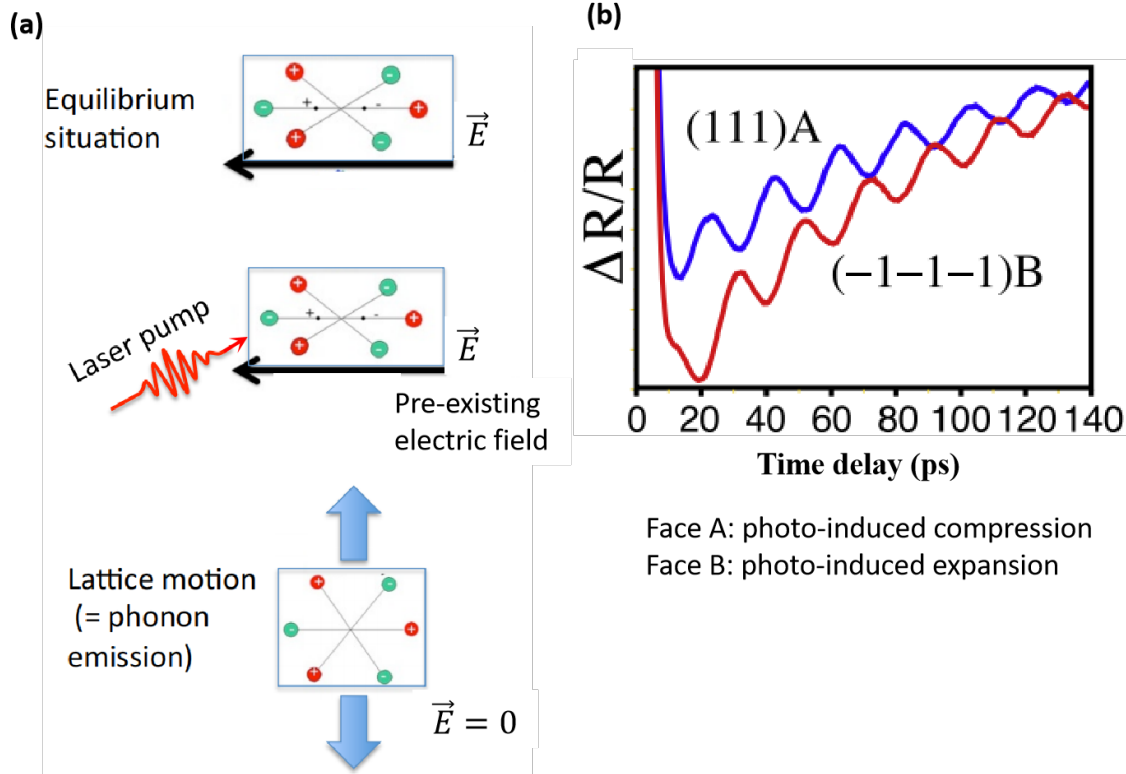


Fig 2.4: (a) Principle of the light-induced phonon (strain) excited by the inverse piezoelectric effect. Cations and anions are represented by red and grey circles, with their corresponding barycenter shown in black dots. (b) Photoexcitation of CAP by inverse piezoelectric effect in piezoactive [111] GaAs wafer. The sign of the emitted acoustic strain changes when the crystallographic direction is reversed from A to B, i.e. when the pre-existing built-in electric E in the vicinity of the free surface of GaAs is reversed [27].

As shown in **Fig 2.4(b)**, the piezoelectric effect can be observed by analyzing the time-resolved Brillouin signal in a highly p-doped GaAs [111] crystal ([111] direction is the piezoactive direction). The preexisting built-in field in this scenario is oriented from the surface to the inside of the sample, regardless of the crystallographic face (A or B). As a result, when photoexcited carriers are injected near the surface with a pump wavelength of 400 nm, the built-in field is rapidly screened, and acoustic pulses are emitted. That change of the strain polarity is illustrated in the change of the sign of the Brillouin signal, shown by the oscillating components in **Fig 2.4(b)**.

2.2.2.4 Electrostriction (ES)

The ultrafast photoinduced stress that occurs when a medium is transparent (no light absorption) is caused by the electrostriction mechanism. This effect is allowed for any symmetry point group. The incident pump laser electric field can polarize the medium, causing the orbitals to deform. This can even be thought as centrosymmetry breaking caused by the light electric field, which leads to a second order piezoelectric effect. That is why, according to the electric field E , electrostriction is a second order phenomenon, whereas piezoelectric effect (non zero first order piezoelectric tensor) is a first order phenomenon.

When the orbitals are distorted, both the electron distributions and orbitals overlapping will be modified, which lead to the modification of the electron density ρ and the dielectric constant ϵ . The variation of dielectric constant can be linked to the variation of density as shown below:

$$\Delta\epsilon = \frac{\partial\epsilon}{\partial\rho}\Delta\rho \quad (2.18)$$

The modification of the dielectric constant ($\Delta\epsilon$) leads to a modification of the electromagnetic density of energy with:

$$\Delta w = \frac{1}{2}\Delta\epsilon E^2 = \frac{1}{2}\frac{\partial\epsilon}{\partial\rho}\Delta\rho E^2 \quad (2.19)$$

The variation of this density of electromagnetic energy Δw is associated to a work (W) provided by the material, with $W = -P\Delta V = \Delta w \times V$. Considering $\Delta\rho/\rho = -\Delta V/V$, the electrostriction stress can then be described as:

$$\sigma_{ES} = -\frac{1}{2}\rho\frac{\partial\epsilon}{\partial\rho}E^2 \quad (2.20)$$

with $\rho\frac{\partial\epsilon}{\partial\rho}$ denoting the electrostrictive coefficient. In the general case, σ_{ES} has a tensorial nature. And it is worth mentioning that the electrostriction phenomenon depends on the polarization of the incident electric field, hence in consequence, in general, both longitudinal or transverse acoustic phonons can be photogenerated [30, 31]

One of the experimental results has been obtained by H. Tanaka *et al* by measuring the complex resonance of spectra of acoustic phonons in CS_2 with a transient optical grating method that selectively generates-detects the GHz mode as shown in **Fig 2.5** [32].

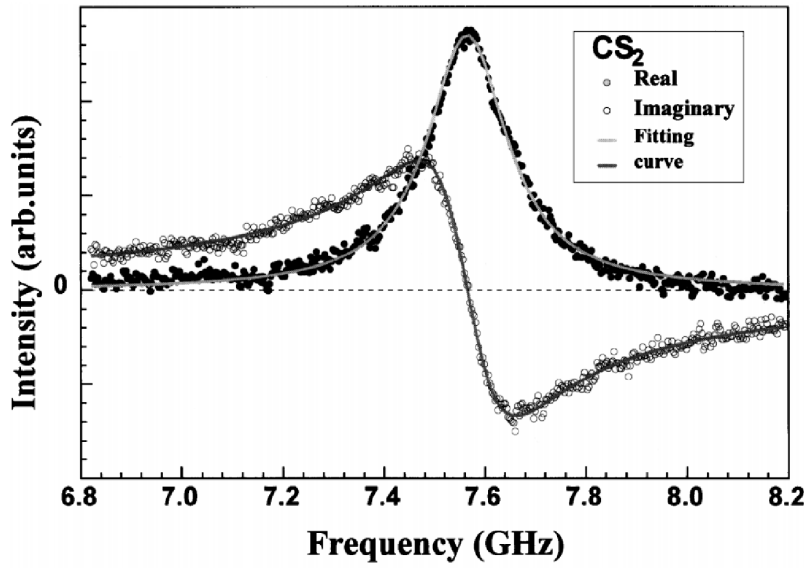


Fig 2.5: Real and imaginary parts of anti-Stokes Brillouin spectra of CS₂ at T = 300 K at $k/2\pi = 0.197 \text{ } \mu\text{m}^{-1}$. The typical behavior of complex resonance spectra of forced oscillators can be clearly seen [32].

Note that electrostriction is also very well known at low frequency (from DC up to kHz regime) for several ferroelectric materials such as ferroelectric relaxors (PMN). In that case, the strain is also proportional to the square of the applied external electric field ($\propto E^2$) and can reach a remarkably large strain up to 1% [33].

2.2.2.5 Magnetostriction (MS)

The interaction of magnetization and mechanical stress are referred to as magnetostriction. The electrostrictive coupling involved in the light and matter interaction (transparent material) has its counterpart connected to the modification of the magnetic energy. Similarly to the previous relation, we can write:

$$\sigma_{MS} = -\frac{1}{2}\rho\frac{\partial\mu}{\partial\rho}B^2 \quad (2.21)$$

where μ and B are the magnetic permeability and the magnetic field. Usually this stress is much smaller than the electrostrictive one since the magnetic permeability is usually small [17].

The efficient magnetostrictive effect is usually reported in magnetic materials and at low frequency [34]. When a ferromagnetic substance is magnetized, it exerts a stress on its surroundings, causing its dimensions to change if they are free to do so. This effect is usually due to a magneto-elastic effect where the spin-orbit coupling has a particular role. The spin gets an orientation under an external magnetic field (usually at low frequency), and through the spin-orbit ($L.S$) coupling, affects the orbitals which in turn affects the lattice. Conversely, if a ferromagnetic undergoes an external stress which affects the lattice structure, the bonds length and angles will be modified which can directly affect the exchange coupling. In that case, it

can be expected that the state of magnetization will change. These two phenomena, the change of dimensions produced by a change in magnetization, and the change in magnetization with stress are both different aspects of the same thing [35, 36].

In the context of ultrafast magnetism, and for a situation where the material absorbs the light, which is contrary to the magnetostrictive effect discussed in equation (2.21), it has been shown recently that the ultrafast light-induced demagnetization (modification of spin and angular momentum distribution) can be accompanied by a short strain pulse emission: magnetoelastic process. Iron [37] as well as Terfenol material, which is used in many application field such as actuators, acoustic and ultrasonic transducers, and magneto-mechanical sensors [38], have been investigated [39].

2.2.3 Detection of ultrafast acoustic phonons and strain

The photoinduced strain can be detected by an optical mean, by X-ray or by an electron beam. The first situation corresponds to the so-called optical pump-probe method that we have used in this PhD for studying both GeTe (**Chapter 4**) and BiFeO₃ (**Chapter 5**) materials. The second approach is called optical pump and X-ray probe (or commonly named time-resolved X-ray diffraction) and has been applied to study BiFeO₃ based compounds (**Chapter 5**). The last one is called time-resolved electron diffraction.

2.2.3.1 Detection with optical pump probe method

Detecting the strain with an optical light (in the spectrum range from near infrared to ultraviolet), involves the physics of the dielectric response. In that case, the strain will be detected by the interaction of photon with phonon: said differently, the strain will be detected through the modification of the refractive index induced by the strain (photoelastic effect). A sketch of the scattering of a probe photon by an acoustic pulse is shown in **Fig 2.6(a)**. While the optical response can be in general described either for an optical transmission or reflection geometry, we will concentrate in the following to the second case that corresponds to the experimental work in this PhD.

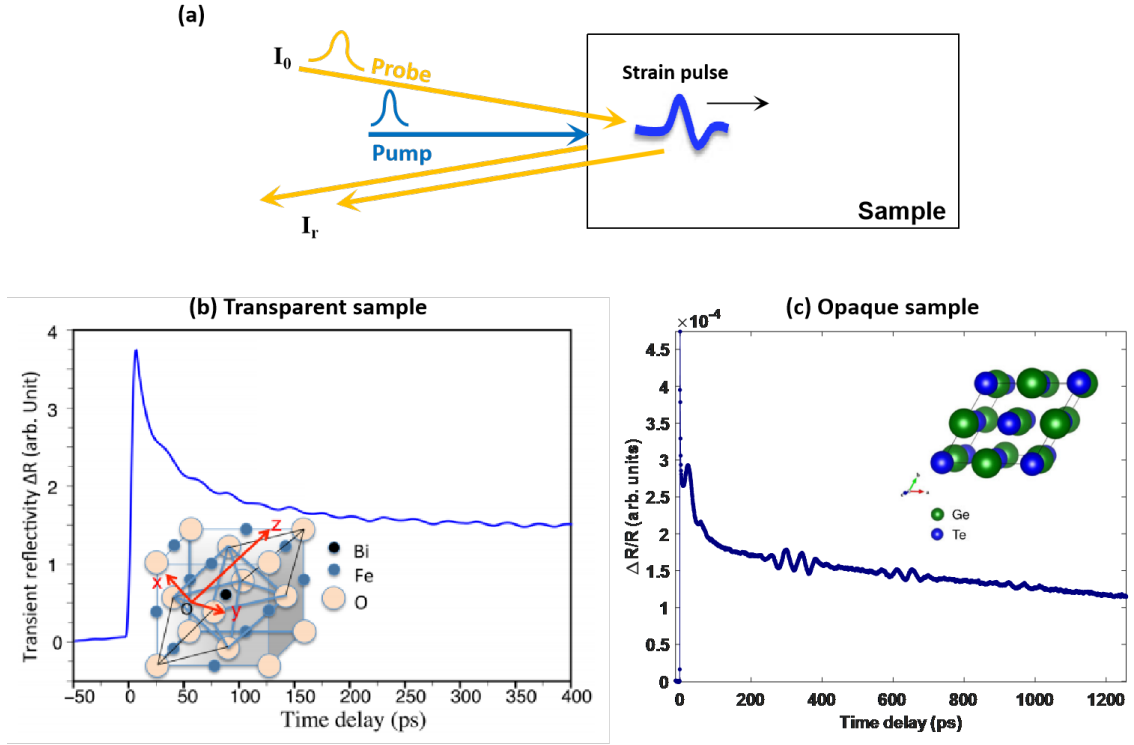


Fig 2.6: (a) Simplified sketch of optical pump-probe experiments where the probe beam is partially reflected at the free surface and partially scattered by the strain pulse: heterodyne detection. (b) Typical transient optical reflectivity measured in a transparent material at the probe wavelength (BiFeO₃ as an example). The long-lining oscillations are Brillouin oscillations. (c) Typical transient optical reflectivity measured with a sample being opaque at the probe wavelength (GeTe thin film deposited on SiO₂/Si as an example). A sequence of 3 acoustic echoes are detected at the free surface of GeTe (limited probe penetration) each time the acoustic pulse comes back to the surface

For a probe with a normal incidence on a semi-infinite medium, the complex optical reflectivity reads:

$$\begin{aligned} r &= \frac{1 - \tilde{n}_{sample}}{1 + \tilde{n}_{sample}} \\ &= r_0 e^{i\phi} \end{aligned} \quad (2.22)$$

By applying the small perturbation to the system, due for instance to the presence of strain, the optical refractive index will be slightly modified by δr , hence the Fresnel coefficient will become:

$$r' = r + \delta r = r_0(1 + \rho)e^{i(\phi + \delta\phi)} \quad (2.23)$$

where ρ and $\delta\phi$ correspond to the modifications in amplitude and in phase. And the reflectivity (noted as $\delta r/r$) can be described as:

$$\begin{aligned} \frac{\delta r}{r} &= \frac{r' - r}{r} \\ &= \frac{r_0(1 + \rho)e^{i(\phi + \delta\phi)} - r_0e^{i\phi}}{r_0e^{i\phi}} \\ &= \frac{(1 + \rho)e^{i\delta\phi} - 1}{1}, \text{ with Taylor expansion} \\ &\simeq (1 + \rho)(1 + i\delta\phi) - 1 \\ &= \rho + i\delta\phi + i\rho\delta\phi, \text{ with } i\rho\delta\phi \ll \rho, i\delta\phi \\ &\simeq \rho + i\delta\phi \end{aligned} \quad (2.24)$$

If we detect only the variation of the intensity of the reflected probe beam, then the transient optical reflectivity signal becomes $\Delta R/R$, with:

$$\begin{aligned} \frac{\Delta R}{R} &= \frac{r'r'^* - rr^*}{rr^*} \\ &= \frac{r_0^2(1 + \rho)^2 - r_0^2}{r_0^2} \\ &= \frac{(1 + \rho)^2 - 1}{1}, \text{ with Taylor expansion} \\ &\simeq 2\rho \\ &= 2\Re\left(\frac{\delta r}{r}\right) \end{aligned} \quad (2.25)$$

All the modulation of the optical properties induced by the presence of the strain is contained in ρ .

The strain field (η) associated to the acoustic phonons pulse modifies the refractive index n as a result of the photoelastic effect (see **Fig 2.6(a)**). The refractive index modulation ($dn/d\eta$) affects the optical reflectivity of the probe beam. It is feasible to monitor the transient optical reflectivity $\Delta R/R$ in the time domain by a delay line and then detect the propagation of the photogenerated acoustic phonons by controlling the arrival time of the probe beam relative to the excitation by the pump beam. This technical element will be presented in the **Chapter 3**. For the detection we can separate the case of a transparent material from that of an opaque medium.

Transparent material and general formulation

Due to momentum conservation during the interaction between the probe light and the moving acoustic phonons, only acoustic phonons at the Brillouin frequency (f_B) are detected. In the back-scattered configuration (see **Fig 2.7(a)**), that momentum conservation is achieved for $q = 2k_{probe}\cos(\psi)$ where q is the momentum of acoustic phonon and k_{probe} the photon momentum of the probe beam while ψ is the angle, both in the medium, between the probe beam momentum and the acoustic phonon momentum. Considering the quasi-elastic approximation $k_i \approx k_s$ (the phonon energy is much smaller than the visible photon energy), the Snell-Descartes law is $\sin(\theta) = n\sin(\psi)$, with n the refractive index of the medium, θ the incident angle of the probe beam, and the incident medium is air. The final momentum conservation law leads to:

$$\begin{aligned} q &= 2k_0\sqrt{n^2 - \sin^2(\theta)} \\ &= \frac{2 \times 2\pi\sqrt{n^2 - \sin^2(\theta)}}{\lambda} \end{aligned} \quad (2.26)$$

with λ the probe wavelength in air.

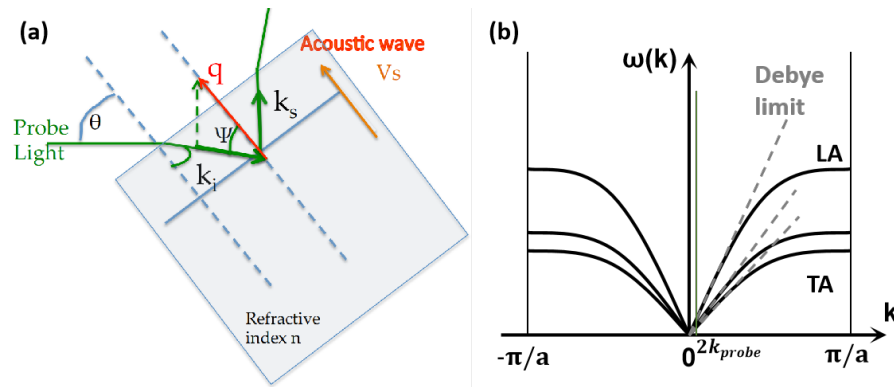


Fig 2.7: (a) Description of the momentum conservation during the scattering of a photon by a phonon. (b) Sketch of phonon dispersion diagram revealing only acoustic branches in the first Brillouin zone. The Brillouin frequencies are detected at the $2k_{probe}$.

Since the wave vector of the probe beam k_{probe} is much smaller than the edge of first Brillouin zone in phonon dispersion law (**Fig 2.7(b)**), we consider that the Debye approximation is valid thus the phonon dispersion law can be simplified as:

$$2\pi f_B = V_S q \quad (2.27)$$

where V_S denotes the sound velocity in BiFeO₃, the Brillouin frequency f_B is finally given by:

$$f_B = \frac{2 \times V_S \times \sqrt{n^2 - \sin^2(\theta)}}{\lambda} \quad (2.28)$$

From the experimental point of view, this translates to a sinusoidal modulation of the optical reflectivity ΔR in the time domain for the experimental signal (see **Fig 2.6(b)**). If the photon is scattered by longitudinal and shear phonons, then a superposition of modulations at different frequencies appears. This is the typical case shown in **Fig 2.7(b)** where three acoustic modes can be detected with the probe beam having a wavevector $2k_{probe}$. It is worth noting that from an optical point of view, these oscillations can be viewed as optical interferences between the beam reflected by the free surface and the beam scattered by the moving acoustic front. These two beams are shown in **Fig 2.6(a)**. The free surface and the moving acoustic front could be recognized as a Fabry-Perot interferometer.

Such interference can be also described as an heterodyne detection as shown by Thomsen et al [19]. In that case the electric field arriving in the detector is the sum of the reflected one ($E_r = r_0 E_0$) and the scattered part ($E_s = r_0 E_0 \rho e^{i\delta\phi}$). This can be written as [19]:

$$\begin{aligned} E &= r_0 E_0 + r_0 E_0 \rho e^{i\delta\phi} \\ &= r_0 E_0 + r_0 E_0 a \int_0^\infty \eta(z, t) e^{-2ik_{probe} \cos(\psi) z} dz \end{aligned} \quad (2.29)$$

where $e^{-2ik_{probe} \cos(\psi) z}$ in the second term represents the scattered part of the electric field consistently with **Fig 2.7(a)**. z represents the direction of propagation of the acoustic phonon which is perpendicular to the irradiated surface. The coefficient a represents the efficiency of the photoelastic effect and also depends on the optical parameters of the system which can be determined by solving the Maxwell equation.

At the first order (neglecting ρ^2 and $\rho\delta\phi$), the amplitude of intensity that arrives in the photodetector becomes:

$$\begin{aligned} E \cdot E^* &= r_0^2 E_0^2 + 2r_0^2 E_0^2 \rho \\ &= r_0^2 E_0^2 + 2r_0^2 E_0^2 \Re \left[a \int_0^\infty \eta(z, t) e^{-2ik_{probe} \cos(\psi) z} dz \right] \end{aligned} \quad (2.30)$$

where $k_{probe} = 2\pi n/\lambda$. As a result, the variation of the optical reflectivity coefficient becomes:

$$\begin{aligned}\Delta R/R &= 2\rho \\ &= 2\Re[a \int_0^\infty \eta(z, t) e^{-2ik_{probe}\cos(\psi)z} dz]\end{aligned}\quad (2.31)$$

The strain pulse $\eta(z, t)$ possesses a given spectrum dependent on the generation process. A Fourier decomposition gives:

$$\eta(z, t) = \int_{-\infty}^{+\infty} \eta(q) e^{i(qz - \omega_q t)} e^{-\alpha_q t} dq \quad (2.32)$$

where $\eta(q)$ and ω_q describes the Fourier component and the frequency in the q space respectively.

We finally arrive to:

$$\Delta R/R \propto 2\Re[a \int_0^\infty \int_{-\infty}^{+\infty} dz dq \eta(q) e^{i(q - 2k_{probe}\cos(\psi))z} e^{-i\omega_q t} e^{-\alpha_q t}] \quad (2.33)$$

For a k vector which is real (i.e. transparent medium), this integral over z is non zero only if $q - 2k_{probe}\cos(\psi) = 0$. This approach is thus consistent with the Brillouin selection rule and we arrive finally to:

$$\Delta R/R \propto \eta(q_B) \cos(2\pi f_B t) e^{-\alpha_{q_B} t} \quad (2.34)$$

Opaque material and general formulation

If a medium is optically opaque, due to the existence of an imaginary part in the refractive index at the probe wavelength, the probe wavevector k_{probe} is no more purely real. In that case, detection cannot be reduced to the single Brillouin mode. A complete discussion of the transition from a detection in transparent to opaque material is given in Ref [27].

The general description of the transient optical reflectivity has been established in the literature by Thomsen *et al* [19]. The final signal is described by a temporal convolution of the acoustic strain pulse with the distribution of the probe electric field in the z direction. For a semi-infinite system, the theoretical transient complex reflection coefficient is [19, 40, 41]:

$$\begin{aligned}\frac{\delta r}{r} &\simeq \rho + i\delta\phi \\ &\simeq -2ik_0\delta z + \frac{4ik_0\tilde{n}}{1 - \tilde{n}^2} \frac{d\tilde{n}}{d\eta} \times \int_0^\infty \eta(z, t) e^{2ik_0\tilde{n}z} dz\end{aligned}\quad (2.35)$$

In (2.35), the first term is purely imaginary, which corresponds to a phase shift due to the motion of the free surface δz , with $k_{probe} = \tilde{n}k_0$ and $k_0 = 2\pi/\lambda_{probe}$ is the probe wave vector in air. The second term is proportional to the photoelastic coefficient $\frac{d\tilde{n}}{d\eta}$. $\tilde{n}_{sample} = n + i\kappa$ is the complex refractive index of the sample. This theoretical expression is established by solving the Maxwell equation with a perturbative approach where refractive index is developed in a Taylor series with, at the first order, $\Delta n(z, t) = \frac{dn}{d\eta}\eta(z, t)$ and $\Delta\kappa(z, t) = \frac{d\kappa}{d\eta}\eta(z, t)$ [19].

In opaque semi-infinite materials, the photoinduced strain pulse can be detected only when the strain leaves the free surface where the light-matter interaction took place. This is possible of course if the probe beam slightly penetrates in the solids. This is opposite to the situation found for transparent materials where the Brillouin oscillations appear as long-living oscillations due to the fact that the probe beam interacts during all the propagation of the acoustic phonon pulse (in the limit of phonon attenuation at least). One example of the opaque material is GeTe as shown in **Fig 2.6(c)**. We can see at short time scale (~ 0 -50 ps), an oscillating signal coming from the waves that leave the free surface. That signal then vanishes and re-appears at time delay around 300 ps. Since this GeTe material is a thin film, the acoustic phonons are reflected on the GeTe/substrate interface and can come back to the surface where the first echo is actually detected at that time of 300 ps with other successive periodic echoes. Thanks to the emergence of acoustic echoes, the study of photogenerated acoustic phonons in opaque materials becomes possible.

2.2.3.2 Detection by X-ray diffraction

The photoinduced strain within a material can also be detected by X-ray diffraction, the principle is illustrated in **Fig 2.8(a)**. Crystalline structures are characterized by a periodic arrangement of atoms (or ions) in a three-dimensional periodic lattice. As crystals are composed of regularly spaced atoms, each crystal contains planes of atoms (Bragg planes) which are separated by a constant distance called interplanar distance d_{hkl} , which is characteristic of the crystalline species.

The phenomenon of diffraction involves the scattering of X-rays by atoms of a crystal and specific interferences of the X-ray beams scattered by the Bragg planes for certain incidence angles of the X-ray beam. It is worth mentioning that such interferences are possible for the X-ray beam wavelengths scaling with the interplanar distances d_{hkl} (h, k, l stands for the Miller indices). Bragg's law states that the distance between atomic planes has a quantitative relationship with scattered ray reinforcement at a particular wavelength, which is [43]:

$$2d_{hkl}\sin(\theta) = n\lambda \quad (2.36)$$

where n is an integer. When a collimated beam of monochromatic X-rays of wavelength λ strikes a crystal, the rays penetrate and are partially scattered from many successive planes within the crystal. There will be a critical angle, θ , at which rays are scattered from successive planes will be in phase along a front as they leave the crystal for a given interplanar spacing, d_{hkl} . For simplification we consider the first order of the diffraction, thus $n = 1$.

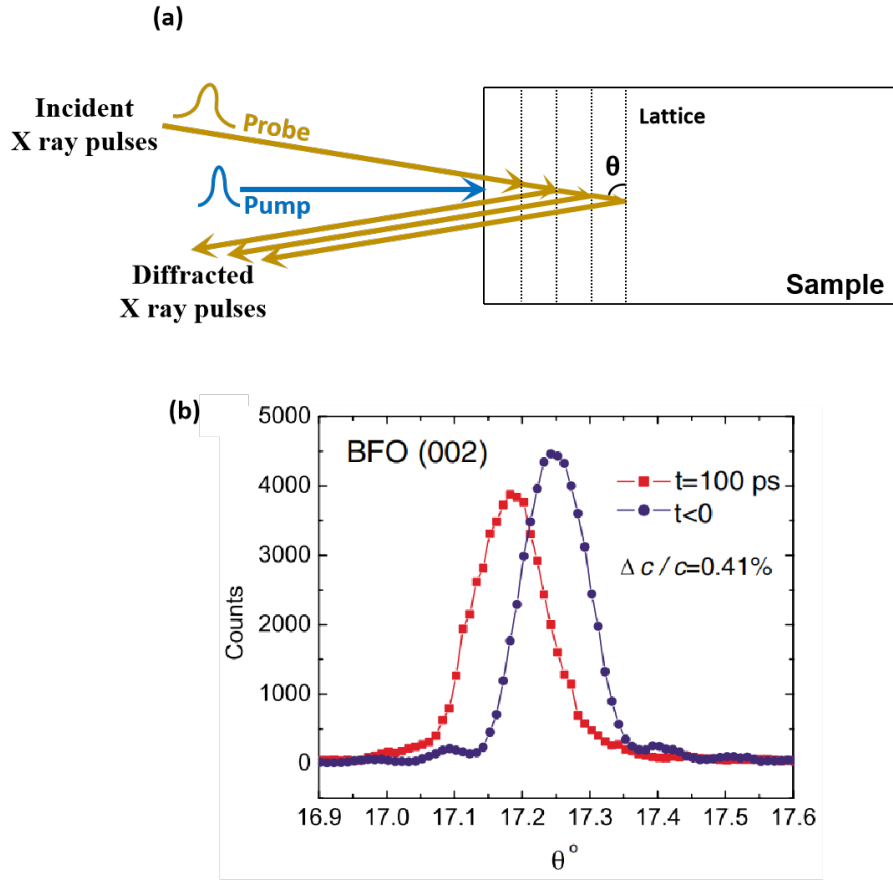


Fig 2.8: (a) Simplified sketch of X-ray diffraction experiments. In this specular geometry, the diffraction is realized with Bragg planes (hkl) parallel to the surface. (b) $\theta-2\theta$ scans of the BiFeO₃ (002) Bragg reflection before and 100 ps after excitation by a 50 fs laser pulse with a central wavelength of 400 nm and the absorbed fluence of 3.2 mJ.cm⁻² [42].

When the pump beam strikes onto the sample, part of its energy is absorbed and transferred to the lattice, hence the equilibrium position of the lattice is disturbed due to the light-induced strain. In consequence, the Bragg condition of the chosen planes (hkl) will be changed. The variation of the Bragg angle can be detected by the conventional $\theta-2\theta$ method, as shown in **Fig 2.8(b)** for the case of a photoexcited BiFeO₃ thin film. We can see the shift ($\Delta\theta$) of the Bragg peak measured at the time delay of 100 ps. Such experiment permits to determine the photoinduced strain in the crystal, i.e. the relative variation of the interplanar distance $\Delta d/d$, by the following equation:

$$\frac{\Delta d}{d} = -\frac{\Delta\theta}{\tan(\theta)} \quad (2.37)$$

Beside this specular ($\theta-2\theta$) geometry, we will present in **Chapter 3** another geometry called grazing incidence geometry. The Bragg condition remains of course always the central equation to extract the strain. Finally, we note that in the

Fig 2.8(a), we present the situation of a variation of interplanar distance for Bragg planes parallel to the surface. In this geometry, we measured the so-called out-of-plane strain. We will discuss such method in **Chapter 3** showing the possibility to measure both in-plane (shear strain) and out-of-plane (longitudinal strain) strain, in a more detailed manner.

Experimental Methods

Contents

3.1	Ultrafast optical spectroscopy	31
3.1.1	Principle of ultrafast optical spectroscopy	31
3.1.2	Experimental setup	31
3.1.3	Image of the focused pump and probe beams	34
3.2	Time-resolved X-ray diffraction (TRXRD)	34
3.2.1	Description of detectors	36
3.2.2	Experimental setup for time-resolved X-ray diffraction with BiFeO ₃ single crystal	37
3.2.3	Experimental setup for time-resolved X-ray diffraction with thin BiFeO ₃ film	40
3.2.4	Time-resolved X-ray diffraction with asymmetric Bragg planes: methodology for the extraction of both the longitudinal and shear strains	42

3.1 Ultrafast optical spectroscopy

3.1.1 Principle of ultrafast optical spectroscopy

The ultrafast optical spectroscopy, also known as ultrafast pump-probe method, involves 2 laser beams to achieve the photogeneration of acoustic strain and to detect the propagation of the strain inside a material. The principle is illustrated in **Fig 3.1**.

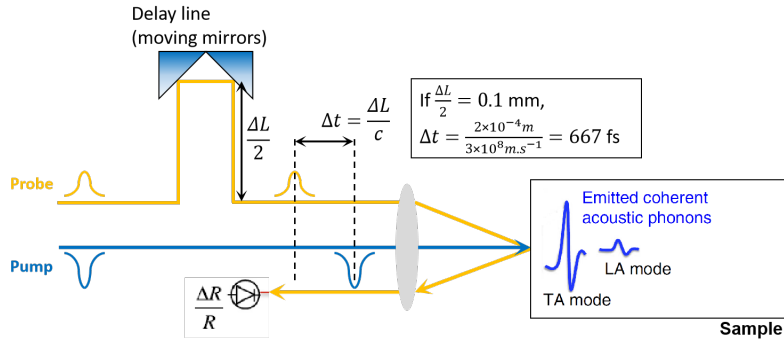


Fig 3.1: Principle of ultrafast pump-probe setup. An optical delay (i.e. change of the optical path by a moving mirror) is introduced by the delay line, which induces a temporal delay between the pump and the probe beam. For illustration, the delay line is here mounted into the optical path of probe beam but in experimental setup, the delay line is applied to the optical path of pump beam. For a displacement of the moving mirrors of 0.1 mm, a temporal delay of $\Delta t = 667 \text{ fs}$ is obtained between the arrival time of the probe beam with respect to that of pump beam.

The principle is the following: a first laser beam (pump beam) is focused on a material where an ultrafast dynamics is triggered (electron excitation, phonon generation, etc...). A second beam (probe beam) is also focused at the same point and the variation of the reflected (or transmitted) intensity ($\Delta R/R$) is analysed by a photodetector. By moving the mirrors on the delay line, this transient reflectivity $\Delta R/R$ is measured at different time delays corresponding to different time delays between the pump and the probe pulse arrivals on the material.

3.1.2 Experimental setup

A picture of the experimental setup built at IMMM laboratory is shown in **Fig 3.2**. **Fig 3.3** represents the schematic illustration with detailed information on each used optical element and instrument. This setup has been used for investigating both GeTe and BiFeO₃ materials. A laser source based on Ti:Sapphire mode-locked solid state laser (Chameleon Ultra II) is used.

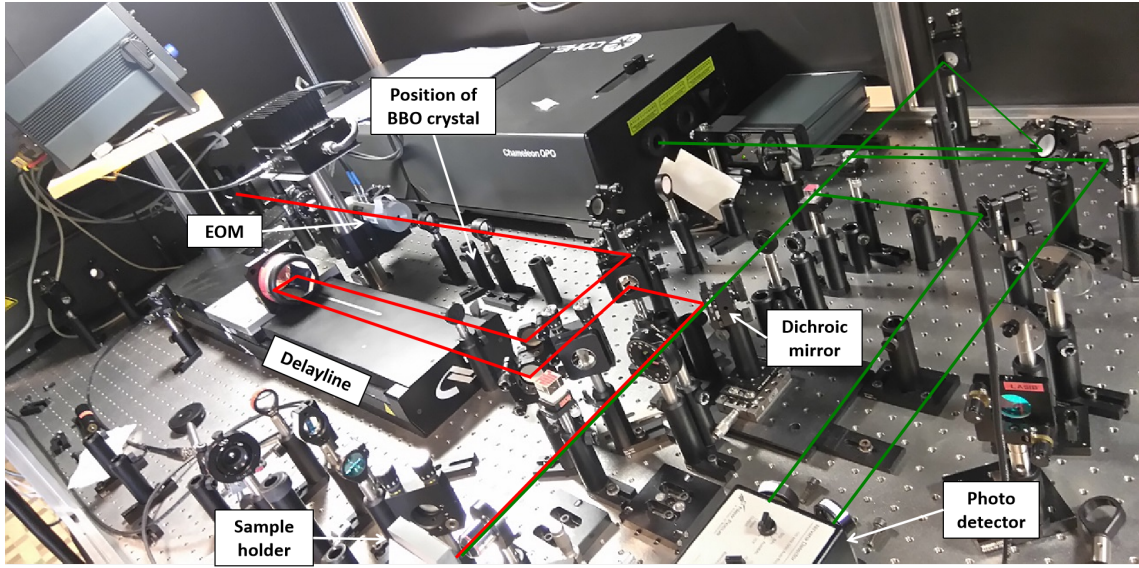


Fig 3.2: Picture of experimental setup established at IMMM. The pump beam is showed in red solid lines and green solid lines for the probe beam.

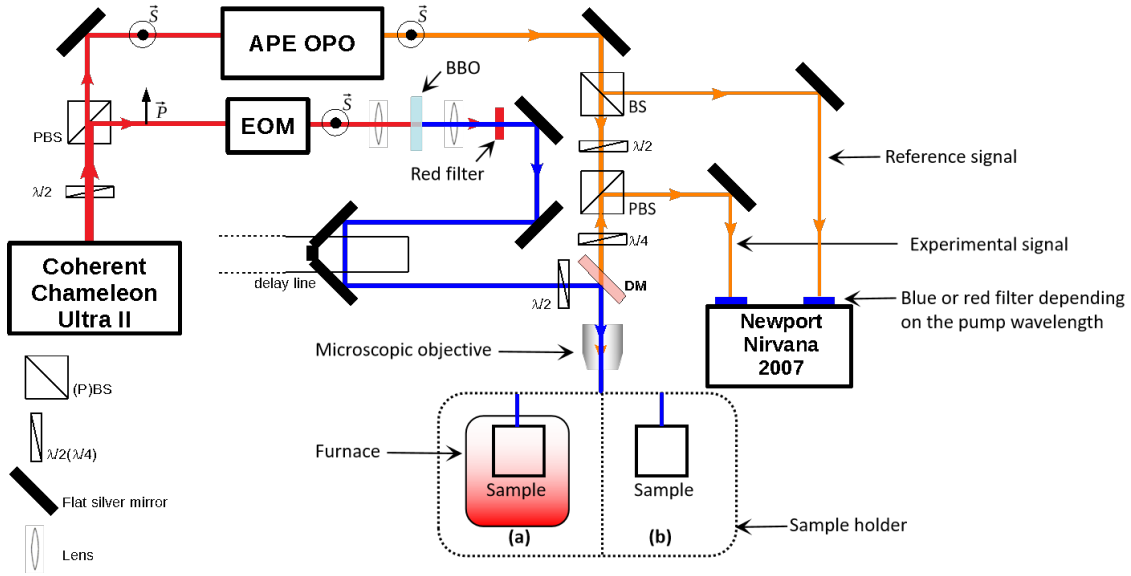


Fig 3.3: Schematic illustration of the ultrafast pump-probe setup used within IMMM laboratory. For illustration, a pump-probe setup using BBO crystal is displayed. Since the output wavelength of the laser source has been set to 830 nm (red solid line). The pump wavelength after the BBO crystal becomes 415 nm (blue solid line). And the probe wavelength is set to 587 nm (orange solid line). In order to use original pump wavelength, both the BBO crystal and the red filter need to be removed. If the experiments takes place at temperature that is different from the room temperature, configuration (a) will be used, otherwise for the experimnets at room temperature configuration (b) is selected.

The output wavelength of the laser source has been set to 830 nm. The pulse duration is around 140 fs and the repetition rate is of 80 MHz, i.e. laser period

between 2 successive laser pulses is of 12.5 ns [44]. The laser beam is splitted into 2 beams by using a half-wave plate and a polarized beam splitter (PBS). One beam is sent to an optical parametric oscillator (OPO) [45], and will serve later as probe beam. Throughout the experiments, the probe wavelength has been usually set to 587 ± 1 nm. The probe beam that comes out from the OPO will then be sent to a neutral beam splitter (BS), one will be sent directly to the photodetector as reference (Reference signal indicated in **Fig 3.3**). Another beam will be sent to another half-plate to adjust the horizontal polarization to go through the second PBS. Then a quarter plate transforms the linear polarized beam into a circular polarized beam by aligning the neutral axis of the plate at 45° with respect to the polarization of incident beam. This probe beam is then sent on the sample. Different focusing optical elements are used such as objectives having magnification of 4 to 10. After the reflection on the sample, the probe beam with clockwise(counter-clockwise) incident polarization becomes counter-clockwise(clockwise). In that case, when this reflected beam goes into the quarter plate, it is transformed into a vertical (linear) polarized beam. In that case, the PBS “extracts” this reflected probe beam which is at the end sent to the photodetector (Experimental signal as shown in **Fig 3.3**). We use the Nirvana auto-balanced photoreceiver model 2007 which is connected to the lock-in amplifier [46]. We work in auto-balanced configuration that gives the output signal which can be calculated with probe and reference optical signal. This balanced signal is then sent to the lock-in detection amplifier (SR signal recovery).

Another beam, serving as pump beam, is sent to an electro-optic modulator (EOM) to modulated at a frequency of 160 kHz. In this case the EOM works as amplitude modulation, based on the polarization rotation. The EOM is coupled with lock-in amplifier, which is also connected to the photodetector for the synchronised detection process. Before entering the delay line, the modulated pump beam is sent to an afocal system constructed by 2 lenses of the same or different focal length. On the one hand, such system permits to adjust the collimation of the pump beam; on the other hand, according to the experimental sample, the photon energy need to be adjusted, and in order to do so, we insert BBO crystal (β -BaB₂O₄) at the focal plane of the afocal system. By adjusting the orientation of the BBO crystal, a blue beam (415 nm) is obtained by the second harmonic generation (SHG) process. During the experiments with the pump wavelength in blue, 1 mm BBO crystal is used, which gives an conversion coefficient over 15 % when the BBO crystal position is optimized. In the use of blue wavelength as pump, a red filter will be added right after the afocal system. After the SHG, the pump beam is sent into the delay line. The pump and the probe beam will meet at the dichroic mirror (DM), which also allows to adjust the overlap of two beams. The dichroic mirror transmits the probe beam while the pump beam is reflected. The DM can also serve to reject the reflected pump beam when we work in normal incidence.

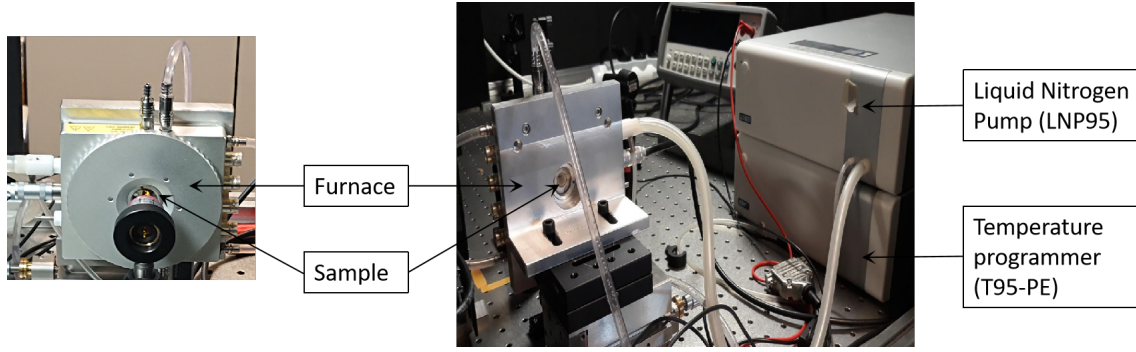


Fig 3.4: Photos of front (left) and back (right) face of the furnace available in IMMM laboratory. The associated temperature control system is also shown on the right. In order to perform optical pump-probe experiments under different temperature condition, the sample is placed inside the furnace.

The sample is mounted on a mechanically mobile stage with (x,y,z) displacement directions. A temperature control system (Linkam T95PE/LNP95 [47]) is installed, when necessary, in order to perform experiments under different temperature conditions (see configuration (a) in **Fig 3.3**). A photo of the instruments is given in **Fig 3.4**. During the experiments only water circulation is used for the cooling process. Such furnace has been used to study GeTe material only. The investigation of BiFeO₃ were performed at room temperature (configuration (b) in **Fig 3.3**).

3.1.3 Image of the focused pump and probe beams

In order to obtain the correct incident fluence of pump and probe pulses at the sample position, the irradiated section is measured with a CMOS camera (DCC1645C, Thorlabs [48]). For the pump wavelength at 415 nm and probe wavelength at 587 nm, the images recorded with the CMOS camera and the results of the Gaussians fit are shown in **Fig 3.5**.

The laser works in fundamental TEM₀₀ mode and the laser beams have a Gaussian shape. Because of the construction of the beam path, the laser beams that arrive on to the sample might be distorted, as shown in **Fig 3.5**. In this case both the horizontal (ω_{1/e^2}^x) and vertical (ω_{1/e^2}^y) diameter have been measured at the intensity of 13.5 % ($1/e^2$) of the peak value. We have $\omega^x = 24.9 \mu\text{m}$ and $\omega^y = 15 \mu\text{m}$ for the pump beam, $\omega^x = 8.28 \mu\text{m}$ and $\omega^y = 8.49 \mu\text{m}$ for the probe beam. As for the radiation section at focal plane of the microscopic objective, it is calculated to be $1173 \mu\text{m}^2$ for the pump, and $220 \mu\text{m}^2$ for the probe.

3.2 Time-resolved X-ray diffraction (TRXRD)

The time-resolved X-ray diffraction experiments has been performed at Synchrotron SOLEIL facility on the CRISTAL beamline in collaboration with Dr. Claire Laulhé and Dr. A. Jarnac. The experiments were performed in the low- α mode, with hard X-ray pulses of 7.155 keV energy and 10 ps of duration [49, 50]. This time-

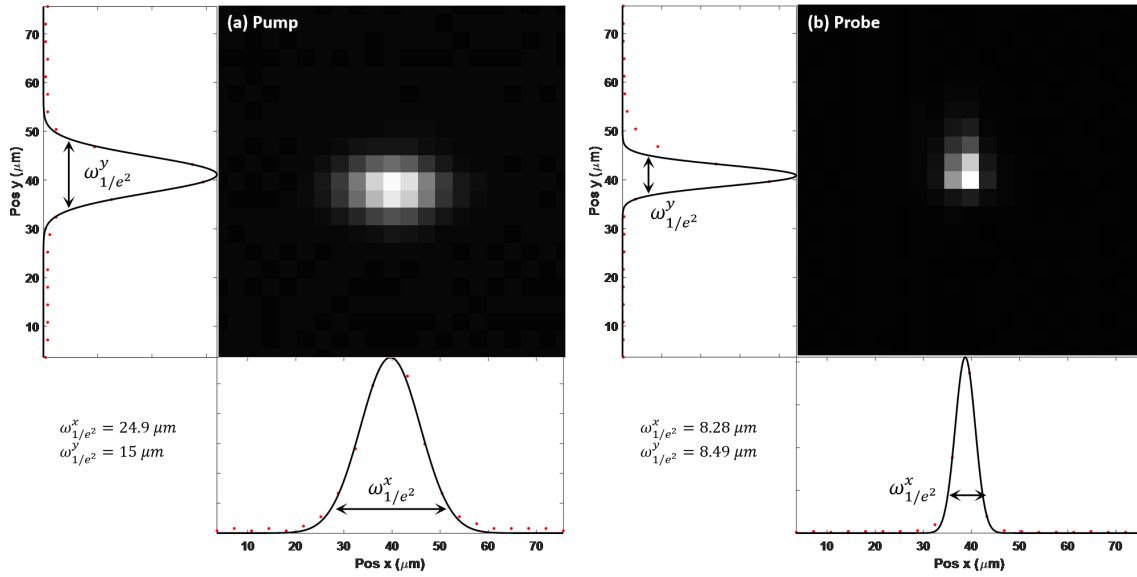


Fig 3.5: Measurements of radiation sections with CMOS camera (DCC1645C, Thorlabs [48]) for the pump (415 nm) beam in (a) and for the probe (587 nm) beam in (b). The microscopic objective applied for focus has a magnification of X10.

resolved X-ray diffraction method has been applied to study the BiFeO_3 material. such method is based on a pump-probe scheme where the material is photoexcited by the pump beam (whose wavelength is fixed at 400 nm) and the light-induced dynamics is probed by a pulsed X-ray. A picture of the setup is shown in **Fig 3.6**.

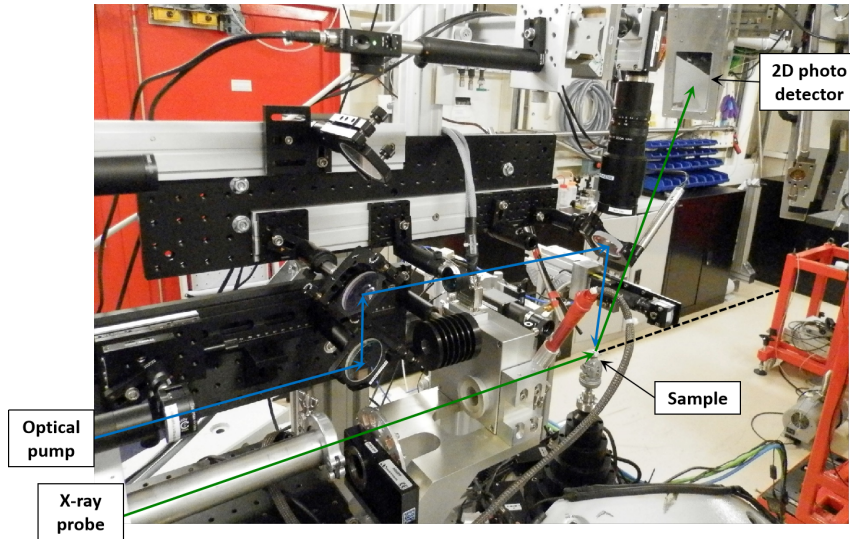


Fig 3.6: Picture of the set-up at the CRISTAL beamline at SOLEIL synchrotron facilities. The pump laser and the X-ray beams are shown in blue and green respectively.

Two configurations were adopted, namely the X-ray diffraction in grazing incidence to study the BiFeO_3 single crystal and the conventional rocking curves with a $\theta - 2\theta$ geometry to study a thin BiFeO_3 film. Before presenting these two experi-

mental setups, we give below some characteristic of the two detectors used for each experiment.

3.2.1 Description of detectors

Two different detectors have been used: the XPAD3.2 detector and the UFXC32k detector. The experiment in 2019 for studying the BiFeO_3 single cristal was conducted with the XPAD3.2 detector while the single domain BiFeO_3 thin film was studied in 2021 with the UFX32k detector.

The specifications of XPAD3.2 and UXFC32k detector are given in **Table 3.1**. The UXFC32k detector, used in the more recent setup, consists of 2 UFXC chips, with each pixel size of $75 \mu\text{m} \times 75 \mu\text{m}$, compared to XPAD3.2 detector used in the previous setup, which has a larger detection surface but with larger pixel size as well ($130 \mu\text{m} \times 130 \mu\text{m}$). The latter one facilitates the search of Bragg peak because of its larger detection surface. By comparing the maximal counting rate of these 2 detectors, UFXC32k detector offers a higher number of counts in image than XPAD3.2 detector. The smaller pixel size in UXFC32k detector also provides a better spatial resolution. In addition, UXFC32k detector provides as well the possibility of “pump-probe-probe” experiments which is not possible with the other detector [49]. This means that after each pump-probe experiment, a conventional X-ray diffraction can be conducted (that’s why there is a second probe) to follow the state of the system regularly in time.

	UFXC32k	XPAD3.2
Sensor	Si - $320 \mu\text{m}$	Si - $500 \mu\text{m}$
Maximal count rate (photons.s ⁻¹ .pixel ⁻¹)	$\sim 2.6 \times 10^6$	$\sim 2 \times 10^5$
Maximal count rate (photons.s ⁻¹ .mm ⁻²)	$\sim 4.6 \times 10^8$	$\sim 1.2 \times 10^7$
Pixel size (μm)	75×75	130×130
Number of pixel	$256 \times 256 = 65792$	$560 \times 560 = 537600$
Detection surface (cm)	1.92×1.93	7.5×15
Gate duration (ns)	80-120	≥ 80
Time-resolved possibilities	Pump-probe-probe	Pump-probe

Table 3.1: Main features of the UFXC32k and XPAD3.2 detectors [49, 51].

The laser pulses were electronically phase-locked to a single electron bunch in the storage ring, allowing synchronization between the laser pulse and the X-ray probe with an accuracy of 5 ps. In order to acquire the XRD signal as a function of time, the time delay between the X-ray pulses and the laser pulses, noted as Δt , was gradually augmented. For each time delay, the XRD signal was measured by the UFXC32k in pump-probe-probe scheme, i.e. two images were taken for each laser pulse. And the frequency of the UFXC32k camera was set as twice of the repetition rate of the laser. For example, if the repetition rate of the laser is 1 kHz, the frequency of the camera is set at 2 kHz [49]. While the XPAD3.2 detector

works in conventional pump-probe scheme, with a single signal measured for each laser pulse. The different sequences of X-ray and pump pulses for both detector technologies (chronograms) are illustrated in **Fig 3.7**. At time Δt , the first image is acquired and measures the XRD intensity when the sample is excited. The second image is taken at time delay $\Delta t + 500 \mu\text{s}$ and the XRD intensity is measured when the sample has returned to its relaxed state.

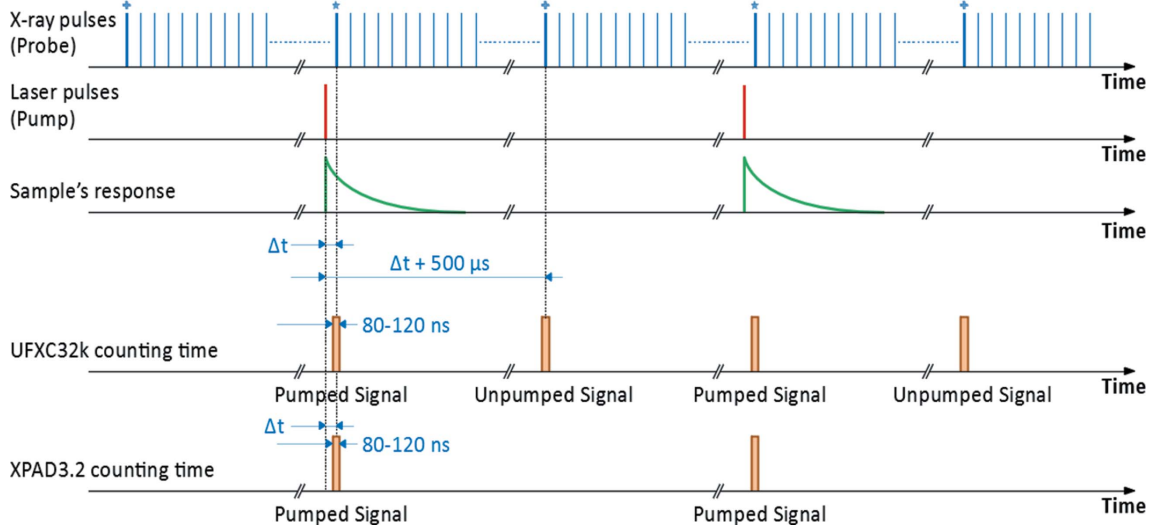


Fig 3.7: Chronogram of the time-resolved X-ray diffraction experiment held at the CRISTAL beamline, showing the arrival of times of laser and X-ray pulses, as well as the electronic gates that define the counting periods of both UFXC32k and XPAD3.2 detectors. [49]

3.2.2 Experimental setup for time-resolved X-ray diffraction with BiFeO₃ single crystal

For the investigation of BiFeO₃ single crystal at SOLEIL Synchrotron facility, a X-ray grazing incidence geometry was used with an incident angle of X-ray pulses around 1°. This X-ray grazing incidence geometry was used to match the optically excited and probed volumes in the BiFeO₃ single crystal. The effective penetration depths of the 3.1 eV pump beam (i.e. wavelength of 400 nm) and of the X-ray beam can be estimated to $\xi_p \approx 40\text{-}60 \text{ nm}$ [52] and $\xi_X \approx 70 \text{ nm}$ [53], respectively. The pump beam size on the sample was about twice as large as the X-ray probe beam size and the incident pump beam fluence was set to either 1.5 or 3 mJ.cm⁻².

For the BiFeO₃ single crystal the X-ray diffraction patterns were recorded with 2D XPAD3.2 detector described in previous part [49]. In order to fulfill the Bragg condition with the experimental X-ray grazing incidence geometry. The possible Bragg plane (hkl)_c need to be determined and we stay with pseudocubic notation for the Miller indices. The conventional scheme is shown in **Fig 3.8**.

At SOLEIL Synchrotron facility, the direction incident direction of X-ray is fixed, and the grazing incident geometry requires the angle between X-ray wave vector and the sample surface to be around 1°. In order to search the Bragg peak for

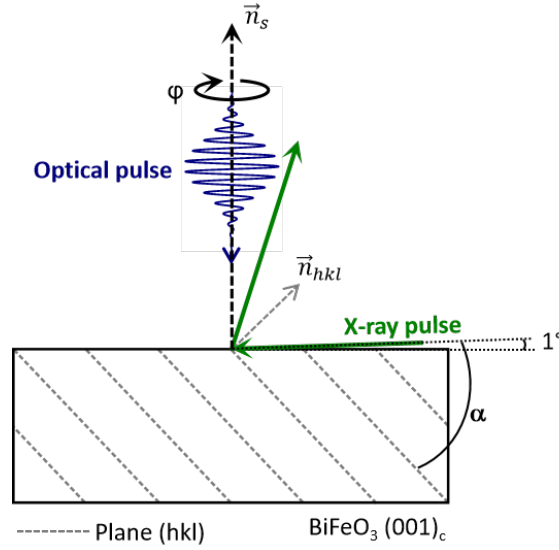


Fig 3.8: Selection of planes (hkl) in BiFeO₃ single crystal that are suitable for investigation of photoinduced strain by X-ray diffraction in grazing incidence geometry.

a given plane (hkl), the sample need to be rotated with an angle φ along \vec{n}_s , as illustrated in **Fig 3.8**, and the angle between the X-ray wave vector and the plane (hkl) is noted as α . For a successful X-ray diffraction measurement of plane (hkl), the X-ray wave vector need to be at Bragg angle (θ_{Bragg}) with respect to plane (hkl). Considering the configuration in **Fig 3.8** corresponds to $\varphi=0^\circ$, for $\varphi=\pm 90^\circ$, the X-ray wave vector becomes parallel to the plane (hkl), i.e. $\alpha = 0^\circ$. Thus the condition $\theta_{Bragg} \leq \alpha$ need to be verified. As a consequence, if θ_{Bragg} varies from 0° to α , the Bragg condition can be achieved, otherwise the plane (hkl) can not be suitable for X-ray diffraction experiments due to grazing incidence geometry. Several planes (hkl)_c (“c” for pseudocubic frame) have been tested and the calculated Bragg angle θ_{hkl} and α are listed in **Table 3.2**. For the experimental reason, only the planes parallel to $[010]_c$ are considered.

Plane (hkl) _c	$\theta_{hkl}(^\circ)$	Angle $\alpha(^\circ)$	$\theta_{hkl} < \alpha$?
(101) _c	18.7	45	yes
(102) _c	30.56	26.5	no
(201) _c	30.56	63	yes
(104) _c	69.6	14	no

Table 3.2: Results of plane (hkl)_c selection for the X ray diffraction experiments on BiFeO₃ single crystal.

In conclusion, for plane (102)_c and plane (104)_c, the condition $\theta_{Bragg} < \alpha$ is not fulfilled. Thus these 2 planes have not been selected. On the contrary, $\theta_{Bragg} < \alpha$ is fulfilled for plane (101)_c and plane (201)_c, hence these 2 planes have been chosen as experimental planes and the complex experimental scheme is shown in **Fig 3.9**. Surprisingly, both chosen planes are antisymmetric, thus $(\bar{1}01)_c$ and $(\bar{2}01)_c$ planes are

also selected. These two pairs of planes can be represented with notation “ $(\pm h01)_c$ plane”.

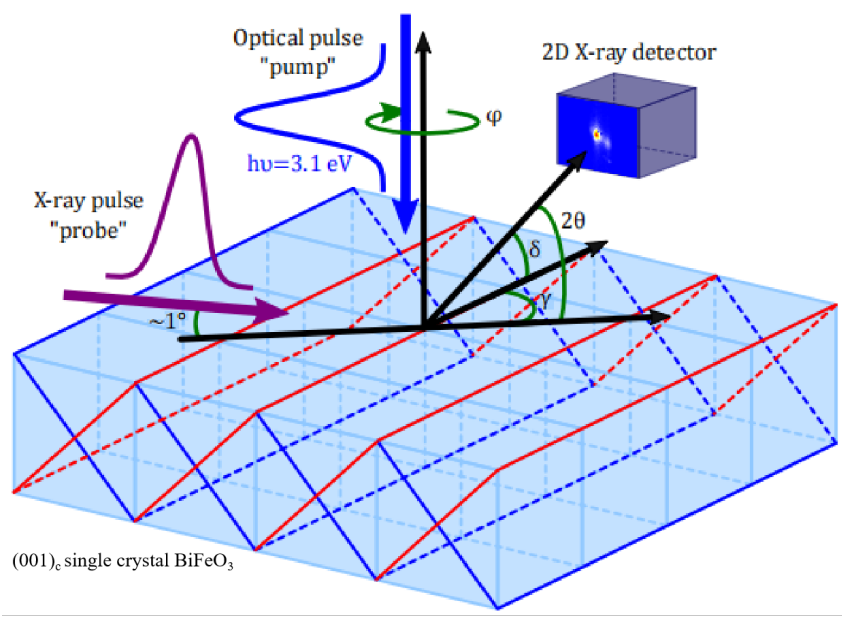


Fig 3.9: Experimental scheme of XRD configuration with grazing incident angle in SOLEIL. The typical asymmetric Bragg planes $(10l)_c$ and $(\bar{1}01)_c$ are depicted in blue and red. The figure is taken from [54] which uses different color coding for the optical and X-ray pulses compared to this thesis.

In this diffraction geometry, the Bragg angle θ is deduced from the relation $\cos(2\theta) = \cos(\delta)\cos(\gamma)$ where γ and δ are coordinates of the diffraction patterns in the 2D XPAD3.2 detector. We have then extracted the center of mass (CoM) for each φ scan to determine γ, δ and the relevant Bragg angle. With the position of the CoM given by γ, δ and the associated light-induced variation of the reciprocal coordinates $\Delta\gamma(t)$ and $\Delta\delta(t)$, considering the Bragg law $\Delta d/d = -\Delta\theta/\tan(\theta)$, we finally deduce the relative variation of the interplanar distance variation as :

$$\frac{\Delta d_{\pm h01}(t)}{d_{\pm h01}} = \frac{1}{2} \frac{\cos(\delta)\sin(\gamma)\Delta\gamma(t) + \sin(\delta)\cos(\gamma)\Delta\delta(t)}{\cos(\delta)\cos(\gamma) - 1} \quad (3.1)$$

where $\frac{\Delta d_{\pm h01}(t)}{d_{\pm h01}} = \frac{d_{\pm h01}^*(t) - d_{\pm h01}}{d_{\pm h01}}$ with $d_{\pm h01}^*(t)$ the interplanar distance after the laser excitation and $d_{\pm h01}(t)$ the not perturbed one.

3.2.3 Experimental setup for time-resolved X-ray diffraction with thin BiFeO₃ film

Contrary to the bulk system, with the thin film, we are not constrained by adjusting the volume that is photoexcited with the one which is probed by X-ray beams. Indeed, with the pump beam wavelength of 400 nm, the thin BiFeO₃ film (~ 180 nm) is nearly entirely photoexcited (penetration depth of about 40-60 nm [52]). In that case, it is possible to measure the Bragg angle of a defined Bragg plane following the conventional Bragg's law. Since the Bragg angle of the film is usually different than that of the substrate, it is possible to probe the lattice dynamics only in the film without being disturbed by the substrate. This geometry has already been employed several times in the past [42, 55].

The Bragg peak position was determined by performing $\theta - 2\theta$ scan as shown in **Fig 3.10(a)**. We call it kw scan. kw scans have been realized for different time delays after the pump photoexcitation. The detector has been put at the relevant Bragg angle and when the lattice becomes distorted after a photoexcitation, only a kw scans is performed to see how the Bragg peak position has shifted (the detector remains at the $\theta - 2\theta$ angles). The Bragg peak shift is captured with the 2D detector.

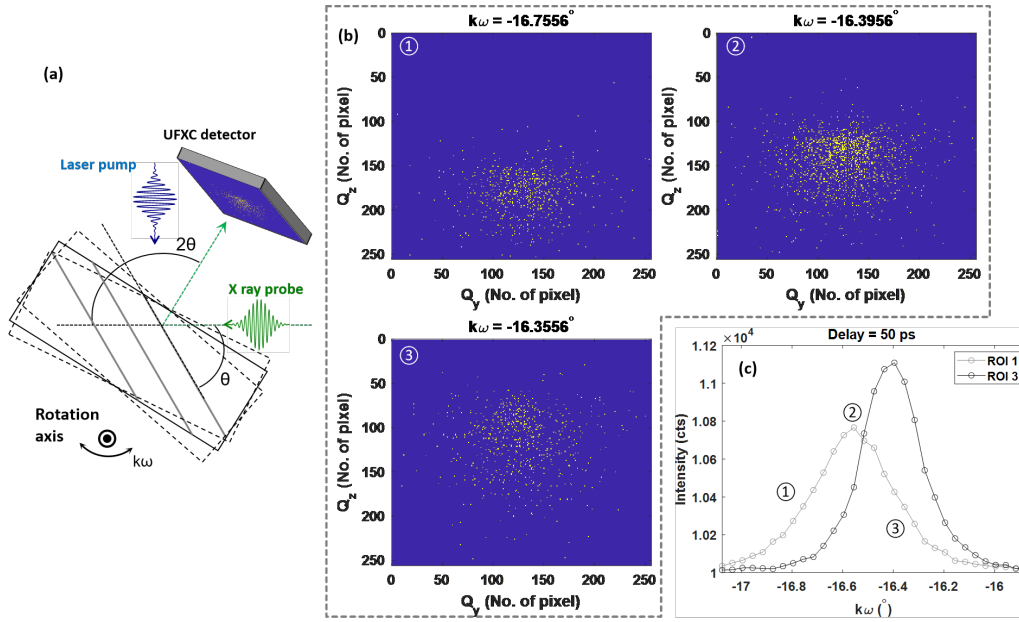


Fig 3.10: (a) Sketch of time-resolved X-ray diffraction setup. The incident direction of optical pump pulses and X-ray pulses are fixed. The UFXC detector is fixed as well. The X-ray diffraction is performed on the chosen plane indicated by gray solid lines. During the experiments only the sample is rotated and the relative angle is noted as kw , as indicated by double arc arrow. The dashed boxes indicate the relative position of sample after the rotation. (b) Intensity map recorded by UFXC detector for different orientations of the sample. (c) Construction of the “rocking curve” by adding up the intensity received by each pixel for each angular position kw . ROI 1 corresponds the results when the sample is photoexcited while ROI 3 corresponds to the X ray diffraction pattern without laser pump.

Since the frequency of UFXC detector used in this experiment is twice of the repetition rate of laser pump pulses (the laser pulses are sent to the sample with a repetition rate of 1kHz, and the UFXC32k camera was set to 2kHz, see **Fig 3.7**) two images were taken by the detector after each laser pulse: one with the sample excited by the laser pulse (called “pumped signal” in **Fig 3.7**) and another without laser pulse excitation (“unpumped” signal). For each situation (pumped or unpumped), a rocking curve is realized which permits to perfectly compare at any time-delay the effect of the light. An example of a typical 2D image recorded by the detector is shown in **Fig 3.10(b)** for some kw values and for a time-delay of 50 ps. The integration of the intensity on the detector for each kw angle permits to reconstruct the full rocking curve: each point in **Fig 3.10(c)** corresponds to the total number of photons counts for that considered kw angle. Said differently, one point in **Fig 3.10(c)** is the sum of the intensities collected on the 2D detector. The typical reconstructed Bragg peak at a time delay of 50 ps after the photexcitation compared to the one obtained with unpumped material is shown in **Fig 3.10(c)**.

The classical Bragg’s law (2.36) is used to evaluate the interplanar distance at thermodynamic equilibrium. With perturbative approach, we deduce, with Taylor expansion, the interplanar distance variation (2.37), where $\Delta\theta(t)$ is the shift of the Bragg peak deduced from the kw scans as illustrated in **Fig 3.10(a)**. In that particular case we can define the shift of the Bragg peak position by Δkw and the latter one corresponds to the shift between the two maxima of Bragg peaks as illustrated in **Fig 3.10(c)**.

The situation $\Delta kw = \Delta\theta$ is illustrated in **Fig 3.11(a)** and we have checked it in our experiment by analysing the shift of the Bragg peak on the 2D detector. For this purpose we measured the physical length corresponding to the shift of the Bragg peak on the 2D detector: this one corresponds to $N \times D$ as shown in **Fig 3.11(b)**. We have then shown that it is consistent with the variation of the kw angle shift, i.e. Δkw , by calculating $\Delta(kw) = \frac{N \times D}{2L}$, where $D=75 \mu\text{m}$ is the size to the pixel, and $L = 550 \text{ mm}$ is the distance between the detector and the sample. In that case we have straightforwardly verified $\Delta\theta = \Delta(kw)$.

Finally, we would like to underline that only asymmetric planes are selected, in other words, the chosen planes should not be parallel to the irradiated surface (we will discuss the choice in more details in part 3.2.4), some planes are naturally excluded because of a large absorption of either the incident or scattered X-ray beam. This situation is met when the Bragg angle is smaller than the angle between the normal of the (hkl) plane and that of the irradiated surface. For example, plane $(112)_c$ is excluded because the Bragg angle ($\theta_{\text{Bragg}}=32^\circ$) is smaller than the angle between plane $(112)_c$ and the free surface ($\gamma=54^\circ$), noted as $\theta < \gamma$. Some other planes are excluded because the condition of detection is not fulfilled with the experimental setup. As an example, plane $(221)_c$ is also suitable for the strain investigation, with a Bragg angle being 41° , larger than $\gamma=19^\circ$. Unfortunately, the configuration can not be achieved with experimental setup, because the $\theta - 2\theta$ scan requires the detector to be at position $2\theta = 82^\circ$ with respect to the incident X-ray pulses. With the experimental setup realized in CRISTAL beamline within Synchrotron SOLEIL facility (photo in **Fig 3.6**), the diffracted X-ray pulses can be

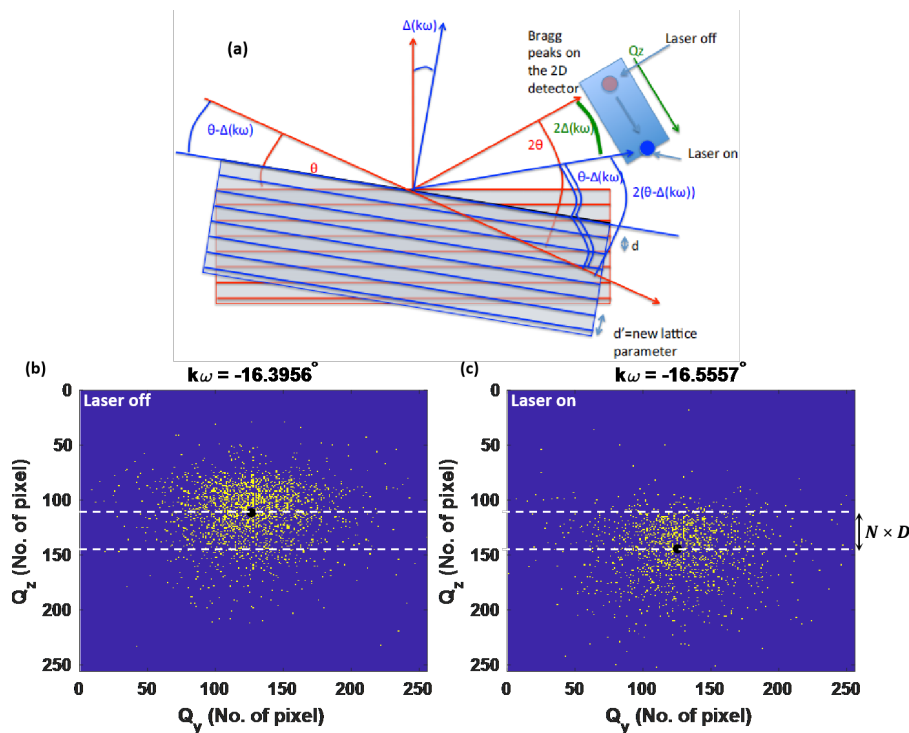


Fig 3.11: (a) Relation between the variations of the θ angle and the kw angle. Note that here only the Bragg plane are shown and not the free surface of a thin film that can be not parallel to (hkl) in case of asymmetric Bragg planes. (b, c) X-ray diffraction image recorded by the 2D detector at Bragg condition for “unpumped” and “pumped” signals. The displacement of center of mass (black dot) is calculated by $N \times D$, with N the number of pixel and D the pixel size of UFXC3.2k detector.

blocked by the camera, hence plane $(221)_c$ could not be selected.

From the photoinduced strain process point of view, it is important to have in mind that these Bragg planes have a different orientation regarding to the normal of the irradiated surface, so this has to be taken into account when comparing the light-induced strain amplitude. As we will explain in part 3.2.4, 4 planes have been selected: $(40\pm3)_m$ equivalent to $(22\pm3)_c$ and $(5\pm30)_m$ equivalent to $(410)_c$ and $(140)_c$. An illustration is given in **Fig 3.12**, showing that the direction $[100]_m$ in monoclinic frame is equivalent to $[110]_c$ in pseudocubic frame. For example, the plane $(403)_m$ has an angle of $\gamma=46^\circ$ with the normal of the surface. Respectively, that angles becomes 30° for the family $(530)_m$ as shown in **Fig 3.12**.

3.2.4 Time-resolved X-ray diffraction with asymmetric Bragg planes: methodology for the extraction of both the longitudinal and shear strains

In this part we explain how it is possible to use time-resolved X-ray diffraction to determine both out-of-plane and in-plane light-induced strain. As it will be shown in the **Chapter 5**, this technique will be applied for both BiFeO₃ single crystal and thin film. More generally, this technique can be of course extended to any material.

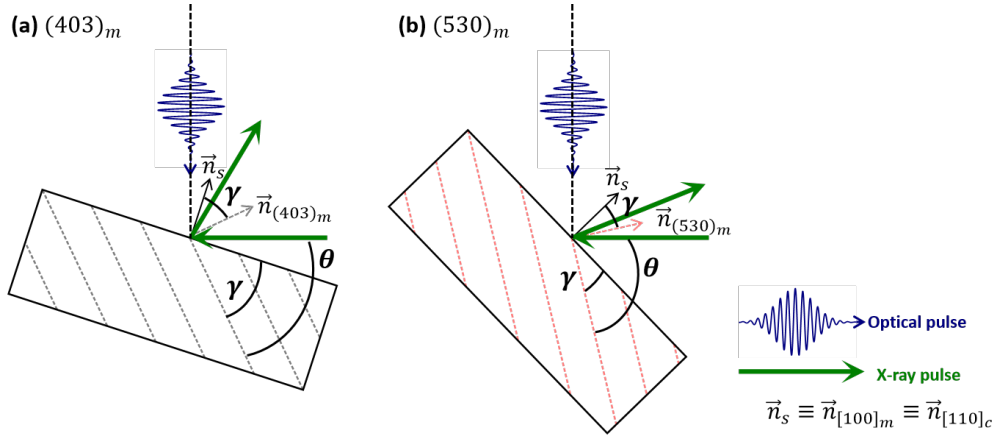


Fig 3.12: Orientation of the $(403)_m$ (a) and $(530)_m$ (b) Bragg planes family regarding to the irradiated surface. γ represents the angle between the $(hkl)_m$ plane and the sample's surface. m stands for monoclinic frame and c for pseudocubic frame.

The principle is based on the combination of measurements of two asymmetric Bragg planes like for example $(h0l)/(\bar{h}0l)$. For this set of Bragg planes, we show for instance that shifting from $+l$ to $-l$ leads to opposite effect of the shear strain on the Bragg peak shift, i.e. on the variation of the interplanar distance $(\Delta d/d)$.

3.2.4.1 Time-resolved diffraction with asymmetric Bragg planes in rhombohedral $(001)_c$ BiFeO_3 single crystal

Selection of Bragg planes

We first describe theoretically how the unit cell is distorted in presence of a longitudinal and shear strain in an assumed cubic BiFeO_3 (subscript c). Knowing that the rhombohedral distortion in bulk BiFeO_3 is weak with rhombohedral angle $\approx 89.5^\circ$, and pseudocubic parameter $a_0 \approx 3.96 \text{ \AA}$, we consider the pseudocubic representation of the BiFeO_3 lattice as depicted in **Fig 3.13(a)**. At equilibrium (before laser excitation), the interplanar distances of the $(101)_c$ and $(\bar{1}01)_c$ planes are nearly identical ($d_{101} \approx d_{\bar{1}01}$). As the laser pulse impinges on the $(001)_c$ surface of BiFeO_3 and due to the existence of in-plane symmetry breaking caused by the ferroelectric polar order, the laser-matter interaction leads to the generation of shear motion in addition to the longitudinal strain. Importantly, the shear strain is expected to lead to an asymmetric change of the interplanar distances d_{101}^* and $d_{\bar{1}01}^*$ with $d_{101}^* > d_{\bar{1}01}^*$ as displayed in **Fig 3.13(b)**. This principle can be applied to all $(\pm h01)$ planes. Note that the atomic displacements associated to the longitudinal and shear strains are symbolized with orange and green arrows respectively in **Fig 3.13**.

Relation between photoinduced strain and interplanar distance

Let us now establish the relation between the evolution of the unit cell distortion and the longitudinal and shear strains. First it is important to remind that in all pump-probe experiments, the geometry is 1D: this means that the irradiated surface has a diameter much larger than the depth over which all the dynamics is

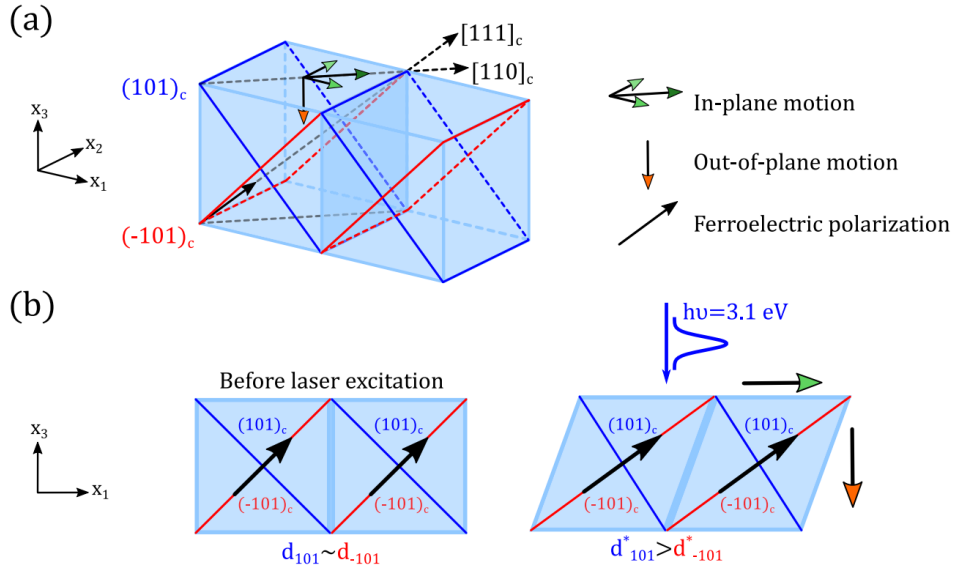


Fig 3.13: (a) 3D view of the BiFeO₃ pseudocubic unit cell with displacement vector associated to the longitudinal and shear photoinduced strain (orange and green arrows). The black arrow is the BiFeO₃ ferroelectric polarization pointing along the $[111]_c$ direction. (b) Side view of the BiFeO₃ pseudocubic unit cell before and after the laser excitation showing the in-plane and out-of-plane motion.

recorded. As a matter of fact, the elastic wave propagates only normally to the surface, i.e. along x_3 coordinate. The deformation of the cubic unit cell associated to the longitudinal ($\eta_L = \eta_3 = \frac{\partial u_3}{\partial x_3}$) and shear ($\eta_{S_5} = \eta_5 = \frac{\partial u_1}{\partial x_3}$, $\eta_{S_4} = \eta_4 = \frac{\partial u_2}{\partial x_3}$) strains, which are depicted in the Figure (**Fig 3.14**). For example, we discuss the effect of the strains on the $(101)_c$ Bragg planes family. We can see that the shear strain $\eta_{S_4} = \eta_4$ does not contribute to the modification of the interplanar distance of the planes $(101)_c$, since it induces only a sliding motion.

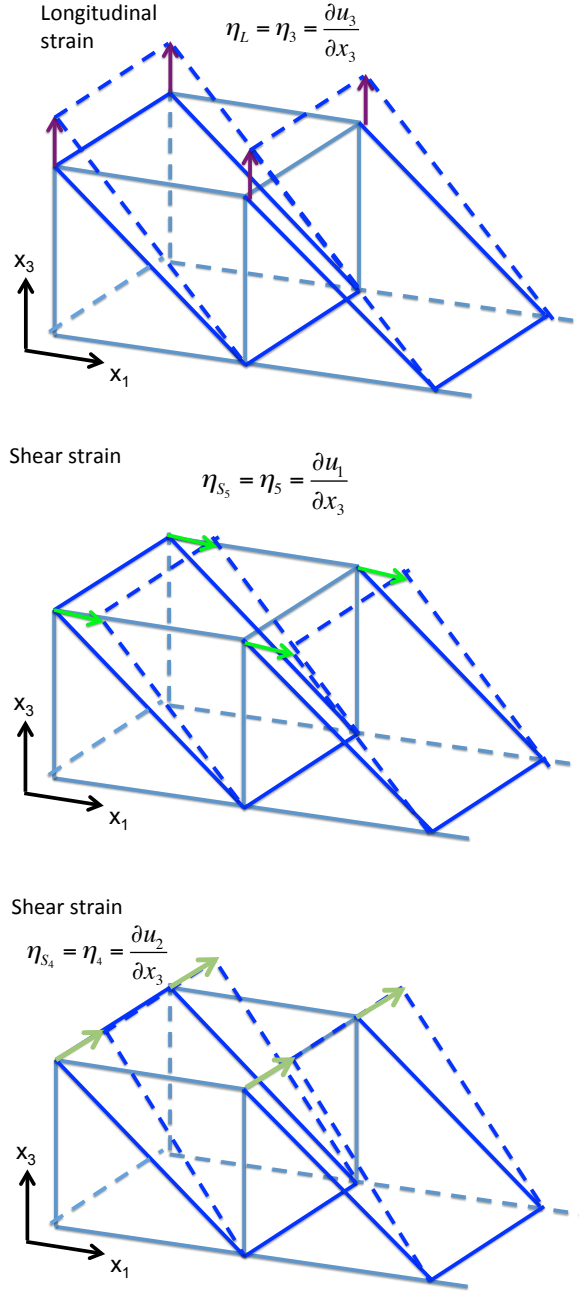


Fig 3.14: Picture of the strained pseudocubic unit cell in presence of a longitudinal ($\eta_L = \frac{\partial u_3}{\partial x_3}$) and shear ($\eta_4 = \frac{\partial u_2}{\partial x_3}$, $\eta_5 = \frac{\partial u_1}{\partial x_3}$) strains.

We can then demonstrate how the interplanar distances evolve in presence of strains thanks to the following geometrical calculation (**Fig 3.15**). In this figure, the projection of the unstrained pseudocubic unit cell in the (O, x_1, x_3) plane is represented in orange. The pseudocubic lattice parameter is denoted a_0 . The $(101)_c$ and $(\bar{1}01)_c$ interplanar distances in the strained unit cells correspond to the lengths of the RD and PB segments, respectively. We have:

$$\begin{aligned}
 PB &= \sqrt{a_0^2 - AP^2} \\
 AP &= a_0 \times \cos(\alpha) \\
 \cos(\alpha) &= \frac{a_0 + \eta_{S_5} a_0}{\sqrt{(a_0 + \eta_{S_5} a_0)^2 + (a_0 + \eta_L a_0)^2}}
 \end{aligned} \tag{3.2}$$

with a Taylor development for which $\eta_L, \eta_{S_5} \ll 1$, we arrive to:

$$PB = d_{-101}^* \approx \frac{a_0}{\sqrt{2}} \left(1 + \frac{\eta_L - \eta_{S_5}}{2} \right) \tag{3.3}$$

Similarly, we can write for $d_{101}^* = RD$:

$$\begin{aligned}
 RD &= \sqrt{a_0^2 - CR^2} \\
 CR &= a_0 \times \cos(\beta) \\
 \cos(\beta) &= \frac{a_0 - \eta_{S_5} a_0}{\sqrt{(a_0 + \eta_L a_0)^2 + (a_0 - \eta_{S_5} a_0)^2}}
 \end{aligned} \tag{3.4}$$

which, with a Taylor development, leads to:

$$RD = d_{101}^* \approx \frac{a_0}{\sqrt{2}} \left(1 + \frac{\eta_L + \eta_{S_5}}{2} \right) \tag{3.5}$$

By combining the above equations and generalizing that situation to the family (h01), we arrive to

$$\frac{\Delta d_{\pm h01}}{d_{\pm h01}} = \frac{d_{\pm h01}^* - d_{\pm h01}}{d_{\pm h01}} = \frac{\eta_L \pm |h| \eta_{S_5}}{1 + h^2} \tag{3.6}$$

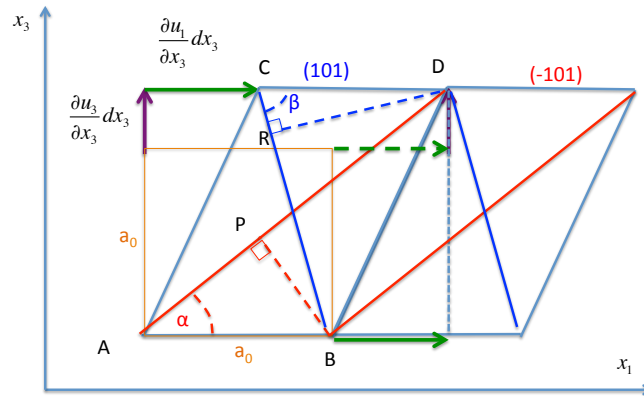


Fig 3.15: 2D Picture of the strained cubic unit cell in presence of a longitudinal ($\eta_L = \frac{\partial u_3}{\partial x_3}$) and shear ($\eta_{S_5} = \frac{\partial u_1}{\partial x_3}$) strain.

It has to be noted previously that only η_{S5} contributes to the symmetry breaking for the $(\pm h01)$ planes. Considering that the total amplitude of the shear strain is $\eta_S = \sqrt{\eta_{S4}^2 + \eta_{S5}^2} = \sqrt{2} \times \eta_{S5}$ as $\eta_{S4} = \eta_{S5}$, then we can write as well:

$$\frac{\Delta d_{\pm h01}}{d_{\pm h01}} = \frac{d_{\pm h01}^* - d_{\pm h01}}{d_{\pm h01}} = \frac{\eta_L \pm |h| \frac{\eta_S}{\sqrt{2}}}{1 + h^2} \quad (3.7)$$

Consequently we deduce the longitudinal and shear strains as follows:

$$\begin{aligned} \eta_L &= \frac{1 + h^2}{2} \times \left[\frac{d_{h01}^* - d_{h01}}{d_{h01}} + \frac{d_{-h01}^* - d_{-h01}}{d_{-h01}} \right] \\ \eta_S &= \frac{1 + h^2}{\sqrt{2} |h|} \times \left[\frac{d_{h01}^* - d_{h01}}{d_{h01}} - \frac{d_{-h01}^* - d_{-h01}}{d_{-h01}} \right] \end{aligned} \quad (3.8)$$

3.2.4.2 Time-resolved diffraction with asymmetric Bragg planes in monoclinic $(110)_c$ BFO thin film

Selection of Bragg planes

For the case of a monoclinic BFO crystal that we will study in the form of a thin film, we can apply the same procedure as before. The main difference between the following calculation and the previous one is the choice of the crystallographic frame. As explained in part 5.4.2, the thin BFO film is grown on a $(110)_c$ STO substrate. This is an epitaxial growth that leads to the formation of a nearly single crystalline monoclinic structure whose lattice parameters of the unit cell are then written in the monoclinic frame such as $(a\sqrt{2}, a\sqrt{2}, a)$. a is the pseudocubic parameter.

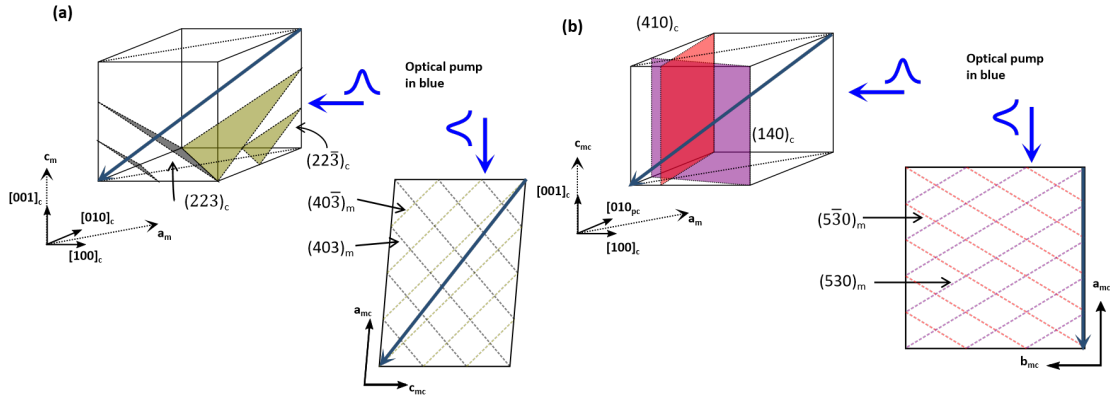


Fig 3.16: Two series of plans are chosen for the XRD experiments, (a) plane $(223)_c$ and plane $(223)_c$ in pseudocubic frame which correspond to $(403)_m$ and $(403)_m$ in monoclinic frame. Both of them are perpendicular to the the surface which contains the intrinsic ferroelectricity of BiFeO_3 . (b) Plane $(140)_c$ and plane $(410)_c$ in pseudocubic frame, corresponding to $(530)_m$ and $(530)_m$, respectively, in monoclinic frame. The identical plans, which are described in either pseudocubic frame or monoclinic frame, are indicated with the same color coding.

The irradiated plane of this monoclinic structure is the (b_m, c_m) plane (with $b_m = \sqrt{2}$ and $c_m = a$). These parameters are shown in **Fig 3.17** and **Fig 3.18**. The monoclinic (b_m, c_m) plane is a symmetry plane, and for this reason the shear strain can exist only in this plane. Considering such symmetry analysis, we have selected two Bragg planes families: the $(403)/(40\bar{3})_m$ which are sensitive to both the longitudinal and the shear strain and the $(530)/(5\bar{3}0)_m$ sensitive only to the longitudinal strain. This complete set of Bragg planes will permit to reconstruct the temporal evolution of the BiFeO_3 unit cell.

Relation between photoinduced strain and interplanar distance

To be more general, we establish in the following the model for $(h0l)_m$ and $(hk0)_m$ families. To simplify the calculation, the monoclinic angle β is considered to be 90° .

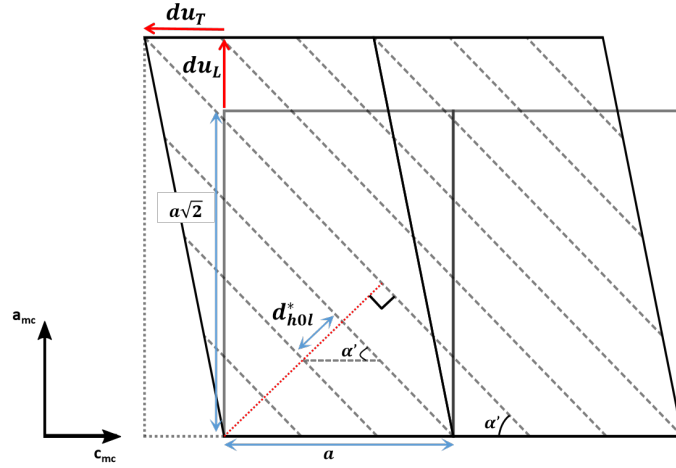


Fig 3.17: Projection on (O, x_a, x_c) surface of BiFeO_3 unit cells in monoclinic frame. The monoclinic angle which is $\beta = 89.5^\circ$ is not displayed. Only the plane $(403)_m$ is shown in the figure for illustration.

By definition, within the monoclinic frame, the interplanar distance after deformation d_{h0l}^* is defined as:

$$d_{h0l}^* = \frac{a}{l} \times \sin(\alpha') \quad (3.9)$$

$$\sin(\alpha') = \frac{a\sqrt{2} + du_L}{\sqrt{(\frac{h}{l} \times a + du_T)^2 + (a\sqrt{2} + du_L)^2}} \quad (3.10)$$

If we consider \vec{e}_1 is the unit vector following the direction of a_{mc} and \vec{e}_3 is the unit vector in c_{mc} direction, the longitudinal and shear deformations can be described as a function of strain:

$$\begin{cases} du_L = \frac{\partial u_1}{\partial x_1} dx_1 \vec{e}_1 \\ du_T = \frac{\partial u_3}{\partial x_1} dx_1 \vec{e}_1 \end{cases} \quad (3.11)$$

with u_1, u_3 the deformation following a_m and c_m directions respectively. The strain can be introduced as $\eta = \frac{\partial u}{\partial x}$, hence with Einstein's notation,

$$\begin{cases} \frac{\partial u_1}{\partial x_1} = \eta_L, & du_L = \eta_L \times a_m^0 \\ \frac{\partial u_3}{\partial x_1} = \eta_S, & du_T = \eta_T \times a_m^0 \end{cases} \quad (3.12)$$

Reminding that $a_m^0 = a\sqrt{2}$, so the expression of $\sin(\alpha')$ becomes:

$$\begin{aligned} \sin(\alpha') &= \frac{a\sqrt{2} + \eta_L \times a\sqrt{2}}{\sqrt{(\frac{h}{l} \times a + \eta_T \times a\sqrt{2})^2 + (a\sqrt{2} + \eta_L \times a\sqrt{2})^2}} \\ &= \frac{\sqrt{2}(1 + \eta_L)}{\sqrt{(\frac{h}{l} + \eta_T \times \sqrt{2})^2 + 2(1 + \eta_L)^2}} \end{aligned} \quad (3.13)$$

If we apply the Taylor series by considering $\eta_L, \eta_T \ll 1$, the interplanar distance can be developed as:

$$\begin{aligned} d_{h0l}^* &= \frac{a}{l} \times \frac{\sqrt{2}(1 + \eta_L)}{\sqrt{(\frac{h}{l} + \eta_T \times \sqrt{2})^2 + 2(1 + \eta_L)^2}} \\ &\simeq \frac{a\sqrt{2}}{\sqrt{2l^2 + h^2}} \left(1 + \frac{h^2}{2l^2 + h^2} \eta_L - \frac{\sqrt{2}hl}{2l^2 + h^2} \eta_T \right) \end{aligned} \quad (3.14)$$

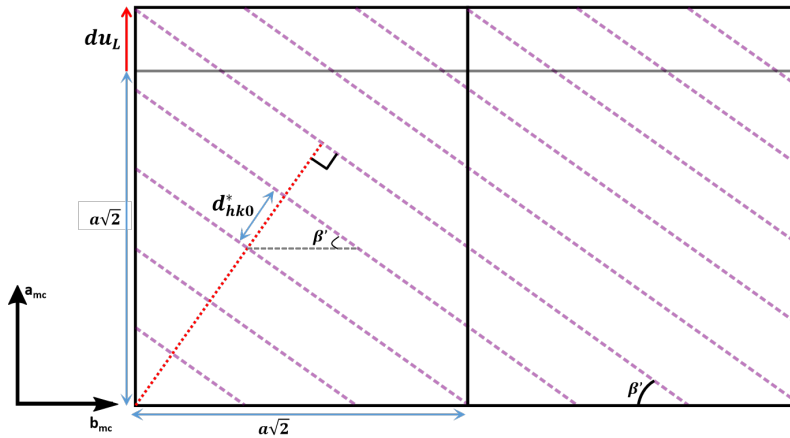


Fig 3.18: Projection on (O, a_m, b_m) surface of BiFeO_3 unit cells in monoclinic frame. Only the $(530)_m$ plane is shown for illustration.

We apply the same methodology for plane $(530)_m$ and $(\bar{5}\bar{3}0)_m$ with the scheme on **Fig 3.18**, the general expression of d_{hk0}^* should be:

$$\begin{aligned}
d_{hk0}^* &= \frac{a\sqrt{2}}{k} \times \sin(\beta') \\
&\simeq \frac{a\sqrt{2}}{\sqrt{h^2 + k^2}} \left(1 + \frac{h^2}{h^2 + k^2} \eta_L \right)
\end{aligned} \tag{3.15}$$

In conclusion, at the equilibrium after the sample has been photoexcited by the optical pump, the relative variation of interplanar distance in $(100)_m$ BiFeO₃ single domain thin film can be described using the Miller index (h, k, l) in monoclinic perspective.

$$\begin{cases} \frac{\Delta d_{h0l}}{d_{h0l}} &= \frac{h^2}{2l^2 + h^2} \eta_L - \frac{\sqrt{2}hl}{2l^2 + h^2} \eta_T \\ \frac{\Delta d_{hk0}}{d_{hk0}} &= \frac{h^2}{h^2 + k^2} \eta_L \end{cases} \tag{3.16}$$

Considering $h, k, l > 0$ and the longitudinal (η_L) and shear (η_T) strains can be deduced as follow:

$$\begin{cases} \eta_L &= \frac{2l^2 + h^2}{2h^2} \left(\frac{\Delta d_{h0l}}{d_{h0l}} + \frac{\Delta d_{\bar{h}0l}}{d_{\bar{h}0l}} \right) \text{ or } \frac{h^2 + k^2}{h^2} \times \frac{\Delta d_{h \pm k0}}{d_{h \pm k0}} \\ \eta_T &= \frac{2l^2 + h^2}{2\sqrt{2}hl} \left(\frac{\Delta d_{\bar{h}0l}}{d_{\bar{h}0l}} - \frac{\Delta d_{h0l}}{d_{h0l}} \right) \end{cases} \tag{3.17}$$

Photoinduced coherent acoustic phonons in Germanium telluride(GeTe)

Contents

4.1	Introduction	53
4.2	Presentation of germanium telluride (GeTe)	54
4.2.1	GeTe as phase change material	54
4.2.2	Phase diagram of GeTe	55
4.2.3	Several physical properties of GeTe	58
4.3	State-of-art of photoinduced strain in GeTe and motivations	62
4.4	Experimental results and analysis	66
4.4.1	GeTe sample description	66
4.4.2	Raman scattering experiments in GeTe	67
4.4.3	Typical signal recorded in optical pump probe experiments	68
4.4.4	Calibration of the experiment	69
4.4.5	Photogeneration and detection of coherent acoustic phonons in amorphous & crystalline GeTe	72
4.4.6	Analysis and discussion: ultrafast non-thermal transport of energy	77
4.5	Conclusion	87

4.1 Introduction

Germanium telluride (GeTe) material is at the cornerstone of the phase change materials (PCM) research field. The interesting properties of GeTe and its related compounds (GeSbTe) rely on the ability to switch between two states, i.e. the amorphous and crystalline states, where the materials exhibit very different physical properties (electrical, optical). The drastic change of these properties between these two states is used as a “bit” for storing information in devices. This amorphous to crystalline phase transition (and vice versa) is by now well controlled with electrical pulses and continuous light excitation (rewritable disc for example), even at the industrial level, but new research directions have appeared in the last ten years towards the manipulation of these states with light pulses [56, 57], unveiling the possibility, with short light pulses, to envision applications in the GHz and THz frequency range. As a consequence, the understanding of the light-matter interaction is a necessary step. Among still debated questions, the transformation of the optical energy into electron, hole and phonon (coherent and incoherent) energy has not been fully addressed as far as we know since the electron and phonon dynamics and their coupling at short time scale are not fully understood at the present time.

In this chapter, a brief introduction about GeTe material will be given in the first place, as a member of the PCM family, including the principle of PCM applications. Several physical properties of GeTe will also be given. Then some literature works will be presented regarding more precisely the study of photoinduced strain in GeTe and GeTe alloys, which is the current direction of this research. In particular, the current understanding of light-induced strain phenomenon in PCM and the related issues will be discussed to define the motivation of this work.

In the second part, experimental results will be presented in order to understand the photogeneration as well as the detection of coherent acoustic phonons in the amorphous and crystalline states of GeTe. Very interestingly, we reveal the existence of large differences in the response to a short light pulse of these two states. Importantly, the analysis of the spectrum of the light-induced coherent acoustic phonons in crystalline GeTe suggests that the photoexcited carriers (electrons) can travel through a large distance beyond optical penetration depth. This observation contrasts with the results found in amorphous GeTe where this effect is not observed. Such information might be important for all optical control of PCM-based photonic technologies.

4.2 Presentation of germanium telluride (GeTe)

GeTe is known as one of the simplest phase change materials. The industrial applications, in the domain of data storage and information, are based on the controlled transformation between the amorphous and the crystalline states. The latter one is then usually achieved in devices by thermal heating assisted by short and intense electrical pulses (Joule effect) as discussed in the following section 4.2.1. In section 4.2.2 the phase diagram of GeTe will be given and in section 4.2.3, some of the crucial physical properties of amorphous and crystalline GeTe will be presented, which are not only employed in the applications but also necessary for the discussions in this chapter.

Even if it will not be addressed in the manuscript, it is worth mentioning that large Rashba effect has been recently observed in rhombohedral crystalline phase of GeTe. The ferroelectric properties and the existence of a large spin-orbit interaction make indeed α -GeTe of great interest for spintronics [58–61]. Moreover, GeTe has also been found applicable as a thermoelectric material [62].

4.2.1 GeTe as phase change material

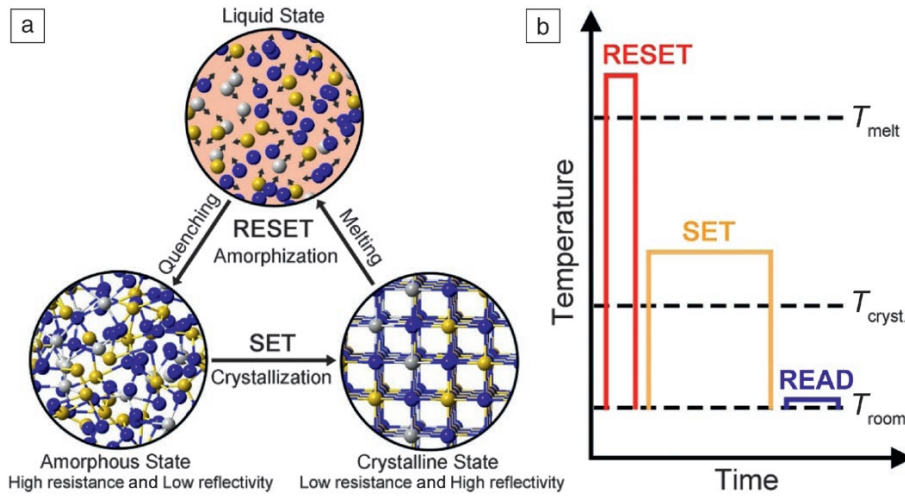


Fig 4.1: Working principle of phase-change materials for memory applications. (a) $\text{Ge}_2\text{Sb}_2\text{Te}_5$ (GST); Ge, Sb, and Te atoms are rendered as white, yellow, and blue balls, respectively. The amorphous and crystalline states are characterized by high resistance/low optical reflectivity and low resistance/high optical reflectivity, respectively. To SET a memory cell, amorphous GST undergoes crystallization, while for RESET, crystalline GST is first melted and then the liquid is rapidly quenched, accomplishing the amorphization process. (b) The RESET and SET operations are triggered by applying voltage or laser pulses, which heat up GST to different temperature levels, either above the melting temperature (T_{melt}) or in between the crystallization temperature ($T_{\text{cryst.}}$) and melting temperature. The READ pulse is typically very weak, leading to little change in temperature. [63]

Phase change materials (PCMs) have been widely used in various application fields, due to the large difference in electrical resistance and in the optical reflectivity between amorphous and crystalline phase. As an example, Antimony doped Germanium Telluride (GeSbTe) has been widely used in nowadays rewritable optical discs and phase change memory devices [64]. This important switching property is now more and more dedicated to the nonvolatile memory devices based on PCM [3, 65]. The high-resistance state can represent a logical “0” while the low-resistance state represents a logical “1” [66]. The phase change process can be achieved by applying a long electrical pulse, heating the material and changing its phase from amorphous to crystalline (SET process). The amorphization (RESET process) requires a short pulse but more powerful in order to raise the temperature of material above its melting temperature. The material will first enter into the liquid state and then, followed by a quenching process, the material returns to its amorphous state (**Fig 4.1**).

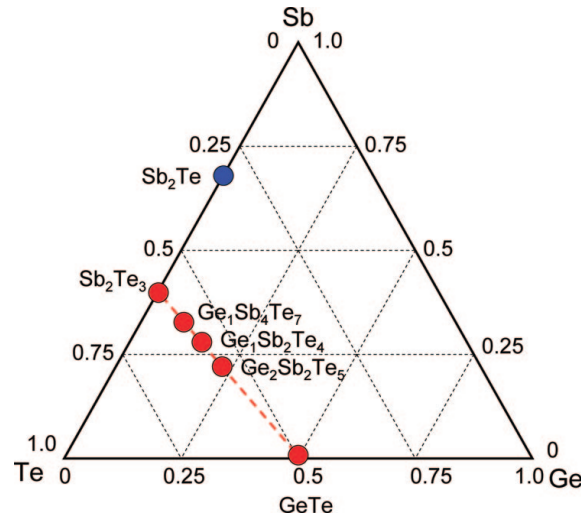


Fig 4.2: Triangle of phase change material based alloy, the alloys lying on the Sb_2Te_3 -GeTe pseudobinary line show remarkable commercial interests and enable the technology of phase change optical storage. [66]

Interestingly, most of industrial or commercial products are found to be based on the pseudobinary GeTe- Sb_2Te_3 material (see **Fig 4.2**) [3, 64]. These alloys not only exhibit large differences in the optical reflectivity between the two states over a wide range of wavelengths but also present favorable cyclability properties regarding the switching process between the two states. Typical materials such as $\text{Ge}_2\text{Sb}_2\text{Te}_5$, $\text{Ge}_1\text{Sb}_2\text{Te}_4$, GeTe or Sb_2Te_3 , show not only an amorphous-crystalline phase transition but also two different crystalline phases.

4.2.2 Phase diagram of GeTe

Known as one of the simplest phase change material, GeTe was studied in detail in the 1960s in the seminal work of K. L. Chopra and S. K. Bahl [67–69]. They managed to grow the GeTe films in different crystalline structures, including amorphous

(a), rhombohedral (α) and rock-salt cubic (β) phases, by controlling the deposition conditions [67, 70].

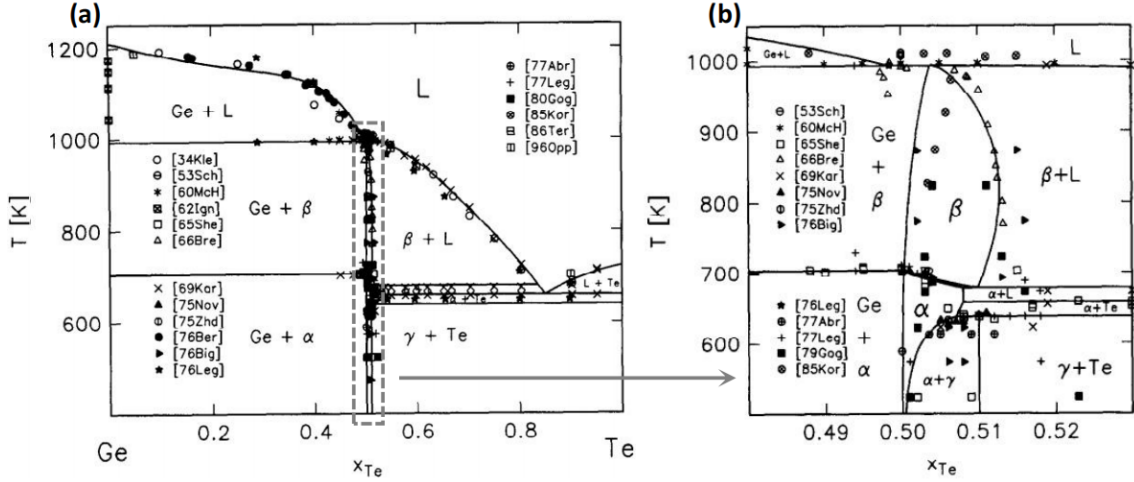


Fig 4.3: (a) Phase diagram of GeTe system as a function of stoichiometric composition above room temperature. The solid line represents the calculations while symbols correspond to experimental results from literature. (b) Zoom of (a) in the range of appearance of GeTe. [71]

Fig 4.3 shows the phase diagram of GeTe above room temperature (300 K). As indicated in the chemical formula, GeTe consists in 50 mol% Ge atoms and 50 mol% Te atoms. Two crystalline phases (α and β) and one liquide (L) phase are identified for this stoichiometric composition. The melting temperature is around 1000 K (727 °C). These two crystalline phases are described as ferroelectric (α) and paraelectric (β) phase of GeTe, with $T_C=700$ K (427 °C, the Curie temperature). The corresponding atomic structure of both crystalline phases are shown below.

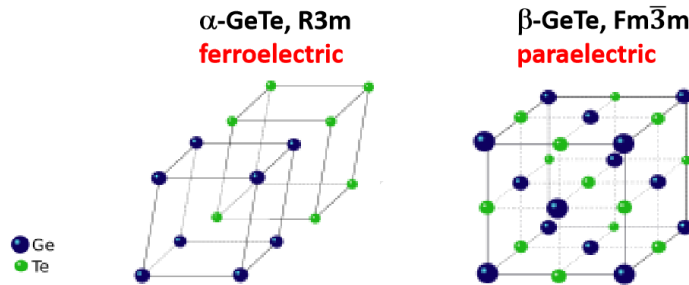


Fig 4.4: Atomic structure of rhombohedral α -GeTe (left) and rock-salt cubic β -GeTe (right).

As confirmed by the density functional theory (DFT) calculations [73], the atomic structures of α -GeTe and β -GeTe are illustrated in **Fig 4.4**. At room temperature, the α -GeTe owns a rhombohedral primitive cell with a lattice parameter of $a = 4.28$ Å

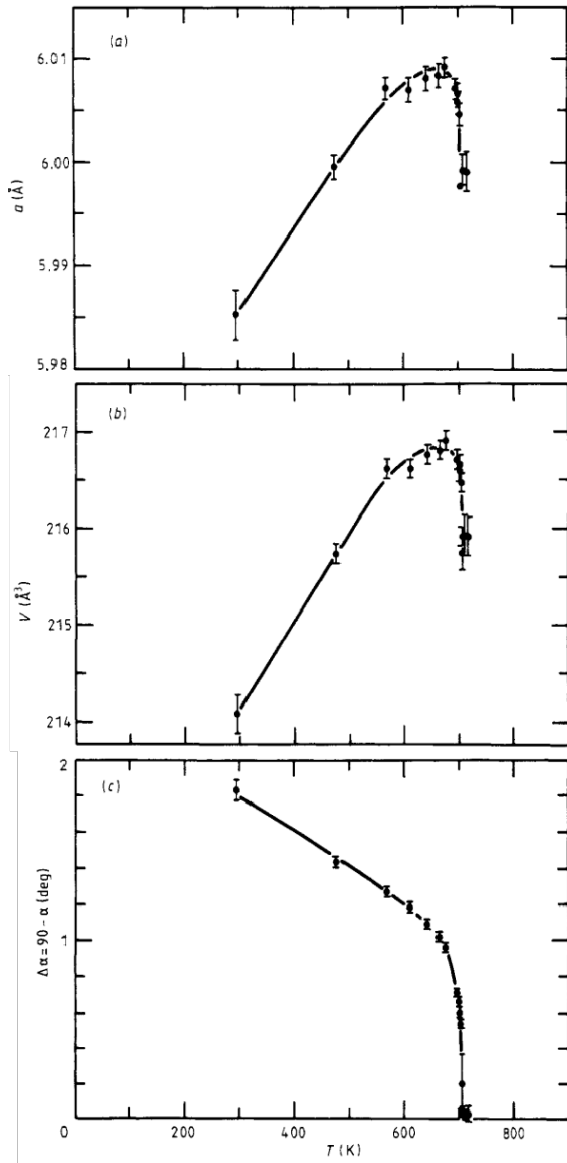


Fig 4.5: Variation of the lattice parameter a (a), the unit cell volume V (b) and the deviation of angle α from 90° (c) as a function of temperature of GeTe single crystal, revealed by neutron diffraction [72].

and a rhombohedral angle of $\angle\alpha = 58.36^\circ$, which is described with $R3m$ as the space group [73, 74]. Such primitive cell contains 1 germanium atom and 1 tellurium atom, germanium atom occupies the Wyckoff positions (0,0,0) and tellurium atom occupies another Wyckoff positions (0.52,0.52,0.52). An inverse symmetry breaking is unveiled by the atomic positions and GeTe shows ferroelectric properties. The rhombohedral structure can also be described as a slight tilted rock-salt structure, with a lattice parameter $a = 5.98 \text{ \AA}$ and $\angle\alpha = 88.17^\circ$ at room temperature, as shown in **Fig 4.5**. Such rhombohedral structure evolves towards the rock-salt structure ($\angle\alpha = 90^\circ$) above the Curie temperature. Such thermal dependence of the structure and the α - β phase transition has been studied by neutron diffraction [72, 75, 76]. It has been reported that both the lattice parameter a and the unit cell volume V decrease drastically at Curie temperature (T_C). GeTe undergoes the transition from α ($R3m$, ferroelectric) to β ($Fm\bar{3}m$, paraelectric) phase. After this transition, the primitive cell consists of two face centered cubic (fcc) sublattices shifted by half the lattice parameter (0.5, 0.5, 0.5) in each direction with respect to each other.

4.2.3 Several physical properties of GeTe

Some physical properties in both amorphous (a) GeTe and rhombohedral (α) crystalline GeTe are given in the following in order to show how they vary between these two phases. In particular, we present the elastic, optical, heat transport and carrier mobility properties. Beyond their importance for the current applications, these fundamental physical properties will be useful to discuss the ultrafast response of GeTe as presented in section 4.4.

Density, bulk modulus & sound velocity

In the following **Table 4.1**, are given the volumetric mass density, the bulk modulus and the sound velocity from the literature.

	ρ (g.cm ⁻³)		B (GPa)		μ (GPa)	v (m.s ⁻¹)
	Experiment	Ab-initio	Experiment	DFT	DFPT	Literature
a-GeTe	5.6 [74]	5.7 [77]	Not found	Not found	Not found	Not found
α -GeTe	6.06 [74]	6.04 [77]	49.9 [78]	44.3 [79]	28.16 [80]	2500 [81]

Table 4.1: Volumetric mass density ρ , bulk modulus B and longitudinal sound velocity v of a-GeTe and α -GeTe reported in the literature

For an elastic wave that propagates in one direction inside an isotropic medium, the longitudinal sound velocity can be described as a function of bulk modulus (B), shear modulus (μ), Poisson's ratio (ν) and the density of GeTe (ρ) by equation

$$v = \sqrt{\frac{B + \frac{4}{3}\mu}{\rho}} = \sqrt{\frac{3B(1 - \nu)}{(1 + \nu)}} \quad (4.1)$$

Optical properties

Amorphous GeTe (a-GeTe) possesses a small optical conductivity and has a band gap (E_g) of around 0.7~0.8 eV as shown in **Fig 4.6(b)** where the imaginary part of the dielectric response ($\epsilon_{2,a}$) starts to be significant only above this characteristic energy. In the rhombohedral crystalline state (α -GeTe), GeTe becomes more conductive with a band gap smaller than 0.5 eV and estimated to be around $E_g = 0.1\sim 0.2$ eV [69]. At room temperature, we also see in **Fig 4.6(b)**, that with such a small band gap, there is also a Drude contribution (i.e. free carriers) illustrated by the important increase of the imaginary part of the dielectric constant $\epsilon_{2,\alpha}$ for energy below 0.5 eV. Such Drude tail does not exist for the amorphous state.

The refractive index n and the extinction coefficient k are also shown in **Fig 4.6(c,d)** for both amorphous GeTe (a-GeTe) and crystalline rhombohedral GeTe (α -GeTe).

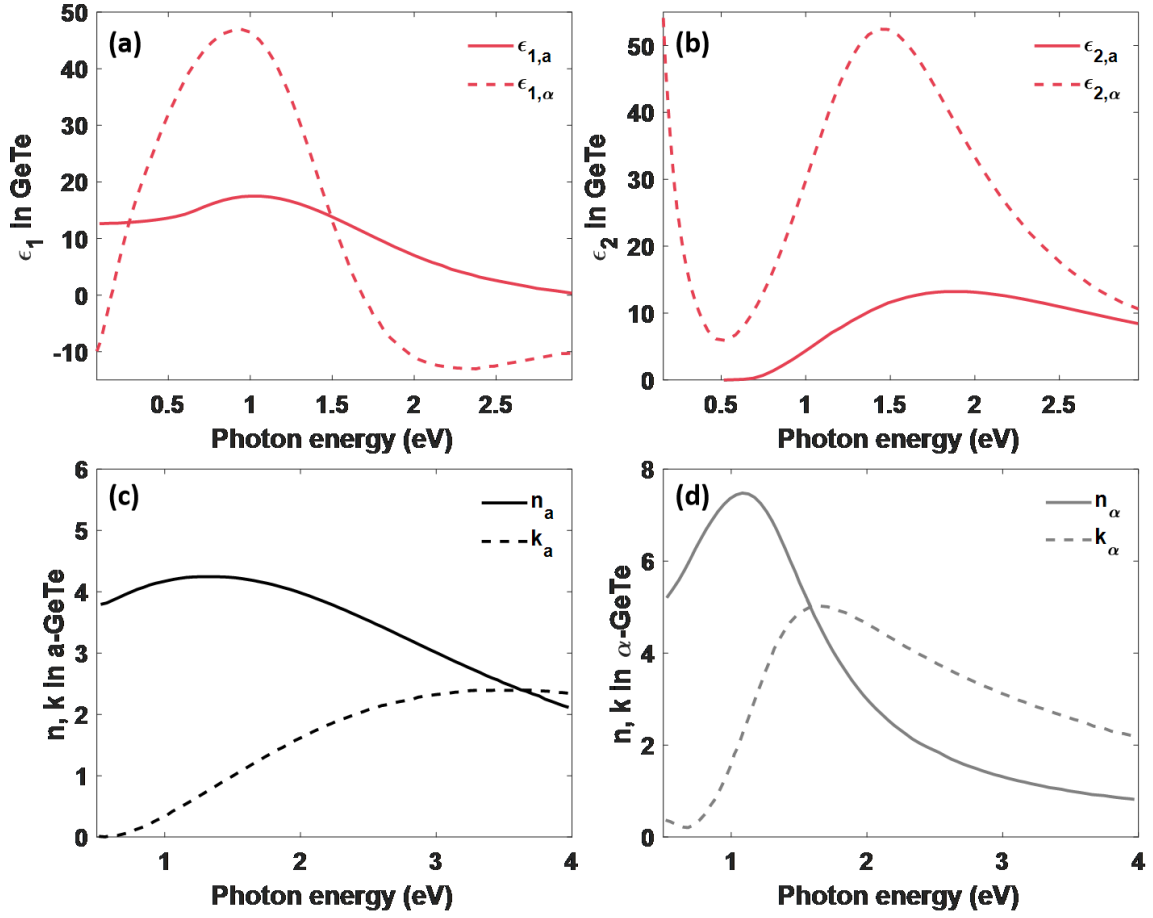


Fig 4.6: Real (a) and imaginary (b) part of dielectric constant in both a-GeTe and α -GeTe [82]. Refractive index and extinction coefficient in a-GeTe (c) and α -GeTe (d) [83].

They are calculated using the dielectric constant reported in the literature [82], and considering the relations given as:

$$\begin{aligned}
 \epsilon &= \epsilon_1 + i\epsilon_2 = (\tilde{n})^2 = (n + ik)^2 \\
 \epsilon_1 &= n^2 - k^2 \\
 \epsilon_2 &= 2nk
 \end{aligned} \tag{4.2}$$

The numerical values of n and k for several given wavelengths are calculated in Table 4.2.

	n			k		
	830nm	415nm	587nm	830nm	415nm	587nm
a-GeTe	4.2329	3.0143	3.8898	0.9936	2.3226	1.7414
α -GeTe	5.6072	1.3233	2.6642	4.8371	3.1270	4.4292

Table 4.2: Refractive index n and extinction coefficients k in a-GeTe and α -GeTe for several given wavelengths, which are relevant to our studies as we will discuss later on. Numerical values are extracted from **Fig 4.6**.

Heat capacity & thermal expansion coefficient

The heat capacity and the thermal expansion coefficient of GeTe are given in the **Table 4.3**.

	C_p (J.g ⁻¹ .K ⁻¹)	β (K ⁻¹)
a-GeTe	Not found	Not found
α -GeTe	~ 0.25 according to Dulong-Petit law	11.2×10^{-6} [84]

Table 4.3: Specific heat C_p and thermal expansion coefficient β of GeTe at room temperature (300 K) reported in literature.

It is worth to underline that since the amorphous a-GeTe is a metastable phase, the value of heat capacity, thermal conductivity as well as the thermal expansion coefficient cannot be thermodynamically defined. While we did not find reliable values for the heat capacity and the thermal expansion coefficient, the total thermal conductivity has been though measured in a-GeTe and a comparison with that of the crystalline state α -GeTe is presented in the following.

Thermal conductivity & diffusivity

The large difference between optical properties discussed in **Fig 4.6** is also accompanied by a large difference in the heat transport properties. In particular, the change from the amorphous to the crystalline state has a drastic consequence on the energy transport as shown in **Fig 4.7** with $\kappa_\alpha > \kappa_a$, where κ_α and κ_a are the heat conductivity of the crystalline (α) and amorphous (a) GeTe respectively. The larger heat conductivity for the crystalline state is due to the existence of both a larger efficient free carrier (κ_e) and phonon (κ_{lat}) heat transport in such state. Several thermal properties of GeTe are given in **Table 4.3**. The thermal diffusion coefficient D_{heat} is estimated by using lattice thermal conductivity κ_{lat} , mass density ρ of GeTe and the heat capacity C_p from the literature with the following equation:

$$D_{heat} = \frac{\kappa_{lat}}{\rho C_p} \quad (4.3)$$

Ghosh et al [81] have measured the thermal resistivity of GeTe deposited on 200 mm silicon wafers covered by a 500 nm thick SiO₂ top layer and covered by

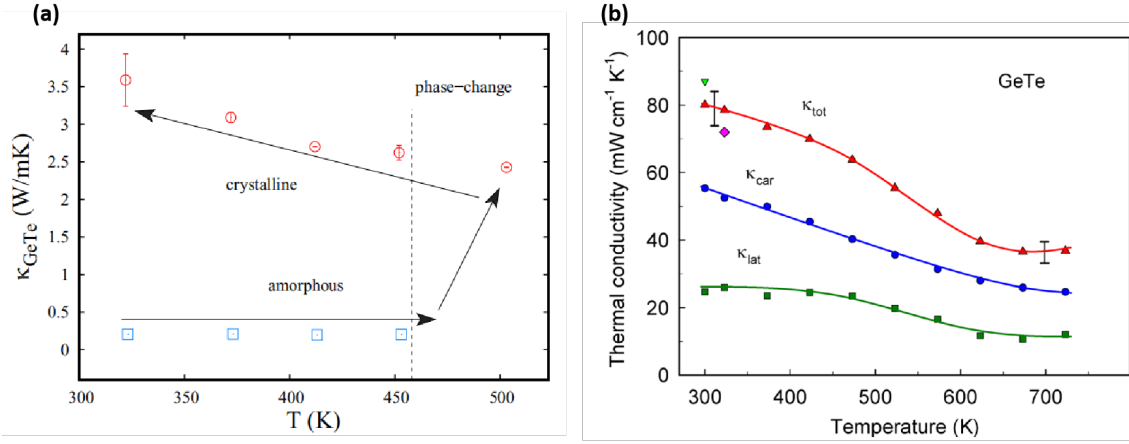


Fig 4.7: (a) Total thermal conductivity in a-GeTe and α -GeTe as a function of temperature from [81]. (b) Thermal conductivity of α -GeTe (including carrier and lattice contribution) as a function of temperature from [85].

100nm thick platinum (Pt) top layer. The conductivity of GeTe has been retrieved by linear regression (see **Fig 4.7(a)**). As in Ref [85], Levin et *al* have measured the total thermal conductivity of GeTe discs sample using the flash thermal diffusivity method. The carrier conductivity is calculated with Wiedemann-Franz law and the lattice thermal conductivity is retrieved by subtracting the electron contribution (see **Fig 4.7(b)**).

	κ_{tot} (W.m ⁻¹ .K ⁻¹)	κ_{car} (W.m ⁻¹ .K ⁻¹)	κ_{lat} (W.m ⁻¹ .K ⁻¹)	D_{heat} (m ² .s ⁻¹)
a-GeTe	~0.2 [81]	Not found	Not found	Not found
α -GeTe	~3.5 [81], 8.0 [84, 85]	5.1 [85]	2.9 [84, 85]	~ 2×10^{-6} [86, 87]

Table 4.4: Total thermal conductivity κ_{tot} , carrier (electron-hole) thermal conductivity κ_{car} , and lattice thermal conductivity κ_{lat} in a-GeTe and α -GeTe at room temperature (300K) reported in the literature. The heat diffusivity D_{heat} (lattice contribution) of α -GeTe is also included in the table.

A large discrepancy is noticed for the total thermal conductivity κ_{tot} of GeTe reported from different research groups, because κ_{tot} depends strongly on the structure of investigated GeTe samples and on related defects that might also change the carrier concentration and mobility.

Electron and hole mobility

The carrier-diffusion coefficients (D_h, D_e), which is characteristic for electron and hole diffusion defined in the physics of semiconductors [88], have been estimated for a-GeTe and α -GeTe using the hole mobility (μ_h) found in the literature. Assuming the Einstein-Smoluchowski relation to be valid, $D_{h,e}$ is given by equation:

$$D_{h,e} \approx \frac{\mu_{h,e} k_B T}{q} \quad (4.4)$$

where k_B and q correspond to Boltzmann constant and the elemental charge of carrier, the results are given at room temperature (300 K). The results given in **Table 4.5** are those for the hole mobility. The amorphous GeTe is a p -type material, the electron mobility is estimated to be very low in order to keep the p -type nature, which can be as large as $0.1 \text{ cm}^2 \cdot \text{V}^{-1} \cdot \text{s}^{-1}$ [89]. As for α -GeTe, the electron mobility has a theoretical value of up to $1066.33 \text{ cm}^2 \cdot \text{V}^{-1} \cdot \text{s}^{-1}$ [90].

	$\mu_h [\text{cm}^2 \cdot \text{V}^{-1} \cdot \text{s}^{-1}]$	$D_h [\text{m}^2 \cdot \text{s}^{-1}]$
a-GeTe	0.1~0.2[89]	$0.25 \sim 0.5 \times 10^{-6}$
α -GeTe	197.9[91], 120[92]	$0.2 \sim 0.4 \times 10^{-3}$

Table 4.5: Hole mobility μ_h and photoexcited carrier (hole) diffusion coefficient D_h of GeTe at room temperature (300K) reported in the literature.

There is a large difference, with more than two orders in magnitude, between the hole diffusion coefficient in a-GeTe and α -GeTe, due to the difference of electron/hole mobility in these 2 states. This is consistent with the important contribution of the mobile carriers to the heat conductivity as discussed previously.

4.3 State-of-art of photoinduced strain in GeTe and motivations

In this section the recent work regarding the study of the photoinduced strain in GeTe and related compounds are presented. As announced in the introduction of this chapter, the study of the transformation of the optical energy into the lattice strain provides a fundamental information about the light-matter interaction and in particular some insights on the coupling between the photoexcited carriers and the lattice.

State-of-the-art

The study of photoinduced strain has been carried out by Fons *et al* using time-resolved X-ray diffraction accompanied with numerical simulations [93]. They used ultrafast optical pump pulses to induce strains in the lattice and used X-ray pulses (100 ps of duration) to measure the corresponding lattice distortions. A typical time-dependent Bragg peak shift is shown in **Fig 4.9**. The authors observe that within the first hundreds of picoseconds, the lattice parameter increases upon the laser excitation (i.e. decrease of the momentum transfer vector Q_z). In order to quantitatively reproduce the experimental data (amplitude, time and spatial distribution of the strain), they claimed that it was necessary to modify both the optical

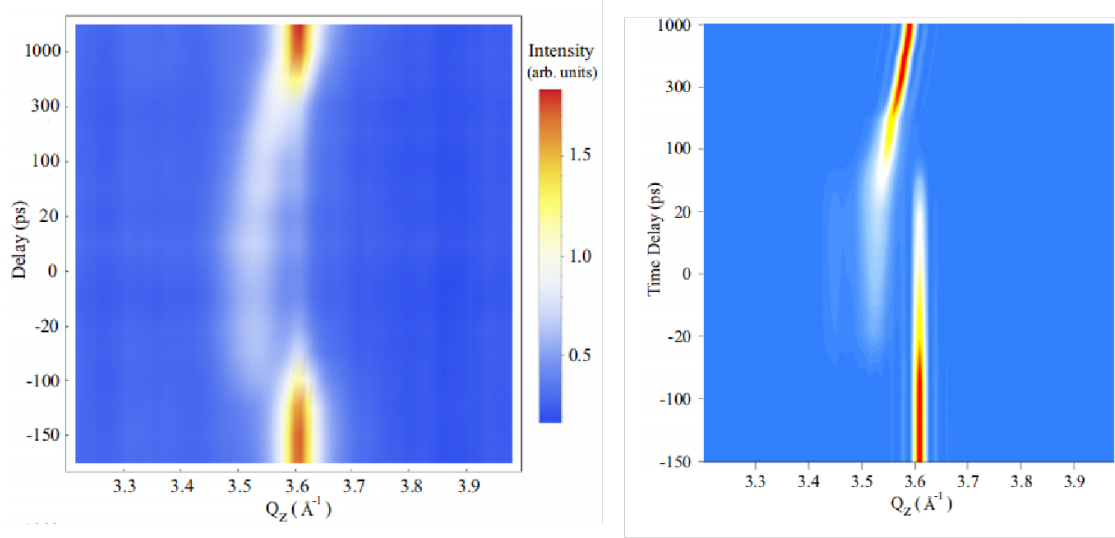


Fig 4.8: (left) Measured time and Q_z dependent intensity of the GST(222) Bragg diffraction peak for a fluence of 16 mJ.cm^{-2} . (right) Simulated time- Q_z intensity plot of the GST(222) diffraction peak carried out using a ball-and-spring model. The Q_z axis corresponds to the reciprocal space direction $\langle 111 \rangle^*$, while the Q_x axis corresponds to the reciprocal space $\langle 110 \rangle^*$ direction [93].

penetration depth and thermal expansion coefficients from their literature values. The value used for the optical penetration depth that maintained the maximum temperature constraint in their simulation model is a factor of approximately 6 times larger ($\alpha = 100\text{-}120 \text{ nm}$) than the expected value estimated at the pump wavelength with the tabulated data of optical properties of GST with of $\alpha \sim 1.9 \times 10^{-6} \text{ cm} = 19 \text{ nm}$. Moreover, the authors had to increase the lattice thermal expansion by 4. All these results lead the authors to propose that an electronic contribution to the light-induced strain might be present, without directly confirming it at that moment.

Photoinduced coherent acoustic phonons in GST thin films have been studied by Hase et al [94]. They carried out the experiments with GST thin films having different thicknesses (40 and 80 nm) and they succeeded in detecting the acoustic phonon response a couple of picoseconds after the optical excitation that give rise to some modulation of the transient optical reflectivity as indicated by thick arrows in **Fig 4.9**. When the optical penetration is much larger than sample thickness (case of the 40 nm thick film), the photoinduced strain takes place in the entire film that leads to a collective mechanical resonance of the entire film. On the opposite, when the optical penetration is much smaller, the coherent acoustic phonon is generated mainly at the surface and a pulse can propagate inside the sample and can be detected as an echo as labeled by * in **Fig 4.9**). The main conclusion of this work is an evidence of some differences in the elastic properties of the amorphous and crystalline states in the GST compound. The authors also reproduced the acoustic phonon signature with the Thomsen's model presented in Chapter 2.

Another group, Shu et al [95] performed ultrafast pump-probe experiment on

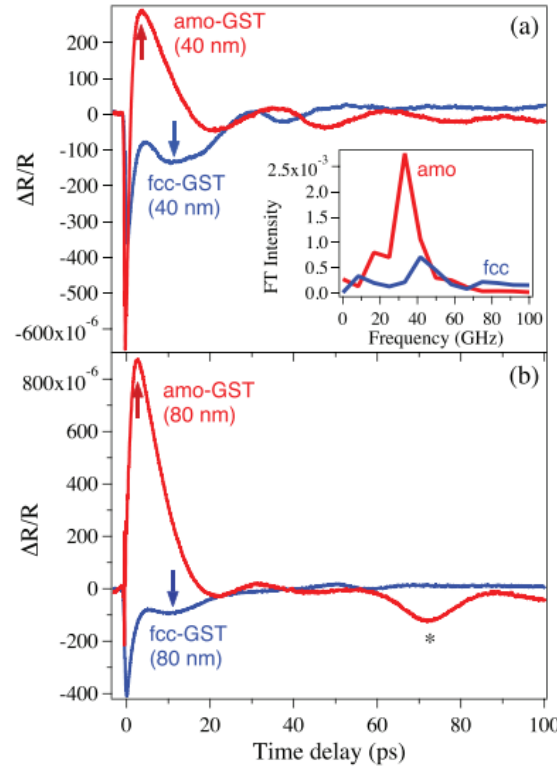


Fig 4.9: The time-resolved transient reflectivity signal observed in 40 nm thick (a) and 80nm thick (b) GST films for the amorphous and crystalline phases pumped with a fluence of 5 mJ.cm^{-2} . The thick arrows represent the positions of the acoustic phonon response a couple of picoseconds after the optical excitation. The inset in (a) represents the Fourier transform spectra obtained from the time-domain data for the case of the 40 nm-thick films. The signal labeled by * in (b) represents the propagating acoustic strain pulse, which is separately detected. [94]

GST films with a thickness of $H=250 \text{ nm}$ deposited on silicon. The authors reported photoinduced lattice distortion as witnessed, in both the amorphous and crystalline GST films, by the short-lived oscillations visible during the first 50 ps on the signal of the transient optical reflectivity shown in **Fig 4.10**. Despite the large thickness of this sample which represents a favorable geometry to reveal some acoustic phonon echoes (see **Chapter 2** for theoretical background), the authors did not report any signature of them within the first 250 ps of observation. Considering a sound velocity $V = 2000 \sim 3000 \text{ m.s}^{-1}$, which is the typical range, an acoustic echo should have been observed at a time delay of $t = 2H/V = 160 \sim 250 \text{ ps}$. The authors have not provided explanation of this effect at the moment and this is not discussed by the authors. One possibility is that the sound velocity is much smaller and the acoustic echo is out of the time range of the measurement.

Motivations of this work

Considering this literature, a short summary is presented here to motivate this PhD work. While phase transformation was initially described as a thermally as-

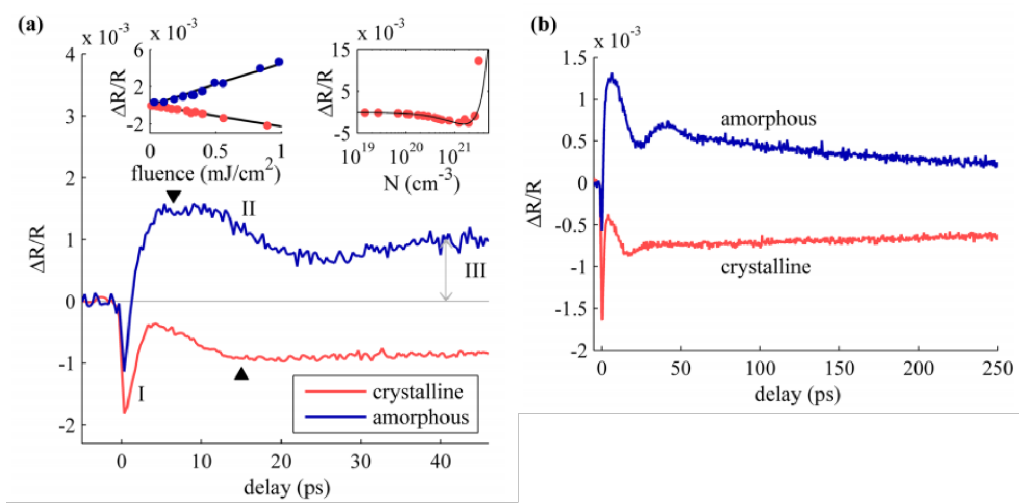


Fig 4.10: (a) Time-resolved reflectivity change for the crystalline GST (light red) and amorphous GST (dark blue) sample at a fluence of $0.4 \text{ mJ}/\text{cm}^2$. Left inset: The fluence dependence showing the linearity of the effect. The data points are taken at the delay times indicated by the black arrows in (a). Right inset: the value of $\Delta R/R$ at 600 fs as a function of excited carrier density for the crystalline film. (b) Longer time scale data of the time-resolved reflectivity change at a fluence of $0.26 \text{ mJ}/\text{cm}^2$. [95]

sisted process, the recent debate about the crucial role of photoexcited carriers in the amorphization process (α -GeTe to a-GeTe) has appeared as more and more plausible [96–98]. A non-thermal contribution might indicate the existence of a non-thermal process. While some elements go in that direction [96–98], this calls for clarification. Photoexcited carrier-lattice coupling is indeed at the core of the crucial mechanism for the transformation of light energy into lattice energy and represents the necessary step for phase transformation. It is important to underline that contradictory assumptions of the characteristic spatial extension of coupling between photoexcited carriers and phonons currently exist in the literature. It is considered that the photoexcited carrier-lattice coupling in PCMs is restricted to the optical penetration depth (light penetration) [94, 96–100], while another report suggests a possible ballistic electron effect [93], without any clear and direct conclusion related to this crucial physical phenomenon.

To address this question, the crucial parameter in this study, besides the high sensitivity of optical measurements, is the choice of the PCM thin-film thickness. Most previous studies [93, 94, 97–100] concern thin films having a thicknesses typically of the same order as the optical-pump light penetration depth ($\sim 30 \text{ nm}$) in the crystalline PCM. These low thicknesses are usually chosen because of experimental constraints associated with time-resolved x-ray or electron-diffraction [93, 97–100]. For such thin layers, there is a natural in-depth confinement of the photoexcited electron-hole plasma, preventing the electron-hole plasma from expanding, if any. Here, we perform in situ pump probe experiments on a much thicker film, with a GeTe film having a thickness of 380 nm , to let the electron-hole plasma a possibility to expand. To probe this effect, as demonstrated in the following, we analyse the

spatial distribution of the light-induced strain. As it was already shown in metals [101–103] and semiconductors [104], the emitted strain pulse can contain indeed a direct fingerprint of fast photoexcited carriers diffusion, i.e. a non-thermal transport of energy.

4.4 Experimental results and analysis

This section comes to the experimental results that have been obtained with optical pump-probe experiments at IMMM laboratory, in order to discuss the questions raised in the previous section. Most of the results presented here have been published in 2021 (GU et al [105]). Beginning with a brief introduction of our experimental sample, experimental results will be described first, then the data analysis and discussions will be presented. At the end some conclusions and perspectives will be given.

4.4.1 GeTe sample description

Our GeTe sample is in its amorphous state after fabrication using radio frequencies sputtering (RF sputtering) performed by our colleagues (Prof. Harish Bhaskaran and Dr. Zengguang Cheng) at University of Oxford. The stoichiometry of the sample is 50 by 50 and it has been deposited on a SiO_2/Si [100] wafer substrate, and GeTe was finally covered by a 10 nm thick ITO protection layer in order to prevent oxidation. The sample itself has a thickness around 380 nm (**Fig 4.11(a)**), which is estimated by quartz balance during the growth.

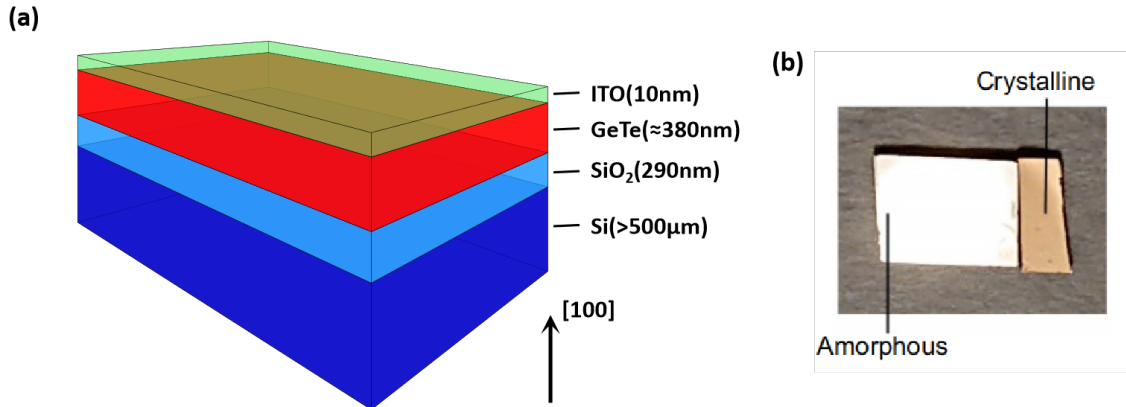


Fig 4.11: (a) Sketch of GeTe sample deposited on SiO_2/Si (100) substrate and covered with protection ITO layer. (b) Photo of amorphous GeTe (a-GeTe) and rhombohedral GeTe (α -geTe) prepared with heating furnace and studied in this work that illustrates the large contrast in the optical reflectivity.

The rhombohedral crystalline GeTe sample (α -GeTe) has been prepared by heating one of the amorphous sample (a-GeTe) with a furnace Linkam (a temperature

programmer, model T95-PE associated with a liquid nitrogen pump, model LNP95 [47]) in our laboratory. The sample has been heated up to 300 °C at a rate of 5 K.min⁻¹ and the target temperature was maintained for 30 minutes. Such method has been applied in other works to induce crystallization [106, 107]. A photo of both samples side by side is given in **Fig 4.11(b)**, which shows a clear contrast of the optical reflectivity between the amorphous and rhombohedral crystalline samples under the illumination with a white light source.

4.4.2 Raman scattering experiments in GeTe

Once the crystalline GeTe sample has been obtained, Raman scattering experiments were performed on both amorphous and crystalline samples, in order to check the quality of crystallization of GeTe.

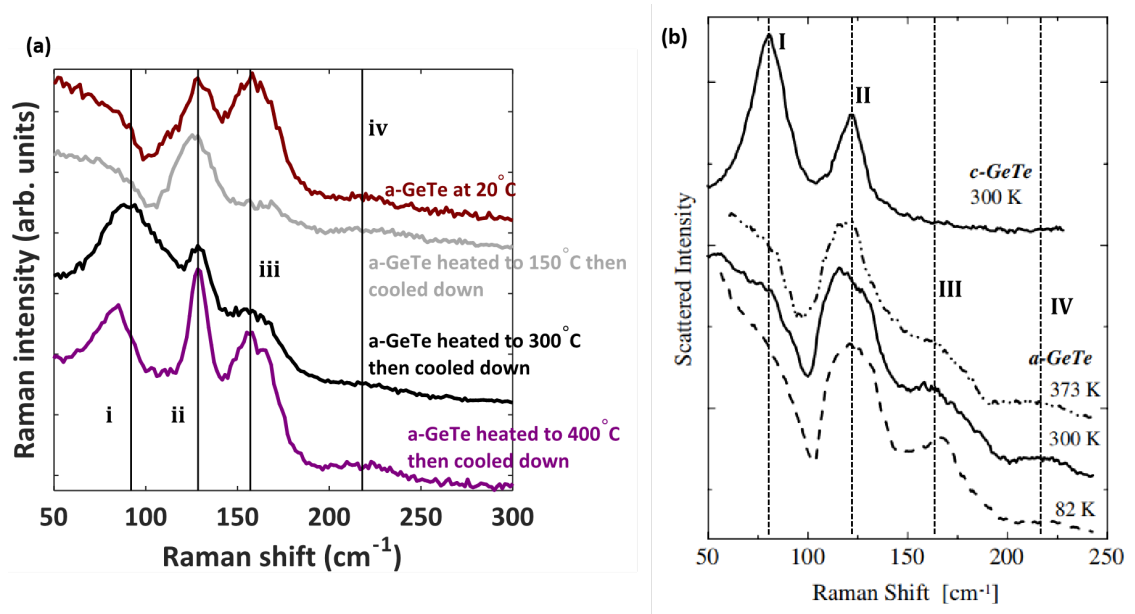


Fig 4.12: (a) Raman spectrum of a-GeTe and α -GeTe performed at IMMM. (b) Stokes-side raw Raman spectra of a-GeTe at 82, 300 and 373 K. The spectrum of c-GeTe at 300 K is also shown for comparison [108].

The Raman scattering experiments have been conducted at IMMM under the supervision of Prof. Alan Bulou. The Raman spectra are recorded with T64000 Jobin-Yvon spectroscopy with a microscope having an objective with a magnification 50 \times . The laser wavelength is set to 647.1 nm (produced by a Ti:sapphire laser pumped by an Ar⁺ ion laser) and the incident power on the sample is 0.2 mW. The Raman scattering experiments have been carried out at room temperature, and different samples have been annealed under 4 different temperature conditions including room temperature (20 °C), 150 °C, 300 °C and 400 °C. The results are given in **Fig 4.12(a)**, only the Stokes-side Raman spectra are shown. Similar experiments conducted by K. S. Andrikopoulos et al [108] are shown in **Fig 4.12(b)** for comparison. They were using the same Raman spectrometer but with different pump

wavelength (763 nm) and different pump power (<0.4 mW).

In **Fig 4.12**, the Raman spectrum of a-GeTe possesses 3 peaks, one at 132 cm^{-1} (ii), another at 165 cm^{-1} (iii), the last one at 218 cm^{-1} (iv). When the sample is annealed at $150\text{ }^{\circ}\text{C}$, peak (iii) begins to vanish. Comparing to **Fig 4.12(b)**, we can tell that the GeTe sample remains in amorphous state, even if some slight Raman shifts peaks are observed. If the sample is annealed at $300\text{ }^{\circ}\text{C}$, a Raman shift at 92 cm^{-1} (i) is identified in the spectrum, which indicates the formation of crystalline phase in GeTe consistently with the literature [108]. The transition might not be 100 % complete due to the existence of peak (iii) which indicates some amorphous state residues. When the sample is annealed at $400\text{ }^{\circ}\text{C}$, Raman shift peak at 165 cm^{-1} (iii) reappears and coexists with peak (i), which implies that part of our crystallized sample might have been melted and has reformed once cool down. Consequently, as we will detail later on, in the pump-probe experiments as a function of temperature, we will limit our temperature to a maximum of $300\text{ }^{\circ}\text{C}$.

4.4.3 Typical signal recorded in optical pump probe experiments

In the following part, the results of pump-probe experiments on both a-GeTe and α -GeTe samples will be given. Beginning with brief description of transient optical reflectivity signal, the ultrafast carriers dynamics as well as the coherent acoustic phonon spectra will be addressed in different GeTe samples.

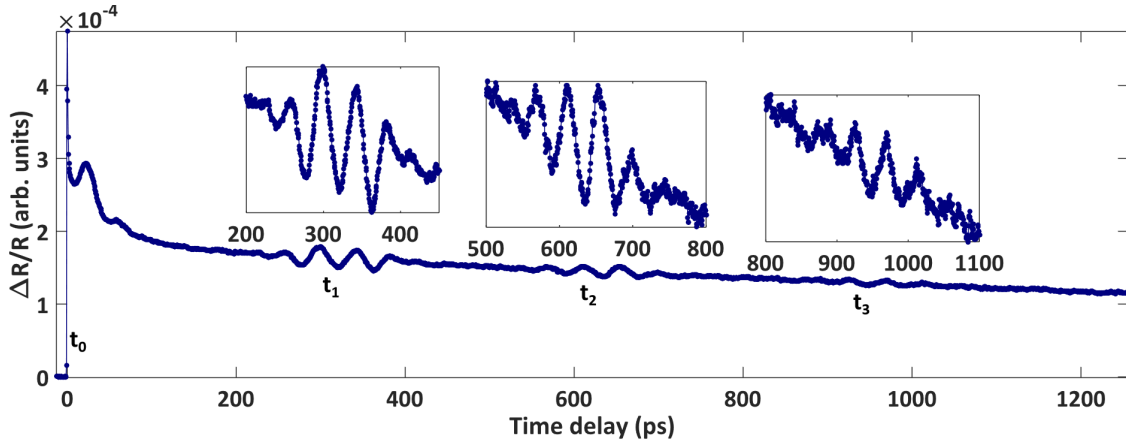


Fig 4.13: Typical signal of transient optical reflectivity $\Delta R/R(t)$ in a-GeTe, recorded with blue pump (415nm) and visible probe (587nm). t_0 corresponds to the electronic excitation, i.e. arrival of the pump beam on to the sample. t_1 , t_2 , t_3 are time delays corresponding to the arrival of successive coherent acoustic phonon echoes due to the bouncing back and forth of the acoustic pulse in the a-GeTe sample. The echo shape has been zoomed in the insets.

The pump-probe experiments have been conducted following the typical scheme presented in **Chapter 2**. And the obtained transient optical reflectivity (TOR, $\Delta R/R$) signal is shown in **Fig 4.13**. The a-GeTe sample was excited with a radiation

of 415 nm and the signal was probed with a visible radiation having a wavelength of 587 nm. A sharp peak has been identified at “ t_0 ” position, followed by some damped oscillations within the first 50 ps. And 3 echoes have been observed at position $t_1 \sim 300$ ps, $t_2 \sim 600$ ps and $t_3 \sim 900$ ps. The photogeneration and detection of coherent acoustic phonon will be described in detail with the following sketch.

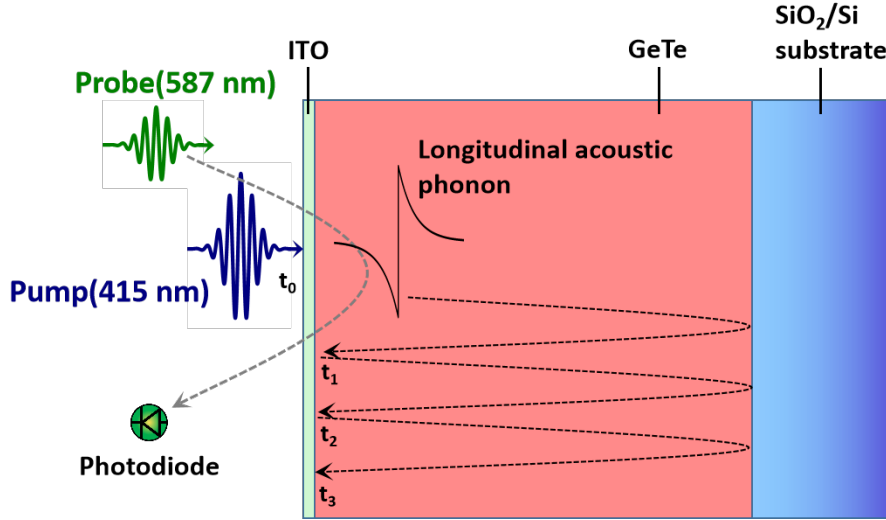


Fig 4.14: Sketch of generation, propagation and detection of coherent longitudinal acoustic phonons in GeTe sample. The positions of the pump and the probe laser beams and of the echo arrivals in the surface are all shifted vertically only for convenience. In experiment the lasers are co-focused. The generated acoustic phonon pulse has a bipolar shape. t_0 correspond the arrival of pump beam (415nm) onto the surface of GeTe, corresponding to the electronic excitation in **Fig 4.13**. The back and forth travelling of coherent acoustic phonons and their arrivals to the interface ITO/GeTe are noted by t_1, t_2 and t_3 , which is detected as periodic acoustic echos.

As shown in **Fig 4.14**, the pump radiation of 415 nm impinges onto the surface of a-GeTe, the electronic cloud is excited, corresponding the large variation of transient optical reflectivity revealed at t_0 in **Fig 4.13**, which is called the electronic peak response and it will be more discussed in the subsection 4.4.5.1. In the next tens of picoseconds, we can see the presence of a damped oscillating signal right after t_0 (see **Fig 4.13**), which corresponds to the photoinduced acoustic strain pulse leaving the surface of GeTe. This acoustic phonon pulse travels back and forth inside the GeTe film. Each time when the acoustic strain is close to the ITO/GeTe interface (see **Fig 4.14**), it is detected by the probe radiation (587 nm) as periodic acoustic echo shown at times t_1, t_2 and t_3 in **Fig 4.13**. Detailed explanation of principle of photogeneration as well as detection of coherent acoustic phonon in materials has been established in **Chapter 2**.

4.4.4 Calibration of the experiment

As mentioned in the beginning of chapter, in the application of phase change material devices, both the amorphization and crystallization are achieved by applying

ultrashort laser pulses [56, 57]. As we want to avoid such photoinduced transition during our experiments, we performed in the first place, a series of pump-probe experiments as a function of incident pump fluence, in order to reveal the evolution of transient optical reflectivity signals. This calibration is used for defining the threshold below which the light pulse does not modify the material.

Phase transition achieved by photo-assisted thermal effect

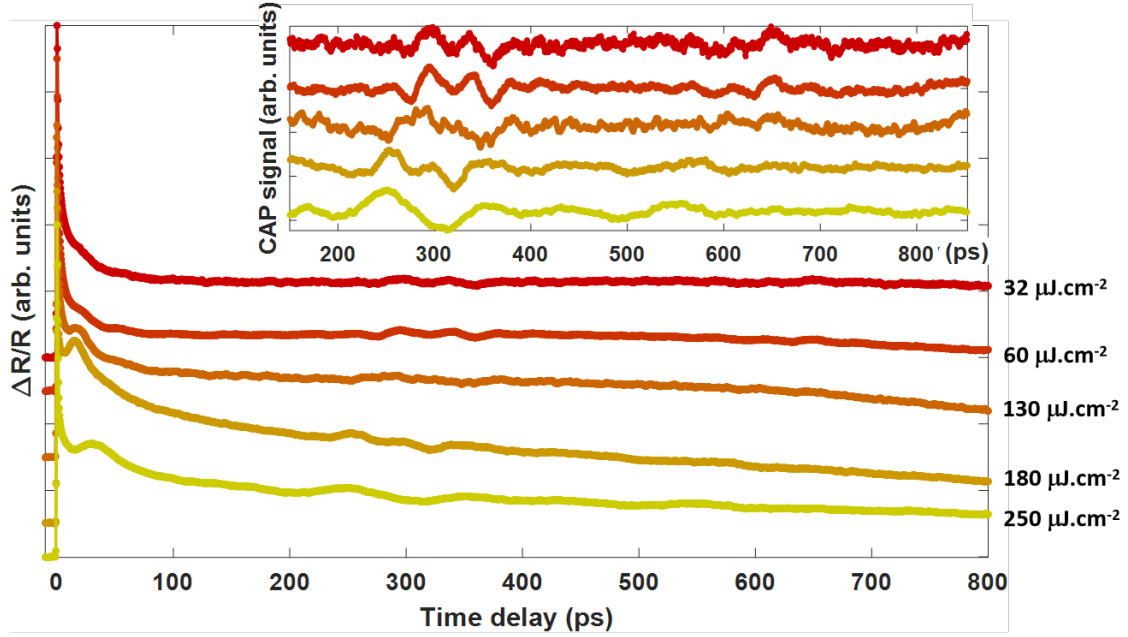


Fig 4.15: Transient optical reflectivity signals recorded in a-GeTe using 830 nm pump and 587 nm probe. The pump fluence varies from 30 $\mu\text{J.cm}^{-2}$ to 250 $\mu\text{J.cm}^{-2}$. The coherent acoustic phonon signals (after removing the thermal relaxation process), are shown in the inset. The signals are upward shifted for better comparison.

As shown in **Fig 4.15**, we recorded several transient optical reflectivity signals on different positions of a-GeTe (metastable) sample, by fixing the pump wavelength at 830 nm and probe wavelength at 587 nm. The pump fluence varies from 30 $\mu\text{J.cm}^{-2}$ to 250 $\mu\text{J.cm}^{-2}$, and the probe fluence was always fixed to be smaller than half of minimum pump fluence ($<10 \mu\text{J.cm}^{-2}$).

As revealed by the transient optical reflectivity signals, for the pump fluence of 32 and 60 $\mu\text{J.cm}^{-2}$, no evident change in $\Delta R/R$ signal as well as in the coherent acoustic phonon signal (see **Fig 4.15** inset). Since the sample is initially a-GeTe, it remains amorphous. As for the pump fluence above 130 $\mu\text{J.cm}^{-2}$, a modification of $\Delta R/R$ signal and different coherent acoustic phonon signal are observed, indicating a change of the properties of a-GeTe under the pump beam excitation. With a fluence of 250 $\mu\text{J.cm}^{-2}$, both the transient optical reflectivity and coherent acoustic phonon signal continue to evolve, showing that the irradiated zone of a-GeTe is transformed into a new state. Additional experiments with small fluence have been performed right after the one with 250 $\mu\text{J.cm}^{-2}$ pump fluence, the coherent acoustic signal has

the same shape of that with $250 \mu\text{J}.\text{cm}^{-2}$ pump fluence, indicating an irreversible effect is established by pump radiation.

In order to characterize more precisely the light-induced transformation of a-GeTe, we have performed the measurement of transient optical reflectivity at given temporal position (11 ns after the arrival of pump pulses onto the sample) in both a-GeTe and α -GeTe.

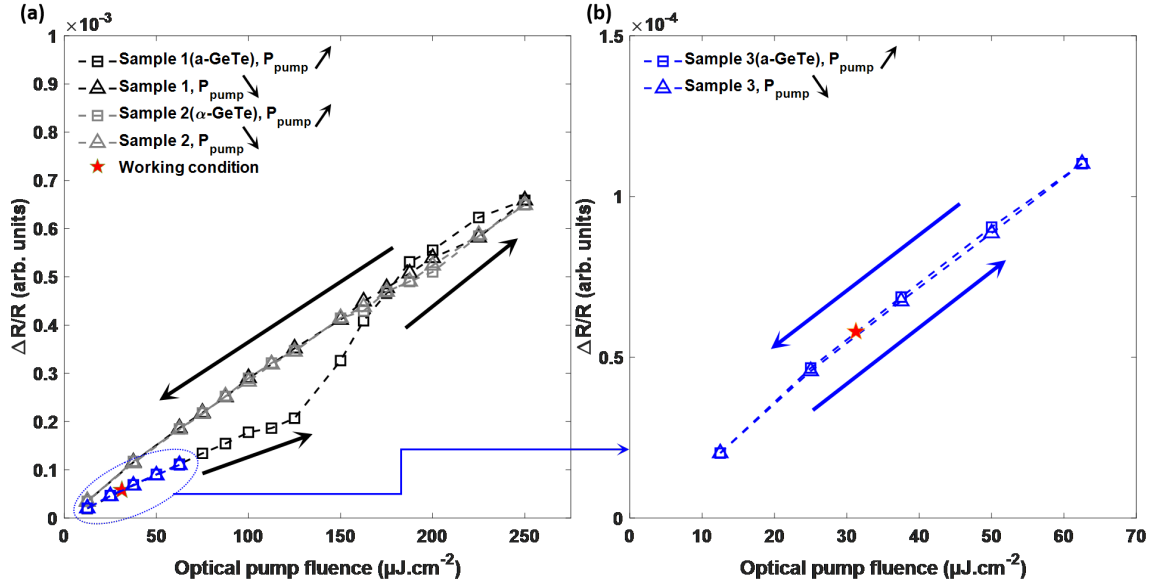


Fig 4.16: (a) Measurement of optical reflectivity at $t= 11\text{ns}$ as function of optical pump fluence varying from 0 to $250 \mu\text{J}.\text{cm}^{-2}$. The a-GeTe is called sample 1 and is the initial state of the layer. α -GeTe is called sample 2 and is the state obtained once the layer has been submitted to high optical fluence. The threshold is around $100 \mu\text{J}.\text{cm}^{-2}$ well revealed by the hysteresis of the optical response. (b) Additional measurements have been performed in another a-GeTe sample (sample 3) within a low fluence regime with the absence of the transformation of the amorphous state under the optical excitation. For comparison, the signal of sample 3 is also presented in the (a) part of the figure.

Fig 4.16 shows the evolution of optical reflectivity measured at 11 ns after the electronic excitation reminding that the repetition rate of our laser is around 80 MHz (12.5 ns), as a function of pump fluence. Both the pump and probe wavelength remain unchanged, and fixed at 830 nm and 587 nm for pump and probe, respectively. The experiment has been conducted with an amorphous GeTe (a-GeTe) as the starting state, which is called “Sample1”. The optical reflectivity has been recorded by first increasing the pump fluence from 0 to $250 \mu\text{J}.\text{cm}^{-2}$ (as indicated by black squares in **Fig 4.16(a)**). For a pump fluence below $100 \mu\text{J}.\text{cm}^{-2}$, the optical reflectivity evolves linearly as a function of the pump fluence. Above $100 \mu\text{J}.\text{cm}^{-2}$, a non-linear response of the optical reflectivity is obtained. With a further increase of the pump fluence above $200 \mu\text{J}.\text{cm}^{-2}$, the optical reflectivity enters into another linear regime with a different slope. When the pump fluence is reduced down to zero (shown by black triangles), there is no reversibility of the measured response:

a clear hysteresis behavior is revealed indicating a transformation of the material. Another cycle of experiments has been conducted with this transformed sample, named “Sample 2”, and the results are indicated by grey squares (for the increasing part of pump fluence) and gray triangles (for decreasing part of pump fluence) in **Fig 4.16(a)**. The optical reflectivity gives a linear response as a function of the pump fluence, which indicates that the hysteresis behavior has disappeared. This shows that the new state (Sample 2) is a stable phase at room temperature and even a large fluence such as $200 \mu\text{J.cm}^{-2}$ does not make the state evolve anymore. This confirms that a photo-assisted phase transition is achieved between the state of sample 1 and that of sample 2. At this moment, this observation is in agreement with the results presented in **Fig 4.15** where the transformation of the full transient optical reflectivity signal was detected at similar pump fluence. The last cycle of measurements has been conducted on a second a-GeTe sample (Sample 3). In that case, the pump fluence varies from 0 to $70 \mu\text{J.cm}^{-2}$ (i.e. below the optical pump threshold) and the results are given in **Fig 4.16(b)**. Within that low fluence regime, we show that sample 3 remains in the amorphous state all along the experiments in this fluence range and no transformation is revealed. These experiments define the relevant pump fluence to be used in the pump-probe experiment to probe the dynamics in a-GeTe without transforming it. The selected pump fluence has been set to $32 \mu\text{J.cm}^{-2}$ (indicated by “star” in **Fig 4.16(a,b)**) in order to work in the linear regime, with 5 times less probe fluence in order to neglect its contribution to the photoexcitation.

4.4.5 Photogeneration and detection of coherent acoustic phonons in amorphous & crystalline GeTe

Once the pump has been set to low fluence, i.e. below the pump fluence threshold over which the irreversible effect appears, we can now investigate the photogeneration and detection of coherent acoustic phonons in both a-GeTe and α -GeTe as a function of temperature. To do so, the a-GeTe sample was placed inside a Linkam furnace setup, and we measured the transient optical reflectivity under several chosen temperature conditions.

The results of transient optical reflectivity signals of a-GeTe recorded under different temperature conditions are shown in **Fig 4.17**, with the coherent acoustic phonon signal after removal of the thermal relaxation background shown in the inset. When $T \leq 150 \text{ }^\circ\text{C}$, both the transient optical reflectivity signal and the coherent acoustic phonon signal show no evident change, since $T < T_{\text{Cryst.}}$, which is around $200 \text{ }^\circ\text{C}$ (see Raman measurements shown in **Fig 4.12**). That is the reason why we observe a drastic change in the transient optical reflectivity signals as well as in the coherent acoustic signals, when T reaches $200 \text{ }^\circ\text{C}$. At this temperature we know that a-GeTe has been transformed into α -GeTe. Additional experiments have been performed on the GeTe sample right after it was annealed at $300 \text{ }^\circ\text{C}$, i.e after the amorphous state has been transformed into the crystalline state. This new run in temperature is shown in **Fig 4.18** where only the coherent acoustic phonon signals are shown. As we can see there is no significant change of coherent acoustic phonon

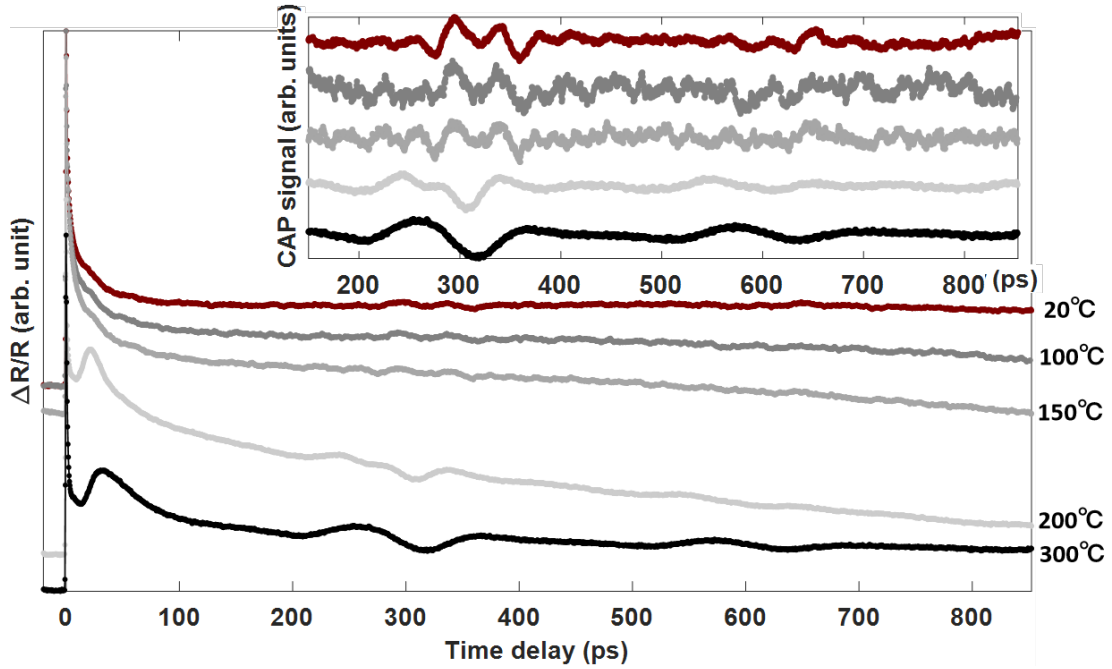


Fig 4.17: Transient optical reflectivity recorded by pump-probe experiments in GeTe from room temperature to 300 °C. Inset: coherent acoustic phonon signal after removal of the thermal relaxation process.

signal within the temperature range 20-300 °C, this shows that the sample does not evolve anymore and that the system has been converted into the stable crystalline state (α -GeTe).

It is worth to underline that if we compare the transient optical reflectivity signal obtained with the α -GeTe (i.e. for temperature at 300 °C ensuring the crystallisation of the amorphous state as seen in **Fig 4.17**) and the signal obtained when illuminating the amorphous sample above the so-called optical threshold (i.e. with a high fluence of 250 $\mu\text{J}\cdot\text{cm}^{-2}$, **Fig 4.15**), we can see that the shapes of coherent acoustic phonon signals for both situations are very similar. This perfectly shows that, starting from the amorphous state, we can obtain the α -GeTe either with a thermal annealing or under light-induced heating effect. In the latter case, we consider that the sequence of the pump pulses (repetition rate of 80 MHz), with that so-called high-fluence, leads to a heating of the sample (through typically the electron-phonon thermalization process). Discussing how the light can transform the amorphous state into the crystalline state is not the topic of this work and has been studied several times in the literature [109].

4.4.5.1 Ultrafast carrier dynamics

Before discussing the phonon dynamics, in this part we will focus on the ultrafast carrier dynamics in both a-GeTe and α -GeTe. For that, we discuss the transient optical reflectivity within 10 ps after optical excitation (noted as $t=0$ ps). The ultrafast response (fit of the electronic peak decay) reveals a clear change in the

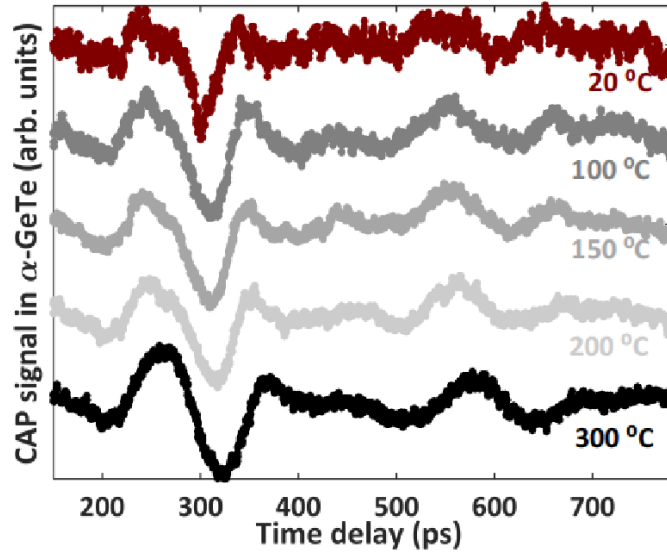


Fig 4.18: Extracted coherent acoustic phonon spectrum in α -GeTe as the same temperature conditions as in **Fig 4.17**.

carrier-phonon thermalization rate through a change of the carrier relaxation time.

The results are shown in **Fig 4.19(a)**, the decay of the ultrafast optical reflectivity is modeled with the following equation:

$$\frac{\Delta R(t, T)}{R} = \frac{1}{2}(\text{erf}(t) + 1) \times (A(T) + B(T)e^{-t/\tau_1} + C(T)e^{-t/\tau_2}) \quad (4.5)$$

where $A(T)$ is the long-living component (plateau like response), exceeding the time scale of electronic response, while $B(T)$ and $C(T)$ are the magnitudes associated to the “fast” and “slow” component, noted as τ_1 and τ_2 , respectively. The results are shown in **Fig 4.19(b)**, we can see that τ_1 does not significantly change upon crystallization, which can be explained by the decay of the obtained signal, constructed by the cross-correlation of the optical pump and probe beam:

$$\frac{\Delta R}{R} \propto \Gamma_{Pp, Pb}(\tau) = \int Pp(t)Pb(t - \tau)dt \quad (4.6)$$

with $Pp(t)$ and $Pb(t)$ represent the optical pump and probe temporal envelop pulse, respectively.

As for the “slow” component τ_2 , it exhibits a longer life time in amorphous GeTe, and a brutal drop when α -GeTe is formed. Such behavior of change in hot carrier relaxation time has already been observed in NdNiO_3 when the system evolves from the insulator to the metallic states [110] or during the formation of charge density waves in semiconductors [111]. Such slowing down of the thermalization of the photoexcited carriers was related to the opening of a band gap near the Fermi level. In GeTe, we do not have an transition between metal and insulator states but rather

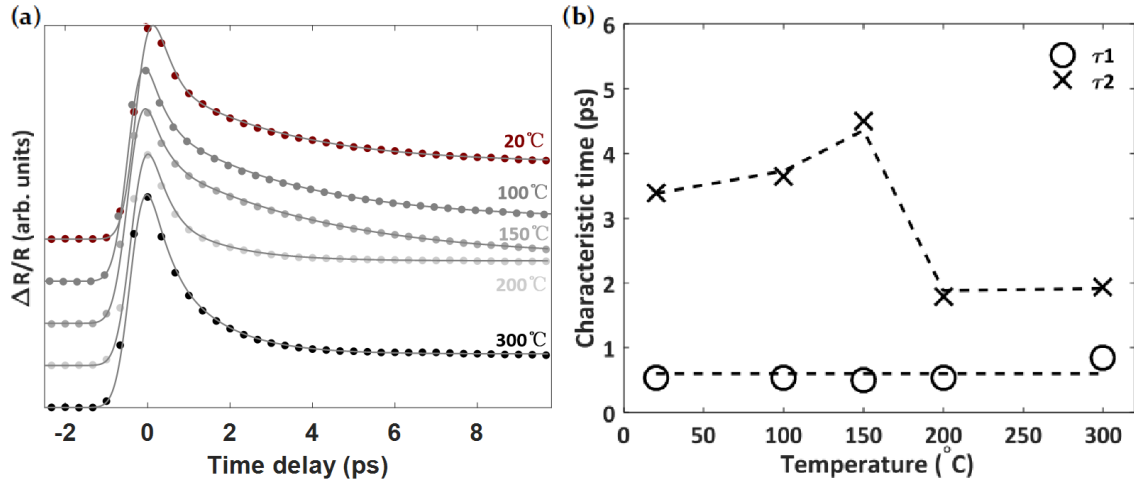


Fig 4.19: (a) Ultrafast electronic response in both a-GeTe and α -GeTe as a function of temperature. The calculated models with equation (4.5), which are shown as solid lines, adapt to $\Delta R/R$ signal at different temperatures. (b) Evolution of the characteristic carrier relaxation times τ_1 and τ_2 .

an decrease of the band gap energy caused by a-GeTe to α -GeTe transition. It is worth noting that the role of the traps (presence at localized states in the band gap [112]) in the amorphous state might also play a role in the carrier relaxation. As a summary, besides the drastic evolution of the photoinduced acoustic phonon signal, this large difference in the photoexcited carrier dynamics is a clear evidence of a different electron-phonon coupling in the amorphous and crystalline states.

4.4.5.2 Evolution of the acoustic phonon spectrum

After the investigation of ultrafast carriers dynamics in GeTe, this part will now mainly focus on the analysis and the discussion of the coherent acoustic phonon response as well as on its spectrum in both a-GeTe and α -GeTe. As mentioned in Chapter 3 we use 2 different wavelengths at 830 nm and 415 nm, for the pump, and the probe wavelength is fixed at 587 nm.

In **Fig 4.20**, the transient optical reflectivity signals, recorded with pump-probe experiment in a-GeTe and α -GeTe samples, are shown on the left part (a). And the extracted coherent acoustic phonon signals are shown in the insets. On the right side (b), the fast Fourier transform (FFT) spectra of the correspondent CAP signals are presented. The FFT spectrum of the entire CAP signal, including successive acoustic echos, is shown in solid line. The echo corresponds to the CAP return to the laser irradiated surface after back and forth propagation in the film. The envelop of the spectrum, represented by the dashed line, corresponds to the FFT spectrum of a single acoustic echo. The acoustic spectrum possesses a central frequency of 25 GHz in a-GeTe, as shown in **Fig 4.20(b)**. In α -GeTe, the central frequency of the FFT spectrum redshifts down to around 10 GHz. The spectrum for the signal obtained at 300 °C is quite similar to that obtained at room temperature, there is only a slight attenuation for the high frequency components, but the central frequency remains

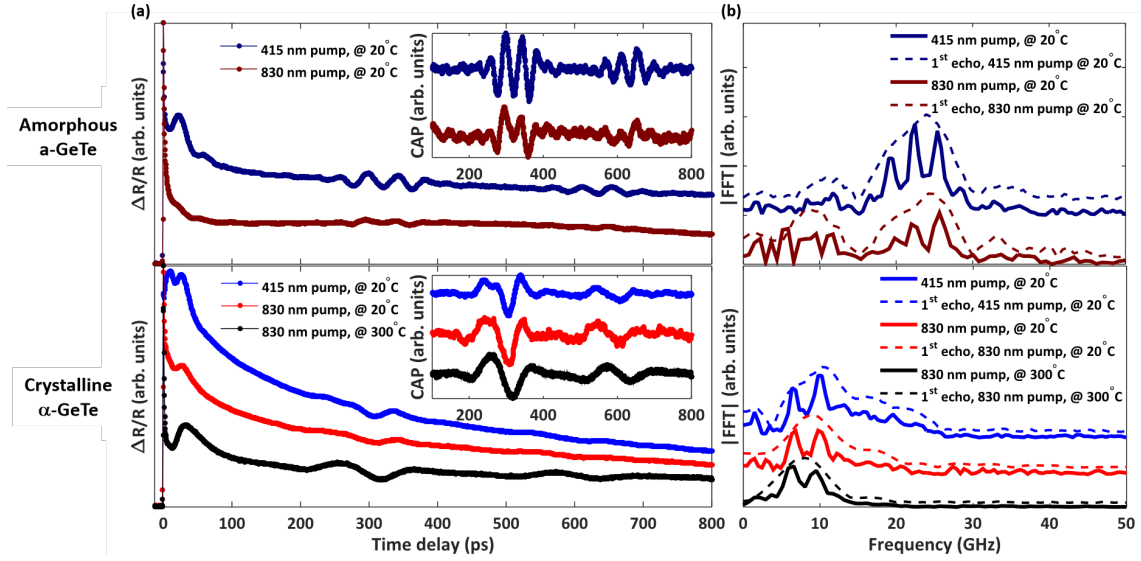


Fig 4.20: (a) Transient optical reflectivity (TOR) at room temperature in a-GeTe (top) and in α -GeTe (bottom), with correspondent coherent acoustic phonons (CAP) signal in the inset. The experiment of α -GeTe at 300 °C is added for comparison. (b) Fast Fourier transform (FFT) spectrum of CAP signals shown in inset in (a). The spectrum of the entire CAP signals including multiple acoustic echos is shown in solid line, while the dashed line represents the FFT spectrum of a single acoustic echo (i.e. the first echo for example).

unchanged.

The FFT spectra can also give access to the sound velocity in a-GeTe and α -GeTe, since the repetition in time domain of these acoustic signals gives rise to a sequence of frequencies in the frequency domain. In the time domain, the periodic signals with two acoustic echoes is the result of a time convolution of the temporal comb (limited here to two echoes of course) with the temporal envelop of an acoustic echo. As a consequence, in the Fourier domain, the spectrum of the full signal is the product of the spectrum of temporal comb (i.e. a frequency comb with a natural limited cut-off due to the generation and detection processes) with the spectrum of the acoustic pulse. The latter one is shown in **Fig 4.20** as aforementioned. The frequency comb is defined by the sequence of frequencies given by:

$$f_n = \frac{nv}{2d} \text{ with } n \in \mathbb{N} \quad (4.7)$$

with v the speed of sound and $d \approx 380$ nm is the thickness of the sample. Some detected frequencies are depicted by arrows in **Fig 4.21(a)**.

The frequencies versus the harmonic number n are plotted in **Fig 4.21(b)**. With the application of linear regression, the longitudinal sound velocity is estimated, using equation (4.7) to be $v_a \approx 2400$ m.s⁻¹ in a-GeTe, and $v_\alpha \approx 2500$ m.s⁻¹ in α -GeTe.

The sound velocity can be predicted in using their density ρ and P-modulus M ,

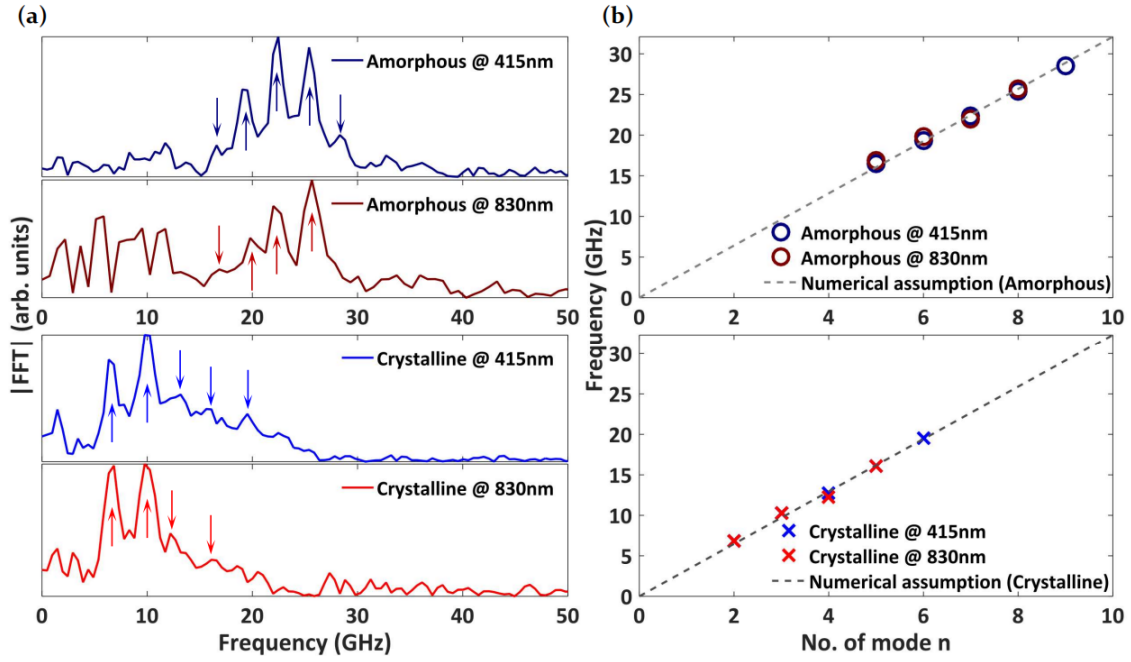


Fig 4.21: (a)FFT spectrum of time-resolved optical reflectivity in a-GeTe and α -GeTe with red and blue pump. (b)Evolution of the frequency with respect to the no. of the peak extracted in (a), the slope of the curves provides access to the evaluation of the sound velocity.

which can be calculated with the bulk modulus B and the Poisson's ratio ν , using the expression: $M = \frac{3B(1-\nu)}{1+\nu}$.

	Longitudinal sound velocity v (m.s ⁻¹)		
	Experimental (this work)	Calculation (this work)	Literature
a-GeTe	~2400	—	—
α -GeTe	~2500	~2700	2500 [81]

Table 4.6: Experimental results and numerical calculation longitudinal sound velocity v in both a-GeTe and α -GeTe.

As shown in **Table 4.6**, the experimental values of sound velocity are compared to the calculated value and that reported in the literature ($v = \sqrt{\frac{M}{\rho}}$). The experimental results are in good agreement with the calculation and reported value [81].

4.4.6 Analysis and discussion: ultrafast non-thermal transport of energy

In the previous part we have shown how much the spectrum of the photogenerated acoustic phonon has evolved upon the crystallization. In particular, the central

frequency of that spectrum exhibits a drastic redshift. In order to understand the physical origin at play, we will first simulate the transient acoustic phonon signal following the Thomsen's model to try reconstructing the spatial profile of the photoinduced strain, and then discuss the dynamics of electrons and phonons in the early stages of the generation of the acoustic pulse.

4.4.6.1 Simulation of the bipolar acoustic strain in GeTe

In a classical semi-infinite material, the transmitted light intensity at position z within the material (with $z=0$ denotes the free surface) can be described by the classical Beer Lambert's law:

$$I(z) = I_0 e^{-\alpha z} \quad (4.8)$$

with I_0 being the incident beam intensity, α the absorption coefficient, which leads to the optical penetration depth ξ :

$$\xi = \frac{1}{\alpha} = \frac{\lambda}{4\pi k} \quad (4.9)$$

where λ is the incident wavelength and k corresponds to the extinction coefficient in the material at that given wavelength. In the case of the GeTe sample investigated in the experiments, the semi-infinite material approach is considered to be valid. When comparing the calculated optical penetration depth and the thickness of GeTe samples (**Table 4.7**), the condition $\xi \ll d$ is indeed always satisfied.

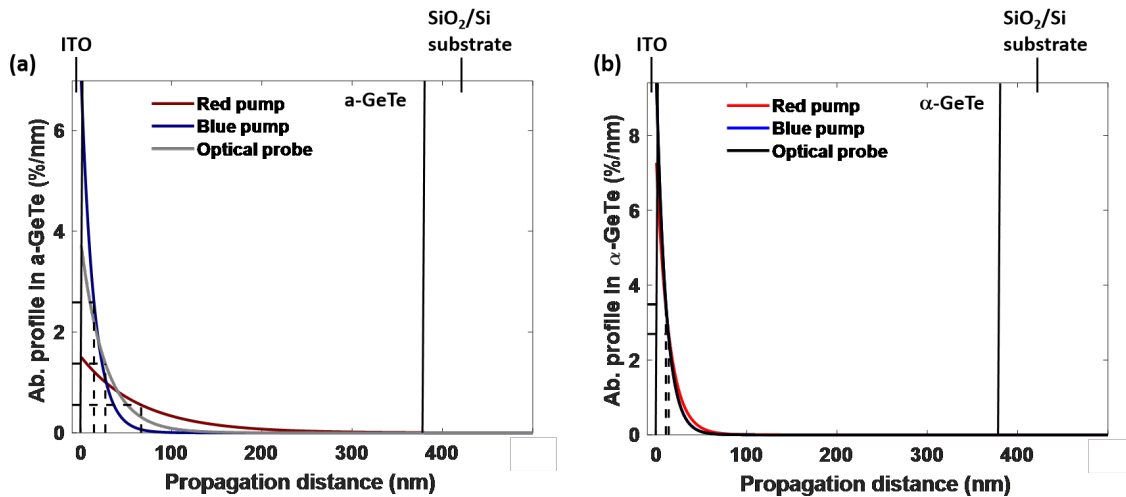


Fig 4.22: Absorption profile calculation of the red pump (830 nm), the blue pump (415 nm) and the optical probe (587 nm) in both a-GeTe (a) and α -GeTe (b) given by the Beer-Lambert's law. The extinction coefficients are taken from **Table 4.2** [82, 83].

in nm	ξ_{red} (830 nm)	ξ_{blue} (415 nm)	ξ_{probe} (587 nm)
a-GeTe	66.5	14.2	26.7
α -GeTe	13.6	10.5	10.5

Table 4.7: Results of optical penetration depth in a-GeTe and α -GeTe of chosen wavelengths.

This is well illustrated in **Fig 4.22** that shows the absorption profile in a-GeTe and α -GeTe for the red pump (830 nm), the blue pump (415 nm) and the optical probe (587 nm). By comparing the penetration depth of different wavelengths, the red pump can penetrate deeper in the thickness of a-GeTe than either the blue pump or the probe. While in α -GeTe, all the wavelengths can penetrate over a similar distance which is significantly reduced.

In **Chapter 2**, the expression of the photoinduced acoustic stain has been developed in details with the expression of the longitudinal acoustic stain given as: $\eta(z, t) = \eta_0[e^{-z/\xi}(1 - \frac{1}{2}e^{-vt/\xi}) - \frac{1}{2}e^{-|z-vt|/\xi}\text{sgn}(z - vt)]$

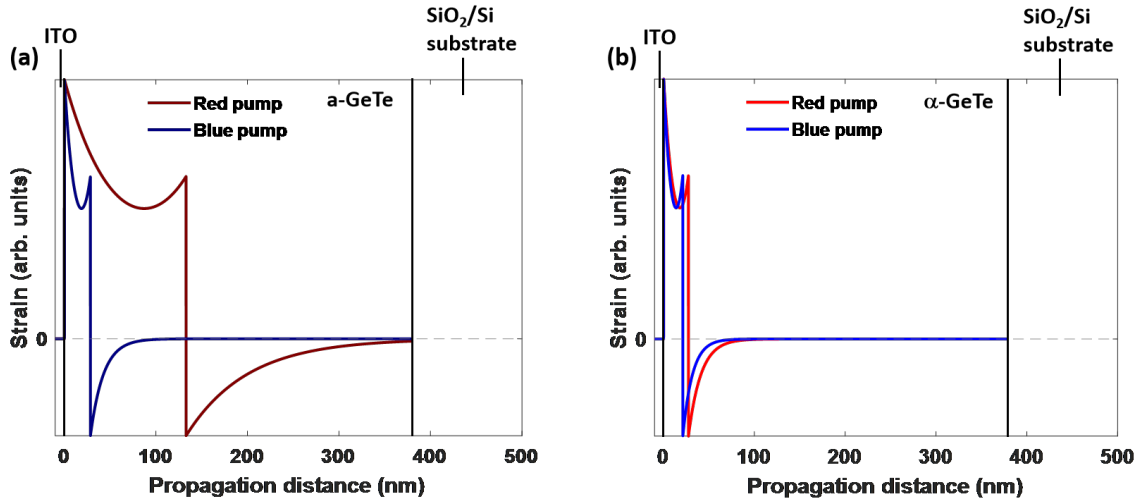


Fig 4.23: Numerical calculation with Thomsen's model revealing the in-depth strain induced by red and blue pump beams in a-GeTe (a) and α -GeTe (b).

We remind that this model considers that the spatial distribution of the photoinduced strain is fully governed by the optical depth penetration of the pump beam, i.e. it follows the mathematical function $\propto e^{-z/\xi}$. Within this assumption, the photoinduced acoustic strains are illustrated in **Fig 4.23** for both the a-GeTe (a) and the α -GeTe (b). The magnitude of the strain is normalized.

With the numerically determined photoinduced acoustic strain, within the semi-infinite material approach, the transient optical reflectivity $\Delta R/R$ can be simulated using the Thomsen's model:

$$\begin{aligned}\frac{\delta r}{r} &\simeq -2ik_0\delta z + \frac{4ik_0\tilde{n}_{GeTe}}{1-\tilde{n}_{GeTe}^2} \frac{d\tilde{n}_{GeTe}}{d\eta} \times \int_0^\infty \eta(z,t)e^{2ik_0\tilde{n}_{GeTe}z} dz \\ \frac{\Delta R}{R} &\simeq 2\Re\left(\frac{\delta r}{r}\right)\end{aligned}\quad (2.35)$$

where k_0 , δz and \tilde{n}_{GeTe} are the probe wavenumber in vacuum, the free surface displacement and the complex refractive index of GeTe at the probe wavelength. The photoelastic coefficient $\frac{d\tilde{n}_{GeTe}}{d\eta}$ remains undetermined to our knowledge. But we can obtain a semi-quantitative estimation with:

$$\frac{d\tilde{n}_{GeTe}}{d\eta} = \frac{d\tilde{n}_{GeTe}}{dE} \times \frac{dE}{d\eta}$$

The first term denotes the derivative of the complex refractive index as a function of the photon energy of the probe pulses E . This term can be calculated considering the tabulated optical properties of GeTe. The results are shown in **Fig 4.24**. The second term is called the deformation potential coefficient with η the strain. This coefficient is unknown. As a consequence, only the shape of the acoustic pulse can be simulated but not the absolute value of the magnitude of the transient optical reflectivity. We note that in these calculations, the contribution of the 10 nm transparent ITO layer has been neglected. Considering the longitudinal velocity of sound of 6500 m.s⁻¹ in ITO [113], the back and forth traveling of the acoustic pulse inside this thin layer contributes only to a delay of about 3 ps, which is much shorter than the detected pulse duration of hundreds of picoseconds. In other words, the presence of the capping layer does not noticeably broaden the photogenerated acoustic pulses because the ITO layer thickness is much smaller than the characteristic in-depth distribution of the photoinduced stress field and the velocity of sound in the ITO layer is higher than that in GeTe.

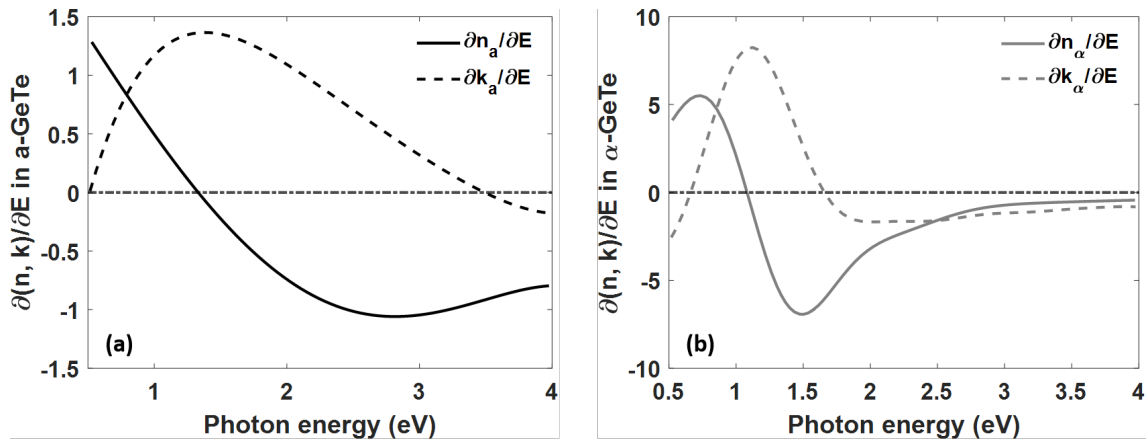


Fig 4.24: Calculation of derivative of optical properties as a function of photon energy for a-GeTe (a) and α -GeTe (b) with the optical properties in **Fig 4.2**

The comparison between the numerical simulation and the experimental $\Delta R/R$ signal are shown in **Fig 4.25**. For better comparison, the thermal background has

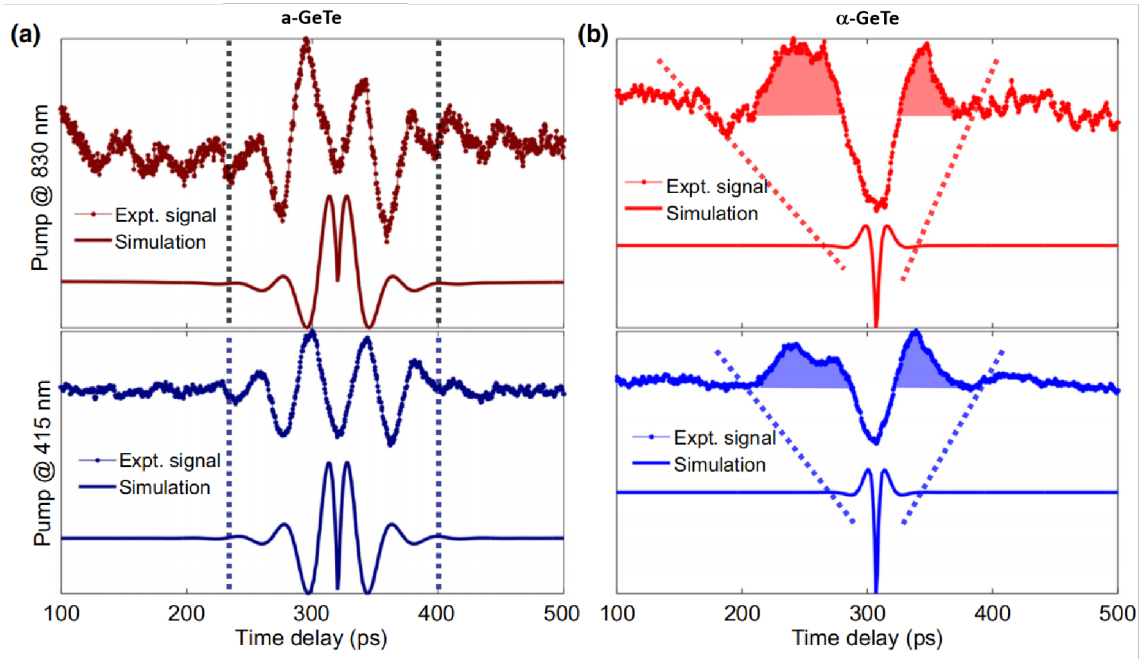


Fig 4.25: Comparison of experimental CAPs signals and numerical simulation of acoustic echo profiles in both a-GeTe (a) and α -GeTe (b) using red and blue pump, by taking into account that the photoinduced strain is limited by the penetration depth of the optical pump beam.

been removed and only the first echo signal are displayed, since we do not observe significant changes between successive echoes from **Fig 4.13**. In the a-GeTe sample, the acoustic echo profile (duration) has been successfully reproduced by the established model, which strongly suggests that the photoinduced acoustic strain profile is directly controlled by the pump light penetration profile. In other words, a local electron-hole-lattice coupling is suggested in a-GeTe. As for α -GeTe, using the respective optical properties shown in **Fig 4.2** [82, 83], the simulation is not quite consistent with the experimental results, for both red and blue pump. Experiments show an evident broadening of the acoustic pulse in α -GeTe comparing to the pulse duration predicted by the calculation that considers the strain profile to be directly related to the optical pump depth penetration profile. This indicates that the spatial extension over which the strain is generated after the ultrafast light action exceeds the optical penetration depth. In the following part, different scenarios will be discussed in order to identify the origin of this acoustic pulse broadening: heat diffusion, acoustic phonon dispersion, nonlinear acoustic effect and hot carrier diffusion.

4.4.6.2 Heat diffusion contribution

Considering the frequency of the emitted coherent acoustic phonon in α -GeTe shown in **Fig 4.20(a)**, of which the central frequency is under 10 GHz, such broadening effect might unlikely be associated with rapid heat diffusion out of the skin layer. If we consider, in the first place, light-induced heating effect is responsible,

then the generation of strain would be driven by thermoelastic processes [19, 20, 41]. The thermoelastic processes, which are widely investigated in metals, are based on the fast heating of lattice after light absorption, the rise of lattice temperature will lead to the expansion of the lattice and thus the generation of acoustic strain. For further discussion, it is important to know the spatial scale of such process, which means the necessity of evaluating the phonon heat flow in α -GeTe and compare the heat transport distance with the optical pump penetration depth. Within the thermoelastic process, the characteristic time for acoustic phonons to leave the region where the optical pump is absorbed is noted as τ : during that time τ , the incoherent phonons (lattice heat transport) can diffuse over a distance defined by:

$$L_{th} \simeq \sqrt{D_{heat}\tau}, \text{ with } \tau = \frac{2\xi_{pump}}{v} \quad (4.10)$$

where D_{heat} is the heat diffusion coefficient. Thus we can derive a ratio between the two characteristic distances:

$$\begin{aligned} \frac{L_{th}}{\xi_{pump}} &= \frac{\sqrt{D_{heat}\tau}}{v\tau/2} \\ &= \sqrt{\frac{2D_{heat}}{\xi_{pump}v}} \end{aligned} \quad (4.11)$$

For α -GeTe, D_{heat} is about $2 \times 10^{-6} \text{ m}^2.\text{s}^{-1}$ [81, 86, 87] (**Table 4.4**), with experimentally determined sound velocity shown in **Fig 4.6** ($v_L \approx 2500 \text{ m.s}^{-1}$), equation (4.11) gives $L_{th}/\xi_{pump} \simeq 0.3 < 1$. As a result, this means that the heat does not have time to escape the penetration depth region before the departure of the acoustic strain (i.e. heat diffusion is subsonic). In conclusion, the acoustic pulse broadening that we observe cannot be explained by a rapid heat diffusion.

4.4.6.3 Acoustic phonon dispersion

In this section, the effect of the acoustic phonon dispersion is discussed. The following calculation is based on the assumption that the emitted acoustic pulse is initially generated over the penetration depth region, with the characteristic width of coherent acoustic-pulse-frequency spectrum given by:

$$f_w \approx \frac{v}{\xi_{pump}}. \quad (4.12)$$

Estimating the phase velocity variation of the different frequencies that compose the acoustic pulse spectrum, we can calculate the associated delay (time broadening) after the propagation of the packet during the relevant duration of our experiment. In the case of α -GeTe, f is calculated to be around 200 GHz for the wavelengths of the red and blue pump pulses in use, with the phonon dispersion diagram (see **Fig 4.26**), the phase velocity remains nearly unchanged (i.e. close to the Brillouin

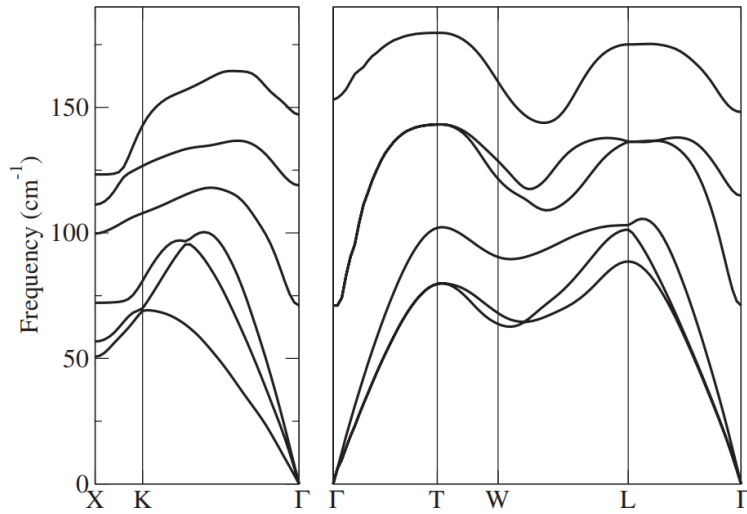


Fig 4.26: Calculated phonon-dispersion curves of ferroelectric α -GeTe [79]. The phonon band structure is obtained by density function perturbation theory (DFPT). For better comparison, 50 cm^{-1} corresponds to a frequency of 1.5 THz.

zone center Γ). Only a significant deviation (couple of %) from the linear regime is measurable for frequency starting around 1 THz, which is much higher than the frequencies present in the acoustic pulse. Consequently, the dispersion effect, described by the difference in the propagation time between the highest and lowest frequency components, over the relevant propagation distance can potentially broaden the coherent acoustic pulse only by a few picoseconds, which is exceedingly short compare to the detected acoustic pulse ($\sim 200 \text{ ps}$, revealed in **Fig 4.20(a)**). In addition, by investigating successive echoes (shown in insets of **Fig 4.20(a)**), the acoustic pulse duration does not drastically change over time at the considered propagation distances, demonstrating that attenuation also plays a minor role in controlling the acoustic pulse duration at such short propagation distances and relatively low frequencies. In conclusion, the spatial broadening of coherent acoustic phonon pulses cannot be explained by the acoustic phonon dispersion.

4.4.6.4 Nonlinear acoustic effect

The nonlinear acoustic effects is also discussed here. A laser excitation producing a strain pulse can lead to some anharmonic effects such as the formation of shock waves and acoustic solitons, as reported recently [41, 114]. Usually, the photoinduced strain has to be large ($>10^{-3}$ in magnitude) and the experiments need to be realized at low temperature to prevent strong acoustic attenuation of GHz frequency phonons before the pronounced development of nonlinear acoustic phenomena. Even though it is not suppressed by the high frequency absorption of sound, the non-linear effect is developing over a given distance, depending on the characteristic length of acoustic pulse noted as L_A , the strain amplitude in the acoustic pulse η and the non-linear acoustic properties of the solid specified by the nonlinear acoustic parameter P_{NL} . Without considering the acoustic absorption, the characteristic length L_{NL} for the

creation of the shock front can be described as [41]:

$$L_{NL} = \frac{L_A}{P_{NL} \times \eta}, \text{ with } \eta = 3\beta B\Delta T. \quad (4.13)$$

In our experiments, the shortest possible characteristic dimension of the acoustic pulse is controlled by the pump light penetration depth, which is 10.5 nm (13.6 nm) for the absorption of 415 nm (830 nm) wavelength optical pulses in α -GeTe (**Fig 4.22** using the optical properties of GeTe extracted from ref. [82, 83]). At high frequency such as GHz frequencies, the acoustic nonlinearities, that could be related to the motion of defects/dislocations or any other possible mesoscopic elements which potentially contribute to internal friction in crystals, are frozen. In other words, the acoustic nonlinearities in GeTe related to defects cannot be detected in the GHz range. And the nonlinearity at these high frequencies is dominated by the nonlinearity of a perfect crystal, where the nonlinear parameter of this quadratic nonlinearity does not exceed $P_{NL} = 10$ [115]. In using the values of the physical properties of GeTe listed in section 4.2.3, the linear thermal expansion coefficient of GeTe is $\beta = 11.2 \times 10^{-6} \text{ K}^{-1}$ [84, 116], and the heat capacity is $C_p \sim 50 \text{ J.mol}^{-1}.\text{K}^{-1}$ [86], the maximum temperature rise in our experimental configuration (pump fluence being $32 \text{ }\mu\text{J.cm}^{-2}$, **Fig 4.16**), is calculated as $\Delta T = 15 \text{ K}$. Finally, this rather small temperature rise limits the maximal acoustic strains to $S_A < 10^{-3}$. Thus, the minimal nonlinear length is estimated to be $L_{NL} \sim 7 \text{ }\mu\text{m}$. Even an underestimated nonlinear acoustic length in our experiments remains not shorter than $7 \text{ }\mu\text{m}$ and is nearly 10 times larger than one round trip distance of the acoustic pulse in α -GeTe film. To conclude, acoustic nonlinear phenomena cannot broaden the acoustic pulses photo-generated in our experiments at such short propagation distances and acoustic nonlinear phenomena cannot explain the broadening of our first acoustic echo.

We can also underline, as mentioned in the end of the previous subsection 4.4.6.3, that the shape of the acoustic echo does not evolve significantly upon the propagation. This is consistent also with the absence of such non-linear acoustic effects.

4.4.6.5 Hot carrier diffusion contribution

Having excluded thermal, dispersion, attenuation, and nonlinear acoustic effects, it is important to remember that the transport of energy, in particular, for photoexcited materials, is not achieved only by incoherent phonons. Some photoexcited carriers can contribute to this transport of energy. Such phenomenon has already been observed in GaAs [40, 117, 118] and Ge [104] semiconductors and is attributed to a supersonic expansion of the electron-hole plasma. In this case, the photoexcited carriers rapidly diffuse over the conduction and valence bands and couple to the lattice over a distance longer than the pump penetration depth. Such mechanism is possible only if the photoexcited carriers do not recombine before they diffuse out of the penetration depth. If the condition is satisfied, the characteristic acoustic phonon pulsation driven by this rapid plasma expansion is given by [41]:

$$\omega \approx \frac{v^2}{D_{e-h}} \quad (4.14)$$

where v is the longitudinal sound velocity, D_{e-h} is the carrier diffusion coefficient.

In the case of α -GeTe, if we assume this process to be the driving one, this characteristic frequency is given by the inverse of the duration of the acoustic pulse:

$$\omega \approx \frac{1}{\Delta t} \approx 10^7 \text{ s}^{-1} \quad (4.15)$$

which correspond to the maximum of the spectrum of a single acoustic echo, as shown by dashed lines in **Fig 4.20(b)**. As a result, we deduce from our measurements $D_{e-h} \approx 0.6 \times 10^{-3} \text{ m}^2 \cdot \text{s}^{-1}$. This value is characteristic for electron and hole diffusion in semiconductors [119].

To show that this value is actually relevant for crystalline GeTe, and if we assume the Einstein relation to be valid, then we can also evaluate the expected diffusion coefficient in α -GeTe with the equation 4.4. The electrical mobility in amorphous and crystalline GeTe are extracted from [89, 91], with numerical values being given in **Table 4.5**.

Finally, we arrive at a value $D_{e-h} \approx 0.5 \times 10^{-3} \text{ m}^2 \cdot \text{s}^{-1}$, which is surprisingly consistent with that deduced from the analysis of the diffusive origin of the acoustic echo broadening. Thus, our observation strongly supports that the photoinduced stress is governed by rapid (supersonic) photoexcited carriers in crystalline α -GeTe. As shown in **Fig 4.27**, the photoexcited electrons and holes are confined within the penetration depth for the amorphous phase (and recombine nonradiatively to produce heat), as for the crystalline phase the photoexcited carriers rapidly diffuse out of the penetration depth of the optical pump pulses. The typical distance where supersonic diffusion takes place is defined as:

$$L_D \approx \sqrt{D_{e-h} \Delta t} \quad (4.16)$$

with previously determined carrier diffusion coefficient, we have $L_D \approx 200 \text{ nm}$, which means that photoexcited carriers can diffuse over a significant distance and are responsible for nonthermal transport energy in crystalline GeTe.

As a final element for discussion, we would like to focus our attention on the asymmetry of the detected pulse, as illustrated by shaded areas in **Fig 4.25(b)**. As discussed regarding the contribution of hot carrier diffusion, in α -GeTe the initially rapid (supersonic) diffusion of photoexcited carriers from the free surface (**Fig 4.27(b)**), $D_{e-h} \gg \xi v$ gives rise to an asymmetric strain pulse, and then leads to an asymmetry in the detected pulse, in accordance with our observations.

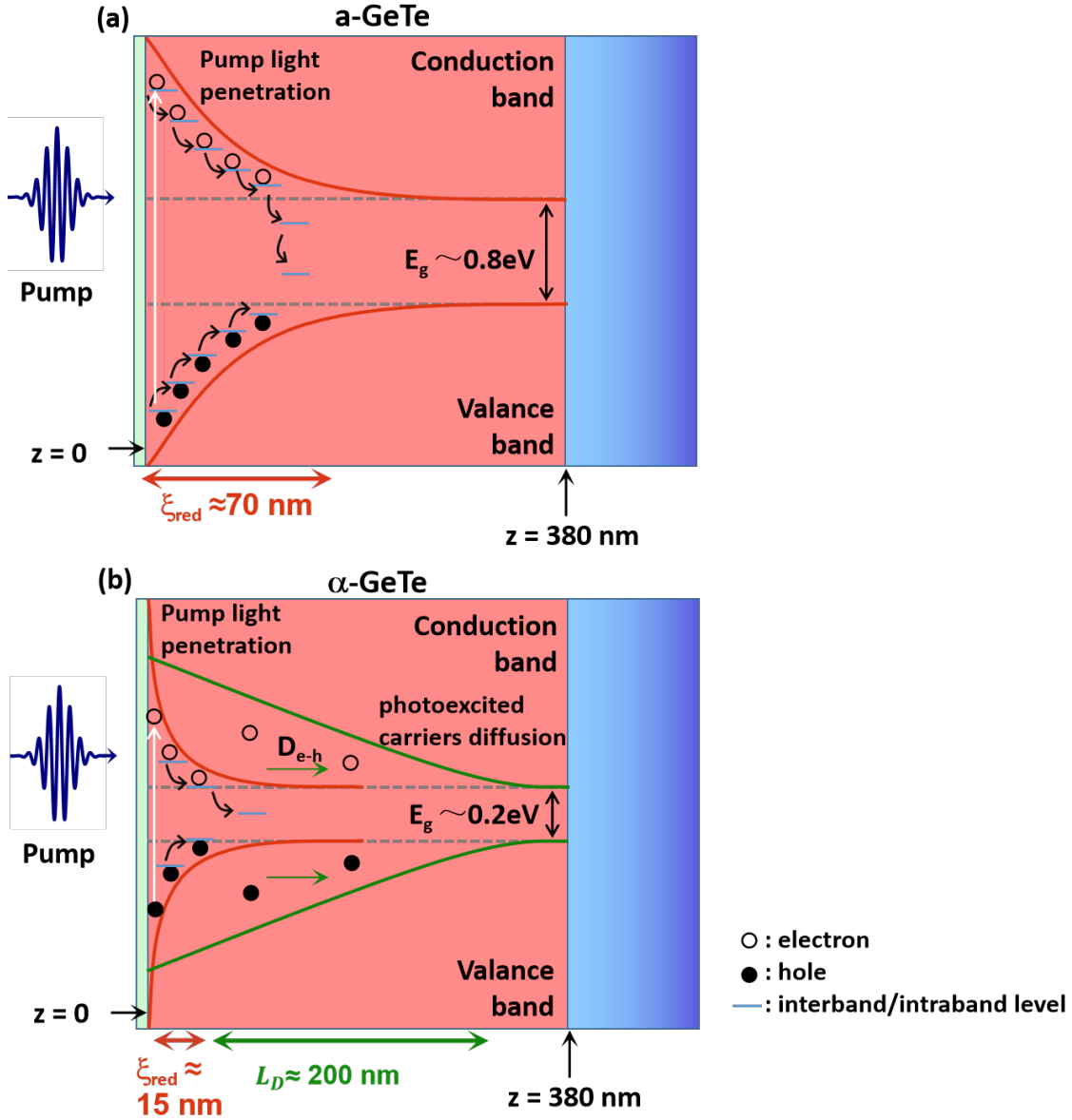


Fig 4.27: Scheme of the spatial distribution of photoexcited carriers in a-GeTe (a) and α -GeTe(b) under the pump irradiation of 830 nm. In a-GeTe, the photoexcited carriers are coupled with the lattice within the optical pump penetration depth, while in α -GeTe, these carriers can diffuse at a much longer distance, away from the narrow penetration depth of the optical pump pulses.

4.5 Conclusion

In this chapter, the photogeneration and photodetection of coherent longitudinal acoustic phonons have been investigated in both amorphous a-GeTe and rhombohedral crystalline α -GeTe samples, with optical pump-probe experiments. The GeTe sample was a thin film of around 380 nm. Since GeTe is an opaque material to the probe pulses (587 nm) with a band gap below 1 eV, these phonons have been generated on the surface. These phonons propagate in the thin film and are reflected on the substrate and are finally detected when they come back to the free surface. We have shown that the shape of the acoustic echo (typically of 100 ps duration), i.e. the respective phonon spectrum, is very different in the amorphous and the crystalline states. In particular, in α -GeTe the detected central frequency of the envelop of the acoustic echo spectrum is redshifted compared to the one in the amorphous state a-GeTe. With a simulation using Thomsen's model, we have been able to explain the signal in the amorphous state. In that case, we arrive at the conclusion that, in a-GeTe, the coupling between photoexcited carriers and the lattice remains localized within the photoexcited volume, meaning that photoexcited carriers release their energy to the lattice within the volume of light absorption. On the opposite, we were not able to reproduce the acoustic phonon signal for the crystalline state (α -GeTe). In particular the calculated acoustic pulse duration is much smaller than the experimental value. Consequently, this observation shows that in rhombohedral α -GeTe, the photoinduced acoustic strain is not localized in the region of absorption of the pump radiation (penetration depth of the pump pulses). This means that the strain is generated over a distance larger than 10 times of the pump penetration depth. We interpret this effect as a fast transport of energy by hot carriers diffusion, i.e. a non-thermal transport of energy, in a sense that this transport of energy is not due to phonons. These fast hot carriers diffuse first and then couple to the lattice to induce a macroscopy strain in the GeTe crystal.

Showing that the photoexcited carriers can diffuse quite efficiently in α -GeTe is an indication of a clear reduction of electron-phonon coupling, compared with the situation found in a-GeTe. The hot carriers can indeed diffuse at a large distance in α -GeTe while these hot carriers do not show that effect in the amorphous a-GeTe. Finally, considering the picosecond dynamics of this superdiffusive process, our findings might have some implications for the development of sub-THz or THz switching technologies and, in particular, for ultrafast processes in phase-change-material-based technologies.

Photoinduced strain in BiFeO₃ based compounds

Contents

5.1 Introduction	91
5.2 General properties of BiFeO ₃ : bulk and thin films	92
5.2.1 Physical properties of BiFeO ₃ bulk material	93
5.2.2 Physical properties of BiFeO ₃ thin films	97
5.3 Literature survey on photoinduced strain in BiFeO ₃ based materials	98
5.4 Experimental results	103
5.4.1 Study of photoinduced strain in (001) _c BiFeO ₃ single crystal . . .	103
5.4.2 Study of photoinduced strain in monoclinic BiFeO ₃ thin films . .	119
5.5 Conclusion	139

5.1 Introduction

Piezotransducers that convert electrical energy into acoustic waves (and vice versa) are widely used in several applications from medical diagnostics to non-destructive testing, monitoring of environments, robotics and telecommunication. However, traditional piezotransducers are controlled by an external bias and thus are restricted to the 1-100 MHz regime, which means that acoustic waves with wavelength of few micrometers are delivered. With the general trend in industries development towards the natural miniaturization, these MHz based piezotransducers are not adapted for sensing nanostructures and nanomaterials. To overcome such limitations and propose solution for industries, it has been proposed to apply new kind of acoustic nanowave sources that are GHz-THz transducers based on the laser ultrasonics principle. Optically controlled GHz-THz transducers based on semiconductors and metals have been extensively studied over the last thirty years and different configurations using thin films and superlattices have been explored [29, 120]. Piezotransducers are based on ferroelectric materials, whose actuation is realized with ultrashort light pulses, namely ultrafast photostriction [29, 120, 121].

Ferroelectric and multiferroic materials are very promising for this area of research due to the fascinating coupling between charges, phonons and spins. These materials are already central for key applications such as smart electromechanical sensor, microelectronic and for advanced devices [122, 123]. With the increasing demand in high rate data processing (magnetic or electric storage), it becomes essential to envision the control of these couplings at shorter time scales such as the picosecond range to reach the GHz-THz range [122–124]. For this reason, describing the ultrafast light-induced lattice dynamics is among the important ingredients.

This chapter will be dedicated to the experiments and to the data analysis of photostriction in bismuth ferrite (BiFeO_3 , BFO). Two systems are investigated: a $[100]_c$ BFO single crystal and a single domain monoclinic BFO film. In the first place, a brief presentation of the fundamental properties of BFO will be given. Only a short survey will be presented compared to the very rich and documented literature. A more focused presentation about the photoinduced strain dynamics in ferroic materials will be introduced to explain the motivation of our investigations. Then I will present the experimental results based on two techniques, namely the optical pump-probe methods and the time-resolved X-ray diffraction. A complete description of the light-induced strain and regarding the spectrum of the time-resolved Brillouin signal will give new insights on the microscopic coupling involving the photons, electrons and phonons in these BiFeO_3 based systems.

5.2 General properties of BiFeO_3 : bulk and thin films

BiFeO_3 is a very important material because it exhibits unique ferroelectric and magnetic properties at room temperature.

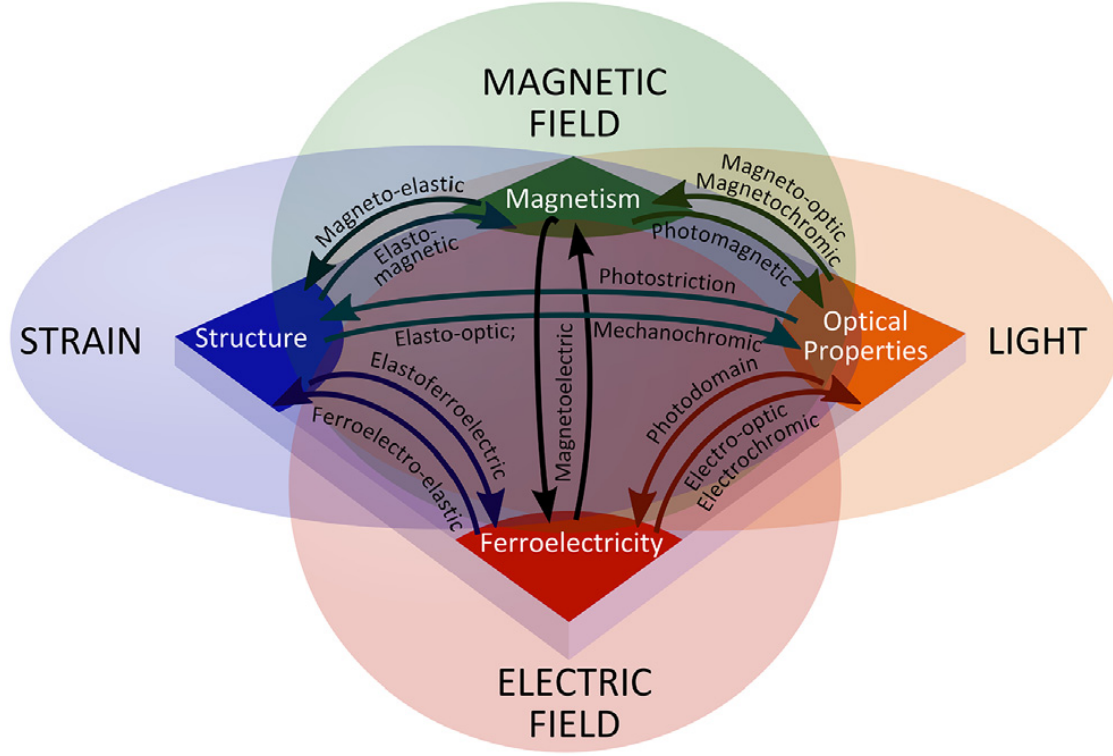


Fig 5.1: Sketch of possible couplings between the various functionalities of BiFeO_3 [6].

Due to the coexistence of multiple ferroic orders, possible coupling between the electric properties, magnetic properties and strain are expected in BiFeO_3 , making this material promising for many applications such as sensors and actuators. BiFeO_3 exhibits ferroelectricity, ferroelasticity, antiferromagnetism (with a magnetic cycloid) and other related interesting optical properties. A diagram of all possible couplings is shown in **Fig 5.1**. In the following, a short description of the main properties of the bulk and thin films of BiFeO_3 is presented. Many reviews exist about BiFeO_3 material and the reader will find exhaustive information in [6, 125], for example.

5.2.1 Physical properties of BiFeO₃ bulk material

Crystallographic structure of BiFeO₃

First synthesized in late 1950's [126], BFO exhibits a rhombohedral R3c perovskite structure which will be described here using a pseudo-cubic notation with $a = 3.96 \text{ \AA}$. The electric polarisation lies along the elongated $[111]_c$ direction (**Fig 5.2(a)**), due to the displacement of the Bi^{3+} from centrosymmetric positions. This is caused by the hybridization between the Bi^{3+} lone pair (6s orbital) and O^{2-} (2p orbital) [127]. In order to construct the rhombohedral frame (**Fig 5.2(b)**), 2 BiFeO₃ pseudo-cubic unit cells are distorted by the displacement of iron (Fe) atom and the rotation of FeO₆ octahedral.

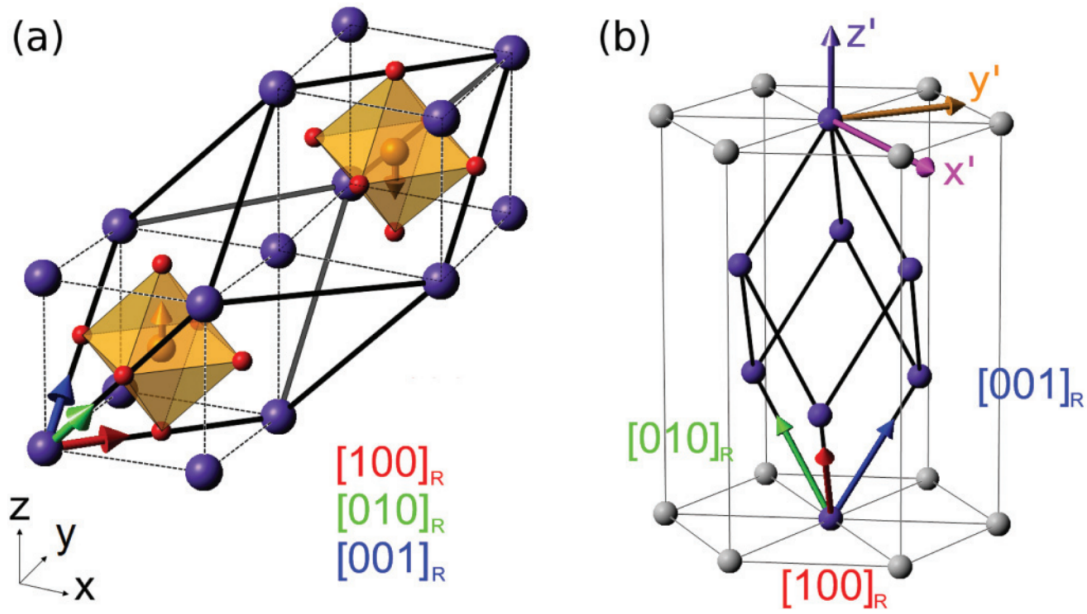


Fig 5.2: (a) pseudo-cubic perovskite unite cell of BiFeO₃ is shown by thin lines and rhombohedral unit cell by thick lines. Bismuth (Bi), iron (Fe), and oxygen (O) atoms are drawn in blue, orange, and red, while orange arrows denote spins. The Cartesian axes x, y, z of the pseudo-cubic structure and the unit vectors of the rhombohedral cell are also shown. (b) The Cartesian axes x', y', z' used to describe the properties of the rhombohedral structure (blue circles, thick lines) are shown along with the alternative trigonal cell (gray circles, thin lines) [128].

Phase diagram of BiFeO₃

As indicated in the chemical formula, the BiFeO₃ samples that we have investigated contain 50% of Fe₂O₃ with another 50% of Bi₂O₃. With increase of the temperature, the structure of BiFeO₃ evolves from a rhombohedral α phase to a orthorhombic β phase or even to cubic γ phase if the BiFeO₃ is heated to higher temperature (**Fig 5.3(a)**).

In addition, BiFeO₃ exhibits a G-type ferromagnetic behavior below the Néel temperature ($T_N \approx 650 \text{ K}$) [130, 131] with the presence of a non-collinear magnetic

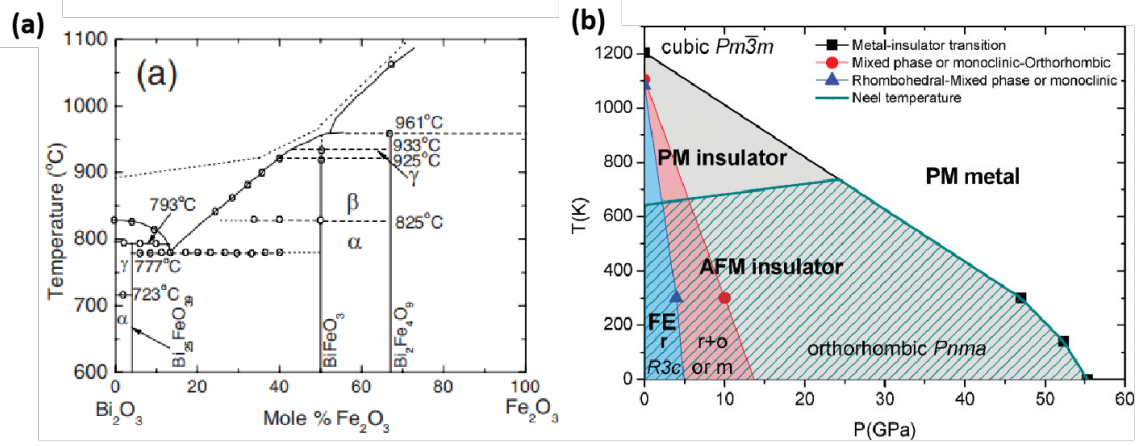


Fig 5.3: (a) Phase diagram of BiFeO_3 as a function of temperature and chemical composition [129]. (b) Ferroelectric and ferromagnetic phase diagram of BiFeO_3 [125].

order due to the anti-symmetric exchange, i.e. the Dzyaloshinskii-Moriya (DM) interaction. This leads to the formation of a magnetic cycloid as shown in **Fig 5.4**.

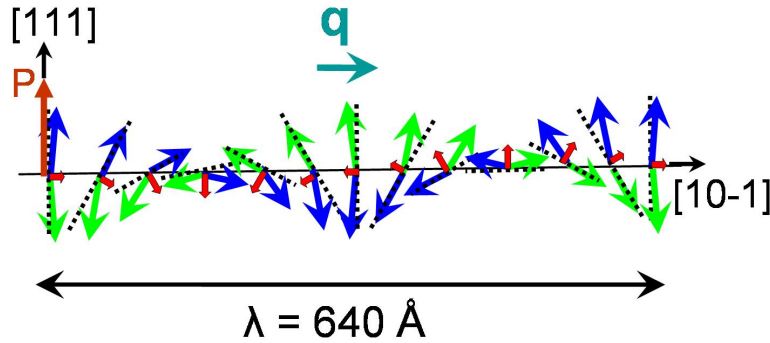


Fig 5.4: Magnetic cycloid in BiFeO_3 where the two opposite magnetic moment on the iron sublattice are shown in blue and green while the ferroelectric polarization is shown in red [132]. The crystallographic orientations are given in cubic coordinates.

The ferroelectric properties exist over a wide range of temperatures with a Curie temperature located at $T_C \approx 1050 \text{ K}$. At T_C , BiFeO_3 undergoes a transition from a ferroelectric phase to a paraelectric phase with its atomic structure changing towards a cubic structure (**Fig 5.3(a)**). Additional crystallographic structures as well as different ferroic order (ferromagnetism, ferroelectricity) are accessible under large hydrostatic pressure as shown in **Fig 5.3(b)**.

Optical properties of BiFeO_3

BiFeO_3 also has remarkable optical properties at room temperature. It is birefringent, both the dielectric coefficients and the optical indices along ordinary and extraordinary axes in BFO are shown in **Fig 5.5**. The extraordinary axis (c-axis in

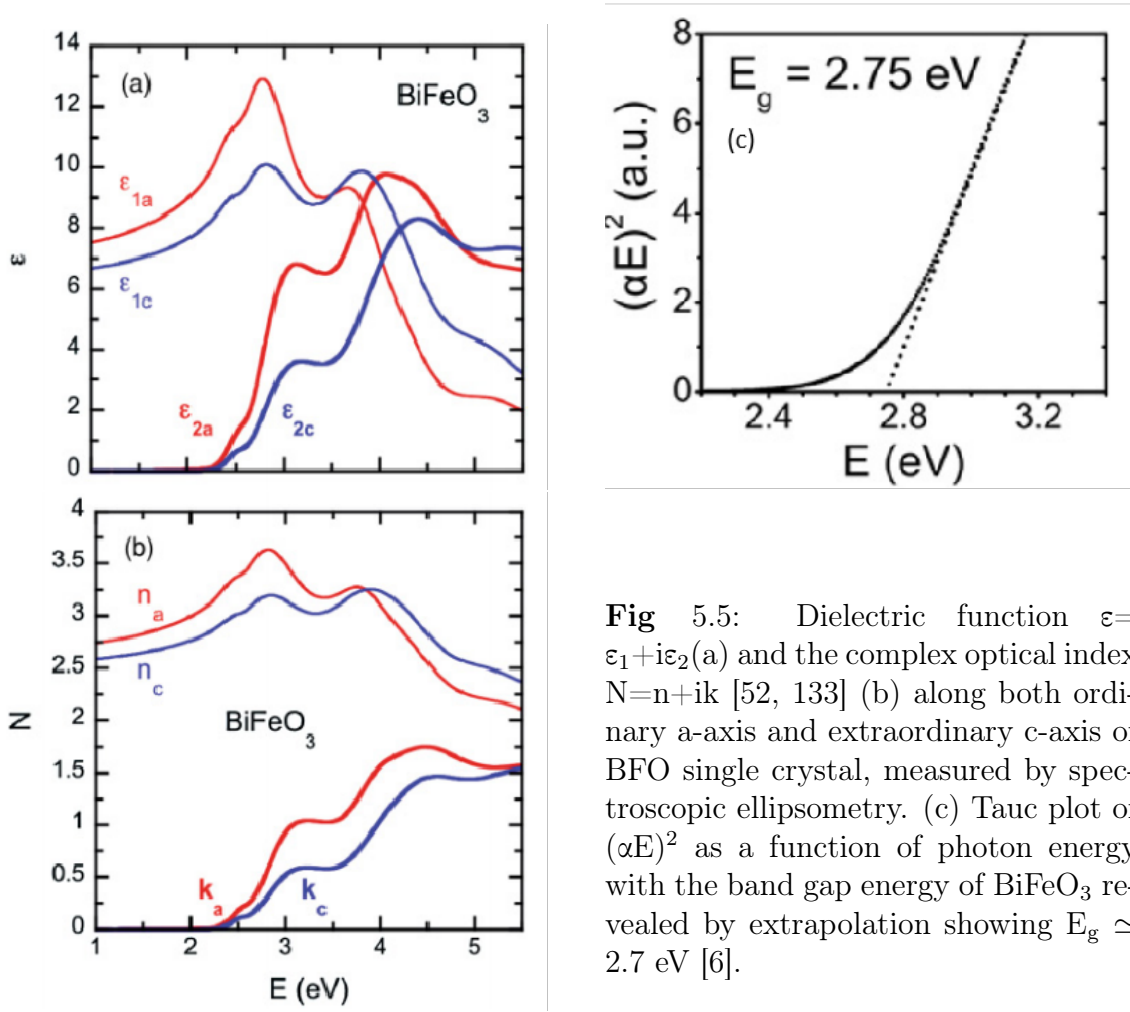


Fig 5.5: Dielectric function $\epsilon = \epsilon_1 + i\epsilon_2$ (a) and the complex optical index $N = n + ik$ [52, 133] (b) along both ordinary a-axis and extraordinary c-axis of BFO single crystal, measured by spectroscopic ellipsometry. (c) Tauc plot of $(\alpha E)^2$ as a function of photon energy with the band gap energy of BiFeO₃ revealed by extrapolation showing $E_g \simeq 2.7$ eV [6].

Fig 5.5), lies along the $[111]_c$ direction, and the ordinary axis (a-axis in **Fig 5.5**) is perpendicular to the $[111]_c$ direction. As shown in the same figure, BiFeO₃ has negative uniaxial anisotropy because $n_a > n_c$ and the linear birefringence in BiFeO₃ is $\Delta n \approx 0.25$ which is almost the largest birefringence in the oxides family [134]. BiFeO₃ also possesses a direct band gap around 2.6-2.8 eV which is in the photon energy range of visible light as shown in **Fig 5.5(c)**. This small band gap, compared to other ferroic materials such as PbTiO₃ or BaTiO₃, to cite a few, is very interesting for many photonic applications. The band gap can be extracted by plotting $[\alpha(E) \cdot E]^2$ as a function of photon energy (also known as Tauc plot), and $\alpha(E)$ is given by [135]:

$$\alpha(E) = \frac{A}{E}(E - E_{g,dir})^{0.5} + \frac{B}{E}(E - E_{g,ind} \mp E_{ph})^2 \quad (5.1)$$

where $E_{g,dir}$ and $E_{g,ind}$ denote respectively direct and indirect energy gaps, E_{ph} is the energy of phonons that can be either absorbed or emitted, A and B are constant.

Ferroelectricity in BiFeO_3

The measurement of the ferroelectric hysteresis loop (P-E loop) in BiFeO_3 can be achieved by measuring the current (I) flowing in a simple resistive circuit as a function of the voltage (V) ($I = f(V)$ characteristic) applied to the sample with a capacitor geometry. Typical results are shown in **Fig 5.6(a)** [136]. When integrating the signal ($P = \int Jdt$), a hysteresis cycle can be reconstructed as shown in **Fig 5.6(b)**. In the presented work, the author found for their BiFeO_3 single crystal at room temperature a remnant polarization $P_{(012)}$ of $35 \text{ C}\cdot\text{cm}^{-2}$ and a coercivity of $15 \text{ kV}\cdot\text{cm}^{-1}$.

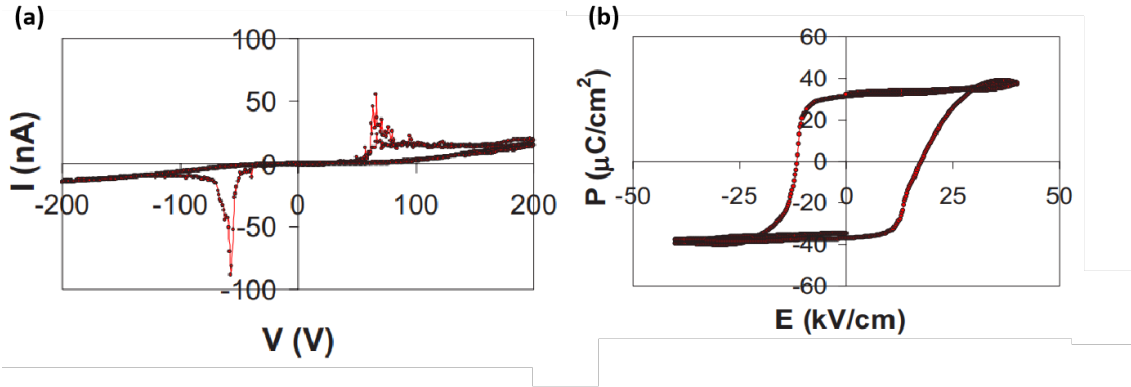


Fig 5.6: (a) Charge current versus applied voltage of a $40 \mu\text{m}$ thick single crystal of BiFeO_3 at room temperature. The raw data are composed of a background leakage current superimposed to the relevant signal. (b) P-E hysteresis loop of the $40 \mu\text{m}$ thick single crystal of BiFeO_3 at room temperature [136].

Domain structure in BiFeO_3

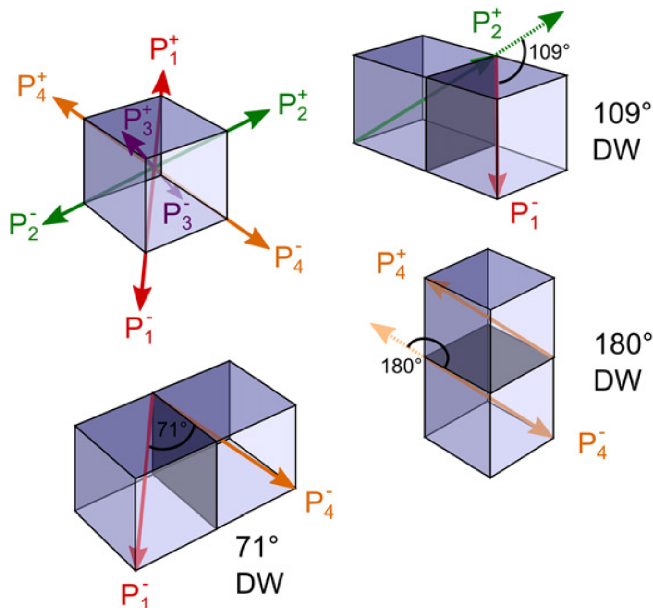


Fig 5.7: Sketch of possible configurations of domain walls in BFO. The ferroelectric polarisation can point along 8 equivalent directions of [111] in the pseudo-cubic structure. 3 possible domain wall configurations are available depending on the relative polarisation of the boundaries: 71° , 109° and 180° [6].

In the simplified pseudo-cubic structure of BFO, the ferroelectric polarisation can point at 1 of the 8 possible directions, between 2 unit cell neighbours 3 types of domain walls can be formed, 71°, 108° and 180° (**Fig 5.7**). The 2 first domain wall boundaries are both ferroelastic and ferroelectric, only the latter one is purely ferroelectric [6, 125].

Magnetoelectric coupling in BiFeO₃

The magneto-electric coupling is revealed when for example an external magnetic field influences the ferroelectric order. The reverse process is also relevant. Such effect is shown in **Fig 5.8** where a non-linear dependance is found, partially due to the huge evolution of the magnetic cycloid that can disappear under strong external magnetic field (~ 200 kOe). This latter effect forces the lattice to evolve leading to a modification of the polar order.

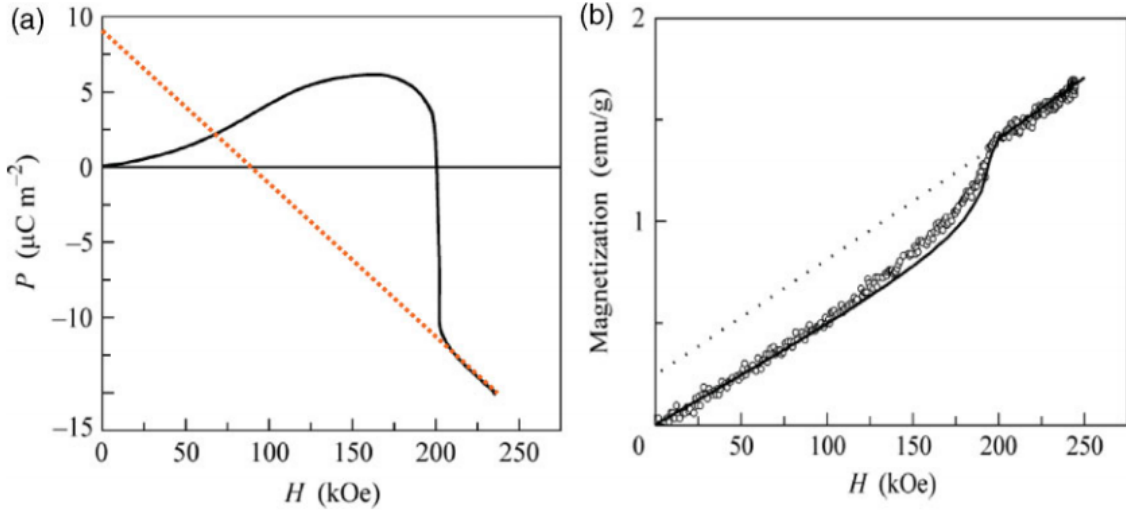


Fig 5.8: (a) Electric polarization induced by magnetic field in BiFeO₃ along the [001]_c (cubic) axis at T=10 K. (b) Magnetization of BiFeO₃ as a function of magnetic field at a temperature of 10 K. Dots are the experimental data obtained in a field oriented along the [001]_c direction, and solid line is the theoretical dependence. Figures are taken from [125], and adapted from [137, 138].

The magnetoelectric, combined to a magnetoelastic effect, has been also shown to play a role in the renormalization of the elastic constant as observed recently by time-resolved Brillouin measurements [139].

5.2.2 Physical properties of BiFeO₃ thin films

The fundamental properties of BiFeO₃ briefly presented before are also present in thin films. But these properties can even be enriched by the particular confinement in a quasi 2D geometry. The growth of BiFeO₃ as a thin film has received a great deal of attention since remarkable new phenomena in these confined nanostructures

have been demonstrated. A large tunability of the crystallographic structure is possible leading to the access to new ferroic orders (polar and magnetic). In some circumstances, it is possible to break the magnetic cycloid. The different new crystallographic structures in thin BiFeO_3 films are actually obtained thanks to a strong epitaxial stress that can be tuned by changing the nature of the substrate as well as its crystallographic orientation. In the fabrication with standard pulsed laser deposition (PLD), the growth parameters such as the temperature and the laser energy need to be precisely controlled [6]. A typical representation of all possible crystal structures stabilized by strain are shown in **Fig 5.9**.

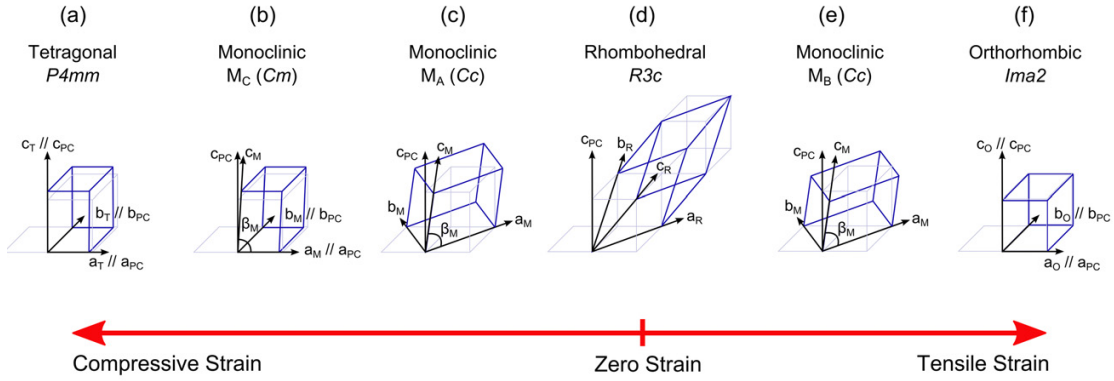


Fig 5.9: Sketch of possible crystallographic structure versus the nature of the epitaxial stress [6].

Besides the richness of the crystallographic phase diagram achievable with epitaxial stress, the ferroelectric and antiferromagnetic domain organization are affected for BiFeO_3 grown as thin film, since the strain is highly coupled to the ferroic orders. As an example, piezoforce microscopy (PFM) images and scanning nitrogen vacancy (NV) tip magnetometry images are presented in **Fig 5.10** [140]. In some cases with specific growth parameters, it is even possible to obtain single domain thin film which actually is one of the systems that has been studied in section 5.4.2. More details about such single domain thin film properties will be presented in part 5.4.2.1.

In **Fig 5.10**, we can see that the magnetic landscape and the cycloid properties can be tuned with the epitaxial stress and that the cycloid can even disappear for BiFeO_3 thin film grown on SmScO_3 where the antiferromagnetic (AFM) state is obtained.

5.3 Literature survey on photoinduced strain in BiFeO_3 based materials

Static and ultrafast photoinduced strain in BiFeO_3

Static photoinduced strain has been investigated in BiFeO_3 in 2010 [141] (see

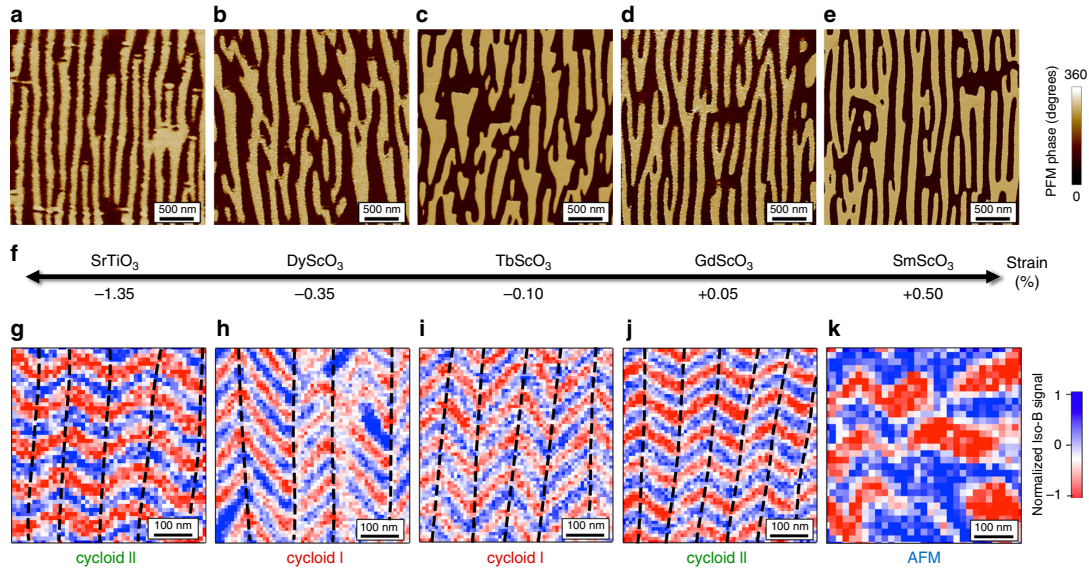


Fig 5.10: (a-e) In-plane PFM image of BiFeO₃ films grown on (a) SrTiO₃, (b) DyScO₃, (c) TbScO₃, (d) GdScO₃ and (e) SmScO₃ sunstrates. (f) Evolution of the epitaxial strain of BiFeO₃ deposited on various substrates. (g-k) NV magnetometry images corresponding to the ferroelectric domains depicted in (a-e). Dashed lines are added for the guidance of view in (g-i), indicating the change of the cycloid propagation vector with respect to the ferroelectric domain walls. (k) shows the pseudo-collinear antiferromagnetic (AFM) order [140].

Fig 5.11(a)) where combined effects of light and magnetic field were investigated. In 2012, Kundys et al [142] investigated the role of the light wavelength and showed the expected larger response for above band gap excitation in a BiFeO₃ single crystal. Other ferroelectrics have been also studied like the ferroelectric CaCu₃Ti₄O₁₂ where strain close to 1% was reported recently with continuous light excitation having a typical power of tens of kW.m⁻² [143]. The investigations of photoinduced strain in ferroelectric are presented in the review of Kundys [2]. The coupling between strain (acoustic phonons) and the ferroelectric order has been revealed by different techniques including static photostriction experiments with continuous-wave laser. The strain or surface displacement have been measured by interferometric, dilatometry methods [2, 141] and the coupling between phonons and ferroelectric orders has been investigated by Raman spectroscopy [144].

First reports about ultrafast photoinduced strain in BiFeO₃ and other ferroelectric materials appeared at about the same time. After around thirty years of investigations of ultrafast photoinduced strain and coherent acoustic phonon in metals and semiconductors [19, 20], several groups have demonstrated that it is possible to drive with ultrashort light pulse some phonons in ferroelectric materials and to monitor strain approaching 1 % by means of time-resolved pump-probe methods. Nearly simultaneous measurements of ultrafast photoexcitation of coherent acoustic phonons that were probed by time-resolved Brillouin scattering have been reported by Chen et al [145] (see **Fig 5.11(b))** and Ruello et al [146] (see **Fig 5.12**). Chen et al studied

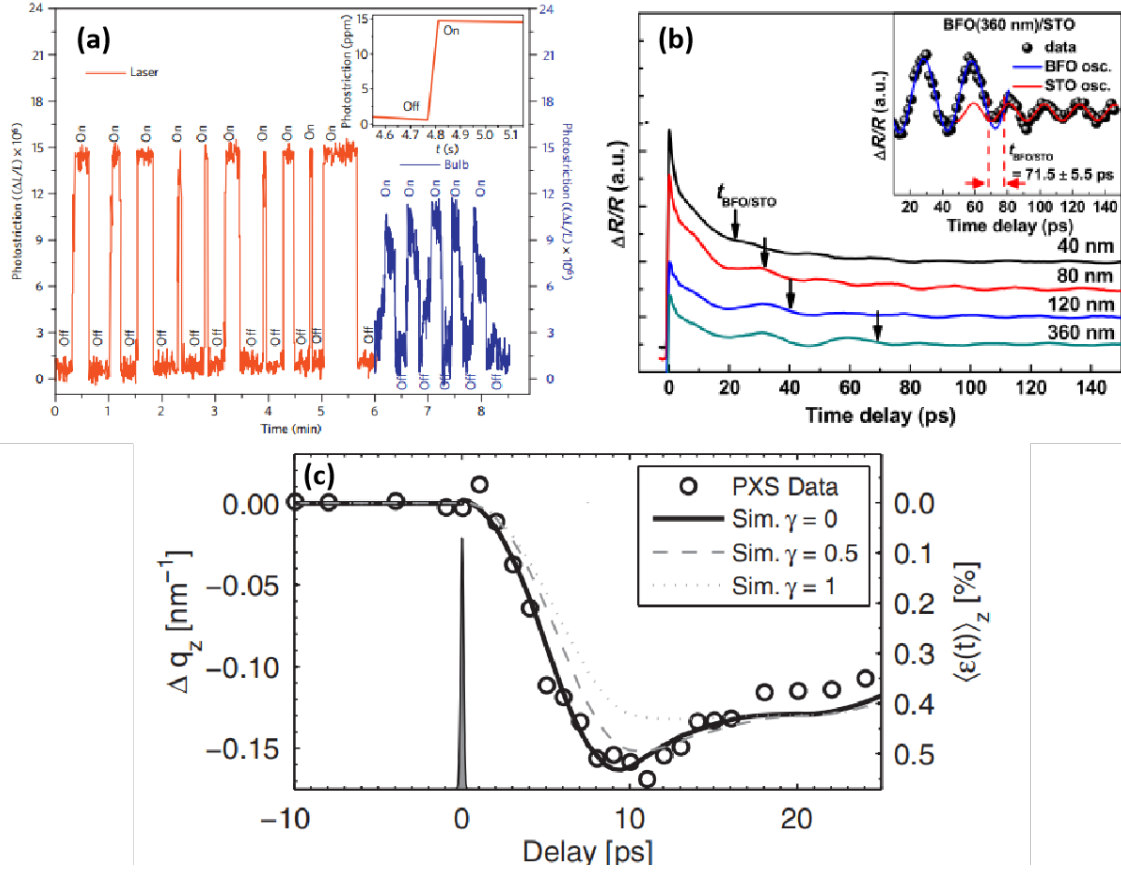


Fig 5.11: (a) Photostriction phenomena as a function of time in BiFeO_3 for different illumination along the $[010]_c$ crystal direction. The measurement carried out in the dark in using HeNe laser (15 mW, 632.8 nm) is shown in red, while in blue the measurement with a commercial white light bulb (230 V, 100 W). The zoom in inset shows the fast response time below 0.1 s [141]. (b) The $\Delta R/R$ on (110) BiFeO_3 thin films with various thicknesses. The pump pulses have a photon energy of 3.1 eV while the probe pulses energy is 1.55 eV. The arrows indicate the BFO/STO interface position. Inset: the oscillation signal was obtained by subtracting the decaying background [145]. (c) Transient shift Δq_z of the $(002)_c$ BiFeO_3 Bragg peak. The black solid line represents the simulated peak shift for an instantaneous stress. A semi-instantaneous stress and a fully diffusive-like stress are shown in gray dashed line and dot line respectively, which both have a time constant $\tau_{\text{rise}} = 2$ ps. The gray Gaussian peak at $t = 0$ indicates the temporal resolution of 200 fs of the plasma X-ray source (PXS) setup [55].

thin BiFeO₃ film up to 360 nm while a single crystal was investigated in the work of Ruello et al. One year later, Doig et al [128] also reported the generation and detection of coherent acoustic phonons in thin films. The same year, Wen et al [42] succeeded in detecting ultrafast strain in BiFeO₃ thin film by time-resolved X-ray diffraction with a time-resolution of 100 ps. Wen et al reported a strain amplitude up to around 0.5 % under a pump fluence of about 3 mJ.cm⁻². In 2014, Schick et al studied the same sample as the one studied in the work of Wen et al, and reported equivalent strain amplitude but with a time resolution better than 1 ps with the plasma X-ray source [55] (see **Fig 5.11(c)**). In 2013, the canonical ferroelectric material PbTiO₃ (as thin film) was also studied by time-resolved X-ray diffraction by Daranciang et al [147].

It is worth noting that in the work of Chen et al, Wen et al, Schick et al and Daranciang et al, only the longitudinal strain (η_L), i.e. the out-of-plane atomic motion was studied. Due to the intrinsic symmetry breaking associated with the ferroelectric order and the fact that the BiFeO₃ structure, like many other ferroic materials, cannot be characterized by a single, isotropic lattice parameter, light-induced in-plane motion is expected. Detecting transverse acoustic phonons (TA), i.e. shear strain (η_T), has been discussed in 2012 in the paper of Ruello et al [146], and later on by Lejman et al [139, 148, 149]. Note that the GHz shear acoustic phonon were already reported in metals [150, 151] and semiconductors [152] before ferroic materials [139, 148, 149]. While the TA waves have been generated and detected in BiFeO₃ single crystal in the paper of Ruello et al [146], Lejman et al [148] have shown that pump-probe experiments could be performed in different large grains (larger than 10 micrometers) of BFO. This has permitted to select different grain orientations and, in other words, to select different crystallographic directions. In that case, it has been possible to generate and detect the two TA modes as shown in **Fig 5.13**.

The possibility of generating these shear phonons has been also recently reproduced by Hemme et al [153]. The generation of GHz shear acoustic wave is a clear indication of ultrafast anisotropic photoinduced stress in BiFeO₃. The origin of the microscopic mechanism at play in the photoinduced strain in BiFeO₃ is still a matter of debate. By comparing the light-induced strain with time-resolved X-ray diffraction and the evolution of the lattice parameter versus temperature at the thermodynamic equilibrium, Wen et al have estimated that the ultrafast strain cannot be only attributed to a thermoelastic process. They concluded that an electronic origin was also at play. Schick et al [55] arrived to similar conclusion. The role of non-thermal processes, i.e. the processes different from the thermoelastic one has been also discussed by Lejman et al [148] and the description of the dependence of the coherent acoustic phonon spectrum (LA and TA modes) as a function of the grain orientation (i.e. as a function of the ferroelectric polarization direction, see **Fig 5.13**) has been qualitatively explained by a contribution of the inverse piezoelectric effect.

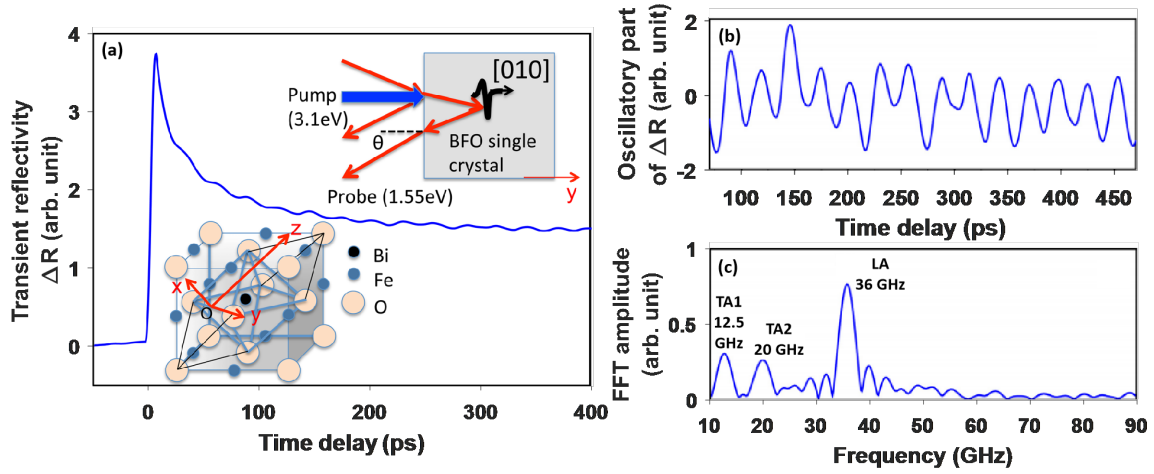


Fig 5.12: (a) Transient optical reflectivity experiment carried out on BiFeO_3 [010] single crystal, with 3.1 eV of UV pump and 1.55 eV of visible probe. The inset shows a face-centered-cubic cell of BiFeO_3 with rhombodral primitive cell crystallographic axis (x, y, z). (b) Oscillation signal after the removal of the background, denotes the coherent acoustic phonons (CAPs). (c) Fast Fourier transform (FFT) reveals the frequency components of CAPs propagation in BiFeO_3 single crystal [146].

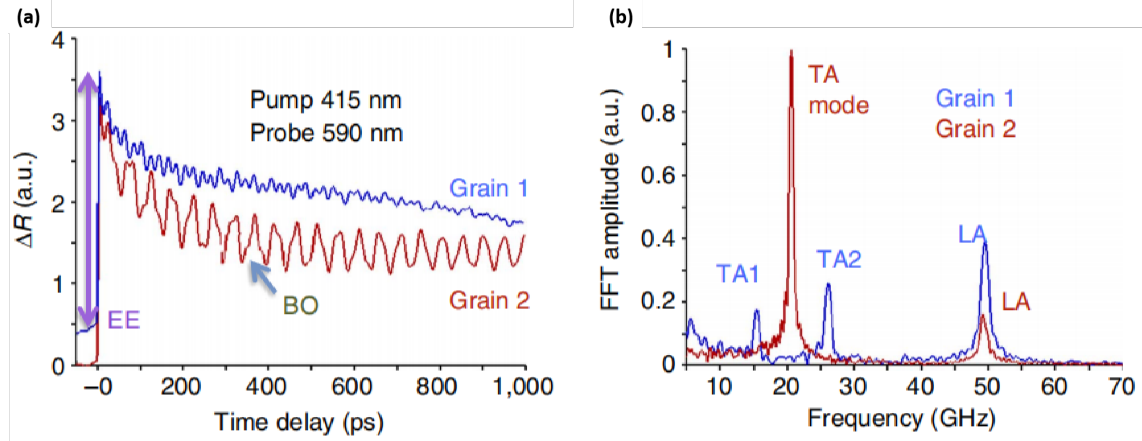


Fig 5.13: (a) Transient optical reflectivity signals obtained for different grains of the polycrystalline BiFeO_3 sample with pump (probe) wavelength of 415 nm (590 nm). “EE” stands for the electronic excitation and “BO” for Brillouin oscillation. (b) Fast Fourier transform spectra of the signals shown in (a). Grain 1 and grain 2 are in different positions where the mean macroscopic polarization is oriented differently [148].

Motivation of the investigation of photoinduced strain in BiFeO₃

The photoinduced strain in BFO material appears as promising since photoinduced strain as large as 0.5 % with moderate pump fluence ($1\text{-}3\text{ mJ.cm}^{-2}$) can be obtained. Such large amplitude competes with commercial electrically driven piezotransducers working at the MHz frequency. An important additional element relies on the fact that this ultrafast photoinduced strain is reported for time scales of tens of picoseconds, i.e. for frequency ranging within hundreds of GHz, which makes such material very interesting for future ultrafast light-induced strain related applications. Moreover, such short light pulses can also induce some shear motion in BiFeO₃, which is an additional interesting ingredient. There is however a lack of a direct measurement of this ultrafast light-induced shear strain amplitude and this is a starting point of the investigations presented in the following.

5.4 Experimental results

5.4.1 Study of photoinduced strain in (001)_c BiFeO₃ single crystal

In this part I present the results that have been published in 2020 (Juvé, Gu et *al* [54]) and were obtained in collaboration with five laboratories in France (SOLEIL synchrotron - C. Laulhé, A. Jarnac; SPMS CentraleSupélec - B. Dkhil; LAUM - V. Goussev, N. Chigarev, S. Raetz; CEA SPEC - M. Viret; C2N - T. Maroutian, S. Matzen, S. Gable) and a lab in USA (MIT, A. Maznev). While the content is similar to the published article, I present it in a slightly different way.

5.4.1.1 Characterization of [001]_c BiFeO₃ single crystal

The single BiFeO₃ crystal comes from the group of M. Viret (SPEC CEA Saclay) and has been grown by D. Colson from the same group. Such single crystal is the same as the one used by Kundys et *al* [141] and details about the growth will be found in this latter publication.

The single crystal has the [001]_c orientation. It has a nearly macroscopic single ferroelectric domain sample. However, X-ray diffraction experiment performed at CRISTAL beamline at SOLEIL synchrotron facility shows the co-existence of a large and a smaller ferroelastic domains. **Fig 5.14** has been taken following the grazing incidence geometry described in **Fig 3.9**. We show indeed in **Fig 5.14** the presence of the large Bragg reflection and just in the neighborhood a second Bragg peak coming from the presence of this second domain. Following a standard $\theta - 2\theta$ X-ray diffraction experiment with a kw scan (rocking curve) performed at CRISTAL beamline, we have also revealed these two Bragg peaks (a large and a small one) separated in kw scan by around 0.1° (not shown here).

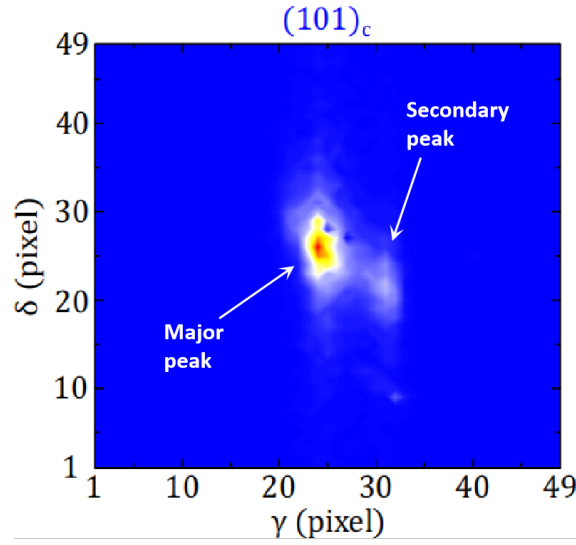


Fig 5.14: Image of the Bragg peak $(101)_c$ obtained with the XPAD3.2 detector with grazing incidence geometry (see part 3.2.2). A major Bragg peak from the main ferroelectric domain is visible with a secondary small peak.

5.4.1.2 Study of coherent acoustic phonon in BiFeO_3 by means of ultra-fast optical spectroscopy

Before the time-resolved X-ray diffraction experiment with the single BiFeO_3 crystal, we have checked the existence of both longitudinal and shear acoustic phonon generation and detection by time-resolved optical measurements. This pump-probe experiment has been conducted according to the standard setup which has been given in **Chapter 3**. The crystal may undergo fluences greater than typically 3 mJ.cm^{-2} , according to several measurements carried out at IMMM and LAUM laboratories in Le Mans with various focusing beams. These observations are consistent with the literature where thin films were photoexcited with such large fluence (Wen *et al* [42], Schick *et al* [55]). Different probe wavelengths with the OPO at IMMM (560, 587, 800 nm) were tested to demonstrate the clear origin of the Brillouin signal in this pump-probe measurement.

In **Fig 5.15**, a typical signal obtained with a pump wavelength of 400 nm and a probe wavelength of 800 nm is shown. After subtracting the background, we reveal (red curve in the bottom of the figure) clear and long-living oscillations with frequencies falling in the range of tens of GHz (see the FFT spectrum in the inset) typical to Brillouin oscillations as already shown for bulk BiFeO_3 (Ruello *et al* [146], Lejman *et al* [148]). As expected, both the longitudinal and shear acoustic waves are photogenerated and photodetected. Note that the Brillouin frequencies are split into two modes. These modes come from the fact that BiFeO_3 is birefringent and that two electromagnetic waves propagate in BiFeO_3 , namely the ordinary (o) and extraordinary (e) light. As a consequence, the light can be scattered, after the photon-phonon collision, on the different “channels” (o or e). Said differently, we can detect the propagating acoustic wave either with the “o” or “e” light, so that the Brillouin frequency can be either $f_o = 2n_o V/\lambda$ or $f_e = 2n_e V/\lambda$. This effect has been

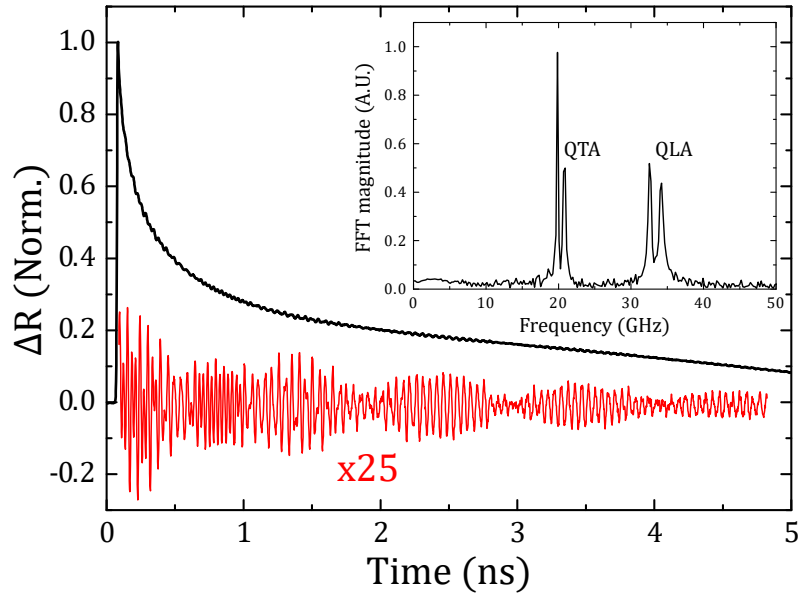


Fig 5.15: Time-resolved optical reflectivity obtained with a BiFeO_3 single crystal obtained with a pump wavelength of 400 nm and a probe wavelength of 800 nm. The bottom curve represents only the oscillating component extracted once the baseline is removed. The inset is the FFT spectrum of these oscillating signals. Modes QLA and QTA are clearly evidenced with a splitting due to the optical birefringence of the crystal [54].

discussed previously and fully described in BiFeO_3 and LiNbO_3 crystals as well as in quartz [149]. It is worth noting that only two modes (QLA and QTA) have been generated and detected. As briefly discussed with **Fig 3.13** in section 3.2.4.1, this is due to the fact that the $(001)_c$ BiFeO_3 crystal has a symmetry plane perpendicular to the surface, i.e. the $(110)_c$ plane. As a matter of fact only one transverse mode is allowed. This property will be discussed later on when we will analyse the lattice dynamics with the Christoffel equation in section 5.4.1.4. With this time-resolved optical measurement, we then confirm what was already revealed in another BiFeO_3 crystal grown with a different method (see Ruello *et al* [146]) and these results are also consistent with what was observed in different grains of a polycrystalline BiFeO_3 sample (Lejman *et al* [148]). In the following, we show how it is possible to evaluate quantitatively the longitudinal and shear strains in this BiFeO_3 single crystal by studying asymmetric Bragg reflections such as $(\pm h01)$ based on a X-ray diffraction experiment whose methodology was presented previously (see part 3.2.4).

5.4.1.3 Photoinduced strain in a BiFeO_3 single crystal by means of ultrafast time-resolved X-ray diffraction

The time-resolved X-ray diffraction of a BiFeO_3 single crystal and with a grazing incidence has been conducted with two Bragg families as mentioned in section 3.2.2. A typical image with the 2D XPAD3.2 detector is shown in **Fig 5.16(a)** for the two asymmetric Bragg planes (101) and $(\bar{1}01)$. The camera has a resolution of

$8.64 \times 10^{-3} \text{ }^\circ/\text{pixel}$. The variation (shift) of the corresponding Bragg peaks induced by the light action is shown in **Fig 5.16(b)**. We can see that the Bragg peaks exhibit a downward shift along the δ coordinate, i.e. along the Q_z in the reciprocal space. The intensity of each Bragg peak has then been integrated over the region of interest (ROI) for each time delay and for each $k\varphi$ angle.

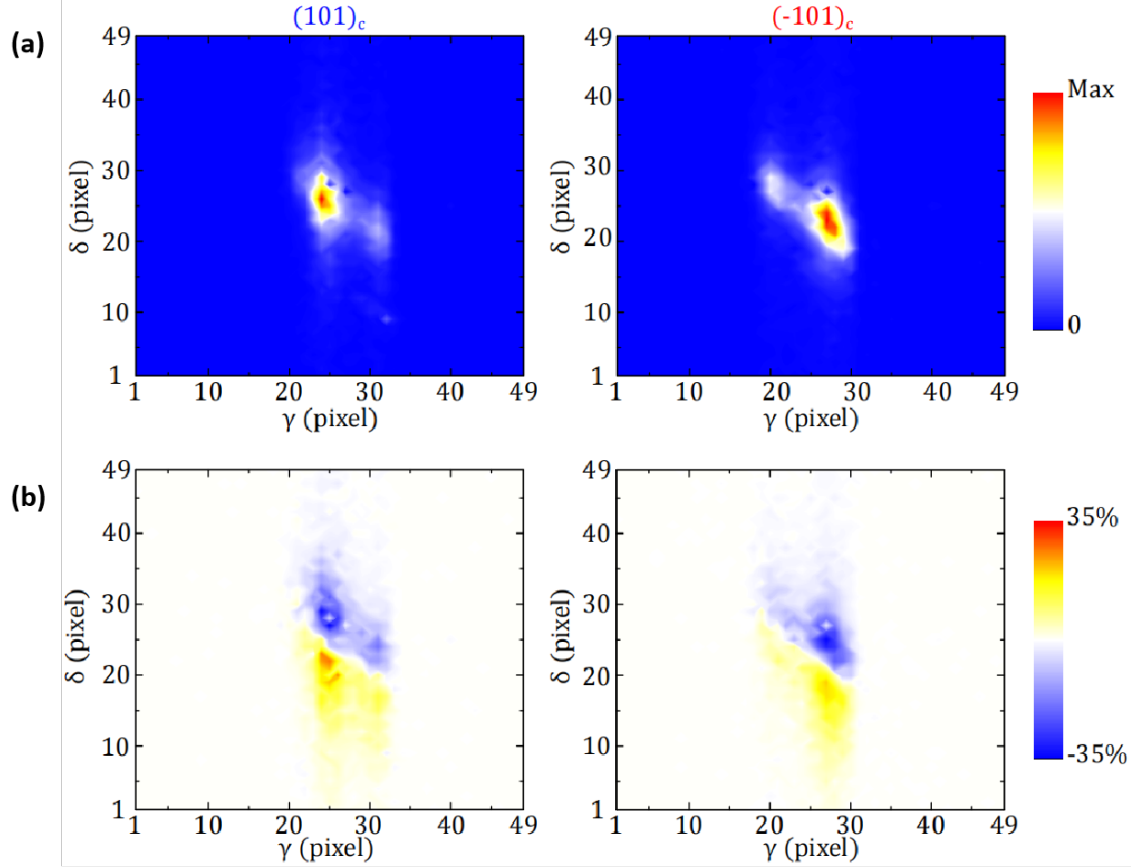


Fig 5.16: (a) X-ray diffraction imaging in reciprocal space of the $(101)_c$ and $(-101)_c$ Bragg diffraction peaks at 200 ps after the pump excitation. The positions (γ, δ) of the $(101)_c$ and $(\bar{1}01)_c$ Bragg diffraction peaks are $(26.1874^\circ, 26.0802^\circ)$ and $(26.0367^\circ, 25.6879^\circ)$ respectively. (b) Differential image plot of the same Bragg diffraction peaks in (a).

A typical 2D integration done for a $k\varphi$ scan is shown in **Fig 5.17** where we can see the asymmetry of the Bragg peak coming from the presence of two ferroelectric domains as discussed earlier in **Fig 5.14** for the presentation of the BiFeO_3 single crystal. A comparison between the Bragg peak obtained at the thermodynamic equilibrium (black curve) and the one after a photoexcitation (red curve) reveals the typical maximum shift of the Bragg peak. Neither the change on the shape of the Bragg peaks nor that of FWHM is witnessed, instead a global shift is observed. This is in contrast with earlier reports of Wen *et al* [42] where the $(002)_c$ Bragg peak in a BiFeO_3 thin film exhibits a quite important increase of the width and the Bragg peak becomes asymmetric (**Fig 2.8(b)**). In our case, because of the presence of two domain contributions, we have to be cautious with the discussion about the shape.

We have averaged the Bragg position by calculating the center of mass (CoM) of the entire Bragg peak shown in **Fig 5.17**.

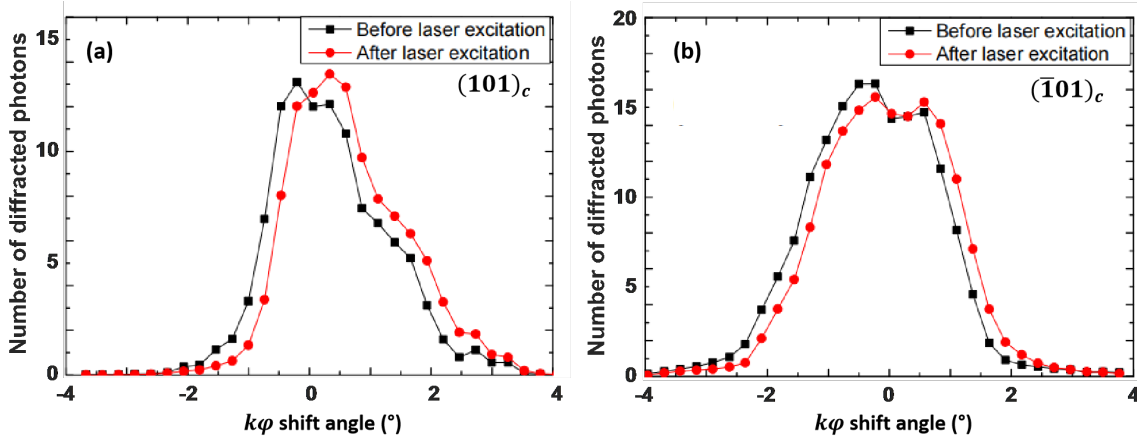


Fig 5.17: $k\phi$ scans recorded for $(101)_c$ (a) and $(\bar{1}01)_c$ (b) Bragg peaks in $(001)_c$ BFO single crystal. The asymmetry of Bragg peak comes from the existence of a second small ferroelectric domain.

As presented earlier in section 3.2.2, this center of mass of each Bragg peak 2D images shown in **Fig 5.14** is estimated as a function of the reciprocal space parameters δ and γ defining the position of the Bragg peak on the detector. With equation (3.1) we have then deduced the evolution of the interplanar distance $\Delta d/d$. Typical temporal evolutions of that relative variation of this interplanar distances for $(101)_c/(\bar{1}01)_c$ and $(201)_c/(\bar{2}01)_c$ Bragg planes families are shown in **Fig 5.18**. We observe a sharp increase of the interplanar distance within the first picoseconds (within our time resolution of 10 ps). Then a kind of plateau is observed that lasts more than 200 ps (signal up to 1 ns has been measured showing a slow recovery). It is interesting to see that there is a non equivalent behavior between $(\bar{h}01)_c$ and $(h01)_c$. For each delay time, the planFes $(\bar{h}01)_c$ exhibit an interplanar variation smaller than the family $(h01)_c$. This is even more visible for planes $(\pm 201)_c$. We see that this asymmetric response is consistent with the model presented in equation (3.7).

With equation (3.8), we can then deduce separately the longitudinal (η_L) and shear (η_T) strain. An average value calculated with the strain extracted from the $(\pm 101)_c$ and $(\pm 201)_c$ families is shown in **Fig 5.19** in orange and blue for the longitudinal and shear contributions respectively. This is the first time, to our knowledge, that both the longitudinal and shear strains have been quantitatively deduced from time-resolved X-ray diffraction in BiFeO_3 and these results have been published in 2020 in Juve, Gu et al [54]. The amplitude of the longitudinal strain of about 0.1 % for an incident absorbed pump fluence of 1.5 mJ.cm^{-2} is roughly three times smaller than the measured longitudinal strain by Schick et al [55]. A detailed discussion about the microscopic mechanisms in the photoinduced strain process will be done later in the next section.

Our measurements show that the shear strain is roughly 6 times smaller than the light-induced longitudinal strain. When comparing these results with the one obtained with time-resolved optical measurements (see **Fig 5.15**) we can immediately

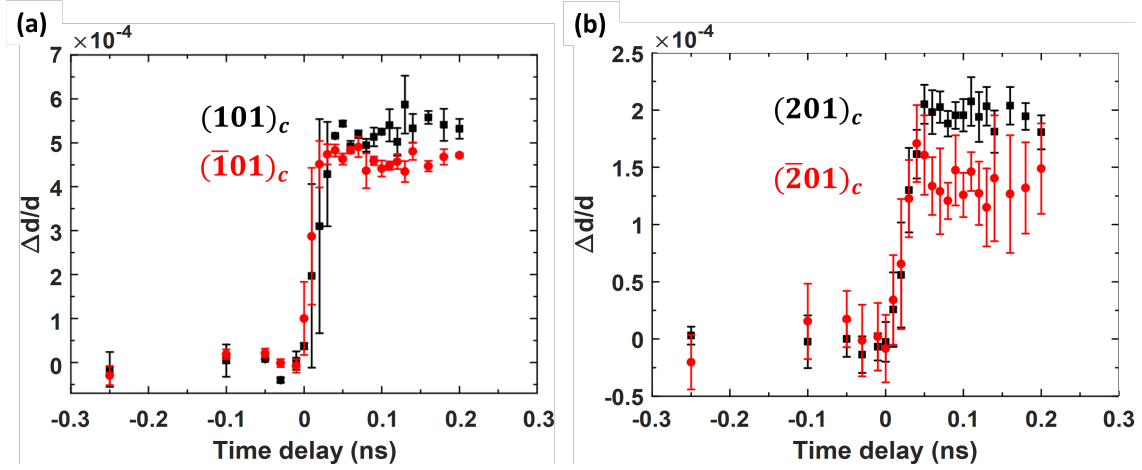


Fig 5.18: Temporal dependence of the interplanar distance measured for the $(\pm 101)_c$ (a) and $(\pm 201)_c$ (b) Bragg planes families in $(001)_c$ BiFeO_3 single crystal.

conclude that in time-resolved Brillouin scattering signal, the large TA mode signal comes from an efficient detection process and not from a large shear strain. Indeed, while in **Fig 5.15** the TA mode signal is larger or equivalent to the LA mode ones, we know now, thanks to the time-resolved X-ray diffraction that the shear strain magnitude is roughly 6 times smaller than the longitudinal strain component. Consequently, the amplitude of the shear strain is not responsible for this large Brillouin TA mode signal in BiFeO_3 , but rather, an efficient detection mechanism is at play in bulk BiFeO_3 . In particular, we can guess that there exists large photoelastic coefficients in BiFeO_3 . To fully envision to determine them, which is out of the scope of these research, several crystal orientations would be necessary to reconstruct the 4 rank photoelastic tensor.

An additional interesting element that appears in **Fig 5.19(a)** is the existence of a different response time of the lattice to develop the longitudinal and the shear strain. We can call it an asynchronous effect that is illustrated by the fact that while the longitudinal strain has reached roughly half of its maximum after the pump excitation, the shear strain, within our error bars, remains nearly zero (illustrated by blue area in **Fig 5.19(a)**). A sketch of this phenomenon is given in **Fig 5.19(b)** where the unit cell exhibits a kind of two-step deformation dynamics. Note that such asynchronous effect has already been discussed in a disoriented single crystal of zinc by full optical pump-probe technique. In this latter work, the detection of this peculiar strain dynamics was not direct in a sense it is convoluted by the dielectric response due to the detection by a visible probe laser beam [150]. In our experiment, we have the opportunity to directly discuss such asynchronous effect with time and space dependence of the light-induced strain components. In the following we propose an interpretation of this phenomenon together with the discussion of the microscopic mechanisms at play in the photoinduced strain process.

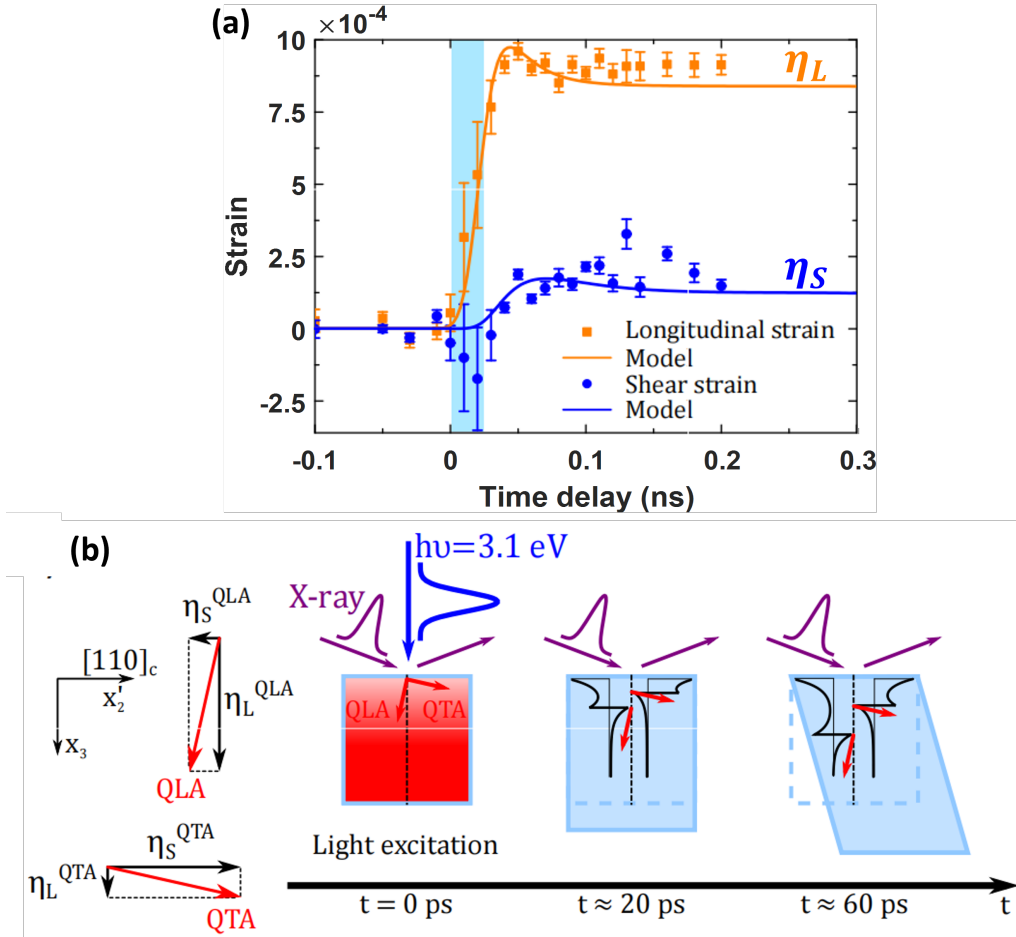


Fig 5.19: (a) Temporal evolution of longitudinal and shear strains extracted from time-resolved X-ray diffraction experiments. A comparison between experimental results of longitudinal and shear strain with numerical simulations is also presented (the model is presented in section 5.4.1.4). (b) Sketch of the temporal evolution of the deformation of the BiFeO_3 unit cell associated to a specific space and temporal dependence of the two quasi acoustic modes (QLA and QTA) [54].

5.4.1.4 Lattice dynamics and photoinduced strain microscopic mechanisms: models and discussion

During the presentation of the results, we have often adopted the pseudo-cubic notation like $(101)_c$. In this part where we develop different models, we will necessarily employ the general rhombohedral (or hexagonal) coordinates to get into the details of lattice dynamics and of the photoinduced stress processes.

Lattice dynamics and origin of the asynchronous effect

In this subpart, we describe the lattice dynamics in the $(100)_c$ BiFeO_3 single crystal which is necessary to discuss the so-called asynchronous effect.

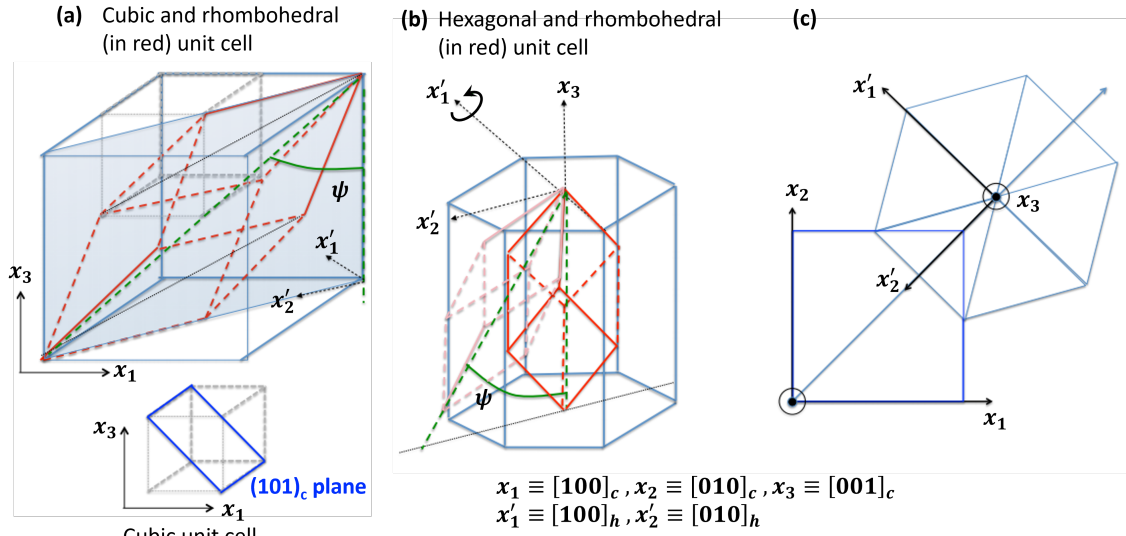


Fig 5.20: (a) Cubic, rhomboedral (trigonal) and (b) hexagonal frames. ψ is the angle between the C_3 axis of the trigonal BiFeO_3 structure and the normal of the irradiated surface (free surface) which is along x_3 . (c) Cubic and hexagonal frames correspondence. The tensors in the hexagonal frame discussed in the text, are expressed in the coordinates $(Ox'_1x'_2x_3)$. The symmetry plane is $(110)_c$ is the quasi-cubic frame which correspond to the plane $(Ox'_1x'_2)$ in the hexagonal frame.

For this purpose, we establish the general expression of the propagating longitudinal and shear strain as a function of the in-plane and out-of-plane components of the quasi-longitudinal and quasi-transverses acoustic modes found by solving the Christoffel equation. We describe all the physical entities in the rotated trigonal frame $(Ox'_1x'_2x_3)$ as shown in **Fig 5.20**. As an example the Voigt component of index 2 refers to axis x'_2 (remark: we remind that the irradiated surface in the quasi-cubic approximation is the surface $(001)_c$ and the surface $(001)_h$ in the “new” hexagonal frame (rotated one)). When the waves propagate along the $[001]_c$ direction, it is equivalent to consider these waves propagate along the $[001]_h$ (i.e. along x_3), but the hexagonal tensor has to be rotated by $\psi = 54^\circ$ which corresponds to the angle between the x_3 direction and the trigonal C_3 axis.

The Christoffel equation permits to describe the displacement vector of the acoustic modes in any direction of a crystal having a given symmetry [154]. For the par-

ticular case of our geometry, for a wave propagating along the x_3 direction (perpendicular to the irradiated surface in the 1D geometry of the pump-probe experiment), the Christoffel tensor becomes:

$$\Gamma_{x_3} = \begin{pmatrix} C_{55} & 0 & 0 \\ 0 & C_{44} & C_{34} \\ 0 & C_{34} & C_{33} \end{pmatrix} \quad (5.2)$$

This indicates that a pure shear wave with a particle displacement along x'_1 propagating at the sound velocity $V_{TA} = \sqrt{C_{55}/\rho}$ can propagate along x_3 . But this wave is not generated for symmetry reason: the $(110)_c$ is a symmetry plane. That plane in the cubic frame corresponds to the so-called (Ox'_2x_3) in the trigonal frame. There are also two waves (named QLA and QTA) having particle displacement in the plane Ox'_2x_3 and by solving the Christoffel determinant:

$$\Delta = \begin{vmatrix} C_{44} - \rho V^2 & C_{34} \\ C_{34} & C_{33} - \rho V^2 \end{vmatrix} = 0 \quad (5.3)$$

We show that the quasi-longitudinal and a quasi-transverse modes velocities are:

$$\begin{aligned} V_{QLA} &= \sqrt{\frac{(C_{44} + C_{33}) + \sqrt{(C_{44} - C_{33})^2 + 4C_{34}^2}}{2\rho}} \\ V_{QTA} &= \sqrt{\frac{(C_{44} + C_{33}) - \sqrt{(C_{44} - C_{33})^2 + 4C_{34}^2}}{2\rho}} \end{aligned} \quad (5.4)$$

The values of the elastic stiffness coefficients in the rotated base used to estimate these velocities, are given in the following tensor (obtained with standardized compliance matrices for general anisotropic materials [155]):

$$\begin{aligned} &C_{ijkl}(\psi = 54^\circ) \\ &= \begin{pmatrix} 207. & 93.291 & 79.709 & -40.5849 & 0. & 0. \\ 93.291 & 130.083 & 77.4306 & 9.93573 & 0. & 0. \\ 79.709 & 77.4306 & 181.056 & -26.8898 & 0. & 0. \\ -40.5849 & 9.93573 & -26.8898 & 57.4306 & 0. & 0. \\ 0. & 0. & 0. & 0. & 19.784 & -11.5777 \\ 0. & 0. & 0. & 0. & -11.5777 & 52.216 \end{pmatrix} \end{aligned} \quad (5.5)$$

The non-rotated tensor values come from the literature. C_{11} , C_{33} , C_{44} and C_{66} come from experimental values found in Ref. [156]. It is worth mentioning that these authors have used a slightly different density for BiFeO_3 as 8.4 g.cm^{-3} . We remind that $C_{66} = (C_{11} - C_{12})/2$. C_{14} and C_{13} are calculated values with generalized

gradient approximation (GGA) method found in Ref. [157]. The non-rotated elastic stiffness tensor is (in GPa):

$$C_{ijkl}(\psi = 0) = \begin{pmatrix} 207. & 123. & 50. & 19. & 0. & 0. \\ 123. & 207. & 50. & -19. & 0. & 0. \\ 50. & 50. & 159. & 0. & 0. & 0. \\ 19. & -19. & 0. & 30. & 0. & 0. \\ 0. & 0. & 0. & 0. & 30. & 19. \\ 0. & 0. & 0. & 0. & 19. & 42. \end{pmatrix} \quad (5.6)$$

Using the elastic stiffness constants in the rotated frame we arrive to: $V_{QLA} \approx 4710$ m/s and $V_{QTA} \approx 2480$ m/s. In our experiments the analysis of the Brillouin frequencies shown in **Fig 5.15** (using the relevant refractive index for the probe wavelength at 800 nm), permits to deduce $V_{QLA} \approx 4970$ m/s and $V_{QTA} \approx 3020$ m/s. The relative difference of around 5 – 20% is important but is typically the one we find when comparing the different data of the literature [156, 157].

The eigen vectors, i.e. the in-plane and out-of plane components of these QLA and QTA waves are: $\vec{u}^{QLA} \approx (0, 1, 4.47)$ and $\vec{u}^{QTA} \approx (0, -4.47, 1)$ and are represented in the left part of **Fig 5.19(b)**. The general expressions of the time and space dependence of the particle displacements associated to the QLA and QTA modes become then:

$$\begin{aligned} \vec{u}^{QLA} &= A \times f\left(t - \frac{x_3}{V_{QLA}}\right) \vec{x}_2' + 4.47A \times f\left(t - \frac{x_3}{V_{QLA}}\right) \vec{x}_3 \\ \vec{u}^{QTA} &= -4.47B \times f\left(t - \frac{x_3}{V_{QTA}}\right) \vec{x}_2' + B \times f\left(t - \frac{x_3}{V_{QTA}}\right) \vec{x}_3 \end{aligned} \quad (5.7)$$

A and B are the amplitudes and $f(t - \frac{x_3}{V_{QLA}})$ and $f(t - \frac{x_3}{V_{QTA}})$ describe the space and time dependences of the acoustic waves associated to the QLA and QTA modes respectively.

The associated strains become:

$$\begin{aligned}
\bar{\eta}^{QLA} &= \frac{\partial \vec{u}^{QLA}}{\partial x_3} \\
&= -A \times \frac{\partial f(t - \frac{x_3}{V_{QLA}})}{dx_3} \vec{x}'_2 \\
&\quad + -4.47A \times \frac{\partial f(t - \frac{x_3}{V_{QLA}})}{dx_3} \vec{x}_3 \\
\bar{\eta}^{QTA} &= \frac{\partial \vec{u}^{QTA}}{\partial x_3} \\
&= 4.47B \times \frac{\partial f(t - \frac{x_3}{V_{QTA}})}{dx_3} \vec{x}'_2 \\
&\quad + -B \times \frac{\partial f(t - \frac{x_3}{V_{QTA}})}{dx_3} \vec{x}_3
\end{aligned} \tag{5.8}$$

The total in-plane (shear) and out-of-plane (longitudinal) strains coming from both contributions of the QTA and QLA modes, consist in the addition of components along x'_2 and x_3 respectively. We have:

$$\begin{aligned}
\eta_T(t) &= \frac{4.47B}{V_{QTA}} f(t - \frac{x_3}{V_{QTA}}) + \frac{-A}{V_{QLA}} f(t - \frac{x_3}{V_{QLA}}) \\
\eta_L(t) &= \frac{-B}{V_{QTA}} f(t - \frac{x_3}{V_{QTA}}) + \frac{-4.47A}{V_{QLA}} f(t - \frac{x_3}{V_{QLA}})
\end{aligned} \tag{5.9}$$

Modeling the photoinduced strain functions

In the previous section, $f(t - x_3/V_{QTA})$ and $f(t - x_3/V_{QLA})$ describe the time and space dependence of the photoinduced strain to QLA and QTA modes. In an anisotropic medium such as BFO, the general motion equations are given below where the photoinduced shear stress is σ_2 (source term for the in-plane displacement u_2 along x'_2) and the longitudinal one is σ_3 (source term for the out-of-plane displacement u_3 along x_3) according to:

$$\begin{aligned}
\rho \frac{\partial^2 u_2(x_3, t)}{\partial t^2} - C_{44} \frac{\partial^2 u_2(x_3, t)}{\partial x_3^2} - C_{43} \frac{\partial^2 u_3(x_3, t)}{\partial x_3^2} &= \frac{\partial \sigma_2(x_3, t)}{\partial x_3} \\
\rho \frac{\partial^2 u_3(x_3, t)}{\partial t^2} - C_{43} \frac{\partial^2 u_2(x_3, t)}{\partial x_3^2} - C_{33} \frac{\partial^2 u_3(x_3, t)}{\partial x_3^2} &= \frac{\partial \sigma_3(x_3, t)}{\partial x_3}
\end{aligned} \tag{5.10}$$

As a first approach, if we consider the photoinduced stresses follow the shape of the pump penetration depth, i.e. σ_2 and σ_3 are proportional to $e^{-z/\xi}$, then

equation (5.10) leads to a set of coupled linear partial differential equations. In that case, the solution for the strain of the QLA and QTA mode follows the mathematical expression we have presented in equation (2.7) [19].

Consequently we obtain:

$$\begin{aligned} f(t, x_3, V_{QTA}) &= [e^{-x_3/\xi}(1 - \frac{1}{2}e^{-V_{QTA}t/\xi}) \\ &\quad - \frac{1}{2}e^{-|x_3-V_{QTA}t|/\xi}\text{sgn}(x_3 - V_{QTA}t)] \\ f(t, x_3, V_{QLA}) &= [e^{-x_3/\xi}(1 - \frac{1}{2}e^{-V_{QLA}t/\xi}) \\ &\quad - \frac{1}{2}e^{-|x_3-V_{QLA}t|/\xi}\text{sgn}(x_3 - V_{QLA}t)] \end{aligned} \quad (5.11)$$

with $\xi \sim 40$ nm the penetration depth of the pump beam whose value was already discussed in section 3.2.2. Consistently with equation (5.9), the general longitudinal and shear strain become a combination of the “Thomsen’s” functions:

$$\begin{aligned} \eta_S(t, x_3) &= \eta_S^{QTA} f(t, x_3, V_{QTA}) + \eta_S^{QLA} f(t, x_3, V_{QLA}) \\ \eta_L(t, x_3) &= \eta_L^{QTA} f(t, x_3, V_{QTA}) + \eta_L^{QLA} f(t, x_3, V_{QLA}), \end{aligned} \quad (5.12)$$

Where $f(t, x_3, V_{QTA})$ and $f(t, x_3, V_{QLA})$ are given by equation 5.11. The parameters η_S^{QTA} , η_S^{QLA} , η_L^{QTA} and η_L^{QLA} which depend on the A , B , V_{QLA} and V_{QTA} , are fitted in our **Fig 5.19(a)** taking into account the X-ray detection as discussed below. Note that the parameters A and B depend on the photogeneration processes that are discussed in the next part, after the presentation of the simulation of the X-ray diffraction signal.

Simulation of the time-resolved X-ray signal

For simulating the transient lattice distortion, we assume the kinematic approximation of X-ray diffraction to be valid. In the kinematic approximation of diffraction theory, the measured strains are average strains weighted by the transmission factor of X-rays along the diffraction path:

$$\langle \eta_{L,S} \rangle (t) = \frac{\int_{x_3=0}^{\infty} dx_3 e^{-\frac{L(x_3)}{\Lambda}} \eta_{L,S}(t, x_3)}{\int_{x_3=0}^{\infty} dx_3 e^{-\frac{L(x_3)}{\Lambda}}}, \quad (5.13)$$

$L(x_3)$ refers to the length travelled by the X-ray beam within the BiFeO_3 sample when diffracted at the depth x_3 . Its expression, which depends not only on x_3 but also on the diffraction angles, is derived in **Appendix A**.

The curves in orange and in blue for the longitudinal and shear strain shown in **Fig 5.19(a)** correspond to the calculated strains by using equation (5.13). The

adjustment is in good agreement with the experimental data (squares and circles). Note that we have adjusted $\vec{\eta}_{QLA}$ and $\vec{\eta}_{QTA}$ amplitudes in order to constrain the vectors orthogonality (properties of eigenmodes QLA and QTA). Our model reproduces this asynchronous effect that originates from the opposite sign of the in-plane components of the QLA and QTA modes ($\vec{\eta}_{QLA}(x'_2)$ and $\vec{\eta}_{QTA}(x'_2)$) which leads to a near cancellation of the total shear strain at early times (< 20 ps) (see sketch in **Fig 5.19(b)**). As the acoustic modes have different velocities, this effect fades away as the acoustic modes separate in space at longer times as sketched in **Fig 5.19(b)**. We also see that the rising times are also very well reproduced by our model underlining the minimal effect of the carrier or heat diffusion for such timescales. This justify at the moment that the photoinduced stress follows the exponential shape of the pump light absorption in the BiFeO₃ single crystal.

Photoinduced strain microscopic mechanisms

We now discuss the origin of the microscopic mechanisms of the photoinduced strain in the BiFeO₃ single crystal. As presented earlier, this discussion is not new and several attempts have been made to elucidate the microscopic mechanisms (see Wen et al [42], Schick et al [55] and Lejman et al [148]). Several previous works have concluded that non-thermal contributions may exist. With our new input in the discussion, i.e. the first measurement of the light-induced shear strain, we can revisit this discussion.

In general, these photoinduced stresses can originate from the inverse piezoelectric, the thermoelastic or the deformation potential stress, or by a combination of these contributions as presented in **Chapter 2**.

Inverse piezoelectric effect: the general expression of the photoinduced stress driven by the piezoelectric effect has been established in a previous paper [148] with:

$$\begin{aligned}\sigma_T^{PE} &= \sigma_{23}^{PE} = (d_{31} - d_{33})\cos(\psi)\sin(\psi)E(t, x_3) \\ \sigma_L^{PE} &= \sigma_{33}^{PE} = (d_{31}\cos^2(\psi) + d_{33}\sin^2(\psi))E(t, x_3)\end{aligned}\tag{5.14}$$

$d_{31} \sim -30/-20$ pm.V⁻¹ [158, 159] and $d_{33} \sim 50/70$ pm.V⁻¹ [160] are the piezoelectric coefficients. $\psi \sim 54^\circ$ and $E(t, x_3)$ corresponds to the space and time dependencies of the transient internal depolarizing field. Since $E(t, x_3)$ is not known, we will show that only a ratio of L and T strain is accessible.

Thermoelastic process: the theoretical contribution of the photoinduced thermoelastic stress (TE) σ_{ij}^{TE} is assessed by calculating the tensorial expression $\sigma_{ij}^{TE} = -C_{ijkl}\beta_{kl}\Delta T$. For that we have to take into account the anisotropic thermal expansion of BiFeO₃. The (001)_c crystal corresponds to a trigonal crystal for which the

$[001]_R$ direction is rotated by an angle of $\psi=54^\circ$ around the (Ox'_1) axis (See **Fig 5.20**). We remind that R means the trigonal coordinates. Doing such a rotation, the relevant thermal expansion coefficients become $\beta_4 = \beta_{23} = (\beta_a - \beta_c)\cos(\psi)\sin(\psi)$, $\beta_2 = \beta_{22} = \beta_a\cos^2(\psi) + \beta_c\sin^2(\psi)$ and $\beta_3 = \beta_{33} = \beta_a\sin^2(\psi) + \beta_c\cos^2(\psi)$, with $\beta_a=0.7.10^{-5} \text{ K}^{-1}$ and $\beta_c=1.2.10^{-5} \text{ K}^{-1}$ the thermal expansion coefficients in the $[100]_R$ and $[001]_R$ directions at 300 K [161]. We have also rotated the elastic stiffness tensor [139] to obtain the final longitudinal (σ_{33}^{TE}) and shear (σ_{23}^{TE}) thermoelastic stress components. The rotated tensor has already been given in equation (5.5). The light-induced thermoelastic shear and longitudinal stresses are then:

$$\begin{aligned}\sigma_T^{TE} &= \sigma_{23}^{TE} = -(C_{41}\beta_1 + C_{42}\beta_2 + C_{43}\beta_3 + 2C_{44}\beta_4)\Delta T \\ \sigma_L^{TE} &= \sigma_{33}^{TE} = -(C_{31}\beta_1 + C_{32}\beta_2 + C_{33}\beta_3 + 2C_{34}\beta_4)\Delta T\end{aligned}\quad (5.15)$$

If ΔT is estimated, then both stresses can be estimated.

Deformation potential process: regarding the deformation potential stress, the electron and hole contribution can be accounted with [19]:

$$\sigma_{ij}^{DP} = \frac{dE_g}{d\eta_{ij}} N \quad (5.16)$$

The deformation potential constant $\frac{dE_g}{d\eta_{ij}}$ is governed by the ability of the band gap E_g to evolve under a given strain η_{ij} . At the moment, none of these parameters are known unfortunately, precluding any precise previsions of this effect. We only have the average parameter $\frac{dE_g}{d\eta} = \frac{1}{3}(2\frac{dE_g}{d\eta_{11}} + \frac{dE_g}{d\eta_{33}}) \sim -B\frac{dE_g}{dP}$, with $\frac{dE_g}{dP} \sim -5.10^{-11} \text{ eV.Pa}^{-1}$ [162], where B is the bulk modulus. Consequently, within this approximation of isotropy, we can estimate a good order for the longitudinal stress with:

$$\sigma_L^{DP} \approx -B\frac{dE_g}{dP} N \quad (5.17)$$

It is worth to mention that in that case the photoinduced stress becomes positive, i.e. it leads to a contraction of the lattice since $\frac{dE_g}{dP} < 0$. This effect is not the one observed in the experiment excluding the DP mechanism.

Estimates of the contributions of each process: once we have established the expression of these photoinduced stresses, we can connect them with the maximum strain we measured. For that we consider, that for a sufficient long time scale, for which the bipolar pulse has left the probed region, the stationary photoinduced stress part is the only one which is probed. We remind that in our model we neglect

diffusion processes for photoexcited carriers and neglect thermal diffusion at the time scale of our study. In that stationary case, we have from equation (5.10):

$$\begin{aligned} C_{44}\eta_2 + C_{43}\eta_3 &= -\sigma_2 \\ C_{43}\eta_2 + C_{33}\eta_3 &= -\sigma_3 \end{aligned} \quad (5.18)$$

These equations lead then (writing $\eta_{2,3} = \eta_{T,L}$ and $\sigma_{2,3} = \sigma_{T,L}$) to:

$$\begin{aligned} \eta_L &= \frac{-\sigma_L C_{44} + \sigma_T C_{43}}{C_{33} C_{44} - C_{43}^2} \\ \eta_T &= \frac{-\sigma_T C_{33} + \sigma_L C_{43}}{C_{33} C_{44} - C_{43}^2} \end{aligned} \quad (5.19)$$

For the thermoelastic process, we use the tabulated elastic parameters and the thermal expansion ones as presented before. The lattice temperature increase has been estimated to $\Delta T \approx 13$ K as explained in the following. The refractive index at 400 nm ($E_{\text{ph}} = 3.1$ eV) was taken from [52] and it reads $\tilde{n}_o = 3.39 + 1.01i$ or $\tilde{n}_e(\psi) = 3.09 + 0.58i$ with $\psi = 54^\circ$ the angle between the surface normal and the optical axis. As we do not know precisely the light pump pulse polarization respect to the optical axis of the BiFeO₃ single crystal, we estimate the sample temperature elevation and the number of excited carriers for both optical index sets. These values lead to the absorption profile given by **Fig 5.21(a)**. In our experiments, the laser fluence was set to 3 mJ.cm^{-2} and with the material's parameters heat capacity $C_p = 0.3 \text{ J.g}^{-1}\text{K}^{-1}$ and density $\rho = 8.34 \text{ g.cm}^{-3}$, one can extract the temperature elevation profile as shown in **Fig 5.21(b)**. We remind that only the excess photon energy is transferred into the BiFeO₃ lattice, which is given by $E = (E_{\text{ph}} - E_g)/E_{\text{ph}} = (3.1 - 2.6)/3.1 \approx 0.16$, with E_{ph} the photon energy and E_g the band gap energy. Then, the mean temperature elevation in the probed region by the X-ray was defined by $\overline{\Delta T} = \frac{\int_{z=0}^{z=\infty} \exp(-z/\xi_X) \Delta T(z) dz}{\int_{z=0}^{z=\infty} \exp(-z/\xi_X) dz}$ and is found to be 13 K for \tilde{n}_o and 12 K for $\tilde{n}_e(\psi)$. The mean excited carriers density was calculated in the same way and reads $4.0 \times 10^{20} \text{ cm}^{-3}$ for \tilde{n}_o and $3.6 \times 10^{20} \text{ cm}^{-3}$ for $\tilde{n}_e(\psi)$.

The estimates of the TE process are given in **Table 5.1**. We have compared the calculated contribution of the TE process with the experimental strain as shown in **Fig 5.19**. These estimates are indicated by dashed horizontal line in orange and blue for the longitudinal and shear strain respectively.

	η_T	η_L	η_L/η_T
Exp.	$\sim 1.3 \times 10^{-4}$	$\sim 9 \times 10^{-4}$	~ 7
TE	1.5×10^{-4}	2.4×10^{-4}	1.6
IPE	—	—	~ 1

Table 5.1: Comparison of longitudinal and shear photoinduced strain that are determined experimentally with the calculated values in considering the contribution of thermoelastic (TE) and inverse piezoelectric (IPE) effect.

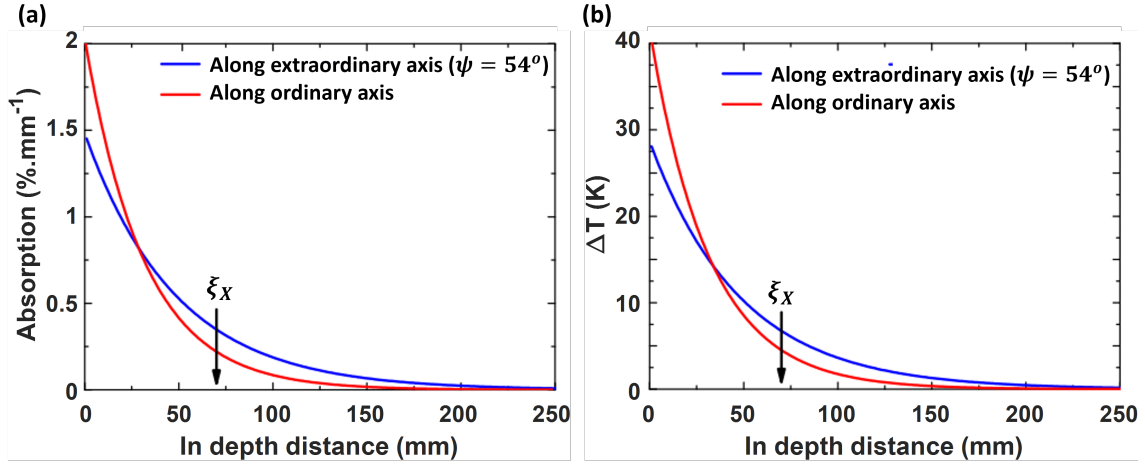


Fig 5.21: (a) Light absorption profile along ordinary and extraordinary axes in BiFeO_3 single crystal. (b) The temperature evolution profile is calculated in using the light absorption along ordinary and extraordinary axes. The arrows indicate the value of penetration depth of X-ray pulses.

For the estimate of the inverse piezoelectric effect, as said before, since we do not know the internal electric field dynamics, only the ratio η_L/η_T can be estimated. For that we just need the elastic constant and the piezoelectric coefficient d_{31} and d_{33} as given previously.

As a summary, there is no general agreement between the experimental strain and our numerical estimations. This clearly indicates that the full understanding of the microscopic origin of the photoinduced strain is not obtained. We see that the thermoelastic stress could explain the measured shear strain signal. But this thermoelastic process cannot solely explain the light-induced longitudinal strain. And the inverse piezoelectric effect cannot reproduce correctly the ratio η_L/η_T either. Maybe a combination of both processes could improve the model, but for that we need to know the internal electric field E . It is worth noting that first principle calculations [163] have actually shown that the inverse piezoelectric effect is an efficient mechanism that very likely contributes to the light-induced distortion of BiFeO_3 excited with above band gap transitions. That latter calculations cannot discuss the contribution of the TE effect since calculations were done at 0 K. Further works and theory are still needed to have a complete comprehensive view of the photoinduced strain processes in BiFeO_3 .

5.4.1.5 Conclusion on the ultrafast light-induced strain dynamics in the BiFeO_3 single crystal

In this study, we have shown that our methodology for extracting both the light-induced longitudinal and shear strains works. This is the first ever reported measurement of an in-plane shear motion in BiFeO_3 to our best knowledge. It is interesting to see that the full optical pump-probe method applied to the study of this BiFeO_3 single crystal provides only the Brillouin component (i.e. the modulation of the tran-

sient reflectivity governed by the amplitude of spectral component of strain at the Brillouin frequency) while the time-resolved X-ray diffraction provides an average value of the total strain. One important result is the demonstration that the large QTA signals in the BiFeO₃ single crystal seen by the optical pump-probe method does not come from a large photoinduced shear strain (which actually is about 6 times smaller than the longitudinal strain we measured). Rather, large photoelastic coefficients play an important role in the efficient Brillouin detection of these QTA modes. To determine in the future the full photoelastic tensor, several single crystal orientations would be necessary.

In this part we also discussed the microscopic mechanisms at play in the photoinduced strain processes. At the moment, we show that the thermoelastic stress cannot explain the measured values of the longitudinal strain indicating the possible contribution of non-thermal effects such as the inverse piezoelectric effect, also discussed in the literature by Wen *et al* [42] and Schik *et al* [55]. On the opposite, the thermoelastic process appears to be consistent with the amplitude of the shear strain we measured.

As a final important result, and independently from the microscopic mechanisms at play in the photoinduced strain processes, we have shown that in BiFeO₃ single crystal, a so-called asynchronous effect is evidenced. This gives rise to the appearance of a two-step unit cell distortion, with first an extension of the out-of-plane lattice parameter and with a delay of around 20-30 ps, a development of the shear strain as sketched in **Fig 5.19(b)**. Such original lattice dynamics has only been revealed because we were able to measure both the longitudinal and shear strains.

5.4.2 Study of photoinduced strain in monoclinic BiFeO₃ thin films

5.4.2.1 Preparation of a single domain BiFeO₃ thin film

As illustrated in **Fig 5.22(a)**, a single-domain epitaxial BiFeO₃ thin film was deposited, by pulsed laser deposition (PLD), on a SrRuO₃-coated (110)_c SrTiO₃ substrate, using conditions reported in ref [164, 165]. This growth was realized by Dr. Daniel Sando (Univ New South Wales, Australia). A KrF laser with a wavelength of 248 nm and a frequency of 5 Hz was used for the ablation. The 12 nm layer of SrRuO₃ was produced at 660 °C in 100 mTorr of oxygen with a fluence of about 2 J.cm⁻² from a stoichiometric target. The BiFeO₃ layer was produced on the substrate, which is held at 590 °C in a background oxygen pressure of 100 mTorr using a Bi_{1.1}FeO₃ ceramic target. Extrapolated from the growth rate, the thickness of the BiFeO₃ layer is estimated at 180±10 nm, taken from a sample grown directly beforehand, on which X-ray reflectivity calibration was performed. The microscopic structure of the sample is shown in **Fig 5.22(b)**, within the monoclinic atomic structure frame. Such monoclinic structure, different from the bulk rhombohedral structure, comes from the epitaxial stress briefly presented in **Fig 5.9**. The dark blue arrow indicates both macroscopic polarisation in the entire BiFeO₃ thin film sample, and the microscopic polarization within the monoclinic BiFeO₃ unit cell. The microscopic polarization

is found in plane $(010)_m$.

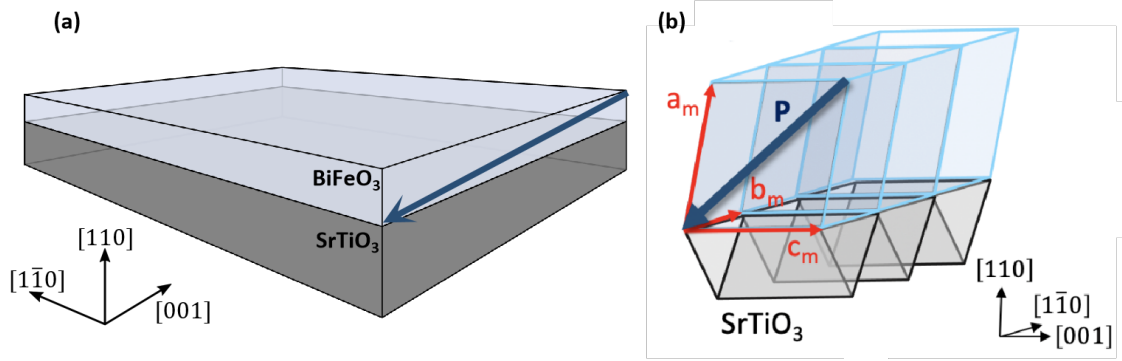


Fig 5.22: Macroscopic (a) and microscopic (b) illustration of single domain monoclinic BiFeO_3 (blue) on SrTiO_3 (110) substrate (grey). The dark blue arrow indicates either the macroscopic polarization (a) or the polarization within a BiFeO_3 monoclinic unit cell (b). The axes are in cubic configuration with a_m , b_m , c_m the monoclinic axis of BiFeO_3 . “m” denotes the notation in the monoclinic frame. An SrRuO_3 (SRO) buffer layer of 8 nm is used for the deposition but it is omitted for clarity.

In our case, in $(110)_c$ oriented BiFeO_3 films, only two ferroelastic variants are possible (i.e., with c_m parallel or antiparallel to $[001]$ SrTiO_3). With respect to **Fig 5.7**, the ferroelectric polarization is allowed to point at four possible ferroelectric directions including P_1^+ , P_1^- , P_3^+ and P_3^- [6, 166].

Characterization of the single domain BiFeO_3 thin film

In order to confirm BiFeO_3 being a “single domain” sample and identify the ferroelectric polarization direction, 2 characterization methods were used: X-ray diffraction (XRD) and piezoresponse force microscopy (PFM). Both these characterizations have been performed by our collaborators Dr. Vincent Garcia and Dr. Stéphane Fusil from UMPy Thales (Univ. Paris Saclay).

The X-ray diffraction is carried out using an X’pert Pro Materials Research Diffractometer (MRD), using $\text{Cu K}\alpha-1$ radiation from a two bounce Ge (220) monochromator ($\lambda = 1.6504 \text{ \AA}$) coupled with 1D detector (PIXcel). And the results are shown in **Fig 5.23**.

The standard $\theta-2\theta$ XRD scan (**Fig 5.23(a)**) shows that the monoclinic thin film of BiFeO_3 is single phase with $(100)_m$ orientation on the (110) SrTiO_3 substrate. With the reciprocal space maps (RSMs) represented in **Fig 5.23(b-e)** near the (220), (221), and (310) SrTiO_3 reflections, the unit cell parameters in monoclinic frame were calculated to be $a_m = 5.662 \text{ \AA}$, $b_m = 5.606 \text{ \AA}$, $c_m = 3.905 \text{ \AA}$, and monoclinic angle $\beta = 89.5^\circ$ by x-ray diffraction (XRD). Fitting 2D Gaussians to the BiFeO_3 peaks in the RSM around the (221) reflection (**Fig 5.23(c)**) yielded the relative domain population of ferroelastic domains. As a result, the film was determined to have a volume fraction of 99.5 %/0.5 %, indicating that it is essentially a single domain.

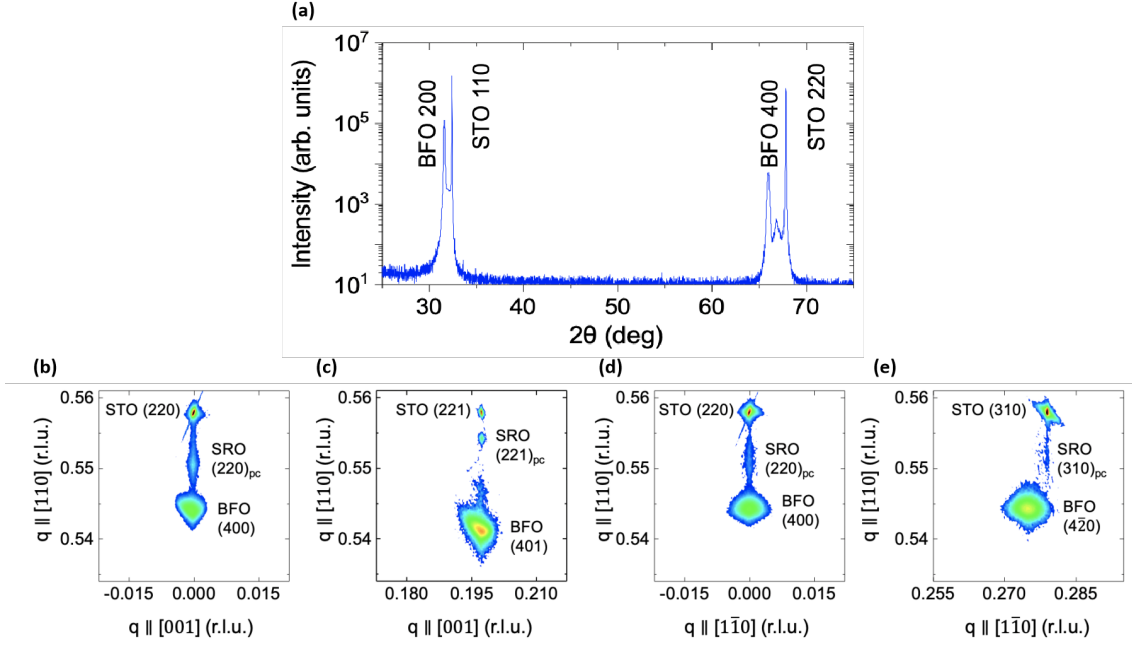


Fig 5.23: X-ray diffraction characterization of the single-domain monoclinic $(100)_m$ BiFeO_3 thin film on (110) SrTiO_3 substrate. (a) $\theta - 2\theta$ x-ray diffraction scan. (b-c) Reciprocal space maps (RSMs) along the $[001]$ direction of SrTiO_3 in the areas of (220) SrTiO_3 (b) and (221) SrTiO_3 . (d-e) RSMs along the $[1\bar{1}0]$ direction of SrTiO_3 in the areas of (220) SrTiO_3 (d) and (310) SrTiO_3 (e).

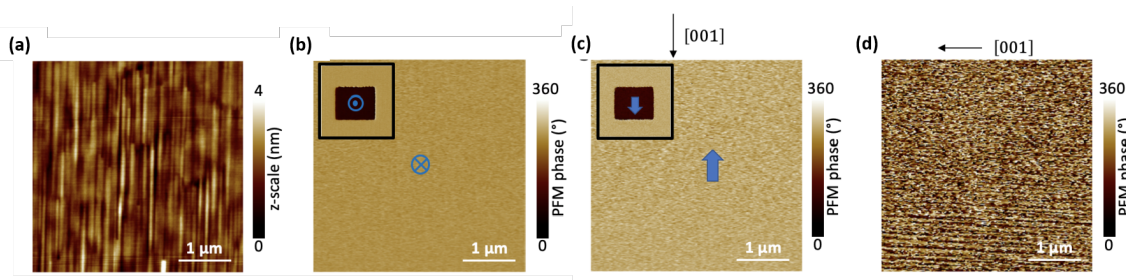


Fig 5.24: Piezoresponse force microscopy (PFM) images revealing the presence of a single ferroelectric domain. The topography (a), the out-of-plane PFM phase (b) and in-plane PFM phase in two different directions (cantilever perpendicular (c) or parallel to (d) $[001]$ SrTiO_3 , respectively) indicate that the polarization is pointing downward with an in-plane component parallel to $[001]$ SrTiO_3 . The insets in (b) and (c) show the 180° switched polarization after applying a DC voltage of 7 V to the bottom electrode.

The single domain nature was then further confirmed with PFM, with the results shown in **Fig 5.24**. The experiments were carried out in a Bruker Nanoscope V multimode, using an external ac source (DS360, Stanford Research) to excite the BiFeO_3 thin film at a frequency of 35 kHz (far off resonance) with typical AC voltage excitations of 2 V peak to peak, and external lock-in amplifiers (SR830, Stanford Research). Cr/Pt coated tips with a cantilever stiffness of 40 N.m^{-1} were used, with two different orientations of the cantilever for the in-plane PFM measurements. The topography image shows uniaxial structures which are oriented parallel to the substrate's c-axis. As shown in **Fig 5.24(b-c)** the homogenous out-of-plane and in-plane PFM phase images show a single domain state with polarization pointing downward and antiparallel to $[001]$ SrTiO_3 . When the sample was rotated by 90° , The absence of in-plane PFM signal confirmed the orientation of such signal domain state, as shown in **Fig 5.24(d)** where undefined in-plane phase is expected if the in-plane polarization component is found parallel to the cantilever. With a DC voltage of +7 V applied between the SrRuO_3 electrode and the PFM tip, while scanning with the slow scan axis along $[001]$, the ferroelectric polarization will be switched by 180° , resulting in another single domain within the same ferroelastic domain, as presented in the insets of **Fig 5.24(b-c)**.

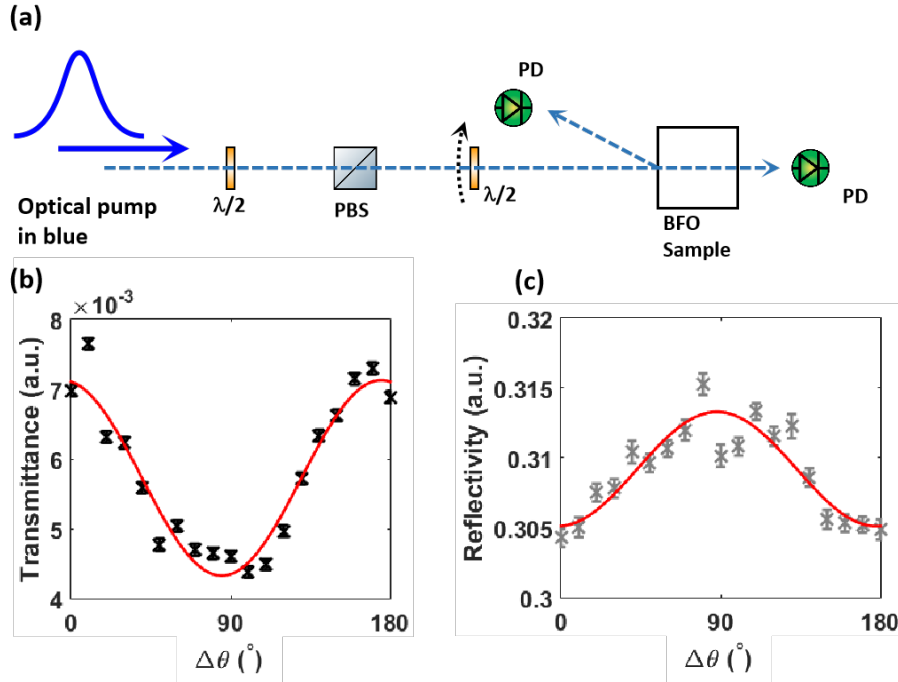


Fig 5.25: (a) Simplified sketch of the setup for the measurement of static transmittance and reflectivity of single domain BiFeO_3 as a function of incident electric field polarization. (b) Static transmittance and (c) reflectivity of single domain BiFeO_3 thin film sample.

Additionally, the birefringence of single domain BiFeO_3 has been verified by optical transmittance and reflectivity measurement with a 410 nm laser, which ensures light absorption in BiFeO_3 . This measurement was conducted at IMMM, Le Mans University. The laser pulses that are sent to illuminate the sample have not been

focused, thus the radiated section has a diameter of around 2 mm, with the sketch shown in **Fig 5.25(a)**. The incident blue laser beam was first sent to a system consisting of a halfwave plate coupled with a polarized beam splitter (PBS). Such system aims to control the incident fluence. Then the incident pump is sent to a second halfwave plate, in order to tune the incident electric field polarization and the birefringence has been checked in both reflection and transmission geometry.

As shown in **Fig 5.25 (b,c)**, both the transmittance and reflectivity has been represented by measuring the transmitted and reflected photon energy with a UV silicon detector (Newport 918D-UV-OD3R [167]), and normalized to the incident photon energy. For the reflectivity, the reflected beam was not perfectly perpendicular to the surface but had an angle of less than 10° which was due to spatial constraint of the setup. The transmittance and the reflectivity have been recorded as a function of incident electric field polarization, $\Delta\theta$. $\Delta\theta$ represents the angle between the incident electric polarization and the in-plane component of ferroelectric polarization in BiFeO_3 , i.e. $\Delta\theta = 0^\circ$ for the light electric field pointing along the c_m axis in **Fig 5.22** while $\Delta\theta = 90^\circ$ for the perpendicular condition. The contribution of SrRuO_3 has been neglected because the thickness of such bottom electrode is much thinner than that of the BiFeO_3 layer. In addition, the SrTiO_3 substrate has a cubic structure thus it is optically isotropic. The clear birefringence confirms the single domain nature of the BiFeO_3 thin film.

5.4.2.2 Study of coherent acoustic phonons in BiFeO_3 by means of ultrafast optical spectroscopy

The ultrafast optical spectroscopy experiments, i.e. optical pump-probe experiments, have been carried out in IMMM laboratory in using 415 nm as pump radiation and 587 nm as probe beam. We remind that for the probe wavelength, there is no excitation of electronic sub system of BiFeO_3 since the photon energy at that probe wavelength is below the band gap E_g of BiFeO_3 . And detailed description of the optical pump-probe setup is given in **Chapter 3**. The pump fluence has been fixed to around $5.2 \mu\text{J}.\text{cm}^{-2}$ and the fluence of the probe radiation is only $5.5 \mu\text{J}.\text{cm}^{-2}$. The pump fluence has been checked to prevent any photo-assisted phase transition in BiFeO_3 , refer to **Chapter B** for details. The incident electric field polarization is normal to the c_m axis of BiFeO_3 , i.e. $\Delta\theta = 90^\circ$ configuration discussed previously (see **Fig 5.25**). No specific dependence of the response of the BiFeO_3 thin film on the pump polarization has been investigated at the moment.

The transient optical reflectivity has been recorded up to 200 ps after the photoexcitation and is shown in **Fig 5.26(a)**. The coherent acoustic phonon (CAP) signal is extracted and amplified by a factor of 9 for the sake of clarity. The CAP signal clearly indicates that at around 35 ps, a drastic change in the amplitude of the transient optical reflectivity has been detected, indicating the photogenerated acoustic phonons arrive onto the BiFeO_3 /substrate interface. It is well known that such effect is usually associated to the arrival of the short acoustic pulse at an interface and affects the phase of the scattered probe beam [168]. Since the LA mode is the largest signal in the Brillouin signal (this will be confirmed later), it is reason-

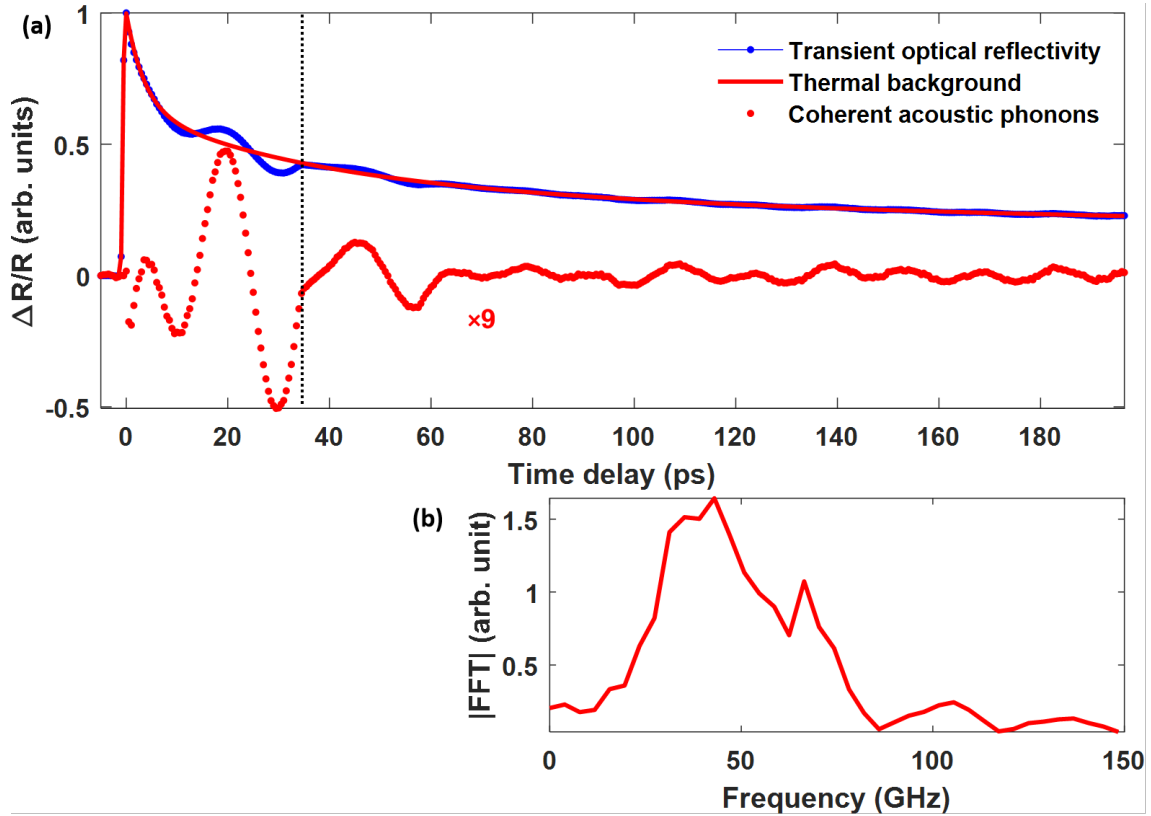


Fig 5.26: (a) Transient optical reflectivity recorded by optical pump-probe experiments on a single domain BiFeO_3 thin film. $\Delta R/R$ signal is shown by connected blue dots, the thermal relaxation by solid red line, the coherent acoustic phonons signal by red dots. A vertical dashed line is added at 35 ps when the transient optical reflectivity suffers a drastic change in magnitude, which indicates that the coherent acoustic phonons arrive on at BiFeO_3 /substrate interface. (b) Fast Fourier transform (FFT) spectrum of the coherent acoustic phonon signal.

able to associate this feature to the arrival the LA mode at the interface. A second change of CAP signal can be observed at around 63 ps with another drop of the Brillouin signal. After 120 ps, the CAP signal contains nearly only one single Brillouin frequency. In between, a mixture of multiple acoustic modes can be observed as revealed by a fast Fourier transform (FFT). The FFT shown in **Fig 5.26(b)**, gives us the Brillouin frequency components. This FFT spectrum is broad indicating the existence of multiple acoustic modes. In order to disentangle these different acoustic modes, a short-time Fourier transform (STFT) process has been employed.

Fig 5.27 illustrates the process of STFT process [169] on top and the associated FFT spectra at the bottom. Mathematically, the Fourier transform can be described by the following function:

$$\text{STFT}\{x(t)\}(\tau, \omega) \equiv X(\tau, \omega) = \int_{-\infty}^{\infty} x(t)w(t - \tau)e^{-i\omega t}dt \quad (5.20)$$

with $x(t)$ the coherent acoustic signal and $w(t)$ the Gaussian window function of which the duration is fixed by $\sigma = 35$ ps. A 2D map can be constructed as a function of temporal delay as well as frequency, which is shown in **Fig 5.28**. For the sake of clarity, the FFT spectrum at each time delay has been normalized by its maximum value. There are three main acoustic modes being identified at around 31, 43 and 67 GHz. We can identify them as the shear (TA) and the longitudinal (LA) acoustic mode in BiFeO₃ for the two first frequencies and as the LA mode in SrTiO₃ substrate for the higher frequency component. With tabulated refractive indices of BiFeO₃ (we have taken the values of the rhombohedral structure since no values exist for the monoclinic structure) and that of SrTiO₃, the corresponding sound velocities have been calculated using equation (2.28), and the results are given in **Table 5.2**.

	f_B (GHz)	V (m.s ⁻¹)	
LA wave	This work	This work	Literature
BFO (Brillouin)	43	4250	~5000 [146]
BFO (Time of flight)	—	5100	—
STO [110] _c	67	8200	8098 [170]
TA wave	This work	This work	Literature
BFO (Brillouin)	31	3000	~2900 [146]

Table 5.2: Results of Brillouin scattering frequencies and correspondent sound velocity extracted by STFT. The results of this work are compared to the reported values from literature.

The results of sound velocity (both LA and TA) in BiFeO₃ determined experimentally are rather consistent with determined values from previous works [146, 148]. However, we note a quite large difference in the estimate to the LA sound velocity

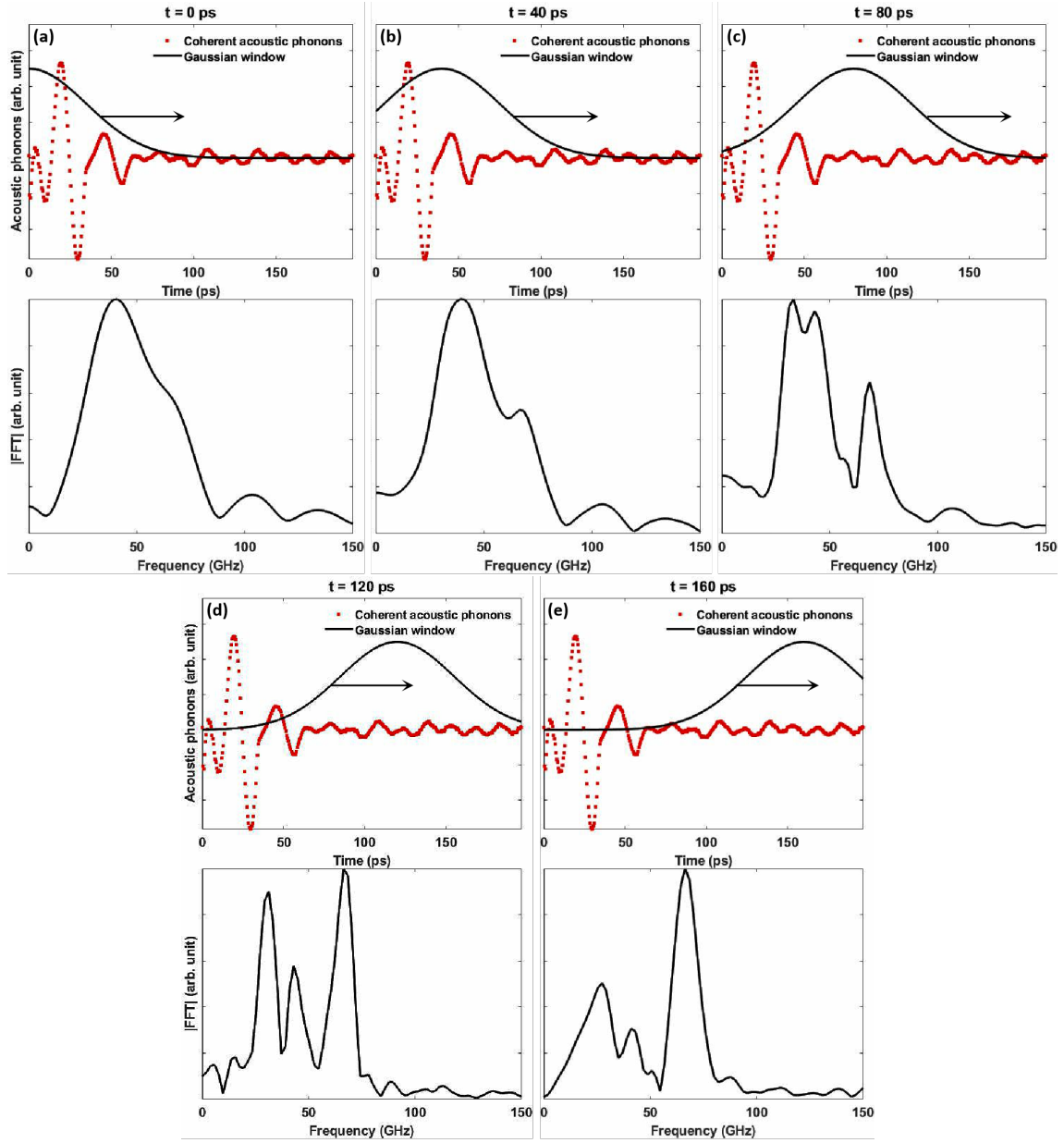


Fig 5.27: Illustration of short-time Fourier transform (STFT) of the coherent acoustic phonon signal in the single domain BiFeO_3 thin film sin using a gaussian window function. (a-e) Temporal signal of $\Delta R/R$ overlaid with Gaussian window (top) and the associated STFT spectra (bottom) of coherent acoustic phonon signal at given temporal position $t=0, 40, 80, 120$ and 160 ps of gaussian window.

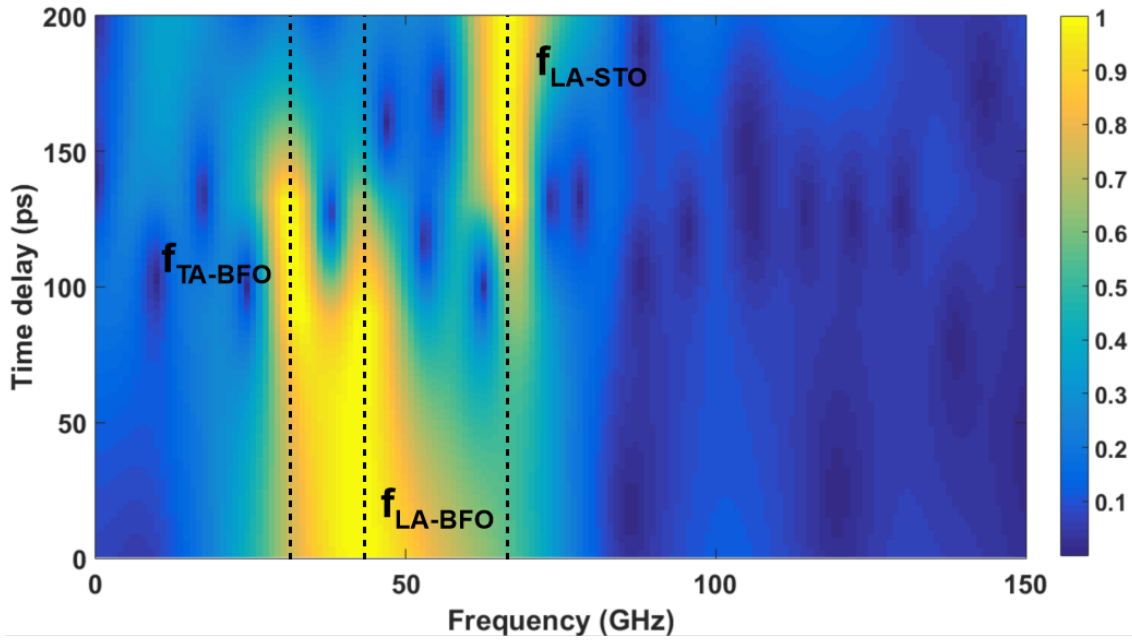


Fig 5.28: 2D mapping of STFT spectra. The frequency components are shown in abscissas and temporal components in ordinates, with normalized FFT magnitude shown in color coding. 3 acoustic modes are identified being longitudinal (LA), shear (TA) mode in BiFeO₃ sample and longitudinal (LA) mode in (110)_c SrTiO₃ substrate.

in BiFeO₃ between the two methods (Brillouin versus time of flight). The time of flight method is based on the fact that at around 35 ps we detect the so-called sharp variation of the Brillouin signal (a kind of discontinuity) discussed previously [168]. In that case $V_{LA} \approx 180 \text{ nm}/35 \text{ ps} \approx 5100 \text{ m.s}^{-1}$. This discrepancy between the two methods could come from the refractive index that we used for rhombohedral (R3c) BiFeO₃ might not be suitable for the monoclinic (*m*) one. The LA waves in SrTiO₃ are clearly detected at the long time scale when the phonons are transmitted into the substrate. This Brillouin mode gives a longitudinal sound velocity of 8200 m.s^{-1} , in agreement with [170].

Analyzing the coherent acoustic phonons dynamics in single domain BiFeO₃ thin film in the frequency domain, our results clearly demonstrate the possibility of generating shear acoustic (TA) motion in a BiFeO₃ thin film structure. This is the first ever demonstration of GHz TA waves generation in BiFeO₃ thin films while all precedent works only reported the generation of LA mode [42, 55, 145, 147]. In the following, we will discuss how we extracted the absolute values of both the longitudinal and shear strains thanks to the time-resolved X-ray diffraction experiments.

5.4.2.3 Study of ultrafast photoinduced strain in single domain BiFeO_3 thin film by means of time-resolved X-ray diffraction

5.4.2.3.1 Characterisation of selected Bragg planes

In section 3.2.4, we have presented the methodology to extract the longitudinal and shear strains in the monoclinic BiFeO_3 thin film. We have briefly explained why the $(403)_m$ Bragg planes family is sensitive to the shear and the $(530)_m$ is not. We develop it a little. As already shown in **Fig 3.16**, when the laser pulse excite the BiFeO_3 thin film, the irradiated surface is the $(110)_c$ or $(100)_m$. The 1D geometry of the experiment implies that the strain pulse plane wave has to fulfill the symmetry of the photo-excited BiFeO_3 layer. In particular, the plane $(010)_m$ (or $(110)_c$) is a symmetry plane. Consequently, there is no reason that, under the light excitation, the atoms displace either on one or the other side of this plane. Said differently, the pure shear strain is forbidden by symmetry principle (similar discussions were made about such pure shear waves for the BiFeO_3 single crystal, see section 5.4.1.4). The shear strain is allowed only in the $(010)_m$ plane (i.e. in the ac plane). Therefore, the interplanar distance of the Bragg plane family $(403)_m$ will undergo a distortion due to both the longitudinal and shear strain, while that of $(503)_m$ family only due to the longitudinal strain. The relations have been presented in equations (3.14) and (3.15) with consideration of the monoclinic angle being 90° in order to simplify the tensorial calculation.

At the thermodynamic equilibrium (without laser excitation), we see the monoclinic distortion by measuring the X-ray diffraction signal since our large Miller indices values provide us a good resolution that we did not have for the single crystal. The interplanar distance of plane $(403)_m$ is calculated as $d_{(403)_m} = 0.966 \text{ \AA}$, and $d_{(40\bar{3})_m} = 0.950 \text{ \AA}$. And the correspondent Bragg angles are $\theta_{(403)_m} = 64.93^\circ$ and $\theta_{(40\bar{3})_m} = 67.17^\circ$ respectively. On the opposite, by symmetry principle, the interplanar distance of both planes $(530)_m$ and $(5\bar{3}0)_m$ are equivalent with $d_{(530)_m} = d_{(5\bar{3}0)_m} = 0.968 \text{ \AA}$ with the same Bragg angle $\theta_{(5\pm 30)_m} = 64.69^\circ$.

In the single crystal BiFeO_3 sample, we only used $(\pm h0l)$ Bragg peaks to extract the longitudinal (L) and shear (T) components of the photoinduced strain tensor. We did not investigate a Bragg plane that was insensitive to light-induced shear strain due to a limited time allocated during the beam time. We think that the conclusions we have drawn for the single crystal remain robust. Here, because of better signal to noise ratio (SNR) and the new “fast” UFXC detector at SOLEIL, we had the opportunity to register more Bragg peaks for the thin films. This strengthens our description of the ultrafast temporal evolution of the BiFeO_3 unit cell in the thin film as demonstrated in the following.

5.4.2.3.2 Time-resolved X-ray patterns

Fig 5.29 shows the results of time-resolved X-ray diffraction experiments for different time delays between the near UV laser pump beam and the X-ray pulse for the family $(40\bar{3})_m$. These measurements are rocking curves, i.e. diffracted X-ray

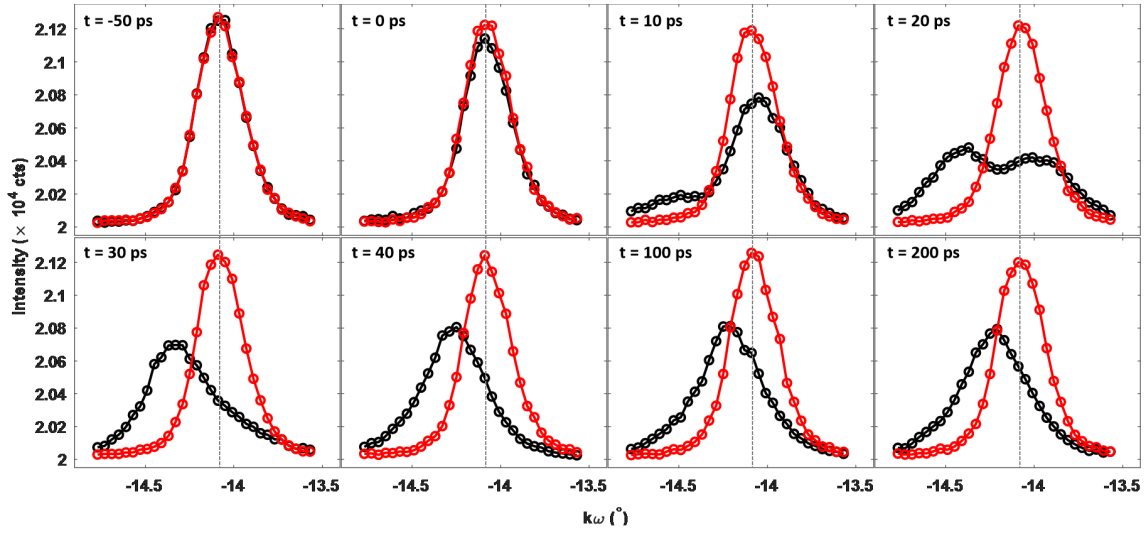


Fig 5.29: Evolution of rocking curves recorded at different time delays for the $(40\bar{3})_m$ Bragg peak with and without laser pump, as shown by black and red markers respectively. The Bragg position without laser pump is indicated by a black dashed vertical line. Only the rocking curves recorded for plane $(40\bar{3})_m$ at several given time delays are presented here for illustration. For all rocking curves recorded for all 4 chosen planes please refer to **Appendix C**.

beam intensity counts as a function of the kw angle. The rocking curves in red represent the XRD of plane $(40\bar{3})_m$ without the laser pulse excitation. The rocking curves in black show the evolution of Bragg peak at different time delays. At $t = -50$ ps, BiFeO_3 is not excited thus the two rocking curves overlap. For $t = 0-200$ ps, we evidence a lattice expansion connected to a negative shift of the kw angle. At short time scale after the photoexcitation, i.e. $0 < t < 30$ ps, a large asymmetric Bragg peak is revealed, as shown by rocking curves in black. Two contributions are observed, as 2 Bragg peaks are revealed. One Bragg peak exhibits a diminution of Bragg angle, which corresponds to an increase of interplanar distance. Another Bragg peak has the counter effect, i.e. a decrease of interplanar distance. This means that within this time window, there exists both a compression and an expansion in the thin film. This effect has already been revealed in GaAs semiconductor by Reis *et al* [171]. The existence of both of these elastic responses of the lattice is fully consistent with the theoretical description of a propagating strain pulse presented in **Fig 2.1 in Chapter 2**. We present the relation between the compressive and tensile contributions by the green and pink arrows in **Fig 5.30**.

Each Bragg peak has been fitted with two Gaussian functions to extract the position of the relevant kw angles. Some examples of these fits are shown in **Fig 5.30**.

A 2D map is then constructed for each plane in order to reveal the evolution of rocking curves as a function of the time delay, and the results are shown in **Fig 5.31**. Different time delays are shown and the variation of the relative Bragg angles (the difference between the Bragg peak with and without optical laser excitation, noted as Δkw) are shown in reverse direction in ordinates, in order to have a coherent representation with the variation of interplanar distance, which will be shown later

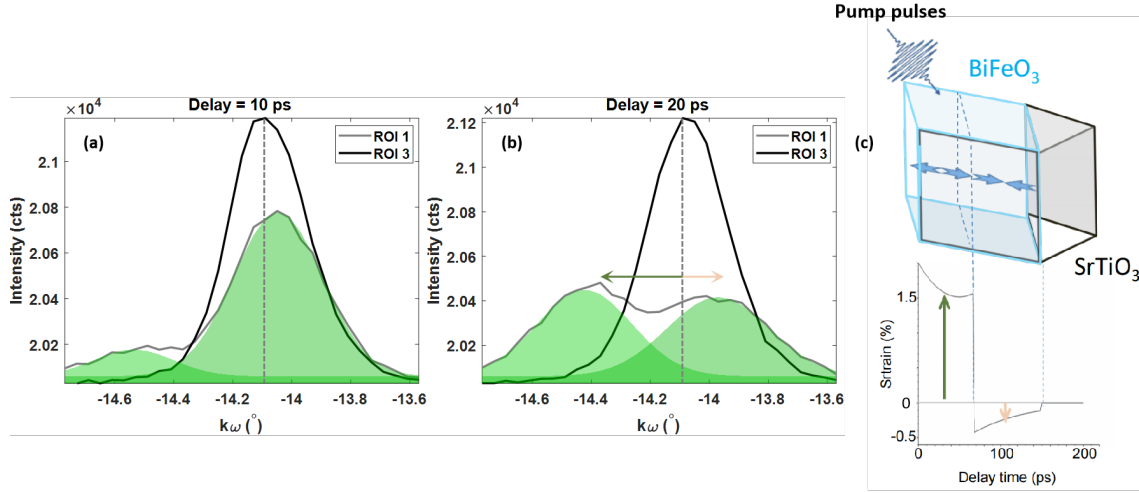


Fig 5.30: Numerical fit of the two Bragg peaks for a time delay of 10 ps (a) and 20 ps (b) for $(40\bar{3})_m$ plane. The Bragg peaks are adjusted with Gaussian curves. The black curve is the Bragg peak for undisturbed BiFeO_3 lattice. (c) Representation of a propagating strain pulse in the BiFeO_3 thin film according to the standard model presented in **Fig 2.1**. The compressive contribution of strain is represented by green arrow, corresponding to the left shift of $k\omega$ angle in (b). While the tensile contribution is shown by pink arrow, corresponding to the right shift of $k\omega$ in (b).

on **Fig 5.32**. The Bragg peak positions are not only shown by the color coding extracted from the full $k\omega$ scans, but their precise values extracted by gaussian fits of the rocking curve are also displayed with the symbol “x”, for the tensile part (negative shift of the Bragg peak in the $k\omega$ scan) and with the symbol “o” for the compressive part (positive shift of the Bragg peak in the $k\omega$ scan).

With the determined shift of the Bragg angle as a function of time delay for each plane (as presented in **Fig 5.31**) and using Bragg’s law, we can deduce the variation of the interplanar distance $\Delta d/d = -\Delta k\omega / \tan(\theta)$. We remind that $\Delta\theta = \Delta k\omega$ (see **Fig 3.11**).

The results are shown in **Fig 5.32**, for $(403)_m$ and $(40\bar{3})_m$ planes in (a); and for $(530)_m$ and $(5\bar{3}0)_m$ planes in (b). For $(403)_m$ and $(40\bar{3})_m$ planes, the tensile (expansion) responses are displayed by black and blue circles respectively; while the compressive response are shown by black and blue triangles. For plane $(530)_m$ and $(5\bar{3}0)_m$, the tensile (expansion) responses are displayed by black and red circles respectively; while the compressive responses are shown by black and red triangles. The maximum of amplitude of photoinduced lattice expansion varies from 4 to 5×10^{-3} . These results take into account the correction of fluence due to the difference of inclination of the $(403)_m$ and $(530)_m$ planes being rotated off the normal of the irradiated surface by an amount of 30° and 46° respectively. To compare the amplitude of $\Delta d/d$ for each Bragg planes family, we need to multiply the interplanar distance variation of the family $(530)_m$ by an amount of $\cos(\theta - 46^\circ) / \cos(\theta - 30^\circ)$, where θ is the Bragg angle and 46° and 30° are the relative angle between the normal of the irradiated surface and that of the normal of $(403)_m$ and $(530)_m$ Bragg planes.

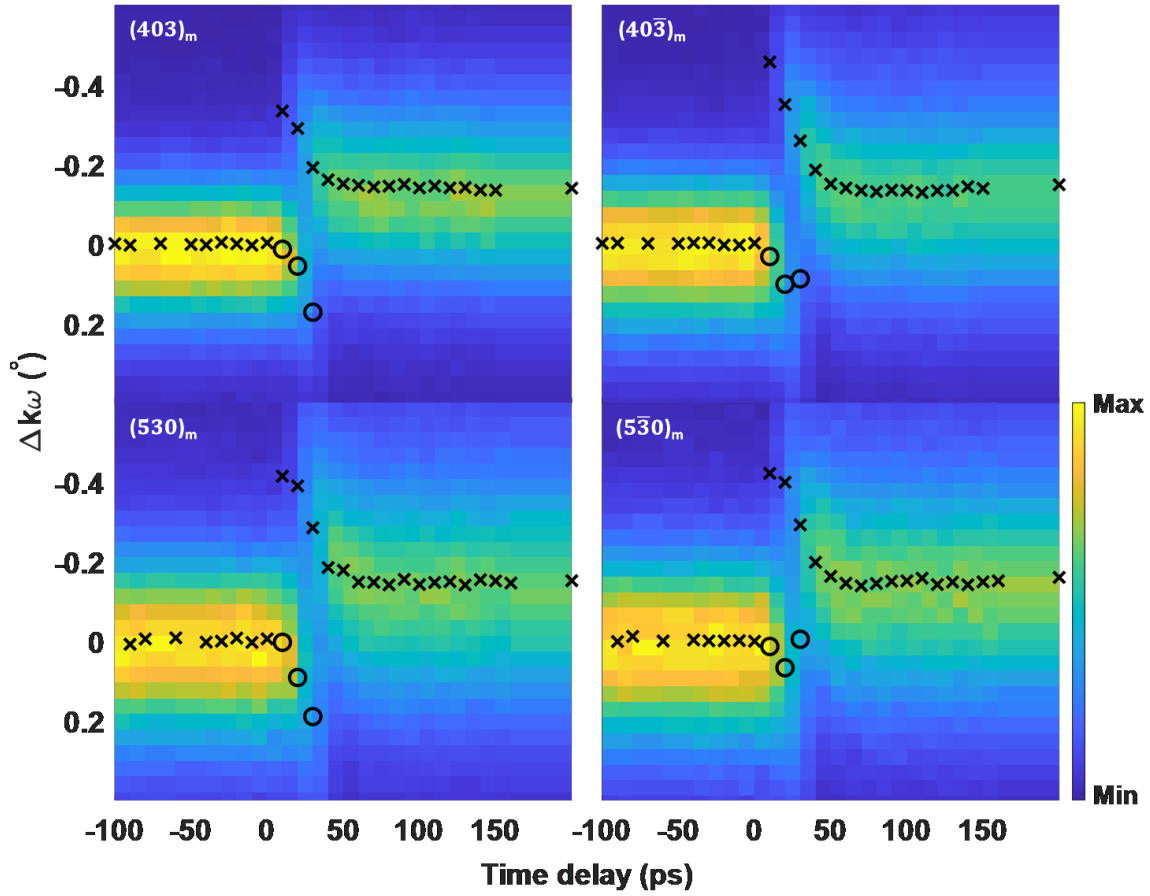


Fig 5.31: Evolution of the rocking curves as a function of time delay for the $(403)_m$, $(40\bar{3})_m$, $(530)_m$ and $(5\bar{3}0)_m$ planes. The time delay is shown in abscissa. The ordinate represent the variation of Bragg angle $\Delta k\omega$ in degree in reverse direction. The decrease of $\Delta k\omega$ and the base line are represented by symbol “x” while the augmentation is indicated by symbol “o”.

Details of this procedure is explained in section 3.2.3 in the **Chapter 3**.

Whatever the plane, the major evolution of the dilatation part is represented by a sharp increase followed by a rapid decay occurring over a typical time of 40 ps and then the strain exhibits a plateau up to the longest time recorded at 200 ps. For the compressive part, we have been able to detect it only during the first 30 ps (nearly same time than the decay of the dilatation part). The magnitude of the compressive part increases during the first 20 ps but we note that at a time delay of 30 ps, a monotonous response is observed. Some possible artifact might have appeared due to the difficulty of fitting this contribution for this time delay. Very interestingly, we can see that the corresponding interplanar distance of planes $(403)_m$ and $(40\bar{3})_m$ follow different behaviors. The inter-atomic distance between planes $(40\bar{3})_m$, endures a more important expansion at a time delay of 10 ps, compared to that of plane $(403)_m$. Furthermore, at a time delay of around 40 ps, there is a crossing point where the interplanar distance of $(403)_m$ becomes then larger than that of the plane $(40\bar{3})_m$ as clearly seen in **Fig 5.32(a)**. This behavior is in deep contrast with the behavior of planes $(530)_m$ and $(5\bar{3}0)_m$. The later two ones have a very similar temporal evolution

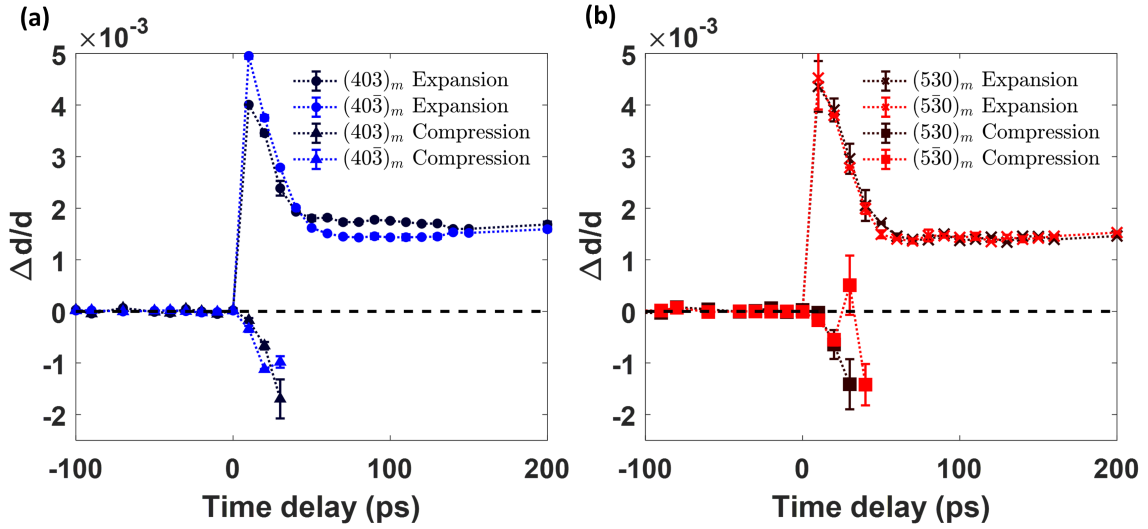


Fig 5.32: (a) Variation of the interplanar distances determined by time-resolved X-ray diffraction of plane $(403)_m/(40\bar{3})_m$. The increase of interplanar distance of plane $(403)_m$, due to the expansion of chosen planes under the photoexcitation of laser pulses are shown by black circles while that of plane $(40\bar{3})_m$ are shown by blue circles. As for the compression which leads to the decrease of interplanar distance of plane $(403)_m$, the results are shown by black triangles, and by blue triangles for plane $(40\bar{3})_m$ respectively. (b) The variation of the interplanar distances plane $(530)_m$ and $(5\bar{3}0)_m$, indicated by black and red crosses respectively for the expansion, while black and red squares for the compression.

for the dilatation part with typically the same maximum amplitude and the same decay time with that long plateau. As for the compressive part, for time-delays of 10 and 20 ps, we see a slight increase of the magnitude and drastic change at the time delay of 30 ps.

First element we can summarize from this analysis is the existence of a different behavior between $(403)_m$ and $(40\bar{3})_m$ which is actually perfectly consistent with our prediction presented in our methodology (see section 3.2.4.2). Our prediction is also supported by the demonstration of a very similar behavior of the interplanar distance variation of the $(530)_m$ and $(5\bar{3}0)_m$ Bragg planes. These ultrafast lattice dynamics perfectly support the existence of ultrafast light-induced shear strain in this single domain BiFeO_3 thin film. In the following section, the photoinduced longitudinal (η_L) and shear (η_T) strain will be disentangled by analysing the specific different behavior of the $(403)_m/(40\bar{3})_m$ Bragg planes.

5.4.2.4 Determination of photoinduced longitudinal (η_L) and shear (η_T) strain in single domain BiFeO₃ thin film

As we have shown in section 3.2.4.2, the macroscopic deformation of BiFeO₃ thin film is described as a linear combination of longitudinal (η_L) and shear (η_T) strains.

Using the general equations (3.14, 3.15) developed in **Chapter 3**, the photoinduced lattice deformation in the monoclinic frame, can be described as follows :

$$\begin{cases} \frac{\Delta d_{40\pm3}}{d_{40\pm3}} = \frac{d_{40\pm3}^* - d_{40\pm3}^0}{d_{40\pm3}^0} = \frac{8\eta_L \mp 6\sqrt{2}\eta_T}{17} \\ \frac{\Delta d_{5\pm30}}{d_{5\pm30}} = \frac{d_{5\pm30}^* - d_{5\pm30}^0}{d_{5\pm30}^0} = \frac{25\eta_L}{34} \end{cases} \quad (5.21)$$

Hence the longitudinal and shear strains can be extracted from the combination of the variations of interplanar distance for planes $(40\bar{3})_m$ and $(403)_m$ with:

$$\begin{cases} \eta_L = \frac{17}{16} \left(\frac{\Delta d_{403}}{d_{403}} + \frac{\Delta d_{40\bar{3}}}{d_{40\bar{3}}} \right) \\ \eta_T = \frac{17}{12\sqrt{2}} \left(\frac{\Delta d_{403}}{d_{403}} - \frac{\Delta d_{40\bar{3}}}{d_{40\bar{3}}} \right) \end{cases} \quad (5.22)$$

The longitudinal strain η_L can also be deduced from the variation of interplanar distance of the $(530)_m$ and $(5\bar{3}0)$ Bragg planes with:

$$\eta_L = \frac{34}{25} \left(\frac{\Delta d_{5\pm30}}{d_{5\pm30}} \right) \quad (5.23)$$

The deduced photoinduced strains are shown in **Fig 5.33**. These longitudinal and shear strains extracted from the tensile (expansion) response are shown in **Fig 5.33(a,b)** and that from the compressive response in **Fig 5.33(c,d)**.

For the $(5\pm30)_m$ planes, only the photoinduced longitudinal strain can be determined following our model. In **Fig 5.33(b, d)** we show a mean value of η_L deduced with equation (5.23), with $\eta_L = (\eta_L(530) + \eta_L(5\bar{3}0))/2$. We also show the difference, $\epsilon_{530} - \epsilon_{5\bar{3}0}$ (with $\epsilon_{5\pm30} = \frac{\Delta d_{5\pm30}}{d_{5\pm30}}$). We see that this difference, for the tensile (expansion) response, is nearly zero within the error bar. This behavior is consistent with the fact that the interplanar distance of $(5\pm30)_m$ Bragg planes is insensitive to the shear strain. For the compressive response measured for the $(5\pm30)_m$ family planes, the data are more “noisy” and the values are not really centered around the expected zero value. Considering the difficulty for extracting the compressive component in particular for time delay of 20 and 30 ps, it is difficult to conclude.

Regarding the strains extracted from the study of $(40\pm3)_m$ Bragg planes, we see that the deduced longitudinal component is in agreement (for the tensile part) with that found with $(5\pm30)_m$ Bragg planes. This indicates that the model works

well. And the predicted light-induced strain in the monoclinic BiFeO_3 is relevant. Furthermore, we observe that the longitudinal strain extracted from the compressive response of the $(40\pm3)_m$ Bragg planes, is negative and increases monotonously up to 30 ps. The fact that it is negative is simply a consequence of the change of sign of the interplanar distance variation $\frac{\Delta d_{40\pm3}}{d_{40\pm3}}$ (tensile versus compressive effect) in equation (5.22).

The behavior of the shear strain is strikingly different than that of the longitudinal one. The shear strain reaches its maximum at nearly the same time (≈ 10 ps) as that of the longitudinal strain. The shear strain changes its sign at around 50 ps while the longitudinal one only shows a positive value. This shear strain remains with a positive value in the range (50-120 ps) and nearly vanishes after 150 ps. In the inset of **Fig 5.33(a, c)**, we present a comparison of the shear strain deduced from the tensile and compressive responses. Within the first 20 ps, there is an opposite sign as expected. At 30 ps the deduced shear strain does not exhibit the same behavior. This discrepancy might be due to the difficulty to fit correctly the Bragg peak associated to the compressive part as we have already mentioned. As we will discuss later on, this compressive tail is rapidly transmitted into the substrate, to our point view, which limits the analysis to a couple of points.

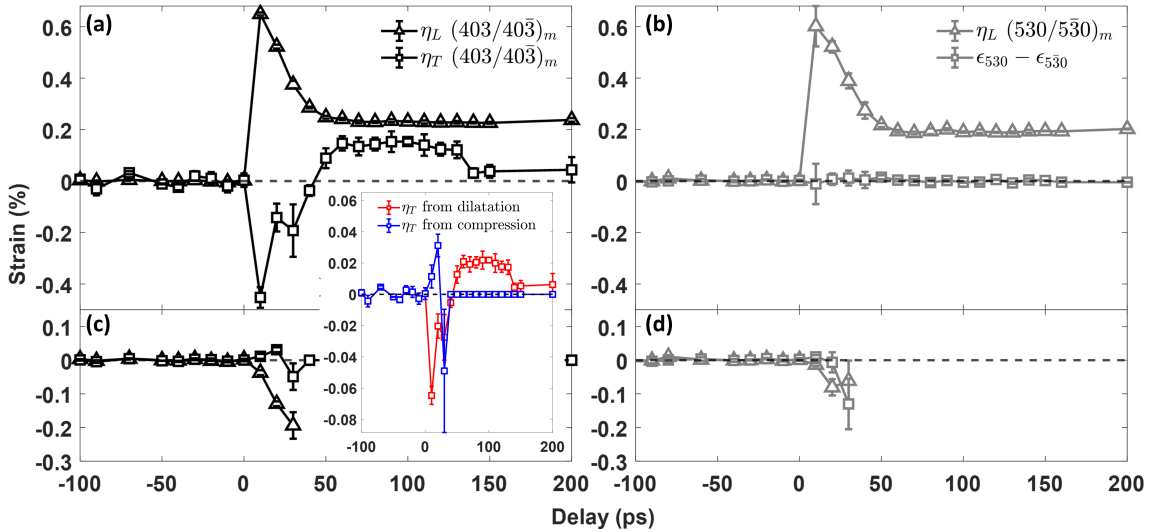


Fig 5.33: Longitudinal and shear photoinduced strains determined from the tensile (a) and compressive (c) responses of the Bragg planes $(40\pm3)_m$. For the sake of clarity, the shear strain $\eta_T(40\pm3)_m$ is multiplied by a factor of 7 in (a). In the inset (a-c), a comparison of the deduced shear strain from the compressive and expansive response of $(40\pm3)_m$ is also given. (b, d) The longitudinal strain is also deduced from the tensile response of the Bragg planes $(5\pm30)_m$. The difference between the interplanar distance variation of plane $(530)_m$ and that of plane $(\bar{5}30)_m$, i.e. $\epsilon_{530} - \epsilon_{\bar{5}30}$, is also shown in (b). The latter one is estimated from for the tensile response in (b) and from the compressive response in (d).

5.4.2.5 Summary of results obtained by optical pump-probe and time-resolved X-ray diffraction experiments

In this section I will summarize the results obtained by time-resolved X-ray diffraction, we will interpret them in terms of unit cell deformation and we will compare these latter results with those obtained by optical pump-probe experiments.

In **Fig 5.33** we have shown that the longitudinal strain for the tensile part is always positive from 0 to 200 ps. This means that there is an expansion of the out-of-plane lattice parameter. On the opposite, the shear strain changes its sign at ~ 50 ps. This means that the atoms have an in-plane motion with successive right and left directions. There is actually a reduction of the monoclinicity of the BiFeO_3 primitive cell with atom motion along $-\vec{c}_m$ for $t < 50$ ps, which means the monoclinic angle β increases towards 90° . For $t > 40$ ps, the in-plane atoms motion become along $+\vec{c}_m$ with a slight increase of the monoclinicity (**Fig 5.34**). Since we measure both $(403)_m$ and $(40\bar{3})_m$ Bragg planes, we have the opportunity to be sure that the monoclinicity is actually first reduced during the first tens of picoseconds. At thermodynamic equilibrium, we have indeed measured a larger Bragg angle for the plane $(40\bar{3})_m$ than for $(403)_m$ consistently with the monoclinic structure. This means that $d_{40\bar{3}} < d_{403}$ with $d_{40\bar{3}} = 0.9540 \text{ \AA}$ and $d_{403} = 0.9623 \text{ \AA}$. Since $\frac{\Delta d_{40\bar{3}}}{d_{40\bar{3}}} > \frac{\Delta d_{403}}{d_{403}}$ at a time-delays of $t < 40$ ps, it necessarily implies that the monoclinic angle is reduced at this time delay.

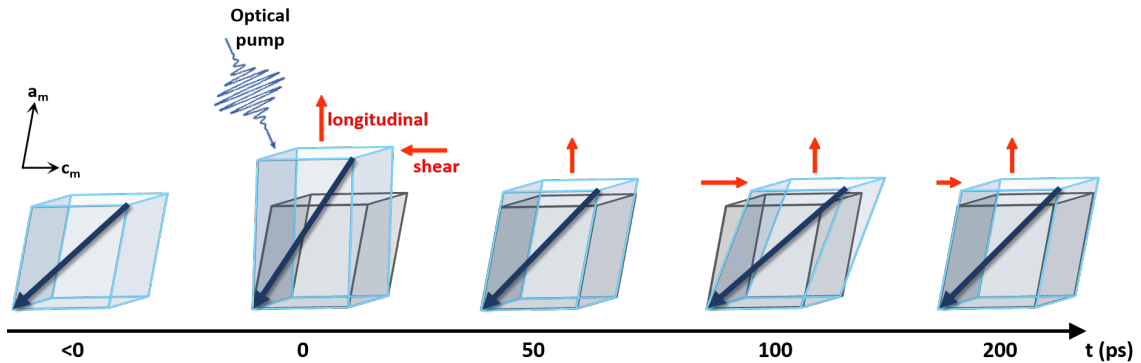


Fig 5.34: Sketch of the light-induced distortion of the monoclinic unit cell of the single domain BiFeO_3 thin film.

Let us now compare the dynamics of the longitudinal and shear strains, deduced from these time-resolved X-ray diffraction experiments, with Brillouin signals obtained with the optical pump-probe method. As we will show, we obtain a consistent description providing a good understanding of the ultrafast light-induced dynamics in this single domain BiFeO_3 thin film.

Fig 5.35 shows a comparison of time dependent acoustic strain response, acoustic phonon response and the fast Fourier transform spectra revealing the Brillouin components. The larger longitudinal strain amplitude (η_L in **Fig 5.35(a)**) measured by X-ray is observed in the time range where we detect the larger LA mode Brillouin signal (**Fig 5.35(b)**) which makes the comparison consistent. The first vertical line l_1 , first guide for eyes, is at a time delay of 35 ps where we estimate the arrival of

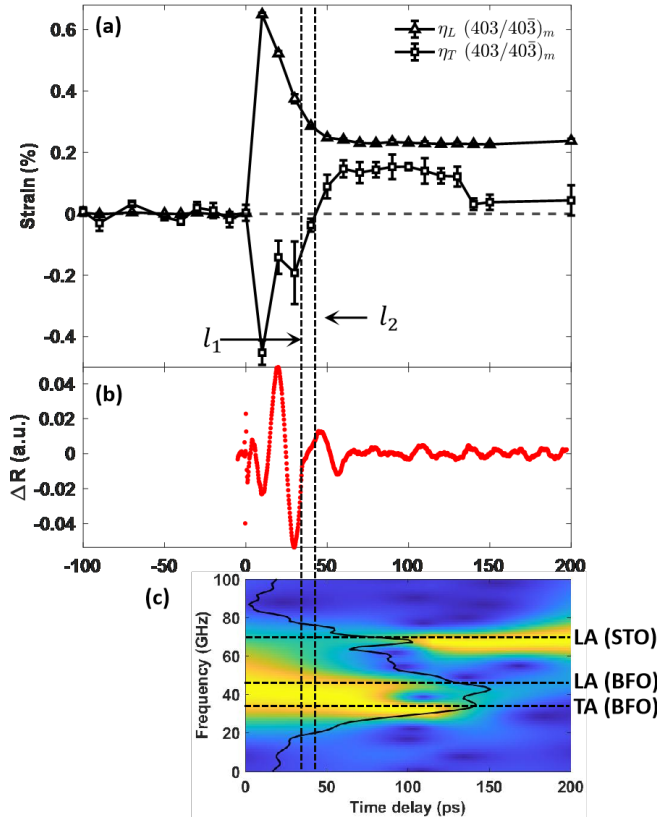


Fig 5.35: Comparison of (a) the time dependent photoinduced strain response with (b) the time-resolved Brillouin signal in the single domain BiFeO_3 thin film. (c) STFT spectra overlapped with conventional FFT spectrum (see text for details). l_1 is added to the estimated temporal position (~ 35 ps) of the arrival of the longitudinal wave at the film/substrate interface. l_2 indicates the time when the experimentally measured shear strain (η_T) changes its sign.

the LA mode at the interface (see discussion in part 5.4.2.2 and see dashed vertical line in **Fig 5.26**). This time of ~ 35 ps matches quite well with the rapid drop of the longitudinal strain η_L . As for η_T , we measure it up to around 120-130 ps in good agreement with the time window where the FFT reveals the TA Brillouin mode (see **Fig 5.35(c)**). The second guide for eyes (vertical line l_2) is added at a time delay of ~ 45 ps when shear strain changes its sign. The fact that the shear strain for instance changes its sign is in deep contrast with previous observations in BiFeO_3 single crystal where such sign change does not exist (see **Fig 5.19**). The thin film is by definition not a semi-infinite system thus it actually confines the acoustic phonons. After the phonons have propagated in the BiFeO_3 film (180 nm), they reach the interface where an acoustic reflection can occur and they propagate back to the surface. We have a kind of mechanical resonator. Within this picture, the change of sign would then correspond to the arrival of the shear strain at the interface where the strain undergoes a reflection/transmission process. If we consider that the shear waves have a time of flight of 45 ps, this gives $V_{TA} \sim 4000$ m/s which is an over estimation compared to the value found by analysing the Brillouin signal (see **Table 5.2**). We need to be careful with the arrival time estimated from X-ray diffraction first because we only have 10 ps time resolution. Secondly, since the Bragg peak (either the tensile or the compressive tail) is constructed on the response of an assembly of unit cells submitted to a “non-local” propagating strain field, we have an “average” view. We have to remember that, in the simplest situation, the typical spatial in-depth extension of the strain typically scales with the double of the pump beam skin depth, i.e. around 80 – 120 nm (see **Fig 2.1** and section 3.2.4 for the estimate of the skin depth). So it is not straightforward to estimate the time

of flight of phonons according to this situation. Moreover, we note that since the TA signal amplitude in the Brillouin measurement (see section 5.4.2.2) is much smaller than that of the LA mode, it was not possible, to our point of view, to reveal the same “anomaly” (sometimes referred as Brillouin phase jump) as we observed for the LA mode at 35 ps in **Fig 5.35(b)**.

If the sign change of the shear strain is an indication of the arrival to the interface, we have to underline that such anomaly is not reported for the longitudinal strain. The time-resolved X-ray diffraction do not reveal an oscillating behavior of the η_L as it was slightly observed in rhombohedral BiFeO₃ thin films [55]. This oscillating behavior reported in [55] is actually due to the acoustic reflection and the mechanical resonator effect played by the thin film (ringing-like of the film).

If our analysis is correct, our results would indicate that there is a kind of good acoustic matching between the longitudinal impedance of the BiFeO₃ film and the substrate. On the opposite, there would be a mismatch for the shear strain. To go further in this direction, a calculation of the acoustic reflection has been done. To do so, we use the following established expression of the acoustic reflection coefficient for the strain:

$$R_{12} = \frac{Z_2 - Z_1}{Z_2 + Z_1} \quad (5.24)$$

with Z_1 the acoustic impedance of incident medium and Z_2 the acoustic impedance of the reflecting medium. In our case, 2 interfaces are considered, BFO/SRO and BFO/STO (when neglecting the 8 nm thick SRO layer). We remind that $Z = \rho \times V$, where ρ is the volumetric density and V the acoustic velocity.

The numerical values of the mass density ρ , longitudinal sound velocity V_L , shear sound velocity V_T and acoustic impedance Z are given in **Table 5.3** for BiFeO₃, SrRuO₃ and SrTiO₃. The calculated acoustic reflection coefficients for the LA and TA waves are given in **Table 5.4**.

	BiFeO ₃	SrRuO ₃	SrTiO ₃
ρ (kg.m ³)	8220	6490	4810
V_L (m.s ⁻¹)	4250 ^a	6312 [172]	8200 ^a
	5100 ^b		
V_T (m.s ⁻¹)	3000 ^a	3083 [172]	4586 ~ 4918 [170]
	4000 ^b		
Z_L (P.s.m ⁻¹)	3.49×10^7 ^a	4.07×10^7	3.94×10^7
	4.19×10^7 ^b		
Z_T (P.s.m ⁻¹)	2.47×10^7 ^a	2×10^7	$2.2 \sim 2.36 \times 10^7$
	3.29×10^7 ^b		

^a: Calculated from the Brillouin scattering spectrum.

^b: Calculated from the propagation time.

Table 5.3: Numerical values of volumetric mass density ρ , longitudinal sound velocity V_L , shear sound velocity V_T and correspondent acoustic impedance Z of BiFeO₃, SrRuO₃ and SrTiO₃.

Interface	R_L	R_T
$\text{BiFeO}_3/\text{SrRuO}_3$	0.076 ^a	-0.11 ^a
	-0.014 ^b	-0.24 ^b
$\text{BiFeO}_3/\text{SrTiO}_3$	0.06 ^a	-0.06 \sim -0.02 ^a
	-0.03 ^b	-0.2 \sim -0.16 ^b

^a: Calculated from the Brillouin scattering spectrum.

^b: Calculated from the propagation time

Table 5.4: Calculated longitudinal R_L and shear R_T acoustic reflection coefficients for interfaces $\text{BiFeO}_3/\text{SrRuO}_3$ and $\text{BiFeO}_3/\text{SrTiO}_3$

We see that the reflection of the shear wave (R_T) at the first interface $\text{BiFeO}_3/\text{SrTiO}_3$ is much larger than that of the longitudinal wave (R_L). The small R_L coefficient (less than 10 %) is consistent with our observation of the absence of “echo” in the temporal evolution of the longitudinal strain presented in **Fig 5.35**. Our calculations also show that R_T is negative which is also consistent with the change of sign of the shear strain signal in **Fig 5.35**. If we neglect the effect of SRO (the SRO electrode layer of only 8 nm in thickness is much thinner than the characteristic wavelength of coherent phonons (LA, TA) estimated at 100 nm, at these Brillouin frequencies), we can see that the reflection coefficient for the LA waves remains small and this is still consistent with our observations. On the opposite, depending on the set of selected data for the sound velocity (a versus b data), the reflection coefficient of the shear waves varies quite a lot but remains negative. But as an overall summary, these estimates give the good tendency.

In order to be more quantitative in the future, we should solve the complete problem of waves propagation in the BiFeO_3 thin with the thin layer (8 nm) of SrRuO_3 . This will be done with standard methods in the future. As a last comment, we would like to stress on the fact that at the moment we did not develop a model of waves equation considering the real elastic anisotropy of the monoclinic BiFeO_3 , as we have done for the single crystal (see section 5.4.1.4). This will add a complexity in this problem since we will have to consider the fact that acoustic mode conversions at the interface (LA to TA and TA to LA) should be taken into account in principle as well [149]. This work is planned for the future.

This perspective of a refined model does not of course change the main message of these interesting observations that are extracted from the combined optical and X-ray measurements as summarized in **Fig 5.34**.

5.4.2.6 Conclusion on the ultrafast light-induced phonons and strain dynamics in a single domain BiFeO₃ thin film

In this section, the single domain (100)_m BiFeO₃ thin film grown on STO has been investigated by means of ultrafast optical transient reflectivity and time-resolved X-ray diffraction. The combination of these two techniques reveals for the first time that both longitudinal and shear acoustic strain can be photo-generated and detected in the BiFeO₃ thin film. With time-resolved optical measurements, multiple acoustic modes have been detected by the conventional time-resolved Brillouin signal: three modes are identified with the correspondent Brillouin frequencies of 43 GHz for LA mode, 31 GHz for TA mode in BiFeO₃ and 67 GHz for LA mode in SrTiO₃.

The observation of photoexcitation of GHz transverse acoustic phonons in a BiFeO₃ thin film has never been reported before in the literature. Our results yield the possibility of controlling both the out-of-plane and in-plane atomic motions with ultrashort light pulses. Time-resolved X-ray diffraction has enabled to estimate the amplitude of the strain. We observe a longitudinal strain which is around 6 times larger than the shear strain in magnitude.

All these experiments strongly support the scenario of a light-induced ultrafast rotation of the ferroelectric direction. This rotation is actually triggered by the light-induced in-plane atomic motion (shear strain) that has always been neglected in previous works carried on ferroelectric thin films [42, 55, 145, 147]. We show in this work and with our methodology that it is possible to have a deeper view of ultrafast lattice dynamics by solving the complete evolution of the unit cell at the picosecond time scale.

5.5 Conclusion

In this chapter, both the ultrafast acoustic phonons and strain dynamics in bulk and thin film BiFeO₃ samples are investigated. We have demonstrated that our methodology for extracting light-induced longitudinal and shear strains works. The Brillouin component (i.e. the modulation of the transient reflectivity governed by the amplitude of the spectrum component of strain at the Brillouin frequency) is provided by the full optical pump-probe method used to study this BiFeO₃ single crystal, whereas the time-resolved X-ray diffraction provides an average value of the total strain.

In the case of a (001)_c BiFeO₃ single crystal, coherent acoustic shear phonons can be observed using appropriate crystallographic orientations. With time-resolved X-ray diffraction, the photoinduced longitudinal and shear stresses in a BiFeO₃ single crystal have been quantitatively determined at the picosecond time scale. A complete model of wave propagation in an anisotropy medium has been developed. The interplay of the propagating quasi-longitudinal and quasi-transverse modes on the measured strains in the unit cell is highlighted by our theoretical modeling, which is in agreement with the experimental data. Under photoexcitation, the

unit cell of the BiFeO₃ begins to expand in the first tens of picoseconds and then a shear deformation begins to appear after roughly 20 ps. We have called this phenomenon an asynchronous response of the lattice that is well explained with the lattice dynamic model.

In the case of a (100)_m BiFeO₃ thin film sample, it is the first time that the in-plane shear motion has been measured in a thin film sample and the first time that ultrafast photoexcitation of shear coherent phonons at tens of GHz is demonstrated.

The combination of time-resolved X-ray diffraction and optical pump-probe studies reveals the entire strain dynamics of a single domain BiFeO₃ thin film at the picosecond time scale. These results support the picture of a light-induced ultrafast ferroelectric direction rotation.

Considering the recent advances in the epitaxial growth of ferroelectrics [140, 173–176] with plethora of ferroelectric textures available (mosaic, self-organized periodic ferroelectric landscapes, different polarization orientations), our results pave the way for exploring rich lattice dynamics in these more “exotic” ferroelectric systems. Among exciting perspectives, we can envision to induce ultrafast symmetry changes to trigger new transient phases, and to generate ultrashort current pulses if the internal ferroelectric polarization is modified. Finally, in the quest for the ultrafast manipulation of the charge and magnetic orders in BiFeO₃, future works will have to take into account the dynamics of the unit-cell strain to account for comprehensive (inverse)piezoelectric and/or (inverse)magnetostrictive effects at the picosecond time scale.

Our findings demonstrate that time-resolved X-ray diffraction is a suitable tool for extracting the temporal evolution of both in-plane and out-of-plane lattice deformations within a material where an in-plane symmetry breaking is present.

Chapter 6

Conclusions and perspectives

In this thesis, we have studied the photoinduced strain process in GeTe and BiFeO₃. Both materials are functional materials and have a central role in phase change material (PCM) family for the first one and in the multiferroic family for the second one. Understanding the interaction of an ultrashort light pulse with these materials is one of the first steps to envision the control at short time scale of some of their properties. The short time scale means potentially the high frequency regime (GHz-THz). Different state-of-the-art techniques have been employed and developed to carry on these investigations. Time-resolved optical spectroscopy (pump-probe method) was systematically employed to generate and to detect GHz coherent acoustic phonons. For BiFeO₃, time-resolved X-ray diffraction was also combined with these optical methods.

The coherent acoustic phonon dynamics have been investigated in detail in both amorphous a-GeTe and rhombohedral α -GeTe samples. Optical pump-probe experiments have been conducted at room temperature but also as a function of the temperature to study the phase transformation from the amorphous to the crystalline state. We have clearly revealed for the first time to our knowledge how the spectrum of photoinduced coherent acoustic phonons depends on the crystalline state of GeTe. With the analysis of the the photoinduced strain profile in amorphous a-GeTe, I have shown that this state exhibits a rather standard response in a sense that the photoinduced strain is controlled by the optical penetration depth of the pump radiation. This means that the photoexcited carriers remain localized within the photoexcited volume, implying that photoexcited carriers release their energy to the lattice within the light absorption region. Surprisingly, we report a non-standard response for the crystalline α -GeTe phase. We show that the light-induced strain takes place much deeper (beneath the irradiated surface) than the pump penetration depth. A factor of around 7 is found. Said differently, the photoinduced strain is not restricted to the volume of light absorption. This phenomenon can be attributed to supersonic diffusion of photoexcited carriers and support the existence of a fast non-thermal transport of energy within the first tens of picoseconds after optical excitation. These results show that the energy transport is faster than expected if heat transfer processes were only responsible. This finding supports some suggestions of the literature regarding the electronic contribution to the strain generation. Our measurements provide a strong support for this scenario. Our findings could have consequences for the development of sub-THz or THz switching technologies, particularly for ultrafast optical processes in PCM-based technologies. One perspective of this work would be to test the alloy (GeSbTe), called GST, which is the most used alloy in PCM applications. In that case, it would be important to test if such ultrafast hot carrier diffusion is also at play in this system. Employing time-resolved X-ray diffraction to fully reconstruct the light-induced strain would also be interesting. Such time-resolved X-ray diffraction has already been conducted with PCM, but each time only for very thin films. To really investigate such rapid carrier diffusion, time-resolved X-ray diffraction should be performed with a thick sample as we studied, i.e. to prevent the confinement of carriers and to let them freely diffusing.

BiFeO₃ has been the most investigated multiferroic materials in the last decades

for its ferroelectric and magnetic properties. BiFeO_3 is also a very nice candidate for ultrafast photostriction as it was already shown in the group at IMMM for the last ten years. In this PhD, the novelty has concerned two parts. First of all, we have been able to generate and detect with optical time-resolved techniques both the longitudinal and shear acoustic phonons in a $(001)_c$ single crystal having a nearly single ferroelectric domain. We also succeeded in photogenerating and photodetecting GHz shear acoustic phonons in BFO thin films (single domain monoclinic $(100)_m$ BiFeO_3). This has never been reported before in the literature dealing with BFO thin films. The second achievement of this study is the development of an original time-resolved X-ray diffraction methodology based on the study of asymmetric Bragg reflections (for instance $\pm h0l$), to quantitatively measure both the longitudinal and shear strains. This approach has been successfully applied to the rhombohedral BiFeO_3 single crystal as well as to the single domain monoclinic BFO thin film. This original measurement enables to understand in details how the crystallographic unit cell evolves at the picosecond time scale after a short laser pulse excitation. Among important observations, we report an ultrafast rotation of the ferroelectric polarization in the BiFeO_3 thin film. This effect is explained as a consequence of the light-induced shear motion that has never been measured before and that has been always neglected in the literature so far. Our findings and methodology applied to model systems (single crystal and single domain thin film) open some exciting perspectives for the investigation of the light-induced lattice dynamics in more “exotic” BiFeO_3 thin films with variable polar landscape as well as different domain organizations. The knowledge of the ultrafast lattice dynamics we provide will be useful to investigate in such nanostructures, the dynamics of the order degrees of freedom such as the polar and magnetic responses. These proposed investigations might help us in better understanding the microscopic mechanisms (thermoelasticity, piezoelectricity, deformation potential, magnetostriction) at play in the ultrafast photoinduced phenomena in BiFeO_3 and related compounds.

Bibliography

- [1] C. Chen and Z. Yi, “Photostrictive Effect: Characterization Techniques, Materials, and Applications”, *Advanced Functional Materials*, vol. 31, no. 22, p. 2010706, 2021. DOI: <https://doi.org/10.1002/adfm.202010706>.
- [2] B. Kundys, “Photostrictive materials”, *Applied Physics Reviews*, vol. 2, no. 1, p. 011301, 2015. DOI: 10.1063/1.4905505.
- [3] S. Raoux, W. Welnic, and D. Ielminin, “Phase Change Materials and Their Application to Nonvolatile Memories”, *Chemical Reviews*, vol. 110, no. 1, pp. 240–267, 2010. DOI: 10.1021/cr900040x.
- [4] L. Wang, W. Gao, L. Yu, J.-Z. Wu, and B.-S. Xiong, “Multiple-matrix vector multiplication with crossbar phase-change memory”, *Applied Physics Express*, vol. 12, no. 10, p. 105002, Sep. 2019. DOI: 10.7567/1882-0786/ab4002.
- [5] X. Li *et al.*, “On-chip Phase Change Optical Matrix Multiplication Core”, in *2020 IEEE International Electron Devices Meeting (IEDM)*, 2020, pp. 7.5.1–7.5.4. DOI: 10.1109/IEDM13553.2020.9372052.
- [6] D. Sando, A. Barthélémy, and M. Bibes, “BiFeO₃ epitaxial thin films and devices: past, present and future”, *Journal of Physics: Condensed Matter*, vol. 26, no. 47, p. 473201, 2014. DOI: 10.1088/0953-8984/26/47/473201.
- [7] I. Tatsuzaki, K. Itoh, S. Ueda, and Y. Shindo, “Strain Along *c* Axis of SbSI Caused by Illumination in dc Electric Field”, *Phys. Rev. Lett.*, vol. 17, pp. 198–200, 4 Jul. 1966. DOI: 10.1103/PhysRevLett.17.198.
- [8] V. M. Fridkin, I. I. Groshik, V. A. Lakhovizkaya, M. P. Mikhailov, and V. N. Nosov, “CURRENT SATURATION AND PHOTO FERROELECTRIC EFFECT IN SbSI”, *Applied Physics Letters*, vol. 10, no. 12, pp. 354–356, 1967. DOI: 10.1063/1.1728210.
- [9] P. S. Brody, “Optomechanical bimorph actuator”, *Ferroelectrics*, vol. 50, no. 1, pp. 27–32, 1983. DOI: 10.1080/00150198308014428.
- [10] G. VAN DER VEEN and W. PRINS, “Photomechanical Energy Conversion in a Polymer Membrane”, *Nature Physical Science*, vol. 230, no. 11, pp. 70–72, Mar. 1971, ISSN: 2058-1106. DOI: 10.1038/physci230070a0.
- [11] J. Lagowski and H. C. Gatos, “Photomechanical Effect in Noncentrosymmetric Semiconductors-CdS”, *Applied Physics Letters*, vol. 20, no. 1, pp. 14–16, 1972. DOI: 10.1063/1.1653958.

- [12] J. Łagowski and H. C. Gatos, “Photomechanical vibration of thin crystals of polar semiconductors”, *Surface Science*, vol. 45, no. 2, pp. 353–370, 1974, ISSN: 0039-6028. DOI: 10.1016/0039-6028(74)90175-7.
- [13] W. B. Gauster and D. H. Habing, “Electronic Volume Effect in Silicon”, *Phys. Rev. Lett.*, vol. 18, pp. 1058–1061, 24 Jun. 1967. DOI: 10.1103/PhysRevLett.18.1058.
- [14] J. C. North and R. C. Buschert, “Length Change of Electron-Irradiated Germanium”, *Phys. Rev. Lett.*, vol. 13, pp. 609–611, 21 Nov. 1964. DOI: 10.1103/PhysRevLett.13.609.
- [15] J. C. North and R. C. Buschert, “Length Changes in Electron-Irradiated *n*- and *p*-Type Germanium”, *Phys. Rev.*, vol. 143, pp. 609–618, 2 Mar. 1966. DOI: 10.1103/PhysRev.143.609.
- [16] J. North and R. Buschert, “Deformation potential of irradiation induced traps in p-type germanium from length measurements”, *Journal of Physics and Chemistry of Solids*, vol. 27, no. 3, pp. 489–492, 1966, ISSN: 0022-3697. DOI: 10.1016/0022-3697(66)90190-9.
- [17] S. Akhmanov and V. Gusev, “REVIEWS OF TOPICAL PROBLEMS: Laser excitation of ultrashort acoustic pulses: New possibilities in solid-state spectroscopy, diagnostics of fast processes, and nonlinear acoustics”, *Soviet Physics Uspekhi*, vol. 35, pp. 153–191, Feb. 1992. DOI: 10.1070/PU1992v035n03ABEH002221.
- [18] A. C. Tam, “Applications of photoacoustic sensing techniques”, *Rev. Mod. Phys.*, vol. 58, pp. 381–431, 2 Apr. 1986. DOI: 10.1103/RevModPhys.58.381.
- [19] C. Thomsen, H. T. Grahn, H. J. Maris, and J. Tauc, “Surface generation and detection of phonons by picosecond light pulses”, *Phys. Rev. B*, vol. 34, pp. 4129–4138, 6 1986. DOI: 10.1103/PhysRevB.34.4129.
- [20] P. Ruello and V. E. Gusev, “Physical mechanisms of coherent acoustic phonons generation by ultrafast laser action”, *Ultrasonics*, vol. 56, pp. 21–35, 2015, ISSN: 0041-624X. DOI: 10.1016/j.ultras.2014.06.004.
- [21] N. D. Ashcroft Neil W. and Mermin, “Solid state physics”, English, in New York: Holt, Rinehart and Winston, 1976.
- [22] V. Gusev, “On the duration of acoustic pulses excited by subpicosecond laser action on metals”, *Optics Communications - OPT COMMUN*, vol. 94, pp. 76–78, Nov. 1992. DOI: 10.1016/0030-4018(92)90409-K.
- [23] J. Bardeen and W. Shockley, “Deformation Potentials and Mobilities in Non-Polar Crystals”, *Phys. Rev.*, vol. 80, pp. 72–80, 1 Oct. 1950. DOI: 10.1103/PhysRev.80.72.
- [24] P. Y. Yu and M. Cardona, “Fundamentals of Semiconductor, Physics and Materials Properties”, in Heidelberg: Springer Berlin, 1996, p. 617, ISBN: 978-3-662-03313-5. DOI: 10.1007/978-3-662-03313-5.
- [25] J. Nye, *Physical Properties of Crystals: Their Representation by Tensors and Matrices*, ser. Oxford science publications. Clarendon Press, 1985, ISBN: 9780198511656.
- [26] C. Rabe Karin M. and Ahn and J.-M. Triscone, *Physics of ferroelectrics: a modern perspective*. Berlin: Springer, 2007, ISBN: 978-3-540-34590-9. [Online]. Available: <https://archive-ouverte.unige.ch/unige:12885>.

-
- [27] P. Babilotte *et al.*, “Picosecond acoustics in p-doped piezoelectric semiconductors”, *Applied Physics Letters*, vol. 97, no. 17, p. 174 103, 2010. DOI: 10.1063/1.3501125.
- [28] Y.-C. Wen, G.-W. Chern, K.-H. Lin, J. J. Yeh, and C.-K. Sun, “Femtosecond optical excitation of coherent acoustic phonons in a piezoelectric p - n junction”, *Phys. Rev. B*, vol. 84, p. 205 315, 20 Nov. 2011. DOI: 10.1103/PhysRevB.84.205315.
- [29] P.-A. Mante *et al.*, “Thz acoustic phonon spectroscopy and nanoscopy by using piezoelectric semiconductor heterostructures”, *Ultrasonics*, vol. 56, pp. 52–65, 2015, ISSN: 0041-624X. DOI: 10.1016/j.ultras.2014.09.020.
- [30] V. Gusev, P. Picart, D. Mounier, and J.-M. Breteau, “On the possibility of ultrashort shear acoustic pulse excitation due to the laser-induced electrostrictive effect”, *Optics Communications*, vol. 204, no. 1, pp. 229–236, 2002, ISSN: 0030-4018. DOI: 10.1016/S0030-4018(02)01211-7.
- [31] Y.-X. Yan, E. B. Gamble, and K. A. Nelson, “Impulsive stimulated scattering: General importance in femtosecond laser pulse interactions with matter, and spectroscopic applications”, *The Journal of Chemical Physics*, vol. 83, no. 11, pp. 5391–5399, 1985. DOI: 10.1063/1.449708.
- [32] H. Tanaka, T. Sonehara, and S. Takagi, “A New Phase-Coherent Light Scattering Method: First Observation of Complex Brillouin Spectra”, *Phys. Rev. Lett.*, vol. 79, pp. 881–884, 5 Aug. 1997. DOI: 10.1103/PhysRevLett.79.881.
- [33] J. Coutte, B. Dubus, J.-C. Debus, C. Granger, and D. Jones, “Design, production and testing of PMN–PT electrostrictive transducers”, *Ultrasonics*, vol. 40, no. 1, pp. 883–888, 2002, ISSN: 0041-624X. DOI: 10.1016/S0041-624X(02)00231-7.
- [34] A. von Reppert, “Magnetic strain contributions in laser-excited metals studied by time-resolved X-ray diffraction”, doctoralthesis, Universität Potsdam, 2021, pp. XV, 311. DOI: 10.25932/publishup-53558.
- [35] E. W. Lee, “Magnetostriiction and Magnetomechanical Effects”, *Reports on Progress in Physics*, vol. 18, no. 1, pp. 184–229, Jan. 1955. DOI: 10.1088/0034-4885/18/1/305.
- [36] É. d. T. de Lacheisserie, D. Gignoux, and M. Schlenker, “Magnetoelastic effects”, in *Magnetism: I-Fundamentals*. New York: Springer-Verlag, 2002, ch. 12, pp. 351–398, ISBN: 9780387230627. [Online]. Available: <https://fr.fr1lib.org/book/2569916/84420f>.
- [37] C. Dornes *et al.*, “The ultrafast Einstein-de Haas effect”, *Nature*, vol. 565, no. 7738, pp. 209–212, Jan. 2019, ISSN: 1476-4687. DOI: 10.1038/s41586-018-0822-7.
- [38] É. d. T. de Lacheisserie, D. Gignoux, and M. Schlenker, “Magnetoelastic effects”, in *Magnetism: I-Fundamentals*. New York: Springer-Verlag, 2002, ch. 18, pp. 351–398, ISBN: 9780387230627. [Online]. Available: <https://fr.fr1lib.org/book/2569916/84420f>.
- [39] T. Parpiiev *et al.*, “Ultrafast strain excitation in highly magnetostriuctive terfenol: Experiments and theory”, *Phys. Rev. B*, vol. 104, p. 224 426, 22 Dec. 2021. DOI: 10.1103/PhysRevB.104.224426.
-

- [40] O. B. Wright, B. Perrin, O. Matsuda, and V. E. Gusev, “Ultrafast carrier diffusion in gallium arsenide probed with picosecond acoustic pulses”, *Phys. Rev. B*, vol. 64, p. 081 202, 8 2001. DOI: 10.1103/PhysRevB.64.081202.
- [41] V. Gusev and A. Karabutov, “Laser Optoacoustics”, *NASA STI/Recon Technical Report A*, vol. 93, p. 16 842, 1991.
- [42] H. Wen *et al.*, “Electronic Origin of Ultrafast Photoinduced Strain in BiFeO₃”, *Phys. Rev. Lett.*, vol. 110, p. 037 601, 3 Jan. 2013. DOI: 10.1103/PhysRevLett.110.037601.
- [43] L. D. Whittig and W. R. Allardice, “X-Ray Diffraction Techniques”, in *Methods of Soil Analysis*. John Wiley & Sons, Ltd, 1986, ch. 12, pp. 331–362, ISBN: 9780891188643. DOI: 10.2136/sssabookser5.1.2ed.c12.
- [44] *Chameleon Ultra and Chameleon Vision Laser Operator’s Manual*, Coherent, Inc., Sep. 2009.
- [45] *OPO PP Auto Manual*, APE-Angewandte Physik & Elektronik GmbH, Plauener Str. 163-165 Haus N, 13053 Berlin Germany, Sep. 2008.
- [46] *Model 2007 & 2017 User’s Manual*, New Focus, Inc., Dec. 2002.
- [47] *PE95/T95 System Controller User Guide*, Linkam Scientific Instruments Ltd., Unit 8 Epsom Downs Metro Centre, Waterfield, Tadworth, Surrey, KT20 5LR, UK, Aug. 2010. [Online]. Available: https://static1.squarespace.com/static/556d800ae4b0e8f91507450c/55783826e4b07076ade934d6/55783826e4b07076ade934f2/1290426886227/T95_System_Controller_LNP95cooling+v1.1.pdf.
- [48] *DCx Camera Functional Description and SDK Manual*, Thorlabs Scientific Imaging, Jul. 2018. [Online]. Available: <https://www.thorlabs.com>.
- [49] D. Bachiller-Perea *et al.*, “First pump–probe–probe hard X-ray diffraction experiments with a 2D hybrid pixel detector developed at the SOLEIL synchrotron”, *Journal of Synchrotron Radiation*, vol. 27, no. 2, pp. 340–350, Mar. 2020. DOI: 10.1107/S1600577520000612.
- [50] M. Tordeux *et al.*, “Low-Alpha Operation for the SOLEIL Storage Ring”, in *Proceedings of the 2012 International Particle Accelerator Conference (IPAC12)*, New Orleans, USA, May 2012, pp. 1608–1609, ISBN: 978-3-95450-115-1.
- [51] P. Pangaud *et al.*, “Xpad3: a new photon counting chip for x-ray ct-scanner”, *Nuclear Instruments and Methods in Physics Research Section A: Accelerators, Spectrometers, Detectors and Associated Equipment*, vol. 571, no. 1, pp. 321–324, 2007, Proceedings of the 1st International Conference on Molecular Imaging Technology, ISSN: 0168-9002. DOI: 10.1016/j.nima.2006.10.092.
- [52] S. G. Choi, H. T. Yi, S.-W. Cheong, J. N. Hilfiker, R. France, and A. G. Norman, “Optical anisotropy and charge-transfer transition energies in BiFeO₃ from 1.0 to 5.5 eV”, *Phys. Rev. B*, vol. 83, p. 100 101, 10 2011. DOI: 10.1103/PhysRevB.83.100101.
- [53] B. Henke, E. Gullikson, and J. Davis, “X-Ray Interactions: Photoabsorption, Scattering, Transmission, and Reflection at E = 50-30,000 eV, Z = 1-92”, *Atomic Data and Nuclear Data Tables*, vol. 54, no. 2, pp. 181–342, 1993, ISSN: 0092-640X. DOI: 10.1006/adnd.1993.1013.

-
- [54] V. Juvé *et al.*, “Ultrafast light-induced shear strain probed by time-resolved x-ray diffraction: Multiferroic BiFeO₃ as a case study”, *Phys. Rev. B*, vol. 102, p. 220303, 22 2020. DOI: 10.1103/PhysRevB.102.220303.
 - [55] D. Schick *et al.*, “Localized Excited Charge Carriers Generate Ultrafast Inhomogeneous Strain in the Multiferroic BiFeO₃”, *Phys. Rev. Lett.*, vol. 112, p. 097602, 9 Mar. 2014. DOI: 10.1103/PhysRevLett.112.097602.
 - [56] C. Ríos *et al.*, “Integrated all-photonics non-volatile multi-level memory”, *Nature Photonics*, vol. 9, pp. 725–732, 2015. DOI: 10.1038/nphoton.2015.182.
 - [57] Q. Yang, Z. Cai, Y. Wang, H. Huang, and Y. Wu, “Controllable crystallization of Ge₂Sb₂Te₅ phase-change memory thin films driven by multiple femtosecond laser pulses”, *Materials Science and Engineering: B*, vol. 193, pp. 189–197, 2015, ISSN: 0921-5107. DOI: 10.1016/j.mseb.2014.12.017.
 - [58] S. Varotto *et al.*, “Room-temperature ferroelectric switching of spin-to-charge conversion in germanium telluride”, *Nature Electronics*, vol. 4, no. 10, pp. 740–747, Oct. 2021, ISSN: 2520-1131. DOI: 10.1038/s41928-021-00653-2.
 - [59] C. Rinaldi *et al.*, “Evidence for spin to charge conversion in GeTe(111)”, *APL Materials*, vol. 4, no. 3, p. 032501, 2016. DOI: 10.1063/1.4941276.
 - [60] H. Wang, P. Gopal, S. Picozzi, S. Curtarolo, M. B. Nardelli, and J. Sławińska, “Spin Hall effect in prototype Rashba ferroelectrics GeTe and SnTe”, *npj Comput Mater*, vol. 6, no. 7, 2020. DOI: 10.1038/s41524-020-0274-0.
 - [61] D. Di Sante, P. Barone, R. Bertacco, and S. Picozzi, “Electric Control of the Giant Rashba Effect in Bulk GeTe”, *Advanced Materials*, vol. 25, no. 4, pp. 509–513, 2013. DOI: 10.1002/adma.201203199.
 - [62] X. Zhang, Z. Bu, S. Lin, Z. Chen, W. Li, and Y. Pei, “GeTe Thermoelectrics”, *Joule*, vol. 4, no. 5, pp. 986–1003, 2020, ISSN: 2542-4351. DOI: 10.1016/j.joule.2020.03.004.
 - [63] W. Zhang, R. Mazzarello, and E. Ma, “Phase-change materials in electronics and photonics”, *MRS Bulletin*, vol. 44, pp. 686–690, Sep. 2019. DOI: 10.1557/mrs.2019.201.
 - [64] N. Yamada, E. Ohno, K. Nishiuchi, N. Akahira, and M. Takao, “Rapid-phase transitions of GeTe-Sb₂Te₃ pseudobinary amorphous thin films for an optical disk memory”, *Journal of Applied Physics*, vol. 69, no. 5, pp. 2849–2856, 1991. DOI: 10.1063/1.348620.
 - [65] M. Wuttig, H. Bhaskaran, and T. Taubner, “Phase-change materials for non-volatile photonic applications”, *Nature Photon*, no. 11, pp. 465–476, 2017. DOI: 10.1038/nphoton.2017.126.
 - [66] M. L. Gallo and A. Sebastian, “An overview of phase-change memory device physics”, *J. Phys. D: Appl. Phys.*, vol. 53, no. 213002, 2020. DOI: 10.1088/1361-6463/ab7794.
 - [67] S. K. Bahl and K. L. Chopra, “Amorphous versus Crystalline GeTe Films. I. Growth and Structural Behavior”, *J. Appl. Phys*, vol. 40, no. 10, pp. 4171–4178, 1969. DOI: 10.1063/1.1657161.
 - [68] S. K. Bahl and K. L. Chopra, “Amorphous versus Crystalline GeTe Films. II. Optical Properties”, *J. Appl. Phys*, vol. 40, no. 12, pp. 4940–4947, 1969. DOI: 10.1063/1.1657318.
-

- [69] S. K. Bahl and K. L. Chopra, “Amorphous versus Crystalline GeTe Films. III. Electrical Properties and Band Structure”, *J. Appl. Phys.*, vol. 41, no. 5, pp. 2196–2212, 1970. DOI: 10.1063/1.1659189.
- [70] K. Chopra, in *Thin Film Phenomena*. New York, USA: McGraw-Hill Book Co., 1969, vol. 19692, ch. 4, p. 196, ISBN: 0070107998.
- [71] A. Schlieper, Y. Feutelais, S. Fries, B. Legendre, and R. Blachnik, “Thermodynamic evaluation of the Germanium — Tellurium system”, *Calphad*, vol. 23, no. 1, pp. 1–18, 1999, ISSN: 0364-5916. DOI: 10.1016/S0364-5916(99)00012-7.
- [72] T. Chattopadhyay, J. X. Boucherle, and H. G. vonSchnering, “Neutron diffraction study on the structural phase transition in GeTe”, *Journal of Physics C: Solid State Physics*, vol. 20, no. 10, pp. 1431–1440, 1987. DOI: 10.1088/0022-3719/20/10/012.
- [73] K. Jeong *et al.*, “Evolution of crystal structures in GeTe during phase transition”, *Sci Rep*, vol. 7, no. 955, 2017. DOI: 10.1038/s41598-017-01154-z.
- [74] T. Nonaka, G. Ohbayashi, Y. Toriumi, Y. Mori, and H. Hashimoto, “Crystal structure of GeTe and Ge₂Sb₂Te₅ meta-stable phase”, *Thin Solid Films*, vol. 370, no. 1, pp. 258–261, 2000, ISSN: 0040-6090. DOI: 10.1016/S0040-6090(99)01090-1.
- [75] J. Goldak, C. S. Barrett, D. Innes, and W. Youdelis, “Structure of Alpha GeTe”, *J. Chem. Phys.*, vol. 44, no. 3323, 1966. DOI: 10.1063/1.1727231.
- [76] T. Zhukova and A. Zaslavskii, “And structure of q-gete”, *Soviet Physics, Crystallography*, vol. 12, no. 1, p. 28, 1967.
- [77] J. Liu, X. Xu, L. Brush, and M. P. Anantram, “A multi-scale analysis of the crystallization of amorphous germanium telluride using ab initio simulations and classical crystallization theory”, *Journal of Applied Physics*, vol. 115, no. 2, p. 023513, 2014. DOI: 10.1063/1.4861721.
- [78] A. Onodera, I. Sakamoto, Y. Fujii, N. Mori, and S. Sugai, “Structural and electrical properties of GeSe and GeTe at high pressure”, *Phys. Rev. B*, vol. 56, pp. 7935–7941, 1997. DOI: 10.1103/PhysRevB.56.7935.
- [79] R. Shaltaf, E. Durgun, J.-Y. Raty, P. Ghosez, and X. Gonze, “Dynamical, dielectric, and elastic properties of GeTe investigated with first-principles density functional theory”, *Phys. Rev. B*, vol. 78, p. 205203, 2008. DOI: 10.1103/PhysRevB.78.205203.
- [80] H. L. Kagdada, P. K. Jha, P. Śpiewak, and K. J. Kurzydłowski, “Structural stability, dynamical stability, thermoelectric properties, and elastic properties of GeTe at high pressure”, *Phys. Rev. B*, vol. 97, p. 134105, 13 Apr. 2018. DOI: 10.1103/PhysRevB.97.134105.
- [81] K. Ghosh, A. Kusiak, P. Noé, M.-C. Cyrille, and J.-L. Battaglia, “Thermal conductivity of amorphous and crystalline GeTe thin film at high temperature: Experimental and theoretical study”, *Phys. Rev. B*, vol. 101, p. 214305, 21 Jun. 2020. DOI: 10.1103/PhysRevB.101.214305.
- [82] K. Shportko, S. Kremers, M. Woda, D. Lencer, J. Robertson, and M. Wuttig, “Resonant bonding in crystalline phase-change materials”, *Nature materials*, vol. 7, pp. 653–8, Aug. 2008. DOI: 10.1038/nmat2226.

-
- [83] A.-K. U. Michel *et al.*, “Optical Properties of Amorphous and Crystalline GeTe Nanoparticle Thin Films: A Phase-Change Material for Tunable Photonics”, *ACS Applied Nano Materials*, vol. 3, no. 5, pp. 4314–4320, 2020. DOI: 10.1021/acsanm.0c00463.
- [84] T. Xing *et al.*, “Superior performance and high service stability for GeTe-based thermoelectric compounds”, *National Science Review*, vol. 6, no. 5, pp. 944–954, Apr. 2019, ISSN: 2095-5138. DOI: 10.1093/nsr/nwz052.
- [85] E. M. Levin, M. F. Besser, and R. Hanus, “Electronic and thermal transport in GeTe: A versatile base for thermoelectric materials”, *Journal of Applied Physics*, vol. 114, no. 8, p. 083713, 2013. DOI: 10.1063/1.4819222.
- [86] R. Shaltaf, X. Gonze, M. Cardona, R. K. Kremer, and G. Siegle, “Lattice dynamics and specific heat of α -GeTe: theoretical and experimental study”, *Phys. Rev. B*, vol. 79, p. 075204, 7 2009. DOI: 10.1103/PhysRevB.79.075204.
- [87] D. Campi, L. Paulatto, G. Fugallo, F. Mauri, and M. Bernasconi, “First-principles calculation of lattice thermal conductivity in crystalline phase change materials: GeTe, Sb_2Te_3 , and $\text{Ge}_2\text{Sb}_2\text{Te}_5$ ”, *Phys. Rev. B*, vol. 95, p. 024311, 2 Jan. 2017. DOI: 10.1103/PhysRevB.95.024311.
- [88] S. Adachi, *GaAs and Related Materials*. Singapore: WORLD SCIENTIFIC, 1994. DOI: 10.1142/2508. [Online]. Available: <https://www.worldscientific.com/doi/abs/10.1142/2508>.
- [89] C. Longeaud, J. Luckas, D. Krebs, R. Carius, J. Klomfass, and M. Wuttig, “On the density of states of germanium telluride”, *Journal of Applied Physics*, vol. 112, no. 11, p. 113714, 2012. DOI: 10.1063/1.4768725.
- [90] X. Zhang, F. Zhao, Y. Wang, X. Liang, Y. Feng, and W. Feng, “Preparation and Electrical Properties of Germanium Telluride Field Effect Transistor”, *Chemical Journal of Chinese Universities -Chinese Edition-*, Jul. 2020. DOI: 10.7503/cjcu20200311.
- [91] Z. Liu *et al.*, “Phase-transition temperature suppression to achieve cubic GeTe and high thermoelectric performance by Bi and Mn codoping”, *Proceedings of the National Academy of Sciences*, vol. 115, no. 21, pp. 5332–5337, 2018. DOI: 10.1073/pnas.1802020115.
- [92] N. V. Kolomoets, E. Y. Lev, and L. M. Sysoeva, “Electrical properties and valence band structure of germanium telluride”, *Sov. Phys. Solid State*, vol. 6, pp. 551–556, 1964.
- [93] P. Fons *et al.*, “Picosecond strain dynamics in $\text{Ge}_2\text{Sb}_2\text{Te}_5$ monitored by time-resolved x-ray diffraction”, *Phys. Rev. B*, vol. 90, p. 094305, 9 2014. DOI: 10.1103/PhysRevB.90.094305.
- [94] M. Hase, P. Fons, A. Kolobov, and J. Tominaga, “Coherent gigahertz phonons in $\text{Ge}_2\text{Sb}_2\text{Te}_5$ phase-change materials”, *Journal of Physics Condensed Matter*, vol. 27, p. 485402, 2015. DOI: 10.1088/0953-8984/27/48/485402.
- [95] M. J. Shu, I. Chatzakis, Y. Kuo, P. Zalden, and A. M. Lindenberg, “Ultrafast sub-threshold photo-induced response in crystalline and amorphous GeSbTe thin films”, *Applied Physics Letters*, vol. 102, no. 20, p. 201903, 2013. DOI: 10.1063/1.4807731.
-

- [96] A. V. Kolobov, P. Fons, A. I. Frenkel, A. L. Ankudinov, J. Tominaga, and T. Uruga, “Understanding the phase-change mechanism of rewritable optical media”, *Nature Materials*, vol. 3, no. 10, pp. 703–708, Oct. 2004, ISSN: 1476-4660. DOI: 10.1038/nmat1215.
- [97] P. Fons *et al.*, “Photoassisted amorphization of the phase-change memory alloy $\text{Ge}_2\text{Sb}_2\text{Te}_5$ ”, *Phys. Rev. B*, vol. 82, p. 041 203, 4 Jul. 2010. DOI: 10.1103/PhysRevB.82.041203.
- [98] M. Hada *et al.*, “Ultrafast time-resolved electron diffraction revealing the nonthermal dynamics of near-UV photoexcitation-induced amorphization in $\text{Ge}_2\text{Sb}_2\text{Te}_5$ ”, *Scientific Reports*, vol. 5, no. 1, p. 13 530, Aug. 2015, ISSN: 2045-2322. DOI: 10.1038/srep13530.
- [99] L. Waldecker *et al.*, “Time-domain separation of optical properties from structural transitions in resonantly bonded materials”, *Nature Materials*, vol. 14, no. 10, pp. 991–995, Oct. 2015, ISSN: 1476-4660. DOI: 10.1038/nmat4359.
- [100] P. Zalden *et al.*, “Femtosecond x-ray diffraction reveals a liquid–liquid phase transition in phase-change materials”, *Science*, vol. 364, no. 6445, pp. 1062–1067, 2019. DOI: 10.1126/science.aaw1773.
- [101] G. Tas and H. J. Maris, “Electron diffusion in metals studied by picosecond ultrasonics”, *Phys. Rev. B*, vol. 49, pp. 15 046–15 054, 21 Jun. 1994. DOI: 10.1103/PhysRevB.49.15046.
- [102] P. Hosseini, A. Sebastian, N. Papandreou, C. D. Wright, and H. Bhaskaran, “Accumulation-Based Computing Using Phase-Change Memories With FET Access Devices”, *IEEE Electron Device Letters*, vol. 36, no. 9, pp. 975–977, 2015. DOI: 10.1109/LED.2015.2457243.
- [103] M. Lejman, V. Shalagatskyi, O. Kovalenko, T. Pezeril, V. V. Temnov, and P. Ruello, “Ultrafast optical detection of coherent acoustic phonons emission driven by superdiffusive hot electrons”, *J. Opt. Soc. Am. B*, vol. 31, no. 2, pp. 282–290, Feb. 2014. DOI: 10.1364/JOSAB.31.000282.
- [104] N. V. Chigarev, D. Y. Paraschuk, X. Y. Pan, and V. E. Gusev, “Coherent phonon emission in the supersonic expansion of photoexcited electron-hole plasma in Ge”, *Phys. Rev. B*, vol. 61, pp. 15 837–15 840, 23 2000. DOI: 10.1103/PhysRevB.61.15837.
- [105] R. Gu *et al.*, “Nonthermal Transport of Energy Driven by Photoexcited Carriers in Switchable Solid States of GeTe”, *Phys. Rev. Applied*, vol. 16, p. 014 055, 1 Jul. 2021. DOI: 10.1103/PhysRevApplied.16.014055.
- [106] J. Pries *et al.*, “Approaching the Glass Transition Temperature of GeTe by Crystallizing $\text{Ge}_{15}\text{Te}_{85}$ ”, *physica status solidi (RRL) – Rapid Research Letters*, vol. 15, no. 3, p. 2 000 478, 2021. DOI: 10.1002/pssr.202000478.
- [107] B. Chen, D. de Wal, G. H. ten Brink, G. Palasantzas, and B. J. Kooi, “Resolving Crystallization Kinetics of GeTe Phase-Change Nanoparticles by Ultrafast Calorimetry”, *Crystal Growth & Design*, vol. 18, no. 2, pp. 1041–1046, 2018. DOI: 10.1021/acs.cgd.7b01498.
- [108] K.S.Andrikopoulos, S.N.Yannopoulos, G.A.Voyiatzis, A.V.Kolobov, M.Ribes, and J.Tominaga, “Raman scattering study of the a-GeTe structure and possible mechanism for the amorphous to crystal transition”, *J. Phys.: Condens. Matter*, vol. 18, pp. 965–979, 2006. DOI: 10.1088/0953-8984/18/3/014.

-
- [109] S. Koshihara *et al.*, “Challenges for developing photo-induced phase transition (PIPT) systems: From classical (incoherent) to quantum (coherent) control of PIPT dynamics”, *Physics Reports*, vol. 942, pp. 1–61, 2022, ISSN: 0370-1573. DOI: 10.1016/j.physrep.2021.10.003.
 - [110] P. Ruello, S. Zhang, P. Laffez, B. Perrin, and V. Gusev, “Ultrafast electronic dynamics in the metal-insulator transition compound NdNiO₃”, *Phys. Rev. B*, vol. 76, p. 165 107, 16 2007. DOI: 10.1103/PhysRevB.76.165107.
 - [111] J. Demsar, K. Biljaković, and D. Mihailovic, “Single Particle and Collective Excitations in the One-Dimensional Charge Density Wave Solid K_{0.3}MoO₃ Probed in Real Time by Femtosecond Spectroscopy”, *Phys. Rev. Lett.*, vol. 83, pp. 800–803, 4 1999. DOI: 10.1103/PhysRevLett.83.800.
 - [112] V. Klimov, P. H. Bolivar, and H. Kurz, “Ultrafast carrier dynamics in semiconductor quantum dots”, *Phys. Rev. B*, vol. 53, pp. 1463–1467, 3 Jan. 1996. DOI: 10.1103/PhysRevB.53.1463.
 - [113] X. Shen, Z. Lu, Y. P. Timalina, T.-M. Lu, M. Washington, and M. Yamaguchi, “Coherent Phonon Transport Measurement and Controlled Acoustic Excitations Using Tunable Acoustic Phonon Source in GHz-sub THz Range with Variable Bandwidth”, *Scientific Reports*, vol. 8, no. 1, p. 7054, May 2018, ISSN: 2045-2322. DOI: 10.1038/s41598-018-25525-2.
 - [114] P. van Capel, E. Péronne, and J. Dijkhuis, “Nonlinear ultrafast acoustics at the nano scale”, *Ultrasonics*, vol. 56, pp. 36–51, 2015. DOI: 10.1016/j.ultras.2014.09.021.
 - [115] S. Rajagopalan and D. N. Joharapurkar, “Temperature dependence of the nonlinearity constant and ultrasonic attenuation in pure silicon and germanium”, *Journal of Applied Physics*, vol. 54, no. 6, pp. 3166–3171, 1983. DOI: 10.1063/1.332474.
 - [116] H. WIEDEMEIER and P. A. SIEMER, “The thermal expansion of GeS and GeTe”, *Z. anorg. allg. Chem.*, vol. 431, pp. 299–304, 1977. DOI: 10.1002/zaac.19774310134.
 - [117] E. S. K. Young, A. V. Akimov, R. P. Champion, A. J. Kent, and V. Gusev, “Picosecond strain pulses generated by a supersonically expanding electron-hole plasma in GaAs”, *Phys. Rev. B*, vol. 86, p. 155 207, 15 2012. DOI: 10.1103/PhysRevB.86.155207.
 - [118] B. A. Ruzicka, L. K. Werake, H. Samassekou, and H. Zhao, “Ambipolar diffusion of photoexcited carriers in bulk GaAs”, *Applied Physics Letters*, vol. 97, no. 26, p. 262 119, 2010. DOI: 10.1063/1.3533664.
 - [119] S. Adachi, *GaAs and Related Materials*. WORLD SCIENTIFIC, 1994. DOI: 10.1142/2508. [Online]. Available: <https://www.worldscientific.com/doi/abs/10.1142/2508>.
 - [120] A. Huynh, B. Perrin, and A. Lemaître, “Semiconductor superlattices: a tool for terahertz acoustics”, *Ultrasonics*, vol. 56, pp. 66–79, 2015, ISSN: 0041-624X. DOI: 10.1016/j.ultras.2014.07.009.
 - [121] A. Huynh, B. Perrin, N. D. Lanzillotti-Kimura, B. Jusserand, A. Fainstein, and A. Lemaître, “Subterahertz monochromatic acoustic wave propagation using semiconductor superlattices as transducers”, *Phys. Rev. B*, vol. 78, p. 233 302, 23 Dec. 2008. DOI: 10.1103/PhysRevB.78.233302.
-

- [122] N. A. Spaldin and R. Ramesh, “Advances in magnetoelectric multiferroics”, *Nature Materials*, vol. 18, no. 3, pp. 203–212, Mar. 2019, ISSN: 1476-4660. DOI: 10.1038/s41563-018-0275-2.
- [123] M. Fiebig, T. Lottermoser, D. Meier, and M. Trassin, “The evolution of multiferroics”, *Nature Reviews Materials*, vol. 1, no. 8, p. 16046, Jul. 2016, ISSN: 2058-8437. DOI: 10.1038/natrevmats.2016.46.
- [124] T. Kampfrath, K. Tanaka, and K. A. Nelson, “Resonant and nonresonant control over matter and light by intense terahertz transients”, *Nature Photonics*, vol. 7, no. 9, pp. 680–690, Sep. 2013, ISSN: 1749-4893. DOI: 10.1038/nphoton.2013.184.
- [125] G. Catalan and J. F. Scott, “Physics and Applications of Bismuth Ferrite”, *Advanced Materials*, vol. 21, no. 24, pp. 2463–2485, 2009. DOI: 10.1002/adma.200802849.
- [126] R. P. and S. K., “System Wismutoxyd-Eisenoxyd im Bereich von 0 bis 55Mol% Eisenoxyd”, *Angewandte Chemie*, vol. 69, no. 799, 1957. DOI: 10.1002/ange.19570692407.
- [127] N. Wang *et al.*, “Structure, Performance, and Application of BiFeO₃ Nanomaterials”, *Nano-Micro Letters*, vol. 12, no. 1, p. 81, Mar. 2020, ISSN: 2150-5551. DOI: 10.1007/s40820-020-00420-6.
- [128] K. I. Doig *et al.*, “Coherent magnon and acoustic phonon dynamics in tetragonal and rare-earth-doped BiFeO₃ multiferroic thin films”, *Phys. Rev. B*, vol. 88, p. 094425, 9 Sep. 2013. DOI: 10.1103/PhysRevB.88.094425.
- [129] R. Palai *et al.*, “ β phase and γ – β metal-insulator transition in multiferroic BiFeO₃”, *Phys. Rev. B*, vol. 77, p. 014110, 1 2008. DOI: 10.1103/PhysRevB.77.014110.
- [130] J. Park *et al.*, “Magnetoelectric Feedback among Magnetic Order, Polarization, and Lattice in Multiferroic BiFeO₃”, *Journal of the Physical Society of Japan*, vol. 80, no. 11, p. 114714, 2011. DOI: 10.1143/JPSJ.80.114714.
- [131] S. Cheong and M. Mostovoy, “Multiferroics: a magnetic twist for ferroelectricity”, *Nature Mater*, vol. 6, pp. 13–20, 2007. DOI: 10.1038/nmat1804.
- [132] D. Lebeugle, D. Colson, A. Forget, M. Viret, A. M. Bataille, and A. Gukasov, “Electric-field-induced spin flop in BiFeO₃ single crystals at room temperature”, *Phys. Rev. Lett.*, vol. 100, p. 227602, 22 Jun. 2008. DOI: 10.1103/PhysRevLett.100.227602.
- [133] J. Allibe *et al.*, “Optical properties of integrated multiferroic BiFeO₃ thin films for microwave applications”, *Applied Physics Letters*, vol. 96, no. 18, p. 182902, 2010. DOI: 10.1063/1.3402763.
- [134] C. Tabares-muñoz, J.-P. Rivera, and H. Schmid, “Ferroelectric domains, birefringence and absorption of single crystals of BiFeO₃”, *Ferroelectrics*, vol. 55, no. 1, pp. 235–238, 1984. DOI: 10.1080/00150198408015377.
- [135] J. I. Pankove, *Optical Processes in Semiconductors*. Dover Publications, 1975.
- [136] D. Lebeugle *et al.*, “Room-temperature coexistence of large electric polarization and magnetic order in BiFeO₃ single crystals”, *Phys. Rev. B*, vol. 76, p. 024116, 2 Jul. 2007. DOI: 10.1103/PhysRevB.76.024116.

-
- [137] Y. F. Popov, A. Zvezdin, G. Vorobev, A. Kadomtseva, V. Murashev, and D. Rakov, “Linear magnetoelectric effect and phase transitions in bismuth ferrite, BiFeO_3 ”, *Jetp Lett*, vol. 57, no. 1, pp. 65–68, 1993.
- [138] A. M. Kadomtseva, A. K. Zvezdin, Y. F. Popov, A. P. Pyatakov, and G. P. Vorob’ev, “Space-time parity violation and magnetoelectric interactions in antiferromagnets”, *Journal of Experimental and Theoretical Physics Letters*, vol. 79, no. 11, pp. 571–581, Jun. 2004, ISSN: 1090-6487. DOI: 10.1134/1.1787107.
- [139] M. Lejman *et al.*, “Magnetoelastic and magnetoelectric couplings across the antiferromagnetic transition in multiferroic BiFeO_3 ”, *Phys. Rev. B*, vol. 99, p. 104103, 10 Mar. 2019. DOI: 10.1103/PhysRevB.99.104103.
- [140] A. Haykal *et al.*, “Antiferromagnetic textures in BiFeO_3 controlled by strain and electric field”, *Nature Communications*, vol. 11, no. 1, p. 1704, Apr. 2020, ISSN: 2041-1723. DOI: 10.1038/s41467-020-15501-8.
- [141] B. Kundys, M. Viret, D. Colson, and D. O. Kundys, “Light-induced size changes in BiFeO_3 crystals”, *Nature Materials*, vol. 9, no. 10, pp. 803–805, Oct. 2010, ISSN: 1476-4660. DOI: 10.1038/nmat2807.
- [142] B. Kundys, M. Viret, C. Meny, V. Da Costa, D. Colson, and B. Doudin, “Wavelength dependence of photoinduced deformation in BiFeO_3 ”, *Phys. Rev. B*, vol. 85, p. 092301, 9 Mar. 2012. DOI: 10.1103/PhysRevB.85.092301.
- [143] X. Li, C. Chen, F. Zhang, X. Huang, and Z. Yi, “Giant photostriction of $\text{CaCu}_3\text{Ti}_4\text{O}_{12}$ ceramics under visible light illumination”, *Applied Physics Letters*, vol. 116, no. 11, p. 112901, 2020. DOI: 10.1063/1.5142882.
- [144] D. A. Tenne *et al.*, “Probing nanoscale ferroelectricity by ultraviolet raman spectroscopy”, *Science*, vol. 313, no. 5793, pp. 1614–1616, 2006. DOI: 10.1126/science.1130306.
- [145] L. Y. Chen *et al.*, “Ultrafast photoinduced mechanical strain in epitaxial BiFeO_3 thin films”, *Applied Physics Letters*, vol. 101, no. 4, p. 041902, 2012. DOI: 10.1063/1.4734512.
- [146] P. Ruello *et al.*, “Photoexcitation of gigahertz longitudinal and shear acoustic waves in BiFeO_3 multiferroic single crystal”, *Applied Physics Letters*, vol. 100, no. 21, p. 212906, 2012. DOI: 10.1063/1.4719069.
- [147] D. Daranciang *et al.*, “Ultrafast Photovoltaic Response in Ferroelectric Nanolayers”, *Phys. Rev. Lett.*, vol. 108, p. 087601, 8 Feb. 2012. DOI: 10.1103/PhysRevLett.108.087601.
- [148] M. Lejman, I. C. Vaudel, G. Wenaëlle, and Infante, P. Gemeiner, V. E. Gusev, B. Dkhil, and P. Ruello, “Giant ultrafast photo-induced shear strain in ferroelectric BiFeO_3 ”, *Nature Communications*, vol. 5, no. 1, p. 4301, Jul. 2014, ISSN: 2041-1723. DOI: 10.1038/ncomms5301.
- [149] M. Lejman *et al.*, “Ultrafast acousto-optic mode conversion in optically birefringent ferroelectrics”, *Nature Communications*, vol. 7, no. 1, p. 12345, Aug. 2016, ISSN: 2041-1723. DOI: 10.1038/ncomms12345.
- [150] T. Pezeril *et al.*, “Generation and detection of plane coherent shear picosecond acoustic pulses by lasers: Experiment and theory”, *Phys. Rev. B*, vol. 75, p. 174307, 17 May 2007. DOI: 10.1103/PhysRevB.75.174307.
-

- [151] T. Pezeril *et al.*, “Laser acoustics with picosecond collimated shear strain beams in single crystals and polycrystalline materials”, *Phys. Rev. B*, vol. 73, p. 132 301, 13 Apr. 2006. DOI: 10.1103/PhysRevB.73.132301.
- [152] O. Matsuda, O. B. Wright, D. H. Hurley, V. E. Gusev, and K. Shimizu, “Coherent shear phonon generation and detection with ultrashort optical pulses”, *Phys. Rev. Lett.*, vol. 93, p. 095 501, 9 Aug. 2004. DOI: 10.1103/PhysRevLett.93.095501.
- [153] P. Hemme *et al.*, “Elastic properties assessment in the multiferroic BiFeO₃ by pump and probe method”, *Applied Physics Letters*, vol. 118, no. 6, p. 062 902, 2021. DOI: 10.1063/5.0039505.
- [154] D. Royer, E. Dieulesaint, and P.-G. de Gennes, *Ondes élastiques dans les solides. Tome 1 . Propagation libre et guidée*, French. Paris: Masson, 1996, ISBN: 2-225-85422-X.
- [155] J. Zhao, X. Song, and B. Liu, “Standardized Compliance Matrices for General Anisotropic Materials and a Simple Measure of Anisotropy Degree Based on Shear-Extension Coupling Coefficient”, *International Journal of Applied Mechanics*, vol. 8, no. 6, Aug. 2015. DOI: 10.1142/S1758825116500769.
- [156] E. Borissenko *et al.*, “Lattice dynamics of multiferroic BiFeO₃ studied by inelastic x-ray scattering”, *Journal of Physics: Condensed Matter*, vol. 25, no. 10, p. 102 201, Mar. 2013. DOI: 10.1088/0953-8984/25/10/102201.
- [157] S. L. Shang, G. Sheng, Y. Wang, L. Q. Chen, and Z. K. Liu, “Elastic properties of cubic and rhombohedral BiFeO₃ from first-principles calculations”, *Phys. Rev. B*, vol. 80, p. 052 102, 5 Aug. 2009. DOI: 10.1103/PhysRevB.80.052102.
- [158] S. Murakami, T. Yoshimura, K. Satoh, K. Wakazono, K. Kariya, and N. Fujimura, “Development of Piezoelectric MEMS Vibration Energy Harvester Using (100) Oriented BiFeO₃ Ferroelectric Film”, *Journal of Physics Conference Series*, vol. 476, pp. 2007–, Dec. 2013. DOI: 10.1088/1742-6596/476/1/012007.
- [159] R. J. Sichel, “Structural and electromechanical properties of epitaxial BiFeO₃ thin films”, Ph.D. dissertation, 2011. [Online]. Available: <https://search.library.wisc.edu/catalog/9910115719902121>.
- [160] Z. Chen *et al.*, “Coexistence of ferroelectric triclinic phases in highly strained BiFeO₃ films”, *Physical Review B: Condensed Matter and Materials Physics (1998-2015)*, vol. 84, no. 9, p. 094 116, 2011. DOI: 10.1103/PhysRevB.84.094116. [Online]. Available: <https://hal.archives-ouvertes.fr/hal-02277393>.
- [161] A. Palewicz, I. Sosnowska, R. Przeniosło, and A. Hewat, “Bifeo₃ Crystal Structure at Low Temperatures”, *Acta Physica Polonica A*, vol. 117, Feb. 2010. DOI: 10.12693/APhysPolA.117.296.
- [162] S. Gómez-Salces *et al.*, “Effect of pressure on the band gap and the local FeO₆ environment in BiFeO₃”, *Physical Review B: Condensed Matter and Materials Physics (1998-2015)*, vol. 85, no. 14, p. 144 109, 2012. DOI: 10.1103/PhysRevB.85.144109. [Online]. Available: <https://hal.archives-ouvertes.fr/hal-01067363>.

-
- [163] C. Paillard, B. Xu, B. Dkhil, G. Geneste, and L. Bellaiche, “Photostriction in Ferroelectrics from Density Functional Theory”, *Phys. Rev. Lett.*, vol. 116, p. 247 401, 24 Jun. 2016. DOI: 10.1103/PhysRevLett.116.247401.
 - [164] Y. Zhang *et al.*, “Controlled Nucleation and Stabilization of Ferroelectric Domain Wall Patterns in Epitaxial (110) Bismuth Ferrite Heterostructures”, *Advanced Functional Materials*, vol. 30, no. 48, Sep. 2020. DOI: 10.1002/adfm.202003571.
 - [165] D. Sando *et al.*, “Designer defect stabilization of the super tetragonal phase in > 70-nm-thick BiFeO₃ films on LaAlO₃ substrates”, *Japanese Journal of Applied Physics*, vol. 57, no. 9, 0902B2, Jun. 2018. DOI: 10.7567/jjap.57.0902b2.
 - [166] D. Sando *et al.*, “A magnetic phase diagram for nanoscale epitaxial BiFeO₃ films”, *Applied Physics Reviews*, vol. 6, no. 4, p. 041 404, 2019. DOI: 10.1063/1.5113530.
 - [167] *Model 918D photodiode detector user’s manual*, Newport Corporation, 1791 Deere Avenue, Irvine, CA, 92606, USA, 2006. [Online]. Available: https://www.newport.com/medias/sys_master/images/images/he2/h50/8797036511262/918D-Manual-RevD.pdf.
 - [168] O. B. Wright, “Thickness and sound velocity measurement in thin transparent films with laser picosecond acoustics”, *Journal of Applied Physics*, vol. 71, no. 4, pp. 1617–1629, 1992. DOI: 10.1063/1.351218.
 - [169] E. Sejdić, I. Djurović, and J. Jiang, “Time–frequency feature representation using energy concentration: An overview of recent advances”, *Digital Signal Processing*, vol. 19, no. 1, pp. 153–183, 2009, ISSN: 1051-2004. DOI: 10.1016/j.dsp.2007.12.004.
 - [170] R. O. Bell and G. Rupprecht, “Elastic Constants of Strontium Titanate”, *Phys. Rev.*, vol. 129, pp. 90–94, 1 Jan. 1963. DOI: 10.1103/PhysRev.129.90.
 - [171] D. A. Reis *et al.*, “Probing impulsive strain propagation with x-ray pulses”, *Phys. Rev. Lett.*, vol. 86, pp. 3072–3075, 14 Apr. 2001. DOI: 10.1103/PhysRevLett.86.3072.
 - [172] S. Yamanaka, T. Maekawa, H. Muta, T. Matsuda, S.-i. Kobayashi, and K. Kurosaki, “Thermophysical properties of SrHfO₃ and SrRuO₃”, *Journal of Solid State Chemistry*, vol. 177, no. 10, pp. 3484–3489, 2004, ISSN: 0022-4596. DOI: 10.1016/j.jssc.2004.05.039.
 - [173] H. Huyan, L. Li, C. Addiego, W. Gao, and X. Pan, “Structures and electronic properties of domain walls in BiFeO₃ thin films”, *National Science Review*, vol. 6, no. 4, pp. 669–683, Jul. 2019, ISSN: 2095-5138. DOI: 10.1093/nsr/nwz101.
 - [174] A. S. Everhardt, S. Matzen, N. Domingo, G. Catalan, and B. Noheda, “Ferroelectric Domain Structures in Low-Strain BaTiO₃”, *Advanced Electronic Materials*, vol. 2, no. 1, p. 1 500 214, 2016. DOI: 10.1002/aelm.201500214.
 - [175] E. Gradauskaite, P. Meisenheimer, M. Müller, J. Heron, and M. Trassin, “Multiferroic heterostructures for spintronics”, *Physical Sciences Reviews*, vol. -1, Dec. 2020. DOI: 10.1515/psr-2019-0072.
-

- [176] L. W. Martin and A. M. Rappe, “Thin-film ferroelectric materials and their applications”, *Nature Reviews Materials*, vol. 2, no. 2, p. 16 087, Nov. 2016, ISSN: 2058-8437. DOI: 10.1038/natrevmats.2016.87.
- [177] P. Scherrer, “Bestimmung der Grösse und der Inneren Struktur von Kolloidteilchen Mittels Röntgenstrahlen, Nachrichten von der Gesellschaft der Wissenschaften, Göttingen”, *Mathematisch-Physikalische Klasse*, vol. 2, pp. 98–100, 1918.
- [178] R. Estrada, “Applications of magnetostrictive materials in the real-time monitoring of vehicle suspension components”, M.S. thesis, University of Texas-Pan American, Jan. 2014. [Online]. Available: https://www.utrgv.edu/railwaysafety/_files/documents/theses-dissertations/rge-thesis-final.pdf.
- [179] V. E. Gusev and P. Ruelo, “Advances in applications of time-domain Brillouin scattering for nanoscale imaging”, *Applied Physics Reviews*, vol. 5, no. 3, p. 031 101, 2018. DOI: 10.1063/1.5017241.
- [180] L. D. Whittig and W. R. Allardice, “X-Ray Diffraction Techniques”, in *Methods of Soil Analysis*. John Wiley & Sons, Ltd, 1986, ch. 12, pp. 331–362, ISBN: 9780891188643. DOI: 10.2136/sssabookser5.1.2ed.c12.
- [181] A. Waterman, “XXI. On the positive ionization from certain hot salts, together with some observations on the electrical properties of molybdenite at high temperatures”, *Philosophical Magazine Series 6*, no. 33:195, pp. 225–247, 1917. DOI: 10.1080/14786440308635634.
- [182] M. L. Gallo and A. Sebastian. IntechOpen, 2018, ISBN: 978-1-78923-531-9.
- [183] J. E. Lewis, “Optical properties and energy gap of GeTe from reflectance studies”, *physica status solidi (b)*, vol. 59, no. 1, pp. 367–377, 1973. DOI: <https://doi.org/10.1002/pssb.2220590138>.
- [184] B. Burganov *et al.*, “Ultrafast modulation of covalency in GeTe driven by a ferroelectric soft mode”, 2020. arXiv: 2010.10361 [cond-mat.str-el].
- [185] J.-W. Park *et al.*, “Optical properties of (GeTe, Sb₂Te₃) pseudobinary thin films studied with spectroscopic ellipsometry”, *Applied Physics Letters*, vol. 93, no. 2, p. 021 914, 2008. DOI: 10.1063/1.2959818.
- [186] K. M. Rabe and J. D. Joannopoulos, “Theory of the structural phase transition of GeTe”, *Phys. Rev. B*, vol. 36, no. 12, pp. 6631–6639, 1987. DOI: 10.1103/PhysRevB.36.6631.
- [187] T. Nonaka, G. Ohbayashi, Y. Toriumi, Y. Mori, and H. Hashimoto, “Crystal structure of GeTe and Ge₂Sb₂Te₅ meta-stable phase”, *Thin Solid Films*, vol. 370, no. 1, pp. 258–261, 2000. DOI: 10.1016/S0040-6090(99)01090-1.
- [188] P. Guo, A. M. Sarangan, and I. Agha, “A Review of Germanium-Antimony-Telluride Phase Change Materials for Non-Volatile Memories and Optical Modulators”, *Appl. Sci.*, vol. 9, no. 3, 2019. DOI: 10.3390/app9030530.
- [189] P. Bauer Pereira, I. Sergueev, S. Gorsse, J. Dadda, E. Müller, and R. P. Hermann, “Lattice dynamics and structure of GeTe, SnTe and PbTe”, *physica status solidi (b)*, vol. 250, no. 7, pp. 1300–1307, 2013. DOI: <https://doi.org/10.1002/pssb.201248412>.
- [190] V. Gusev, “Laser hypersonics in fundamental and applied research”, *Acustica*, vol. 82, S37–S45, 1996.

-
- [191] J.-J. Lin and Z.-Q. Li, “Electronic conduction properties of indium tin oxide: single-particle and many-body transport”, *Journal of Physics: Condensed Matter*, vol. 26, no. 34, p. 343 201, 2014, ISSN: 1361-648X. DOI: 10.1088/0953-8984/26/34/343201.
 - [192] T. Ashida *et al.*, “Thermal transport properties of polycrystalline tin-doped indium oxide films”, *Journal of Applied Physics*, vol. 105, no. 7, p. 073 709, 2009. DOI: 10.1063/1.3093684.
 - [193] Đ. Dangi ć, A. R. Murphy, É. D. Murray, S. Fahy, and I. Savi ć, “Coupling between acoustic and soft transverse optical phonons leads to negative thermal expansion of GeTe near the ferroelectric phase transition”, *Phys. Rev. B*, vol. 97, p. 224 106, 22 2018. DOI: 10.1103/PhysRevB.97.224106.
 - [194] M. Wuttig and N. Yamada, “Phase-change materials for rewriteable data storage”, *Nature materials*, vol. 6, pp. 824–32, Dec. 2007. DOI: 10.1038/nmat2009.
 - [195] P. Nath and K. L. Chopra, “Thermal conductivity of amorphous and crystalline Ge and GeTe films”, *Phys. Rev. B*, vol. 10, pp. 3412–3418, 8 Oct. 1974. DOI: 10.1103/PhysRevB.10.3412.
 - [196] A. Fainstein, N. D. Lanzillotti-Kimura, B. Jusserand, and B. Perrin, “Strong Optical-Mechanical Coupling in a Vertical GaAs/AlAs Microcavity for Sub-terahertz Phonons and Near-Infrared Light”, *Phys. Rev. Lett.*, vol. 110, p. 037 403, 3 Jan. 2013. DOI: 10.1103/PhysRevLett.110.037403.
 - [197] J.-P. Rivera and H. Schmid, “On the birefringence of magnetoelectric BiFeO₃”, *Ferroelectrics*, vol. 204, no. 1, pp. 23–33, 1997. DOI: 10.1080/00150199708222185.
 - [198] H. Bouyanfif, “Heterostructures et super-réseaux à base du relaxeur PbMg_(1/3)Nb_(2/3)O₃ et du ferroélectrique PbTiO₃: Croissance et étude des effets de contrainte par diffraction de rayons X et par spectroscopie raman”, Ph.D. dissertation, UPJV Amiens, 2005.
 - [199] J. E. Giencke, C. M. Folkman, S.-H. Baek, and C.-B. Eom, “Tailoring the domain structure of epitaxial BiFeO₃ thin films”, *Current Opinion in Solid State and Materials Science*, vol. 18, no. 1, pp. 39–45, 2014, ISSN: 1359-0286. DOI: 10.1016/j.cossms.2013.11.003.
 - [200] M. D. Scafetta, A. M. Cordi, J. M. Rondinelli, and S. J. May, “Band structure and optical transitions in LaFeO₃: theory and experiment”, *Journal of Physics: Condensed Matter*, vol. 26, no. 50, p. 505 502, 2014. DOI: 10.1088/0953-8984/26/50/505502.
 - [201] D. Pavelyev *et al.*, “Short GaAs/AlAs superlattices as THz radiation sources”, 2008.
 - [202] B. Carcan, “Super-réseaux à base de BiFe₃ et de LaFeO₃ : croissance, étude structurale et transitions de phases”, Ph.D. dissertation, UPJV Amiens, 2016. [Online]. Available: <http://www.theses.fr/2016AMIE0024>.
 - [203] S. Das *et al.*, “Perspective: Emergent topologies in oxide superlattices”, *APL Materials*, vol. 6, no. 10, p. 100 901, 2018. DOI: 10.1063/1.5046100.
 - [204] R. Ramesh and D. G. Schlom, “Creating emergent phenomena in oxide superlattices”, *Nature Reviews Materials*, vol. 4, no. 4, pp. 257–268, Apr. 2019, ISSN: 2058-8437. DOI: 10.1038/s41578-019-0095-2.
-

X-ray beam path in the grazing incidence geometry

In the following, we derive the expression of the length travelled by the X-ray beam within the BFO sample when diffracted at the depth x_3 . For that we present in the **Fig A-1** the geometry of the diffraction experiment with the incident $L_{in} = [OP]$ and scattered $L_{out} = [PL]$ beam paths. The entrance point of the incident beam is O and the exit point of the scattered beam is L . The scattering process takes place at point P . The incident and output paths length are:

$$\begin{aligned} L_{in} &= x_3 / \sin(1^\circ) \\ L_{out} &= \sqrt{(x_L - L_{in})^2 + y_L^2 + z_L^2} \end{aligned} \tag{A.1}$$

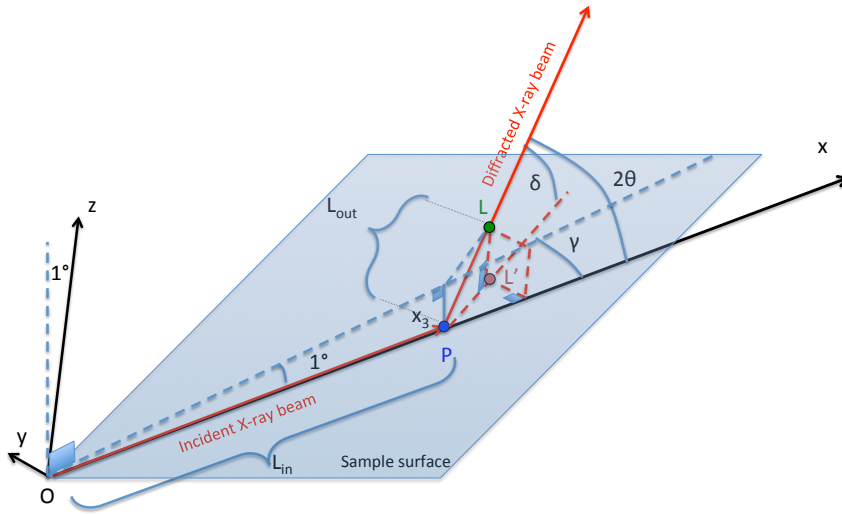


Fig A-1: Calculation of the path of the incident and scattered X-ray beam as a function of the depth x_3 .

The coordinates (x_L, y_L, z_L) are defined by the Bragg conditions, i.e. by the angles (δ, γ) , with:

$$\begin{aligned} y_L &= (x_L - L_{in})\tan(\gamma) \\ z_L &= x_L\tan(1^\circ) \end{aligned} \tag{A.2}$$

Another expression of z_L can be derived by considering the projection of $[PL]$ in the (O,x,y) plane, denoted $[PL']$:

$$\begin{aligned} [PL']^2 &= [(x_L - L_{in})^2 + y_L^2 + z_L^2]\cos^2(\delta) = (x_L - L_{in})^2 + y_L^2 \\ z_L &= \tan(\delta)\sqrt{(x_L - L_{in})^2[1 + \tan^2(\gamma)]} \end{aligned} \tag{A.3}$$

We need then to find x_L as a function of the experimental parameters. With $z_L = x_L\tan(1^\circ)$ and considering Eq. A.3, we arrive to $x_L\tan(1^\circ) = \tan(\delta)\sqrt{(x_L - L_{in})^2[1 + \tan^2(\gamma)]}$ which, once squared, leads to a second-degree polynomial expression:

$$x_L^2[\tan^2(1^\circ) - G] + x_L[2L_{in}G] - L_{in}^2G = 0 \tag{A.4}$$

with $G = \tan^2(\delta)[1 + \tan^2(\gamma)]$. The solution of this equation is:

$$x_L = L_{in} \left(\frac{G + \sqrt{G}\tan(1^\circ)}{G - \tan^2(1^\circ)} \right) = L_{in}F \tag{A.5}$$

The total path $L = L_{in} + L_{out}$ becomes:

$$\begin{aligned} L &= L_{in} \left[1 + (F - 1)\sqrt{1 + \tan^2(\gamma) + \tan^2(\delta)(1 + \tan^2(\gamma))} \right] \\ &= L_{in} [1 + F'] = \frac{x_3}{\sin(1^\circ)} [1 + F'] \end{aligned} \tag{A.6}$$

The F' factor is found equal to 0.0416 for the (± 101) Bragg peaks and equal to 0.0407 for the (± 201) Bragg peaks.

Appendix B

Optical pump fluence dependency of transient optical reflectivity in single domain BiFeO₃ thin film

In this appendix, the optical pump fluence has been verified to prevent the photo-assisted phase transition in single domain BiFeO₃ before performing the time-resolved pump-probe experiments.

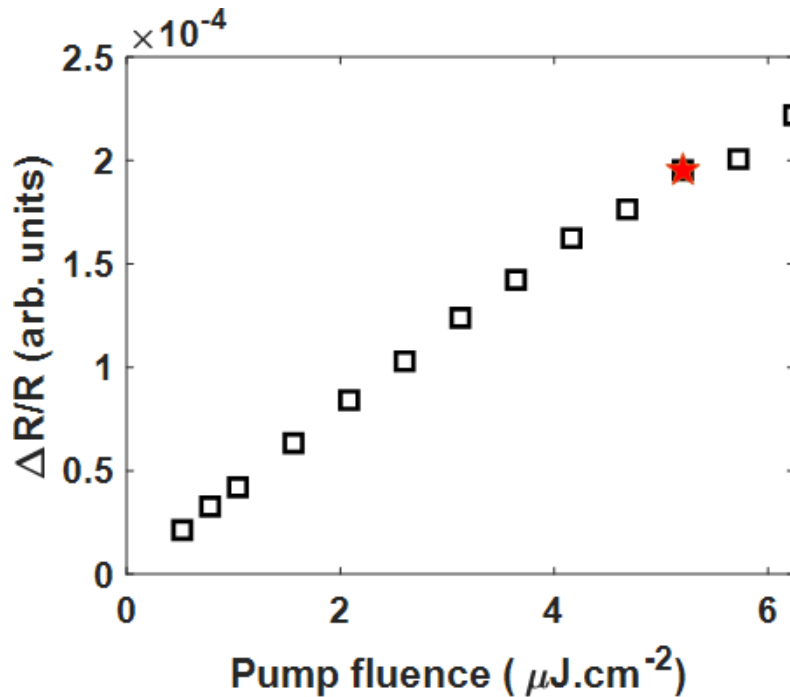


Fig B-1: Measurement of transient optical reflectivity at $t = 11$ ps on single domain BiFeO₃ as a function of optical pump fluence at 415 nm. The working fluence is indicated by “star”.

Fig B-1 shows the variation of the transient optical reflectivity as a function of optical pump fluence (415 nm) varying from 0 to over 6 $\mu\text{J}.\text{cm}^{-2}$. We can see that the transient optical reflectivity varies linearly when the optical pump fluence is gradually increased. Since the optical reflectivity is proportional to the variation of optical refractive index of BiFeO₃, this linear behavior indicates the BiFeO₃ atomic structure remain unchanged under the pump irradiation. In other words, no phase transition is triggered with the tested pump fluence. Finally the optical pump fluence is fixed to 5.2 $\mu\text{J}.\text{cm}^{-2}$ for the time-resolved optical spectroscopy measurement.

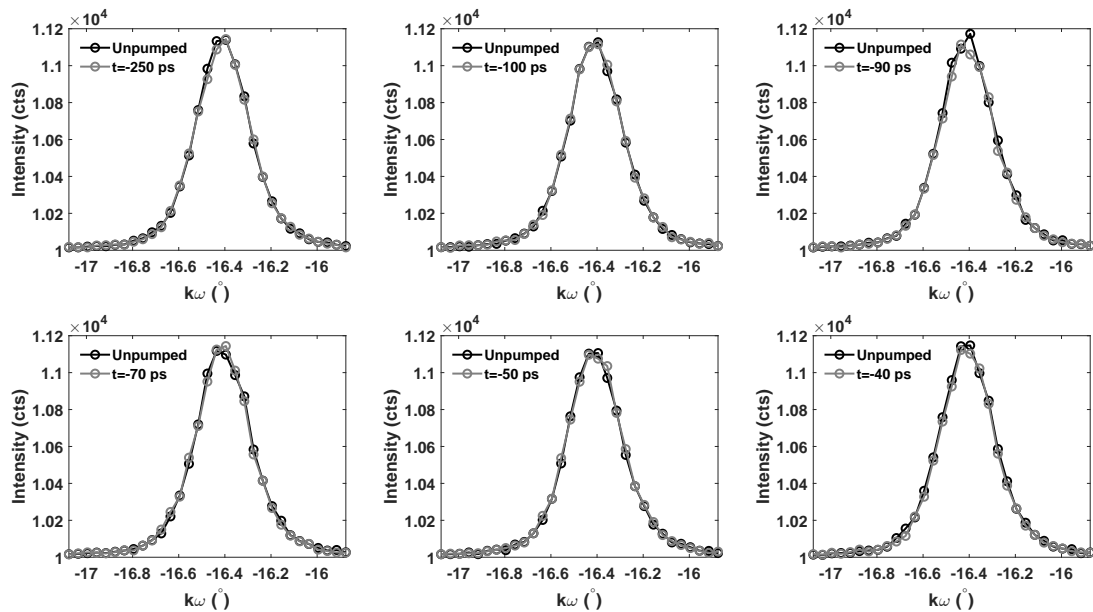
Appendix

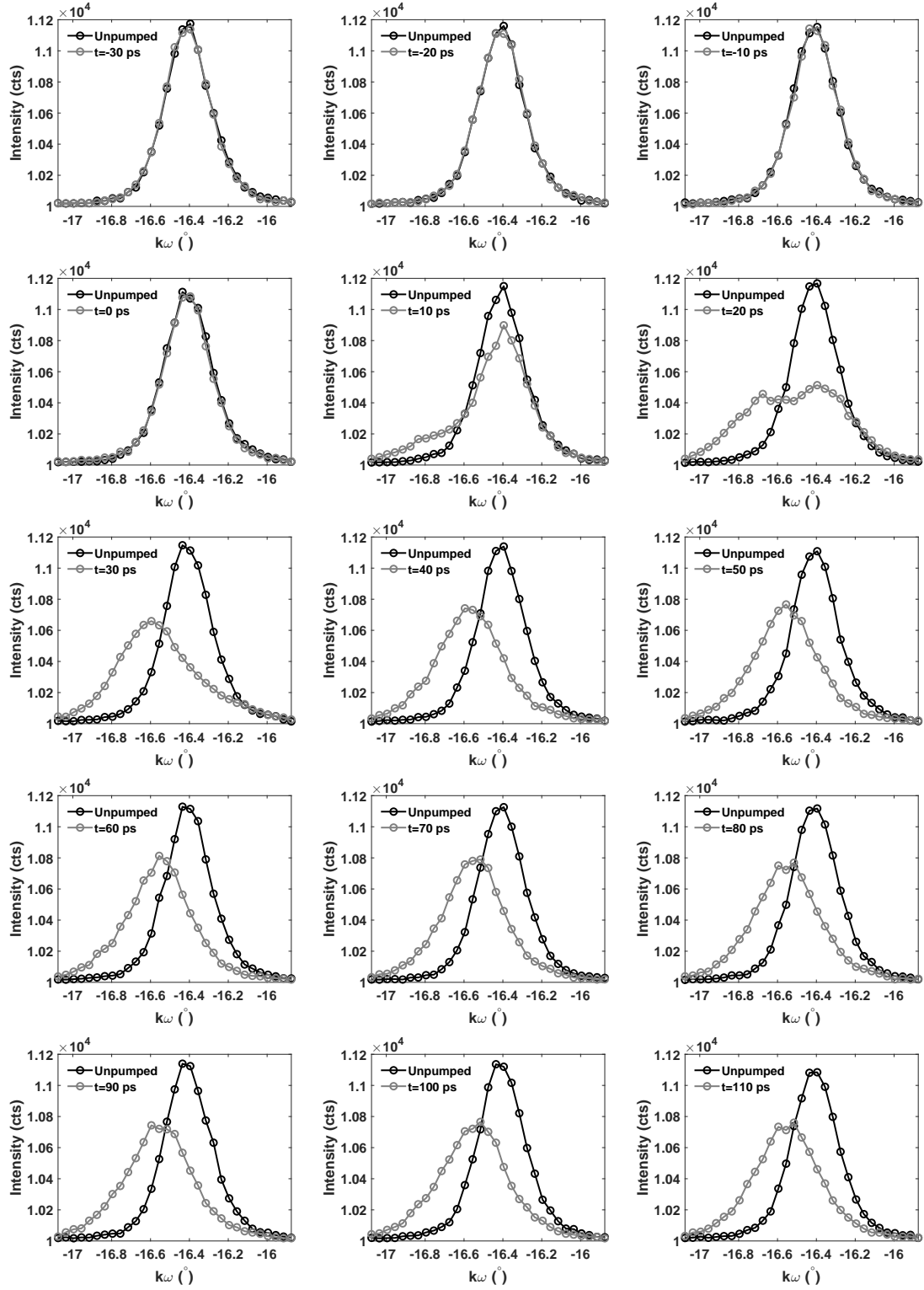
C

θ - 2θ scans for 4 chosen planes

In this part, the $k\omega$ scans will be presented for $(403)_m$, $(40\bar{3})_m$, $(530)_m$, $(5\bar{3}0)_m$ planes in the main text, for time delays from 250 ps before the arrival of optical pump pulses to 200 ps after the photoexcitation. Near $t=0$ ps, we have a temporal resolution of 10 ps.

$(403)_m$ plane





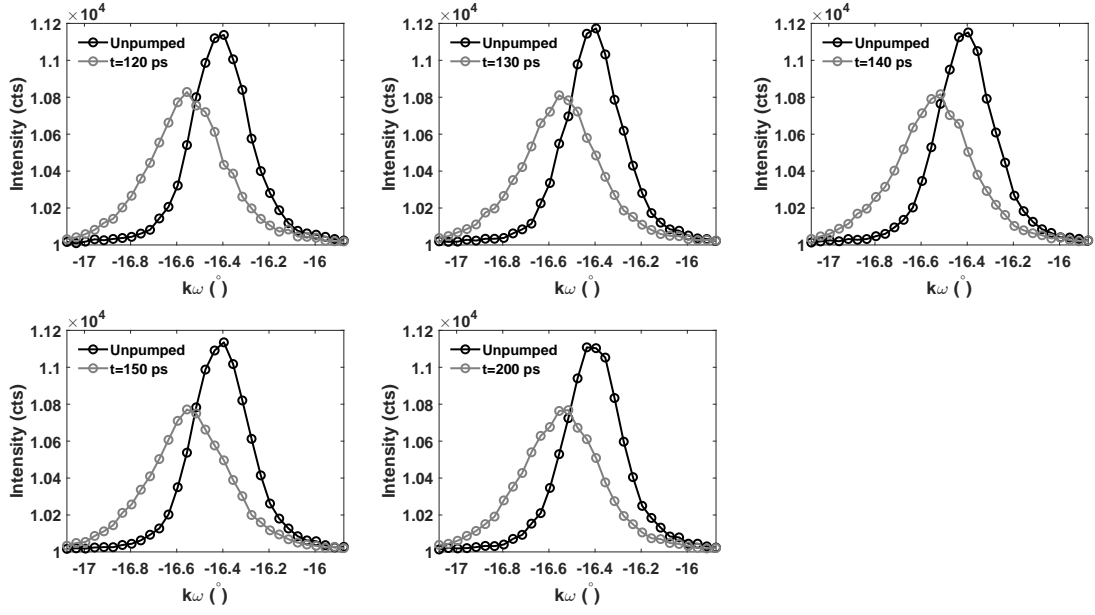
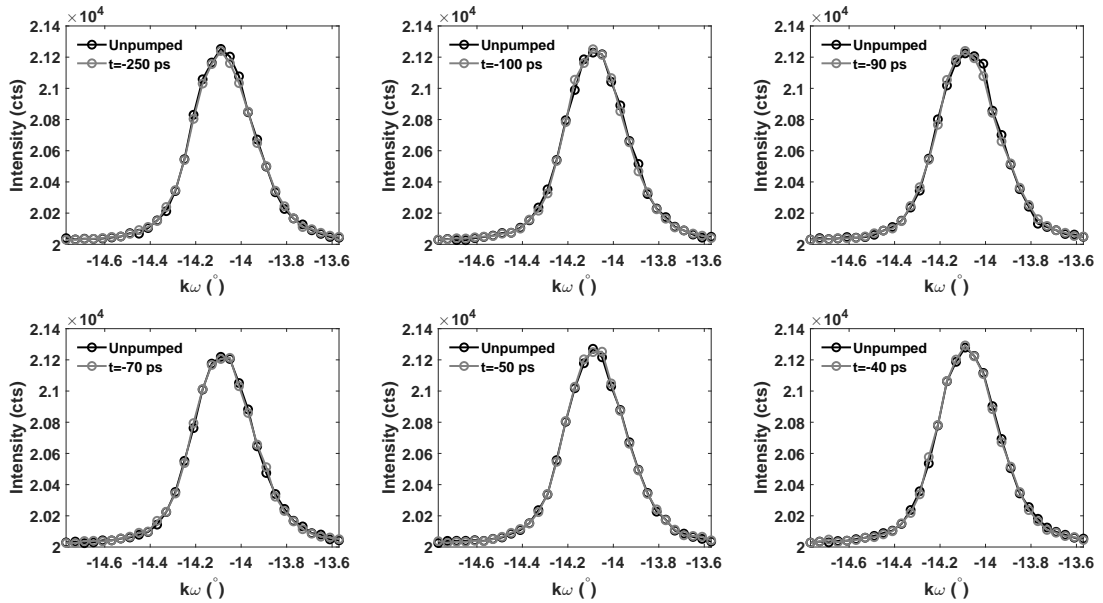
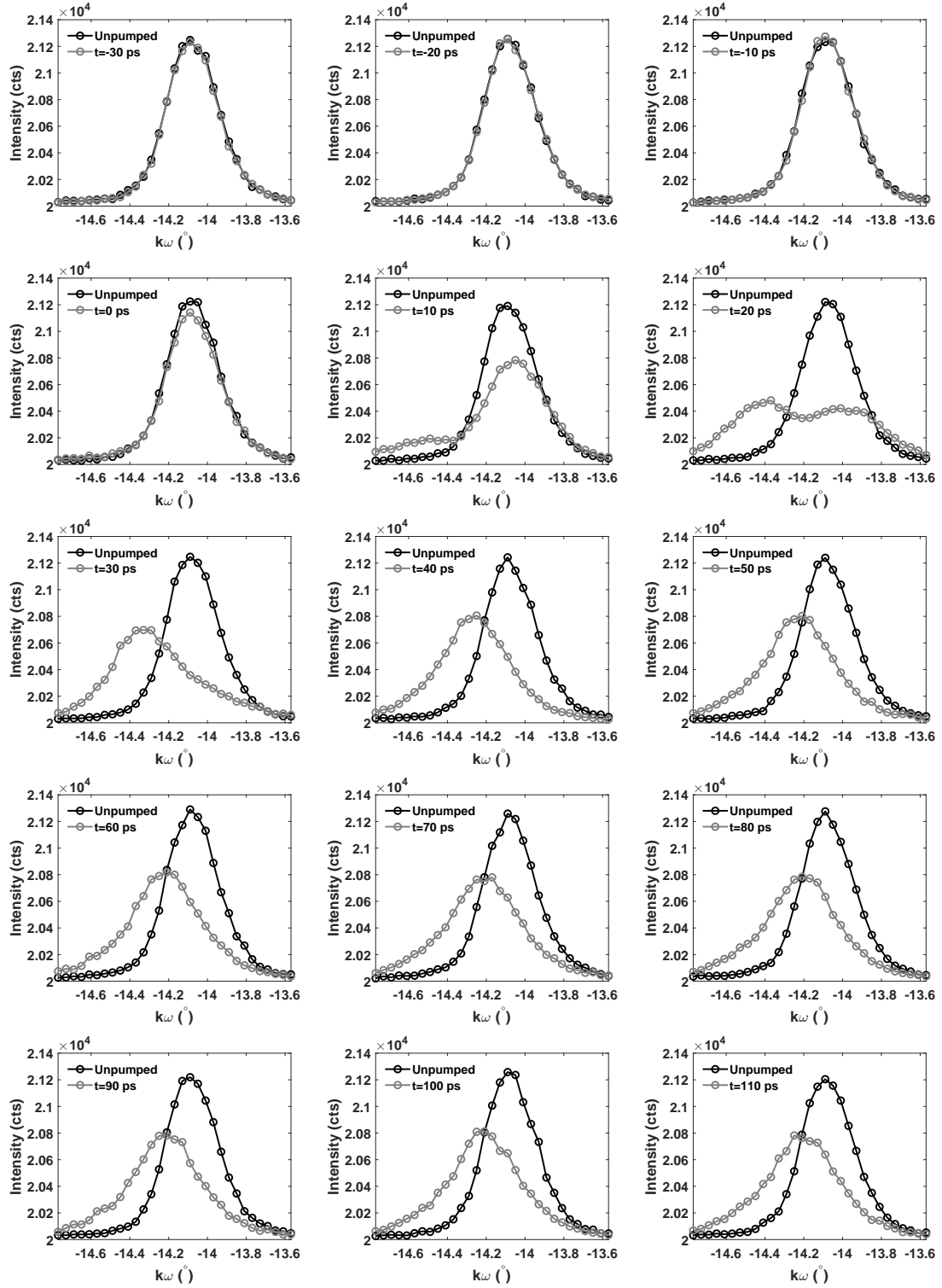


Fig C-1: Rocking curve of X ray diffraction on $(403)_m$ plane of single domain BiFeO_3 thin film form -250 ps to 200 ps with 0 ps corresponding to the arrival of the pump beam onto the sample's free surface. $k\omega$ is measured in relative angle.

$(40\bar{3})_m$ plane





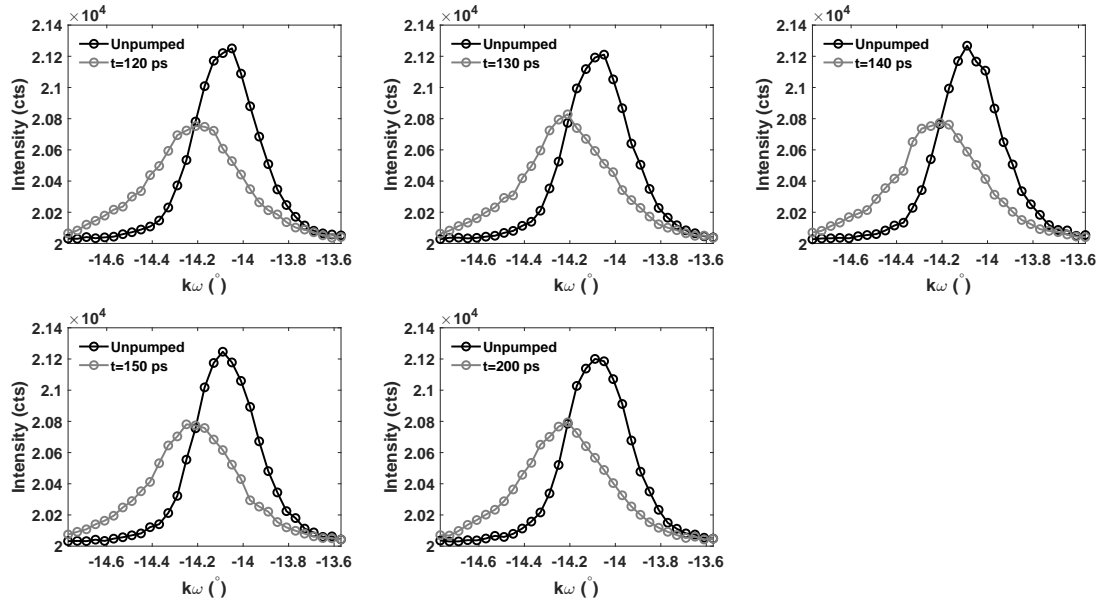
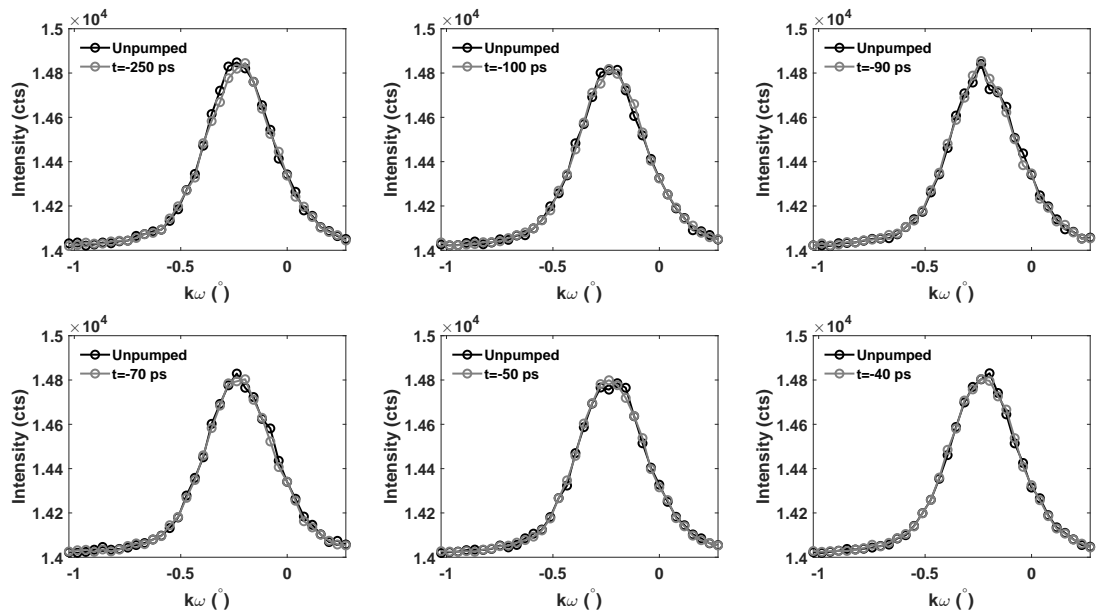
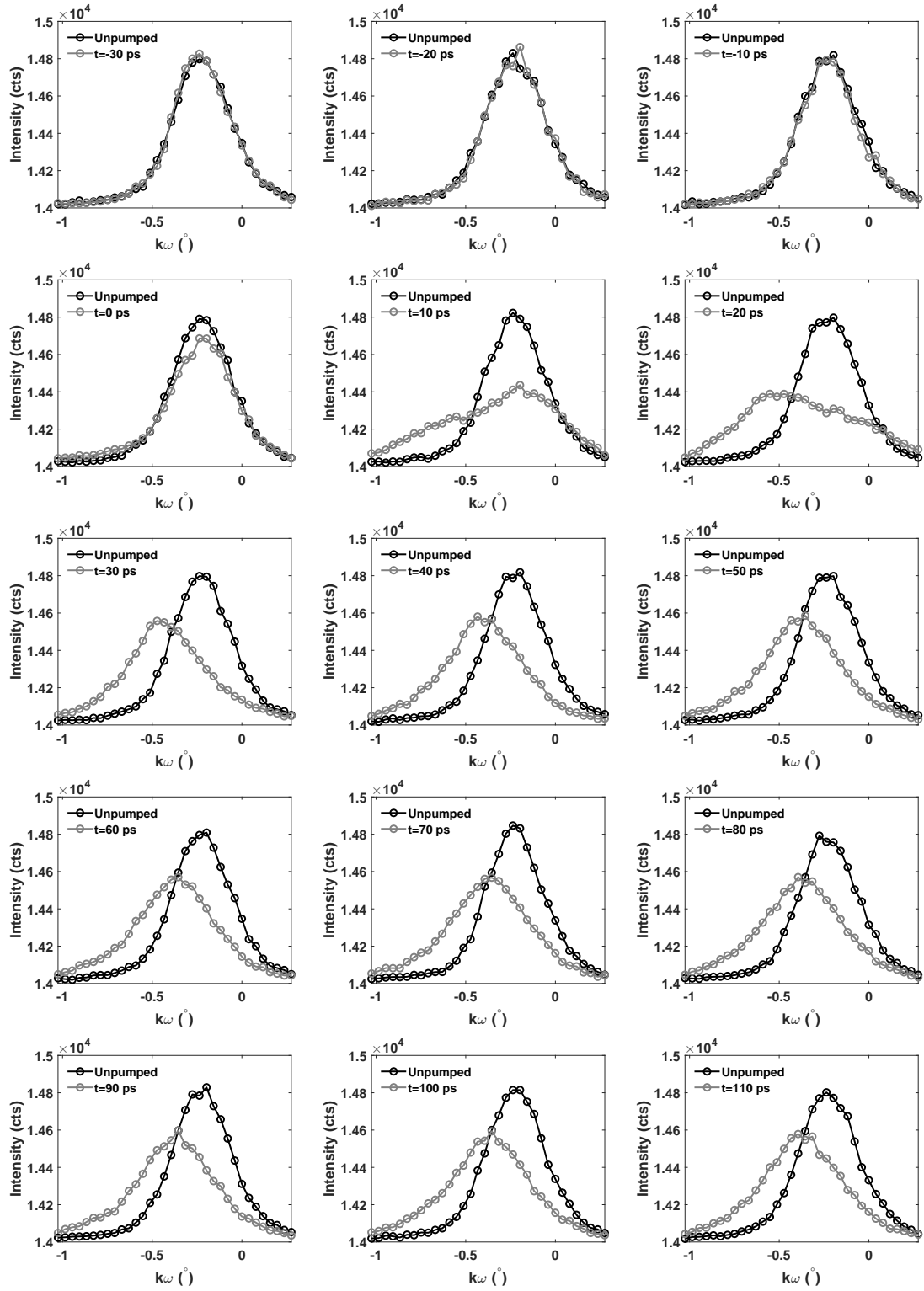


Fig C-2: Rocking curve of X ray diffraction on $(40\bar{3})_m$ plane of single domain BiFeO_3 thin film from -250 ps to 200 ps with 0 ps corresponding to the arrival of the pump beam.

$(530)_m$ plane





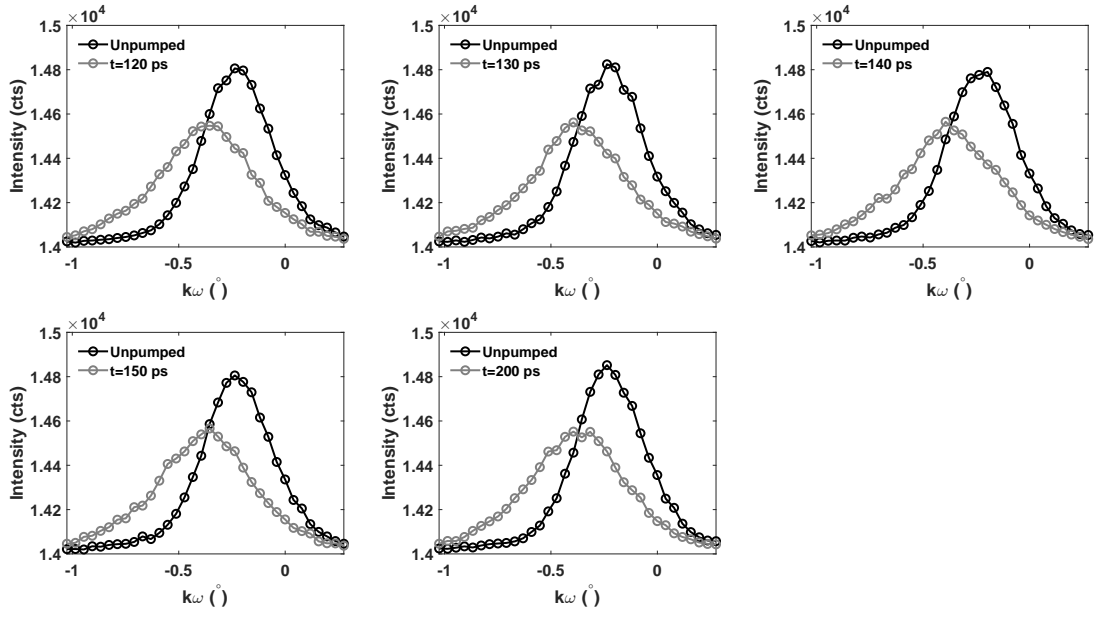
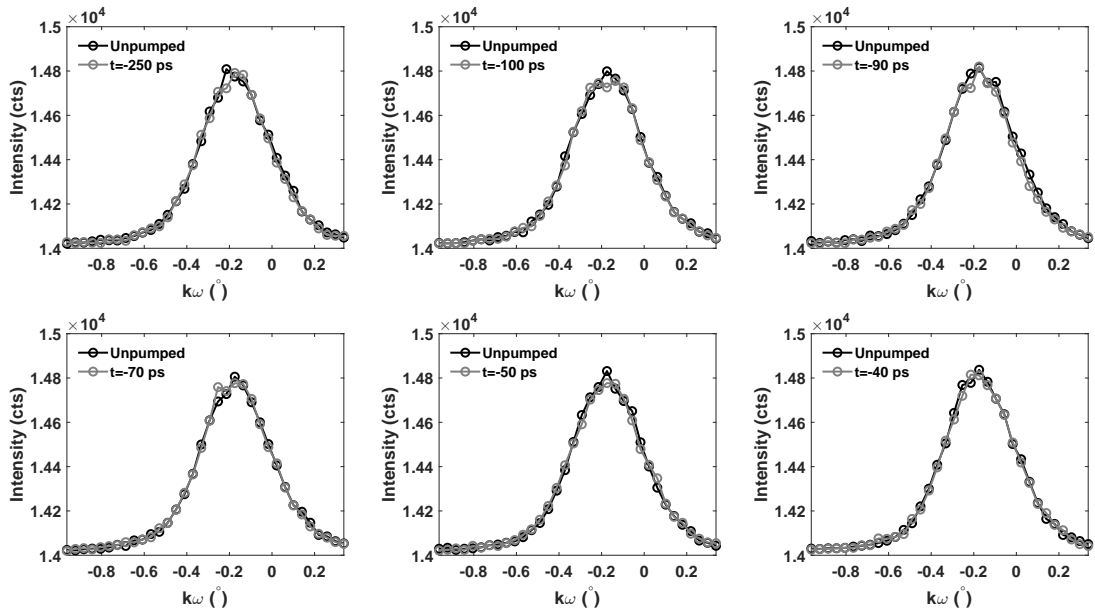
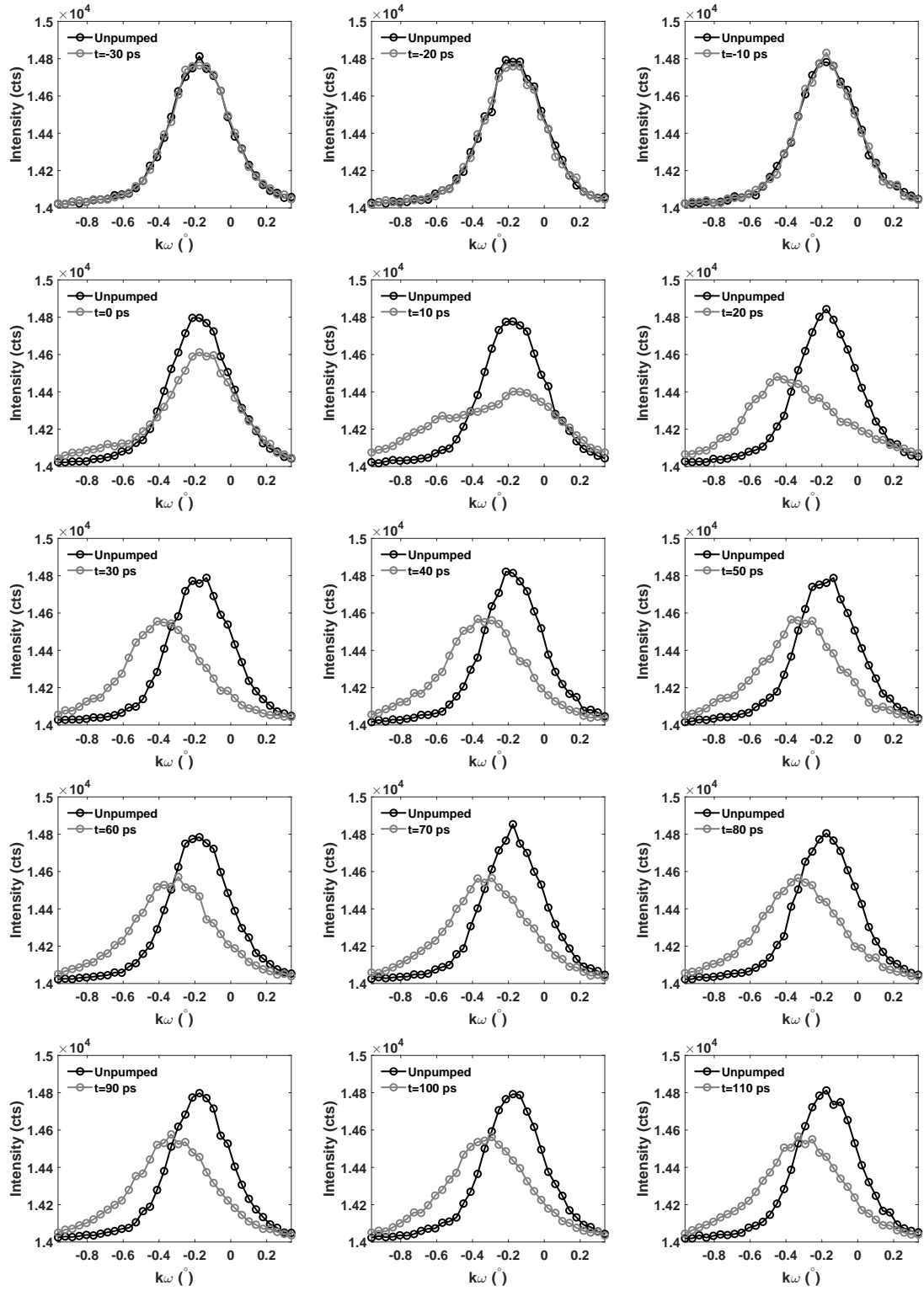


Fig C-3: Rocking curve of X ray diffraction on $(530)_m$ plane of single domain BiFeO_3 thin film form -250 ps to 200 ps with 0 ps corresponding to the arrival of the pump beam.

$(\bar{5}30)_m$ plane





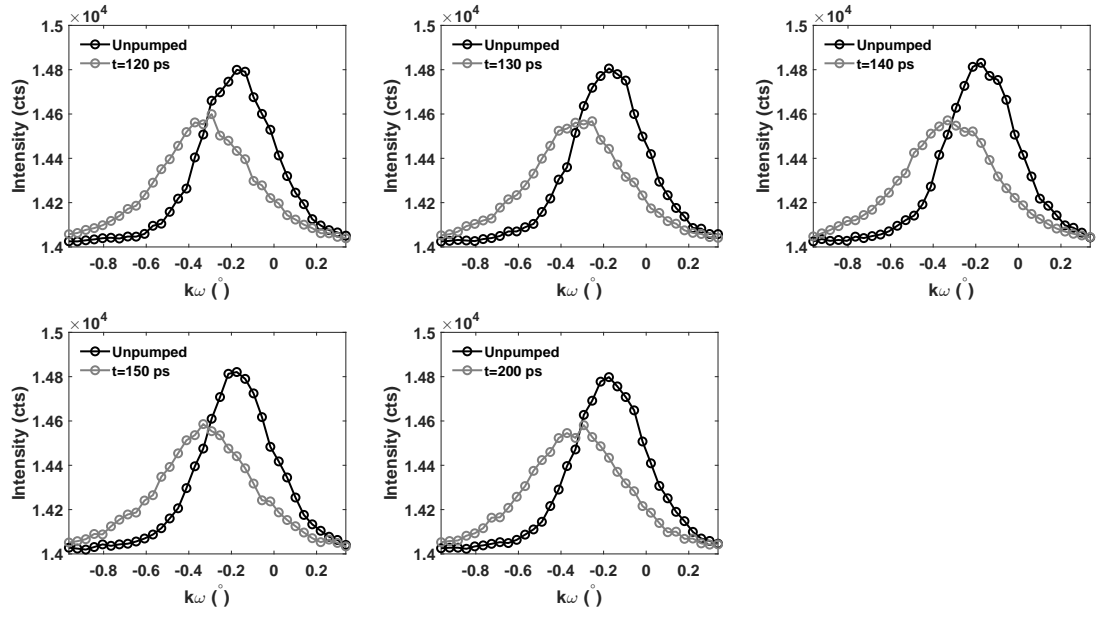


Fig C-4: Rocking curve of X ray diffraction on $(5\bar{3}0)_m$ of single domain BiFeO_3 thin film form -250 ps to 200 ps with 0 ps corresponding to the arrival of the pump beam.

For $(530)_m$ and $(5\bar{3}0)_m$ planes, a temporal shift of 10 ps is added in order to correct the temporal gating of the X-ray pulses, compared to the experiments on $(403)_m/(40\bar{3})_m$ planes.

Appendix D

Additional analysis of θ - 2θ scans of time-resolved X-ray diffraction on single domain BiFeO₃ thin film

Intensity variation of θ - 2θ scans

In this section, the variation of intensity of diffracted photons in time-resolved X-ray diffraction is checked for 4 chosen planes in single domain BiFeO₃ thin film.

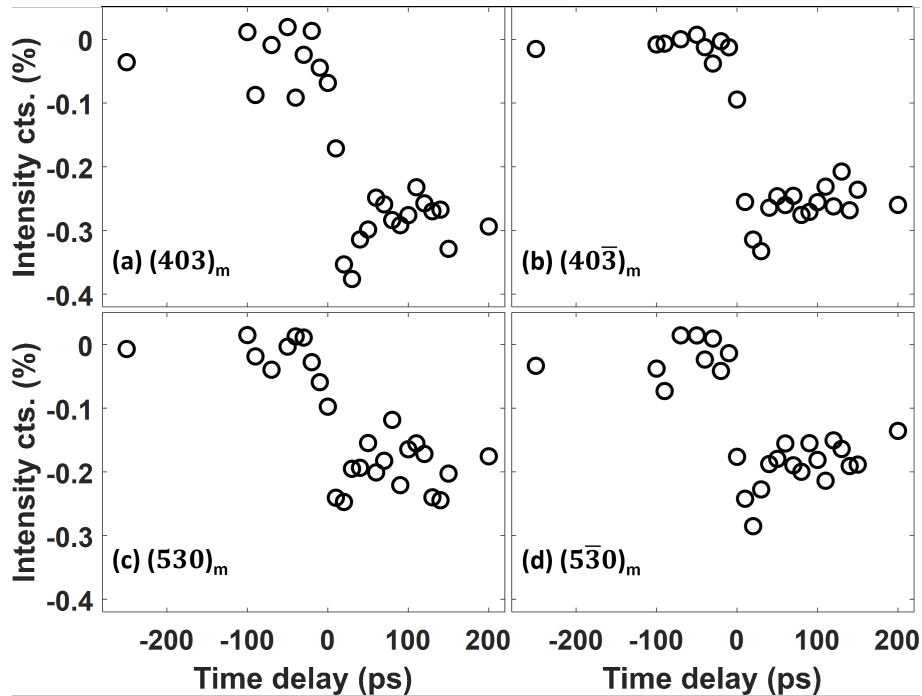


Fig D-1: Variation of diffracted photons intensity in time-resolved X-ray diffraction for $(403)_m$ (a), $(40\bar{3})_m$ (b), $(530)_m$ (c), $(5\bar{3}0)_m$ (d) planes.

As shown in **Fig D-1**, the intensity variation of diffracted photons has been recorded as a function of time delay for $(403)_m$, $(40\bar{3})_m$, $(530)_m$, $(5\bar{3}0)_m$ planes. The intensity counts are displayed in %, i.e. the difference of intensity recorded by UXFC 2D detector before and after the photoexcitation of BiFeO_3 by the optical pump pulses.

Before $t = 0$ ps, no optical pump pulses arrive onto the sample, so the intensity variation of diffracted photons is close to 0. Upon arrival of the pump pulses onto the sample, an negative intensity variation is obtained for all the planes, i.e. we have a loss of diffracted photons. And for the time delay up to 200 ps after the photoexcitation, a loss of small amount of diffracted photons is always present. But the variations are within 0.5 % and each time more than 10^4 photons are capture by the detector, the diffracted intensity loss can be neglected.

Width variation of Bragg peak of θ - 2θ scans

In this section, the variation of full-width-half-maximum (FWHM) of Bragg diffraction peak on $(403)_m$, $(40\bar{3})_m$, $(530)_m$, $(5\bar{3}0)_m$ planes has also been investigated as a function of time delay.

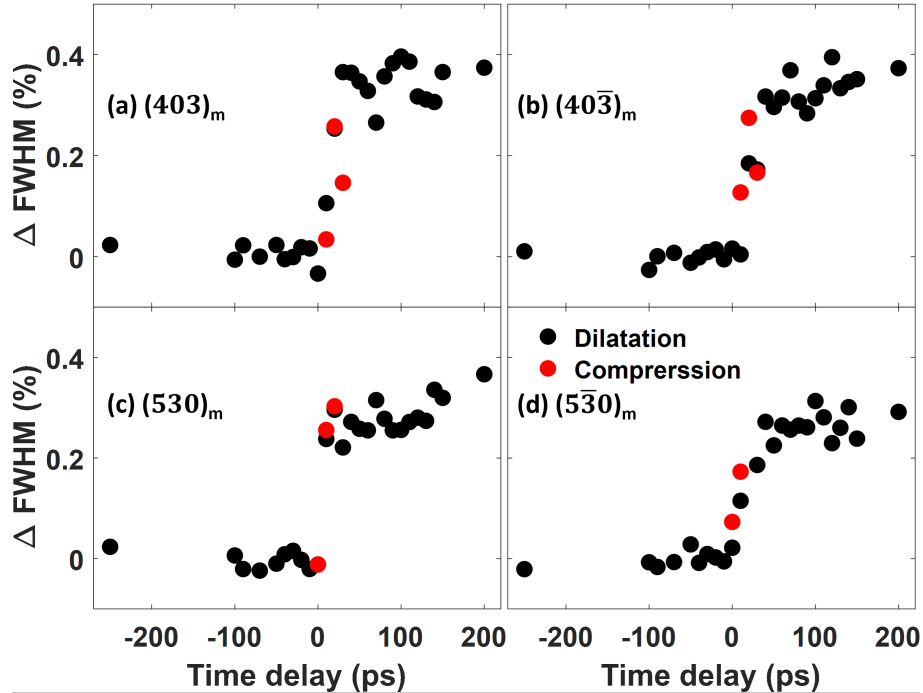


Fig D-2: Variation of FWHM of the Bragg diffraction peak on $(403)_m$, $(40\bar{3})_m$, $(530)_m$, $(5\bar{3}0)_m$ planes as a function of time delay. Black and red circles correspond to the tensile and compressive part of the BiFeO_3 interplanar distance upon photoexcitation

The results are shown in **Fig D-2**, both the dilatation and compression of the interplanar distance (see **Fig 5.32** in main text), i.e. decrease and increase of the

Bragg angle respectively (see **Fig 5.31** in main text), are indicated by black and red dots. For these 4 selected planes, an increase of the FWHM of the Bragg diffraction peak is observed for either an expansion or a compression of the structure.

According to the Scherrer equation [177], the average crystallite size L_c is related to the FWHM (β) the diffraction peak profile:

$$L_c = \frac{K\lambda}{\beta \cos(\theta_{Bragg})} \quad (\text{D.1})$$

with K a constant related to crystallite shape. As we observe an increase of the FWHM, the average crystallite size should be decreased.

Titre : Dynamique des phonons et des contraintes acoustiques ultra-rapides dans les matériaux ferroïques

Mot clés : Physique du solide, Optique ultra-rapide, Diffraction des rayons X résolue en temps, Couplage électron-phonon, Matériaux ferroïques, GeTe, BiFeO₃

Résumé : Dans ce travail de thèse, il est question de l'étude de la dynamique ultra-rapide des électrons et des phonons dans les matériaux ferroïques, tels le GeTe et BiFeO₃. Ces travaux expérimentaux sont réalisés en faisant appel à des techniques d'optique ultra-rapide et de diffraction des rayons X résolue en temps. Dans la première partie de ces recherches, nous avons étudié ces dynamiques dans le matériau GeTe qui est le système de référence des matériaux dit à « transition de phase » ou « mémoire optique ». Nous avons pu montrer par méthode pompe-sonde optique que lorsque le matériau cristallin GeTe était optiquement excité, les électrons « chauds » pouvaient diffuser à une distance environ sept fois plus grande que la pénétration optique du faisceau excitateur, ce qui n'a cependant pas été observé dans la phase amorphe où les électrons « chauds » restent localisés dans la zone d'absorption optique. Dans la seconde par-

tie, nous avons abordé comment il est possible de manipuler avec la lumière la structure des matériaux multiferroïques à l'échelle de la picoseconde. L'archétype est le BiFeO₃ qui présente à température ambiante un ordre ferroélectrique et magnétiques. Pour comprendre comment des impulsions de lumière ultra-rapide agissent sur la structure, nous avons notamment étudié la diffusion Brillouin résolue en temps qui nous a permis de mettre en évidence l'émission de phonon longitudinaux (LA) et transverse (TA) dans les couches minces de BiFeO₃. Dans un second temps, afin de quantifier l'amplitude de la déformation (non accessible par Brillouin), nous avons réalisé la diffraction des rayons X résolue en temps. Nous avons ainsi pu décrire comment la maille de BiFeO₃ se distord et notamment, nous avons montré et quantifié les champs de déformation longitudinaux (LA) et transversaux (TA) à l'échelle de la picoseconde.

Title: Ultrafast acoustic phonon and strain dynamics in ferroic materials

Keywords: Solid state physics, Ultrafast optics, Time-resolved X-ray diffraction, Electron-phonon coupling, Ferroic materials, GeTe, BiFeO₃

Abstract: In this thesis work, we study the ultrafast dynamics of electrons and phonons in ferroic materials, such as GeTe and BiFeO₃. This experimental work is carried out using ultra-fast optics and time-resolved X-ray diffraction techniques. In the first part of this research, we studied these dynamics in the GeTe material, which is the reference system for materials known as “phase transition” or “optical memory”. We were able to show by optical pump-probe method that when the crystalline material GeTe was optically excited, the “hot” electrons could diffuse at a distance approximately seven times greater than the optical penetration of the pump beam, which was however not observed in the amorphous phase where the “hot” electrons remain localized in the optical absorption zone. In the second part, we

discussed how it is possible to manipulate with light the structure of multiferroic materials at the picosecond scale. The archetype material is BiFeO₃ which presents a ferroelectric and magnetic order at room temperature. To understand how ultra-fast light pulses act on the structure, we have studied time-resolved Brillouin scattering to show the richness of the phonon emitted in BiFeO₃ thin films with the coexistence of longitudinal and transverse modes (LA, TA). In a second step, in order to quantify the amplitude of the deformation (not accessible by Brillouin), we carried out time-resolved X-ray diffraction. We were thus able to describe how the BiFeO₃ lattice distorts and in particular, we showed and quantified the longitudinal (LA) and transverse (TA) deformation fields at the picosecond scale.